



# **NEXT-GENERATION GENETICALLY-ENCODED FLUORESCENT SENSORS**

EDITED BY: Elizabeth C. Carroll and Shai Berlin

PUBLISHED IN: Frontiers in Cellular Neuroscience



# frontiers

## Frontiers eBook Copyright Statement

The copyright in the text of individual articles in this eBook is the property of their respective authors or their respective institutions or funders. The copyright in graphics and images within each article may be subject to copyright of other parties. In both cases this is subject to a license granted to Frontiers.

The compilation of articles constituting this eBook is the property of Frontiers.

Each article within this eBook, and the eBook itself, are published under the most recent version of the Creative Commons CC-BY licence.

The version current at the date of publication of this eBook is CC-BY 4.0. If the CC-BY licence is updated, the licence granted by Frontiers is automatically updated to the new version.

When exercising any right under the CC-BY licence, Frontiers must be attributed as the original publisher of the article or eBook, as applicable.

Authors have the responsibility of ensuring that any graphics or other materials which are the property of others may be included in the CC-BY licence, but this should be checked before relying on the CC-BY licence to reproduce those materials. Any copyright notices relating to those materials must be complied with.

Copyright and source acknowledgement notices may not be removed and must be displayed in any copy, derivative work or partial copy which includes the elements in question.

All copyright, and all rights therein, are protected by national and international copyright laws. The above represents a summary only. For further information please read Frontiers' Conditions for Website Use and Copyright Statement, and the applicable CC-BY licence.

ISSN 1664-8714

ISBN 978-2-88966-401-6

DOI 10.3389/978-2-88966-401-6

## About Frontiers

Frontiers is more than just an open-access publisher of scholarly articles: it is a pioneering approach to the world of academia, radically improving the way scholarly research is managed. The grand vision of Frontiers is a world where all people have an equal opportunity to seek, share and generate knowledge. Frontiers provides immediate and permanent online open access to all its publications, but this alone is not enough to realize our grand goals.

## Frontiers Journal Series

The Frontiers Journal Series is a multi-tier and interdisciplinary set of open-access, online journals, promising a paradigm shift from the current review, selection and dissemination processes in academic publishing. All Frontiers journals are driven by researchers for researchers; therefore, they constitute a service to the scholarly community. At the same time, the Frontiers Journal Series operates on a revolutionary invention, the tiered publishing system, initially addressing specific communities of scholars, and gradually climbing up to broader public understanding, thus serving the interests of the lay society, too.

## Dedication to Quality

Each Frontiers article is a landmark of the highest quality, thanks to genuinely collaborative interactions between authors and review editors, who include some of the world's best academicians. Research must be certified by peers before entering a stream of knowledge that may eventually reach the public - and shape society; therefore, Frontiers only applies the most rigorous and unbiased reviews.

Frontiers revolutionizes research publishing by freely delivering the most outstanding research, evaluated with no bias from both the academic and social point of view. By applying the most advanced information technologies, Frontiers is catapulting scholarly publishing into a new generation.

## What are Frontiers Research Topics?

Frontiers Research Topics are very popular trademarks of the Frontiers Journals Series: they are collections of at least ten articles, all centered on a particular subject. With their unique mix of varied contributions from Original Research to Review Articles, Frontiers Research Topics unify the most influential researchers, the latest key findings and historical advances in a hot research area! Find out more on how to host your own Frontiers Research Topic or contribute to one as an author by contacting the Frontiers Editorial Office: [researchtopics@frontiersin.org](mailto:researchtopics@frontiersin.org)



# NEXT-GENERATION GENETICALLY-ENCODED FLUORESCENT SENSORS

Topic Editors:

**Elizabeth C. Carroll**, Delft University of Technology, Netherlands

**Shai Berlin**, Technion Israel Institute of Technology, Israel

**Citation:** Carroll, E. C., Berlin, S., eds. (2021). Next-Generation Genetically-Encoded Fluorescent Sensors. Lausanne: Frontiers Media SA.  
doi: 10.3389/978-2-88966-401-6

# Table of Contents

- 04 Editorial: Next-Generation Genetically-Encoded Fluorescent Sensors**  
Shai Berlin and Elizabeth C. Carroll
- 06 Development and Application of Sub-Mitochondrial Targeted  $\text{Ca}^{2+}$  Biosensors**  
Markus Waldeck-Weiermair, Benjamin Gottschalk, Corina T. Madreiter-Sokolowski, Jeta Ramadani-Muja, Gabriela Ziomek, Christiane Klec, Sandra Burgstaller, Helmut Bischof, Maria R. Depaoli, Emrah Eroglu, Roland Malli and Wolfgang F. Graier
- 18 Fluorescent Biosensors for Neurotransmission and Neuromodulation: Engineering and Applications**  
Anna V. Leopold, Daria M. Shcherbakova and Vladislav V. Verkhusa
- 36 Engineering Photoactivatability in Genetically Encoded Voltage and pH Indicators**  
Sungmoo Lee, Yoon-Kyu Song and Bradley J. Baker
- 46 Biosensors Show the Pharmacokinetics of S-Ketamine in the Endoplasmic Reticulum**  
Kallol Bera, Aron Kamajaya, Amol V. Shivange, Anand K. Muthusamy, Aaron L. Nichols, Philip M. Borden, Stephen Grant, Janice Jeon, Elaine Lin, Ishak Bishara, Theodore M. Chin, Bruce N. Cohen, Charlene H. Kim, Elizabeth K. Unger, Lin Tian, Jonathan S. Marvin, Loren L. Looger and Henry A. Lester
- 58 Live-Cell Assays for Cell Stress Responses Reveal New Patterns of Cell Signaling Caused by Mutations in Rhodopsin,  $\alpha$ -Synuclein and TDP-43**  
Kevin M. Harlen, Elizabeth C. Roush, Joseph E. Clayton, Scott Martinka and Thomas E. Hughes
- 72 Reversible Loss of Hippocampal Function in a Mouse Model of Demyelination/Remyelination**  
Aniruddha Das, Chinthasagar Bastian, Lexie Trestan, Jason Suh, Tanujit Dey, Bruce D. Trapp, Selva Baltan and Hod Dana
- 84 A Bright and Colorful Future for G-Protein Coupled Receptor Sensors**  
Luca Ravotto, Loïc Duffet, Xuehan Zhou, Bruno Weber and Tommaso Patriarchi
- 93 Red Photoactivatable Genetic Optical-Indicators**  
Wessal Hussein and Shai Berlin
- 107 Nanobody-Based Probes for Subcellular Protein Identification and Visualization**  
Marit A. de Beer and Ben N. G. Giepmans



# Editorial: Next-Generation Genetically-Encoded Fluorescent Sensors

Shai Berlin<sup>1\*</sup> and Elizabeth C. Carroll<sup>2\*</sup>

<sup>1</sup> Department of Neuroscience, The Ruth and Bruce Rappaport Faculty of Medicine, Technion Israel Institute of Technology, Haifa, Israel, <sup>2</sup> Department of Imaging Physics, Delft University of Technology, Delft, Netherlands

**Keywords:** biosensor, fluorescent, genetically encoded activity indicators, photoactivable, neuron, activity, disease

## Editorial on the Research Topic

### Next-Generation Genetically-Encoded Fluorescent Sensors

Fluorescent probes, or biosensors, are cleverly designed molecules that are able to transform the act of binding/reacting with a unique target (e.g., analyte) into a fluorescent signal ( $\Delta F/F$ ). Of the various kinds (e.g., small molecules, fluorescent proteins), genetically-encoded fluorescent sensors are particularly popular as these can be targeted to select cells or subcellular regions via gene promoters, conditional expression systems, protein recombination schemes or localization sequences, to name a few. In particular, the field of Genetically-Encoded Indicators (GExI;  $x$ —calcium, neurotransmitter, voltage, etc.) continues to flourish as researchers explore and develop new methods to improve sensitivity, specificity, and compatibility of probes for multi-channel microscopy. Contemporary GExIs include a single fluorescent protein as their fluorescent core (commonly GFP or RFP), making them smaller than FRET-based probes as well as allowing users to more easily combine these—crosstalk free—with added optogenetic or photochemical tools that require their own set of wavelengths for activation. Owing to these features, GExIs have become valuable tools for cell biologists with a broad range of questions. In this Research Topic on “Next Generation Genetically-Encoded Fluorescent sensors,” we collate reviews and research articles representative of the breadth of the field today, including descriptions of the functioning principles of genetically-encoded fluorescent biosensors, their potential and pitfalls, examples of applications, and original reports describing the development of new probes or use of novel biosensors to study diseases.

We present three retrospective articles by leading scientists in the field. The review by Leopold et al. provides a concise overview of current biosensors best suited for imaging neurotransmission and neuromodulation in neurons. The authors describe operating principles of how binding of target molecules changes the fluorescence of the probe, and detail a workflow for their development. Complementary to this, Ravotto et al., offer a fresh perspective on probes that link G-Protein Coupled Receptors to circularly-permuted GFP (cpGFP), and their potential for remote and real-time monitoring of various neurotransmitters, such as dopamine, in the brains of living animals. The authors discuss potential challenges when using these emerging tools and further suggest new designs. Finally, a comprehensive review by de Beer and Giepmans details the use of probes based on single-chain antigen binding proteins (nanobodies) for subcellular identification of endogenous proteins. The authors review the current state of the art of nanobodies fused to fluorophores and peroxidases, including discussion of different labeling strategies and applications for multi-modal nanobody probes in correlative light and electron microscopy.

## OPEN ACCESS

### Edited and reviewed by:

Arianna Maffei,  
Stony Brook University, United States

### \*Correspondence:

Shai Berlin  
shai.berlin@technion.ac.il  
Elizabeth C. Carroll  
E.C.M.Carroll@tudelft.nl

### Specialty section:

This article was submitted to  
Cellular Neurophysiology,  
a section of the journal  
Frontiers in Cellular Neuroscience

**Received:** 10 November 2020

**Accepted:** 12 November 2020

**Published:** 03 December 2020

### Citation:

Berlin S and Carroll EC (2020)  
Editorial: Next-Generation  
Genetically-Encoded Fluorescent  
Sensors.  
Front. Cell. Neurosci. 14:627792.  
doi: 10.3389/fncel.2020.627792

Four articles in the collection focus on probing diseases by developing novel assays and adapting GExIs to meet a specific need. Waldeck-Weiermair et al., describe their efforts to understand sub-organellar  $\text{Ca}^{2+}$ -uptake by mitochondria. To address this, the authors explore novel targeting peptides to localize extant green- and red-emitting GECIs (c-calcium) to the intermembrane space and cristae lumen of mitochondria. Their approach proved successful and they employ it to examine the effects of gene knock-down on  $\text{Ca}^{2+}$ -dynamics in mitochondria. They go on to show that several GECIs of different colors can be combined in the same cell to examine  $\text{Ca}^{2+}$ -levels in distinct sub-compartments of the organelle. Harlen et al., focus their attention on  $\text{Ca}^{2+}$ -dynamics of the endoplasmic reticulum (ER). Here, the authors try to understand how different disease-relevant mutations in rhodopsin or  $\alpha$ -synuclein affect cell stress and intrinsic ER-signaling. This goal motivated them to devise a semi-high throughput live-cell assay for ER-mediated cell stress and second messenger signaling. They analyze single-cell  $\text{Ca}^{2+}$ -profiles by combining use of a green GECI, a red cAMP biosensor (R-cADDIS) and an optical actuator bPAC (blue light-activated adenylyl cyclase). Together these provide new views on disease processes. Bera et al., also look to the ER, where instead of studying endogenous analytes within the organelle, they engineer a novel family of biosensors—iSKetSnFR (Intensity-based S-ketamine-sensing fluorescent reporters)—to examine whether S-ketamine, an antidepressant drug, can pass the plasma membrane and enter the ER lumen. The authors find that S-ketamine can rapidly enter and exit the ER, which leads them to propose that the antidepressant actions of the drug may also involve intracellular activity of the drug on organellar ion channels, receptors, and transporters. Das et al. also explore a disease of the central nervous system, namely multiple sclerosis (MS). They ask whether prolonged demyelination and remyelination have any effect on neuronal activity in the hippocampus. The authors combine electrophysiological recordings and imaging of GECIs to monitor neural firing during demyelination over a period of 100 days. They find that demyelination greatly reduces synaptic transmission and firing rates in CA1 and DG neurons *in vivo*. The authors suggest that GECIs can also be used to examine effects of therapeutics on CNS neurons.

Lastly, two original reports focus on the development of photoactivatable (PA) fluorescent probes. PA-probes are particularly useful when trying to obtain relevant fluorescent

signals solely from cells defined by the user without excessive background fluorescence from nearby cells. Lee et al., engineer photoactivatable genetically encoded voltage- (GEVI) and pH (GEPI)-indicators and characterize these in HEK293 cells. They first explore several probe designs for a GEVI, namely using a single fluorescent protein (cpGFP), a FRET pair or a pH-sensitive variant of GFP, ecliptic pHluorin. The candidate bearing the ecliptic pHluorin exhibited both coveted features, explicitly photoactivation and voltage-dependent fluorescence changes. This led the team to the engineering of a pH-sensitive photoactivatable GFP that varies its brightness in response to different intracellular pH. Analogously, Hussein and Berlin explore the photoactivation of red GECIs, leading them to develop PA-R-GECO, a red photoactivatable  $\text{Ca}^{2+}$ -probe. This expands the color palette of photoactivatable  $\text{Ca}^{2+}$ -indicators. In the process of testing photoactivation in several other red GECIs, they also create a new photoactivatable RFP variant, namely PA-mRuby3, that undergoes strong photoactivation.

Collectively this collection of articles highlight the rich possibilities for discovery remaining in the field of genetically-encoded fluorescent sensors.

## AUTHOR CONTRIBUTIONS

SB and EC wrote the manuscript. Both authors contributed to the article and approved the submitted version.

## FUNDING

Support was provided by the Israel Science Foundation (SB; 1096/17) and the Mallat Family Fund for Medical research (SB; 1015018).

**Conflict of Interest:** The authors declare that the research was conducted in the absence of any commercial or financial relationships that could be construed as a potential conflict of interest.

Copyright © 2020 Berlin and Carroll. This is an open-access article distributed under the terms of the Creative Commons Attribution License (CC BY). The use, distribution or reproduction in other forums is permitted, provided the original author(s) and the copyright owner(s) are credited and that the original publication in this journal is cited, in accordance with accepted academic practice. No use, distribution or reproduction is permitted which does not comply with these terms.



# Development and Application of Sub-Mitochondrial Targeted $\text{Ca}^{2+}$ Biosensors

Markus Waldeck-Weiermair<sup>1\*</sup>, Benjamin Gottschalk<sup>1</sup>, Corina T. Madreiter-Sokolowski<sup>1,2</sup>, Jeta Ramadani-Muja<sup>1</sup>, Gabriela Ziomek<sup>1</sup>, Christiane Klec<sup>1,3</sup>, Sandra Burgstaller<sup>1</sup>, Helmut Bischof<sup>1</sup>, Maria R. Depaoli<sup>1</sup>, Emrah Eroglu<sup>4</sup>, Roland Malli<sup>1,5</sup> and Wolfgang F. Graier<sup>1,5</sup>

<sup>1</sup> Molecular Biology and Biochemistry, Gottfried Schatz Research Center, Medical University of Graz, Graz, Austria, <sup>2</sup> Energy Metabolism Laboratory, Institute of Translational Medicine, D-HEST, Swiss Federal Institute of Technology (ETH), Zurich, Switzerland, <sup>3</sup> Department of Internal Medicine, Division of Oncology, Medical University of Graz, Graz, Austria, <sup>4</sup> Department of Medicine, Brigham and Women's Hospital, Harvard Medical School, Boston, MA, United States, <sup>5</sup> BioTechMed-Graz, Graz, Austria

## OPEN ACCESS

### Edited by:

Shai Berlin,  
Technion Israel Institute  
of Technology, Israel

### Reviewed by:

Dmitry Lim,  
University of Eastern Piedmont, Italy  
Varda Shoshan-Barmatz,  
Ben-Gurion University of the Negev,  
Israel

### \*Correspondence:

Markus Waldeck-Weiermair  
markus.weiermair@medunigraz.at

### Specialty section:

This article was submitted to  
Cellular Neurophysiology,  
a section of the journal  
Frontiers in Cellular Neuroscience

**Received:** 12 July 2019

**Accepted:** 20 September 2019

**Published:** 04 October 2019

### Citation:

Waldeck-Weiermair M,  
Gottschalk B,  
Madreiter-Sokolowski CT,  
Ramadani-Muja J, Ziomek G, Klec C,  
Burgstaller S, Bischof H, Depaoli MR,  
Eroglu E, Malli R and Graier WF  
(2019) Development and Application  
of Sub-Mitochondrial Targeted  $\text{Ca}^{2+}$   
Biosensors.  
Front. Cell. Neurosci. 13:449.  
doi: 10.3389/fncel.2019.00449

Mitochondrial  $\text{Ca}^{2+}$  uptake into the mitochondrial matrix is a well-established mechanism. However, the sub-organellar  $\text{Ca}^{2+}$  kinetics remain elusive. In the present work we identified novel site-specific targeting sequences for the intermembrane space (IMS) and the cristae lumen (CL). We used these novel targeting peptides to develop green- and red-  $\text{Ca}^{2+}$  biosensors targeted to the IMS and to the CL. Based on their distinctive spectral properties, and comparable sensitivities these novel constructs were suitable to visualize  $\text{Ca}^{2+}$ -levels in various (sub) compartments in a multi-chromatic manner. Functional studies that applied these new biosensors revealed that knockdown of MCU and EMRE yielded elevated  $\text{Ca}^{2+}$  levels inside the CL but not the IMS in response to  $\text{IP}_3$ -generating agonists. Knockdown of VDAC1, however, strongly impeded the transfer of  $\text{Ca}^{2+}$  through the OMM while the cytosolic  $\text{Ca}^{2+}$  signal remained unchanged. The novel sub-mitochondrially targeted  $\text{Ca}^{2+}$  biosensors proved to be suitable for  $\text{Ca}^{2+}$  imaging with high spatial and temporal resolution in a multi-chromatic manner allowing simultaneous measurements. These informative biosensors will facilitate efforts to dissect the complex sub-mitochondrial  $\text{Ca}^{2+}$  signaling under (patho)physiological conditions.

**Keywords:**  $\text{Ca}^{2+}$  measurements, biosensors, mitochondrial  $\text{Ca}^{2+}$ , mitochondrial cristae,  $\text{Ca}^{2+}$ , live cell imaging, mitochondria

## INTRODUCTION

Embedded between the outer (OMM) and the inner mitochondrial membrane (IMM) the mitochondrial intermembrane space (IMS) including the cristae lumen (CL) represents the smallest mitochondrial sub-compartment. This specialized area is of utmost importance for the regulation of mitochondrial protein import, lipid homeostasis, energy metabolism and metal ion exchange to maintain cellular functions (Frey and Mannella, 2000; Herrmann, 2010; Shoshan-Barmatz et al., 2018). While the OMM is permeable for molecules below 5 kDa via VDAC1 (Camara et al., 2017), the IMM is impermeable. Thus, the transfer of biomolecules across the IMM into the mitochondrial

matrix relies on transporters, carriers and exchangers. Among these the mitochondrial  $\text{Ca}^{2+}$  uptake machinery displays a frequently studied mechanism due to its importance for the regulation of various mitochondrial functions. The molecular nature of the mitochondrial  $\text{Ca}^{2+}$  uniporter is a complex formation of several interacting proteins located in the IMM including the pore forming subunit mitochondrial  $\text{Ca}^{2+}$  uniporter (MCU) (Baughman et al., 2011), the essential mitochondrial regulator (EMRE) (Sancak et al., 2013) and the two gatekeeper opponents, the mitochondrial  $\text{Ca}^{2+}$  uptake 1 and 2 (MICU1 and MICU2) (Kamer and Mootha, 2014). Recently, we and others demonstrated that MICU1 forms multimers and rearranges its oligomeric state as soon as  $\text{Ca}^{2+}$  enters by binding to the EF hand motifs that are localized toward the IMS (Wang et al., 2014; Waldeck-Weiermair et al., 2015), which in turn regulates MCU/EMRE channel activity. Notably in most non-excitatory cells the endoplasmic reticulum (ER) represents the main source of  $\text{Ca}^{2+}$  to be requested into the mitochondrial matrix. The direct transfer of  $\text{Ca}^{2+}$  from the ER into the mitochondrial matrix has been studied intensively and was described to take place in focal contact sites between the two organelles, the mitochondria-associated membranes (MAMs) (van Vliet et al., 2014). The formation of MAMs and as a consequence the transfer of  $\text{Ca}^{2+}$  from the ER to the mitochondria is crucially dependent on the distance between the two organelles (Szymański et al., 2017). On the other hand, the voltage dependent anion channel 1 (VDAC1) represents the most abundant porin in the OMM accounting for its permeability for cations like  $\text{Ca}^{2+}$  (Camara et al., 2017). As one of the most studied mitochondrial proteins VDAC1 does not just serve as a non-selective hole, but contributes to numerous  $\text{Ca}^{2+}$  dependent functions such as  $\text{Ca}^{2+}$ -induced apoptosis (Weisthal et al., 2014),  $\text{Ca}^{2+}$ -modulated energy production (Cárdenas et al., 2010; Shoshan-Barmatz and Mizrahi, 2012), global  $\text{Ca}^{2+}$  signaling (Berridge et al., 2003) and ER-to-mitochondria  $\text{Ca}^{2+}$  transport (Szabadkai et al., 2006; Gautier et al., 2016). For the latter it has been suggested that VDAC1 may form supra-molecular complexes that occur at MAMs by the interaction with GRP75 (Szabadkai et al., 2006), mitofusin-2 (Shoshan-Barmatz et al., 2018) and the  $\text{IP}_3$  receptor 1 (Szabadkai et al., 2006). Indeed, regulation of mitochondrial  $\text{Ca}^{2+}$  uptake is especially critical in neurons. On the one hand excessive mitochondrial  $\text{Ca}^{2+}$  induce cell death by the release of pro-apoptotic proteins like cytochrome C that is mainly harbored within mitochondrial cristae (Cogliati et al., 2016) leading to neurodegenerative pathologies like Parkinson's disease (PD), Alzheimer's disease (AD), Huntington's disease (HD), amyotrophic lateral sclerosis (ALS) (Britti et al., 2018). Although these diseases are commonly based on mitochondrial  $\text{Ca}^{2+}$  dysfunction, the progression of each depends on its specific molecular mechanism. Accordingly, dysregulation of VDAC1 has been described to induce both, PD and AD, either by altered dopamine homeostasis (Alberio et al., 2014) or mediating amyloid  $\beta$  toxicity (Smilansky et al., 2015). In HD it has been reported that the capacity of  $\text{Ca}^{2+}$  buffering is impaired (Gellerich et al., 2008) and in ALS it is hypothesized that chronic excitotoxicity induce permanent ER  $\text{Ca}^{2+}$  depletion leading to mitochondrial  $\text{Ca}^{2+}$  overload (Grosskreutz et al.,

2010). On the other hand regulated mitochondrial  $\text{Ca}^{2+}$  uptake is a prerequisite for neuronal function and survival (Rugarli and Langer, 2012). Aside from stimulating ATP production, transient increases in mitochondrial  $\text{Ca}^{2+}$  particularly occur at synapses and regulates neurotransmitter release, synaptic transmission and excitability (Pivovarova and Andrews, 2010) by rapidly clearing  $\text{Ca}^{2+}$  from the cytosol (MacAskill et al., 2010). For instance, in a recent work it has been demonstrated by simultaneously detecting cytosolic and mitochondrial  $\text{Ca}^{2+}$  using targeted genetically encoded indicators, namely cytosolic G-GeCO1 and mitochondrial R-GeCO1, that  $\text{Ca}^{2+}$  is strongly biased toward mitochondria in axon terminals in zebrafish neurons (Mandal et al., 2018). However, since mitochondrial  $\text{Ca}^{2+}$  buffering is tightly shaping the spatiotemporal profiles of intracellular  $\text{Ca}^{2+}$  we herein sought to fill the "missing link" of genetically encoded  $\text{Ca}^{2+}$  probes between the cytosol and the mitochondrial matrix. In order to develop such tools that allow sub-mitochondrial recordings of respective  $\text{Ca}^{2+}$  signals as prerequisite in a more detailed investigation of the sub-mitochondrial  $\text{Ca}^{2+}$  signaling and homeostasis, in the present work we focused on the targeting of already widely used genetically encoded  $\text{Ca}^{2+}$  sensors (i.e., GeCO1-like  $\text{Ca}^{2+}$  indicators) to the IMS or the mitochondrial cristae. We identified specific targeting sequences for distinct sub-mitochondrial protein targeting and fused them with single FP-based various GeCO1-like  $\text{Ca}^{2+}$  indicators (**Figure 1A**) that even allow simultaneous recordings of the  $\text{Ca}^{2+}$  signals in two (sub-) compartments and enabled us to take a closer look in the kinetics of  $\text{Ca}^{2+}$  transfer from the ER to mitochondria.

## MATERIALS AND METHODS

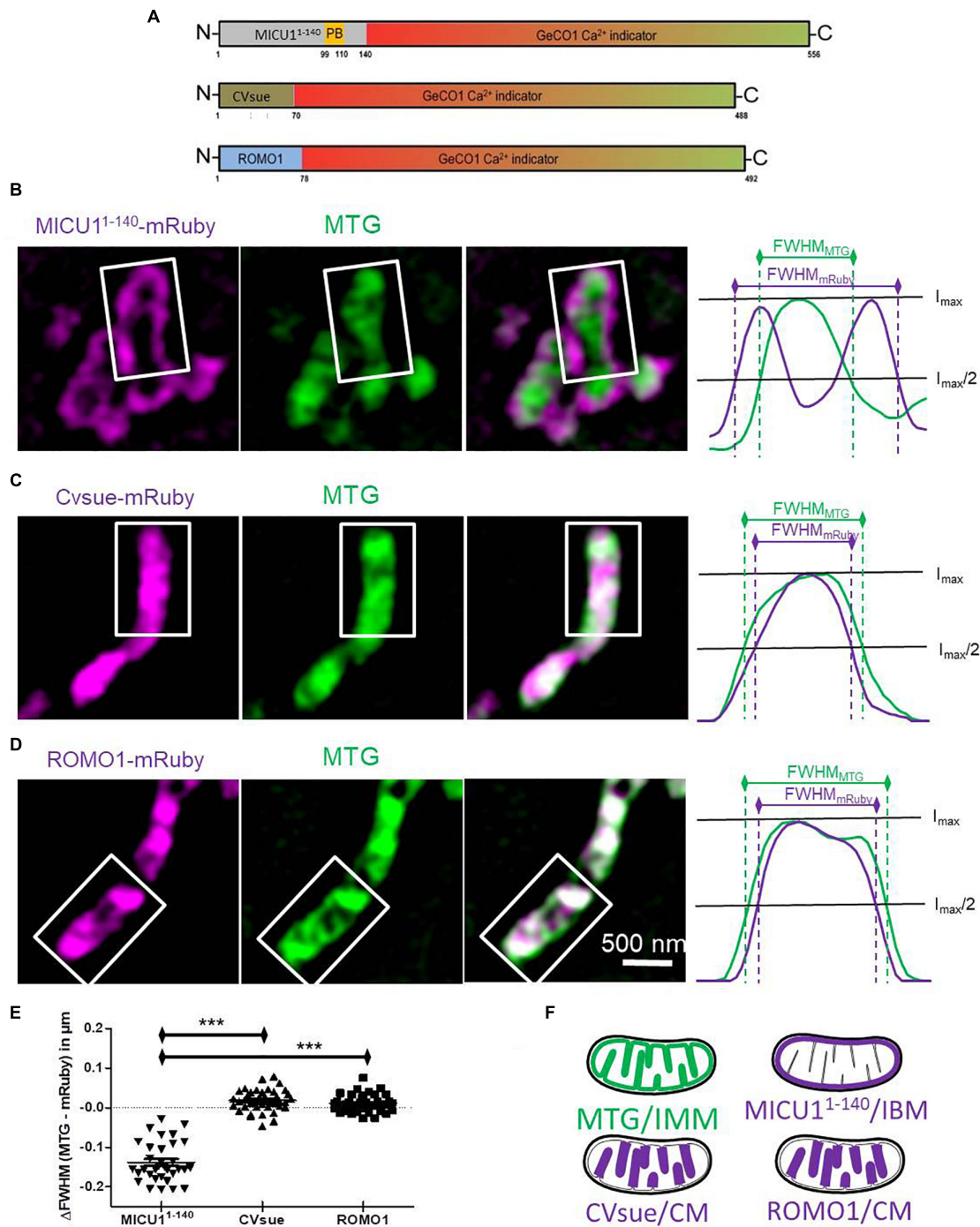
### Materials and Buffers

Chemicals and reagents for solutions and buffers were purchased from Carl Roth (Karlsruhe, Germany). Histamine, monensin, and BHQ were obtained from Sigma-Aldrich (Vienna, Austria). Nigericin was from Tocris (Abingdon, United Kingdom) and ionomycin from Abcam Biochemicals (Cambridge, United Kingdom). For storage cells were maintained in a buffer (storage buffer) containing (in mM): 2  $\text{CaCl}_2$  135 NaCl, 5 KCl, 1  $\text{MgCl}_2$ , 1 HEPES, 2.6  $\text{NaHCO}_3$ , 0.44  $\text{KH}_2\text{PO}_4$ , 0.34  $\text{Na}_2\text{HPO}_4$ , 10 D-glucose, 0.1% vitamins, 0.2% essential amino acids, and 1% penicillin/streptomycin pH adjusted with NaOH to 7.4 prior to imaging experiments. Therefore, cells were perfused in a physiological HEPES-buffered solution (2CaNa) composed of (in mM): 2  $\text{CaCl}_2$  135 NaCl, 5 KCl, 1  $\text{MgCl}_2$ , 1 HEPES, 10 D-glucose, pH adjusted with NaOH to 7.4 and stimulated with either BHQ or histamine in either a  $\text{Ca}^{2+}$  free solution or a nominal  $\text{Ca}^{2+}$  free solution containing EGTA instead of 2  $\text{CaCl}_2$ .

### Cell Culture and Transfection

In this study we exclusively used a HeLa cell model that was cultivated at passage >50 on low fluorescence glass cover slips with a diameter of either 15 or 30 mm in DMEM (Sigma-Aldrich, Vienna, Austria) containing 10% FCS (PAA, Pasching, Austria), penicillin (100 U/ml) and streptomycin (100 U/ml)





**FIGURE 1 |** Differential sub-mitochondrial localization of MICU1<sup>1-140</sup>-, CVsue- and ROMO1-mRuby. **(A)** Illustration of construct design of sub-mitochondrial targeting sequences fused with GeCO1 Ca<sup>2+</sup> indicators. MICU1<sup>1-140</sup> including polybasic domain (PB), full length complex V subunit e and full length mutated reactive oxygen modulator 1 (ROMO1) were C-terminally tagged with red and green GeCO1 Ca<sup>2+</sup> indicators. Numbers indicates amino acid positions. **(B–D)** Representative dual-color structural illumination microscopy (SIM) images of HeLa mitochondria stained with inner mitochondrial membrane (IMM-) label MitoTracker Green (MTG, green, middle images) and expressing mRuby2 (magenta, left images) C-terminally tagged with either MICU1<sup>1-140</sup> **(B)**, CVsue **(C)** or ROMO1 **(D)**. Merged images show co-localization of green MTG and magenta mRuby fluorescence (right images). Sum of line scans within the representative rectangle areas were performed for the green and red fluorescence (right panels). Overlay of normalized fluorescence intensity curves indicates distances in full width at half maximum (FWHM) of sub-mitochondrial targeted mRuby (magenta curves) vs. MTG (green curves). **(E)** Calculation of differences in FWHM<sub>MTG</sub> to FWHM<sub>mRuby</sub> was performed by subtracting the distance given by the magenta curve from the green one. Statistical evaluation of  $\Delta\text{FWHM}$  values calculated per mitochondrion; \*\*\* $P < 0.001$ . Images were obtained from 5 cells in each of 8 independent experiments on 4 different days ( $n = 8$ ) for each targeting. **(F)** Schemes illustrating sub-mitochondrial localization given by the distinct targeting sequences.

in a humidified incubator (37°C, 5%  $\text{CO}_2$ /95% air). Cells were transfected in a serum-free medium using 3  $\mu\text{g}/\text{ml}$  TransFast™ Transfection reagent (Promega, Madison, WI, United States) together with 1–2  $\mu\text{g}$  of plasmid(s) and/or 100 nM of the respective siRNA(s) per ml 2 days before experiments.

## Plasmid and siRNA Material

The plasmid encoding mutated ROMO1 at positions 15, 27, and 42 from potential ROS modulating cysteines to serines (ROMO1) was synthesized by General Biosystems Inc., (Morrisville, NC, United States) and the vectors encoding for GEMGeCO1, CARGeCO1, and mt-CARGeCO1 were purchased from Addgene (Cambridge, MA, United States) and used as vector templates for the N-terminal insertion via *XhoI/BamHI* of either MICU1<sup>1–140</sup>, CVsue or ROMO1 using the primers as follows: MICU1 forward 5'-CCCTCTAGACTCGAGCATGTTTCGTCTGAACCTCACT-3'; MICU1 position 420 reverse 5'-GGTTGGATCCTTCAAGGTGGCAAAATATCGG-3'; CVsue forward 5'-AAACTCGAGCATGGTGCCACCGGTGCAGGT-3'; CVsue position 206 reverse 5'-CCCGGATCCTTTAATATGCTGTCATCTTCTGCC-3'; ROMO1 forward 5'-AAATCTAGACTCGAGCATGCCGGTGGCCGTGGGT-3' and ROMO1 position 255 reverse 5'-CATAGGATCCCGGATGCCCATCCCAATGG-3'. For SIM these targeting sequences were subcloned in frame with a C-terminal red fluorescent protein (mRuby). All siRNAs were purchased from Microsynth (Balgach, Switzerland) and their (sense strands, 5'-3') sequences were: ACACUAGGCACCGAGAUUA (siVDAC1) for silencing hVDAC1 (Arif et al., 2019); GCCAGAGACAGACAAUACU (hMCU-si1) and GGAAAGGGAGCUUAUUGAA (hMCU-si2) for silencing hMCU; GAACUUUGCUGUCUACUU for silencing hEMRE and UUCUCCGAACGUGUCACGU as a scrambled Control siRNA. It should be noted that the siRNAs for the knockdown of hMCU and hEMRE had been already verified and used before in the present HeLa cell type (Waldeck-Weiermair et al., 2015; Gottschalk et al., 2019) and thus a verification of the efficiency due to the siRNA mediated knockdown was only performed for VDAC1 siRNA in this work (**Supplementary Figure S6**).

## Quantitative RT-PCR

Total cellular RNA was isolated from HeLa cells transfected with either siRNA against VDAC1 or the scrambled Control siRNA with the PEQLAB total RNA isolation kit (Peqlab, Erlangen, Germany), followed by reverse transcription to cDNA, performed in a thermal cycler (Peqlab) using the high-capacity cDNA reverse transcription kit (Applied Biosystems, Foster City, CA, United States). The qPCR reaction was set up with the GoTag® qPCR Master Mix (Promega, Mannheim, Germany) together with gene-specific primers (Invitrogen, Vienna, Austria). Experiments were performed on a LightCycler 480 (Roche Diagnostics, Vienna, Austria). Relative expression of specific genes was normalized to human GAPDH, as a housekeeping gene. Primer sequences were as follows: VDAC1 for: 5'-GGACTGAGTACGGCCTGACGTT-3', VDAC1 rev: 5'-CAGTCCACGTGCAAGCTGATCT-3',

GAPDH (QuantiTect® Primer Assay Hs\_GAPDH, Qiagen, Hilden, Germany).

## $\text{Ca}^{2+}$ Imaging Experiments

$\text{Ca}^{2+}$  imaging was performed on a digital wide field microscope, the iMIC (Till photonics, Gräfelfing, Germany) equipped with a 40× objective (alpha Plan Fluor 40×, Zeiss, Göttingen, Germany) and an ultrafast switching monochromator, the Polychrome V (Till Photonics). Illumination of GEM-GeCO1 targeted sensors was performed at 430 nm excitation and emissions were collected with a dichrotome dual emission filter set (dichroic 535dcxr, CFP emitter 482/18 nm, and YFP emitter 535/3 nm). pH calibration was performed as described previously (Burgstaller et al., 2019) in a  $\text{Ca}^{2+}$ -free or  $\text{Ca}^{2+}$  containing buffer supplemented with 10  $\mu\text{M}$  ionomycin each to establish  $\text{Ca}^{2+}$  unbound and  $\text{Ca}^{2+}$  bound states of targeted GEMGeCO1. CARGeCO1 based  $\text{Ca}^{2+}$  indicators were excited at 575 nm and emitted at 600 nm. For simultaneous measurements, GEM- and CARGeCO1 targeted sensors were alternately excited for 400 ms each at 430 and 575 nm. Emissions derived from both sensors were taken in 3 s interval. Alternatively, we used an ultrafast switching mode where both  $\text{Ca}^{2+}$  indicators were excited for 150 ms in a 310 ms interval. During the measurements cells were continuously perfused by using a gravity-based perfusion system (NGFI, Graz, Austria) and images were recorded with a charged-coupled device (CCD) camera (AVT Stingray F-145B, Allied Vision Technologies, Stadtroda, Germany). Data acquisition and control of the digital fluorescence microscope was performed using the live acquisition software version 2.0.0.12 (Till Photonics).

## Super-Resolution Structured Illumination Microscopy (SIM)

Structured Illumination Microscopy experiments were performed as described previously (Gottschalk et al., 2018). In brief, transfected HeLa cells either expressing MICU1<sup>1–140</sup>-mRuby, CVsue-mRuby or ROMO1-mRuby were loaded with 0.5  $\mu\text{M}$  MitoTracker™ Green (MTG, Thermo Fisher Scientific, Waltham, MA United States) in storage buffer for 40 min, once washed and imaged in 2CaNa with a super-resolution CFI SR Apochromat TIRF 100x-oil (NA 1.49) objective mounted on a Nikon-Structured Illumination Microscopy (N-SIM®) System with standard wide field and SIM filter sets and equipped with two Andor iXon3® EMCCD camera mounted to a Two Camera Imaging Adapter (Nikon Austria, Vienna, Austria). Co-localization of MTG fluorescence intensities with MICU1<sup>1–140</sup>-mRuby, CVsue-mRuby and ROMO1-mRuby in the CM and IBM were measured via line scan analysis within a defined rectangle area. Normalized sum of intensities profiles derived from green (MTG) and red (mRuby) fluorescence were calculated to define the full width at half maximum (FWHM) as a measurement for the label latitude. MTG-staining was used as an internal reference for the IMM to determine the distance variation of sub-mitochondrial targeted mRuby at basis of the FWHM.

## Statistical Analysis of Data

Statistical analysis for SIM experiments were performed using one way ANOVA and Bonferroni's *post hoc* test. The acquired data of  $\text{Ca}^{2+}$  measurements were analyzed by the GraphPad Prism software version 5.01 (GraphPad Software, San Diego, CA, United States). Data are presented as mean  $\pm$  standard error of mean (SEM) of independent experiments (*n*) throughout the whole manuscript. For comparisons between two groups, two-tailed Student *t*-test was used for evaluation of statistical significance and a *P* value between 0.01 and 0.05 (*p* Student's *t*-test) was considered significant and indicated with "\*\*", *P* between 0.001 and 0.01 as very significant with "\*\*\*", and *P* < 0.001 as highly significant with "\*\*\*\*." For comparisons across multiple groups, one-way ANOVA with Bartlett's test for equal variances and Bonferroni's Multiple Comparison test were used for evaluating statistical significance expressed as described above.

## RESULTS

### Development of Sub-Mitochondrial Targeted $\text{Ca}^{2+}$ Biosensors

We and others have predicted that the mitochondrial calcium uptake 1 protein (MICU1) is a specific IMS protein via its N-terminal targeting sequence (Petrungaro et al., 2015; Waldeck-Weiermair et al., 2015). Accordingly, we generated a potentially IMS-targeted mRuby variant using the first 140 amino acids that includes the polybasic region of MICU1, but none of the two EF-hand motifs or the multimerization sites. HeLa cells expressing MICU1<sup>1–140</sup>-mRuby were subsequently loaded with the IMM specific dye MitoTracker<sup>TM</sup> Green (MTG). Super-resolution structure illumination microscopy (SIM) revealed that MICU1<sup>1–140</sup>-mRuby was exclusively directed to the inner boundary membrane (IBM) (Figures 1B,E and Supplementary Figure S1A). For targeting the sensor into the CL, we utilized a recently identified protein referred to as reactive oxygen species modulator 1 (ROMO1) that acts especially in the CL (Norton et al., 2014; Cogliati et al., 2016). Moreover, we used the subunit c of complex V (CVsue) that has been already shown to target within the CL (Rieger et al., 2014; Figures 1C,E and Supplementary Figure S1A) to structurally and functionally verify the targeting of ROMO1. In its size ROMO1 is comparable with CVsue and is also anchored with only one transmembrane domain into the cristae membrane. To disable ROMO1's function as ROS modulator while preserving its feature as a targeting peptide we mutated all four ROS sensitive cysteine residues to rather ROS-inert serine residues at the amino acid positions 15, 27, 42, and 79. Fusion of ROMO1 to the N-terminus of an mRuby yielded predominantly CL localization that was comparable to that of CVsue targeting as revealed via SIM (Figures 1D,E and Supplementary Figure S1A). SIM data were randomly recorded under all conditions and line plot analyses were performed showing no influence of ROMO1-, CVsue- or MICU1<sup>1–140</sup>-mRuby expression on mitochondrial thickness (Supplementary Figures S1B,C). Using these newly identified targeting sequences

MICU1<sup>1–140</sup>, CVsue, and ROMO1 we generated differentially targeted green and red GeCO1 biosensors aiming to visualize  $\text{Ca}^{2+}$  within the IMS or CL compartments (Figures 1A,F).

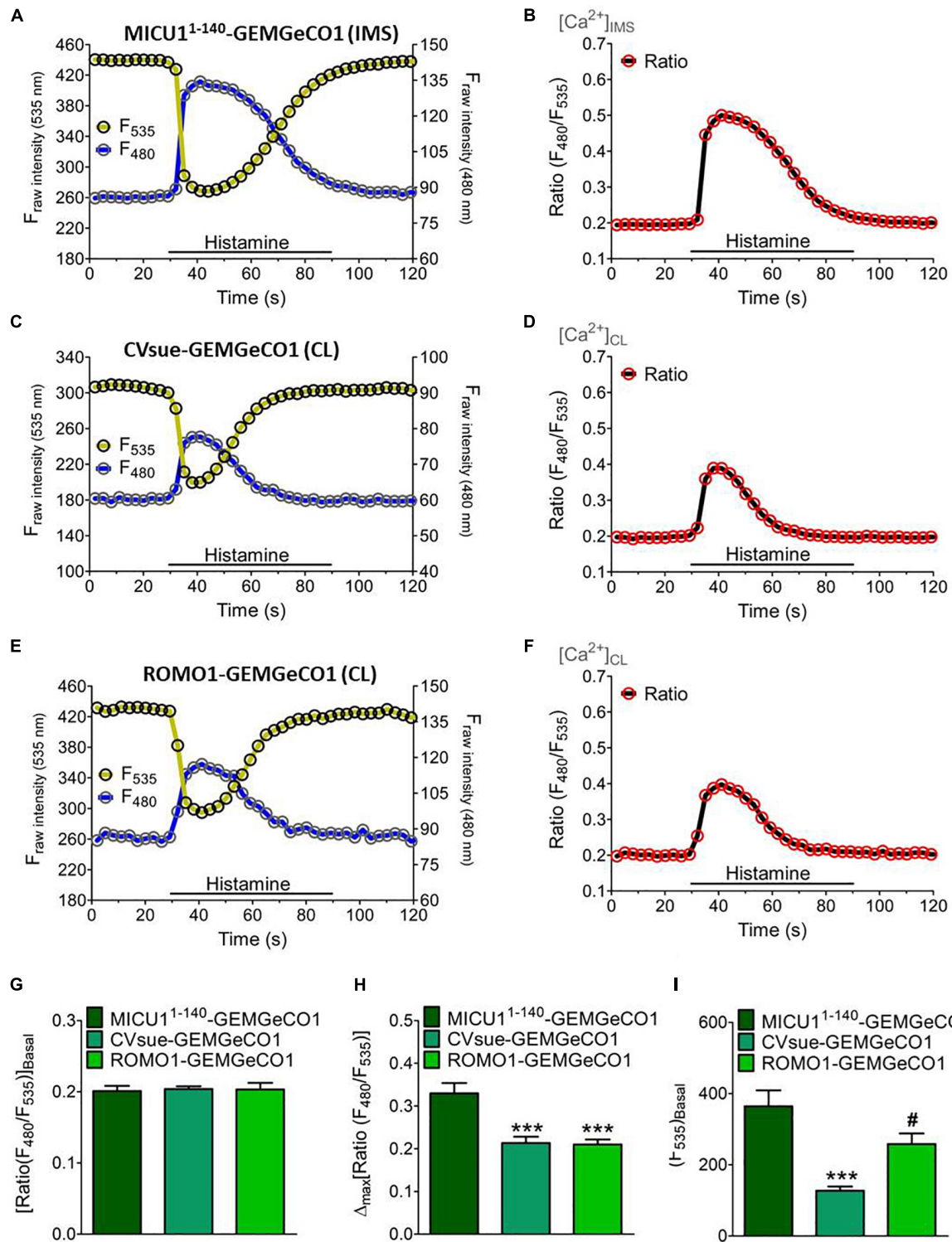
### Testing the Functionality of the Sub-Mitochondrially Targeted $\text{Ca}^{2+}$ Biosensors

We generated two groups of differentially targeted  $\text{Ca}^{2+}$  biosensors including the ratiometric GEMGeCO1 (Zhao et al., 2011) or intensimetric CARGeCO1 (Wu et al., 2013; Supplementary Table S1). For imaging of the ratiometric GEMGeCO1 we used a standard CFP/YFP emission filter. Recording the single fluorescence intensities of the localized sensor constantly revealed a 5-fold higher signals in the YFP channel compared to the CFP emission at basal  $\text{Ca}^{2+}$  levels (Figures 2A,C,E). Analyses of all three sub-mitochondrial constructs resulted in comparable ratio signals under resting conditions (Figures 2B,D,F,G). However, the signals upon IP<sub>3</sub>-mediated  $\text{Ca}^{2+}$  mobilization by histamine (100  $\mu\text{M}$ ) was more than 50% higher by using the IMS specific MICU1<sup>1–140</sup>-GEMGeGO1 in comparison to both CL targeted probes (Figure 2H). Although the two  $\text{Ca}^{2+}$  indicators within the CL, CVsue-GEMGeCO1 and ROMO1-GEMGeCO1, performed almost identical, the expression level of the ROMO1 targeted probe was significantly higher enabling a better resolution of signals (Figure 2I). Moreover, testing pH sensitivity of MICU1<sup>1–140</sup> or ROMO1 localized GEMGeCO1 revealed relative pH insensitivity of the probes at neutral and higher pH as previously reported for the recombinant GEMGeCO1 protein (Zhao et al., 2011; Supplementary Figure S2). We also constructed the corresponding sub-mitochondrial targeted intensimetric red CARGeCO1 variant which displays a low fluorescent signal under resting conditions and greatly lights up in the presence of  $\text{Ca}^{2+}$ . According to the low expression level together with the low fluorescence intensity of a CVsue-CARGeCO1 indicator we assumed that this probe is hardly detectable at basal  $\text{Ca}^{2+}$  levels and thus, visualization of CL localized CAR-GeCO1 was only performed by using the ROMO1 targeting sequence. In line with the results obtained by the ratiometric GEMGeCO1, statistical analyses of IMS or CL targeted CARGeCO1 derived signals resulted in comparable histamine responses indicating to distinct sub-mitochondrial  $\text{Ca}^{2+}$  concentrations upon  $\text{Ca}^{2+}$  mobilization with an IP<sub>3</sub> generating agonist (Supplementary Figure S3).

### Multi-Chromatic Imaging of Sub-Mitochondrial $\text{Ca}^{2+}$ Responses

The distinct spectral properties of the green and red GeCO1 biosensors allow simultaneous  $\text{Ca}^{2+}$  recordings in two distinct (sub-)compartments. First, we tested the suitability of the biosensors for simultaneous measurements by co-expressing MICU1<sup>1–140</sup>-GEMGeCO1 with MICU1<sup>1–140</sup>-CARGeCO1 and alternately recorded the respective emission. Since both biosensors exhibit a similar *K<sub>D</sub>* for  $\text{Ca}^{2+}$ , i.e., 340 nM for GEMGeCO1 (Zhao et al., 2011) and 490 nM for CARGeCO1 (Wu et al., 2013), simultaneous measurements resulted in





**FIGURE 2 |** Dynamics of sub-mitochondrial targeted GeCO1-like  $\text{Ca}^{2+}$  indicators. Single fluorescence intensities over time of MICU1<sup>1-140</sup>-GEMGeCO1 (**A**), CVsue-GEMGeCO1 (**C**) and ROMO1-GEMGeCO1 (**E**) in HeLa cells excited at 430 and 480 nm (blue curve) and 535 nm (yellow curve) emission upon stimulation with 100  $\mu\text{M}$  histamine in a nominal  $\text{Ca}^{2+}$  free buffer. Calculated ratio (green curves) from the respective left panels by the division of  $F_{480}$  by  $F_{535}$ , representing  $\text{Ca}^{2+}$  concentration levels ( $[\text{Ca}^{2+}]$ ) in the IMS (**B**) and the CL (**D,F**). (**G–I**) Statistical analysis of HeLa cells expressing either MICU1<sup>1-140</sup>-GEMGeCO1 (dark green,  $n = 17$ ), CVsue-GEMGeCO1 (aqua green,  $n = 16$ ) or ROMO1-GEM-GeCO1 (light green,  $n = 15$ ) and evaluation of ratiometric signals at basal levels (**G**) in response to histamine treatment (**H**) and intensimetric basal intensities at 535 nm reflecting sensor expression levels (**I**). \*\*\* $P < 0.001$  of CVsue-GEMGeCO1 and ROMO1-GEMGeCO1 vs. MICU1<sup>1-140</sup>-GEMGeCO1 and # $P < 0.05$  of ROMO1-GEMGeCO1 vs. CVsue-GEMGeCO1.

almost analog  $\text{Ca}^{2+}$  traces in both channels even at randomly occurring oscillatory  $\text{Ca}^{2+}$  spikes in one given HeLa cell (**Supplementary Figure S4**). These results demonstrate that both, the red and green biosensor retain their full functionality even in sub-mitochondrial regions and further demonstrate the suitability of these constructs to image  $\text{Ca}^{2+}$  in a multi-chromatic manner. Accordingly, we co-expressed each sub-mitochondrial targeted GEM-GeCO1 with either the cytosolic- (CARGeCO1) or the mitochondrial matrix-targeted (mt-CARGeCO1) red  $\text{Ca}^{2+}$  biosensor and imaged the responses upon histamine stimulation and store-operated  $\text{Ca}^{2+}$  entry within individual cells. Targeting of the various sensors is illustrated in **Figure 3A** and the respective sub-mitochondrial  $\text{Ca}^{2+}$  measurements simultaneously with cytosolic  $\text{Ca}^{2+}$  signals (CARGeCO1) are presented in **Figures 3B,D,F**. Furthermore, simultaneous measurements of the mitochondrial matrix  $\text{Ca}^{2+}$  with the newly targeted  $\text{Ca}^{2+}$  sensors for the IMS, and for both CL probes were shown in **Figures 3C,E,G**. Notably, the various sensors exhibited a distinct kinetics that further reflecting the individual  $\text{Ca}^{2+}$  signaling of the very sub-compartment of the mitochondria. Hence, co-imaging of IMS with cytosolic  $\text{Ca}^{2+}$  in a fast temporal sampling mode revealed almost simultaneous occurring  $\text{Ca}^{2+}$  increase (**Supplementary Figures S5A,B**), while mitochondrial matrix  $\text{Ca}^{2+}$  was clearly delayed upon histamine stimulation (**Supplementary Figures S5C,D**).

### Knockdown of MCU/EMRE Augments the $\text{Ca}^{2+}$ Accumulation Within the Mitochondrial Cristae

To verify the effect of an inhibition of mitochondrial  $\text{Ca}^{2+}$  uptake on the IMS and CL  $\text{Ca}^{2+}$  signals, the expression of MCU and its positive key regulator EMRE (Baradaran et al., 2018) were reduced by transfection with the respective siRNAs. Knockdown of MCU and EMRE resulted in an effective decrease of mitochondrial  $\text{Ca}^{2+}$  uptake upon intracellular  $\text{Ca}^{2+}$  mobilization (**Figure 4A**), while the respective  $\text{Ca}^{2+}$  signal in the IMS remained unaffected (**Figure 4B**). However, ablation of MCU and EMRE yielded enhanced  $\text{Ca}^{2+}$  signals in the CL measured with CVsue-GEMGeCO1 (**Figure 4C**) as well as with ROMO1-GEMGeCO1 (**Figure 4D**) upon stimulation with histamine. These results point to a specific  $\text{Ca}^{2+}$  accumulation that occurs especially within the CL under conditions where mitochondrial  $\text{Ca}^{2+}$  uptake is prevented by the knockdown of MCU/EMRE (**Figure 4E**).

### Knockdown of VDAC1 Impedes the $\text{Ca}^{2+}$ Transfer Through the OMM

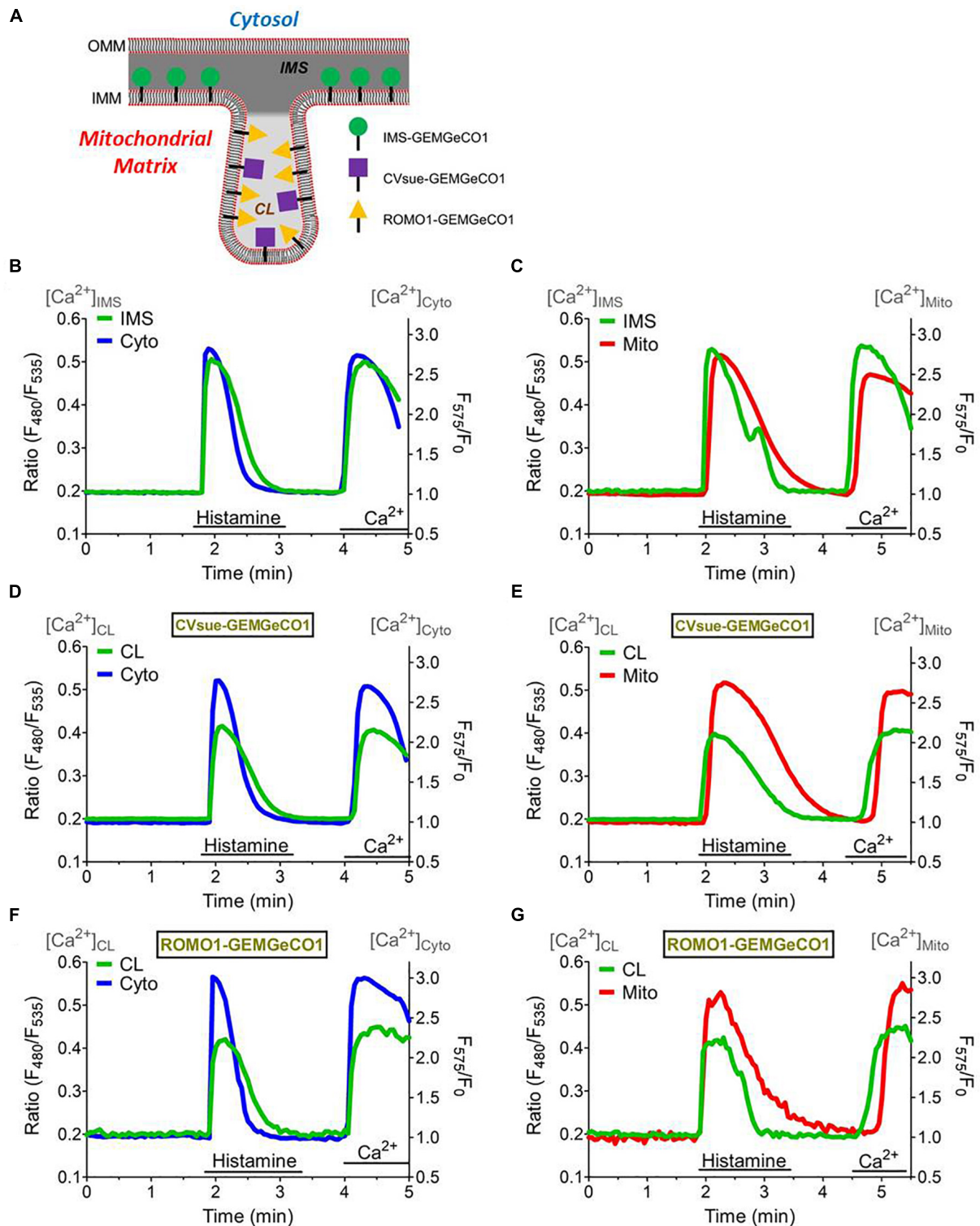
Several studies have shown that VDAC1 serves as a gate for  $\text{Ca}^{2+}$  ions within the OMM (De Stefani et al., 2011). Hence, we performed siRNA mediated knockdown of VDAC1 that was validated on the mRNA level by qRT-PCR (**Supplementary Figure S6**). To monitor the  $\text{Ca}^{2+}$  transfer through the OMM we used the IMS targeted MICU1<sup>1-140</sup>-GEM-GeCO1 in comparison with cytosolic CARGeCO1 or mt-CARGeCO1 and established a protocol where we exposed the biosensors to either slow/low or fast/high ER  $\text{Ca}^{2+}$  release and store operated  $\text{Ca}^{2+}$  entry

by the re-addition of extracellular  $\text{Ca}^{2+}$  after excessive ER store depletion. Notably, in comparison to the IP<sub>3</sub>-mediated ER  $\text{Ca}^{2+}$  release the SERCA inhibitor BHQ mediates a lower  $\text{Ca}^{2+}$  rise in the cytosol (**Figure 5A**) and the IMS (**Figure 5B**) that is marginally entering the mitochondrial matrix (**Figure 5C**). Knockdown of VDAC1 did not affect  $[\text{Ca}^{2+}]_{\text{Cyto}}$  (**Figure 5A**). In contrast, depletion of VDAC1 resulted in a reduced  $\text{Ca}^{2+}$  elevation in the IMS (**Figure 5B**) and, much more pronounced, in the mitochondrial matrix (**Figure 5C**) under all conditions of cytosolic  $\text{Ca}^{2+}$  elevations.

## DISCUSSION

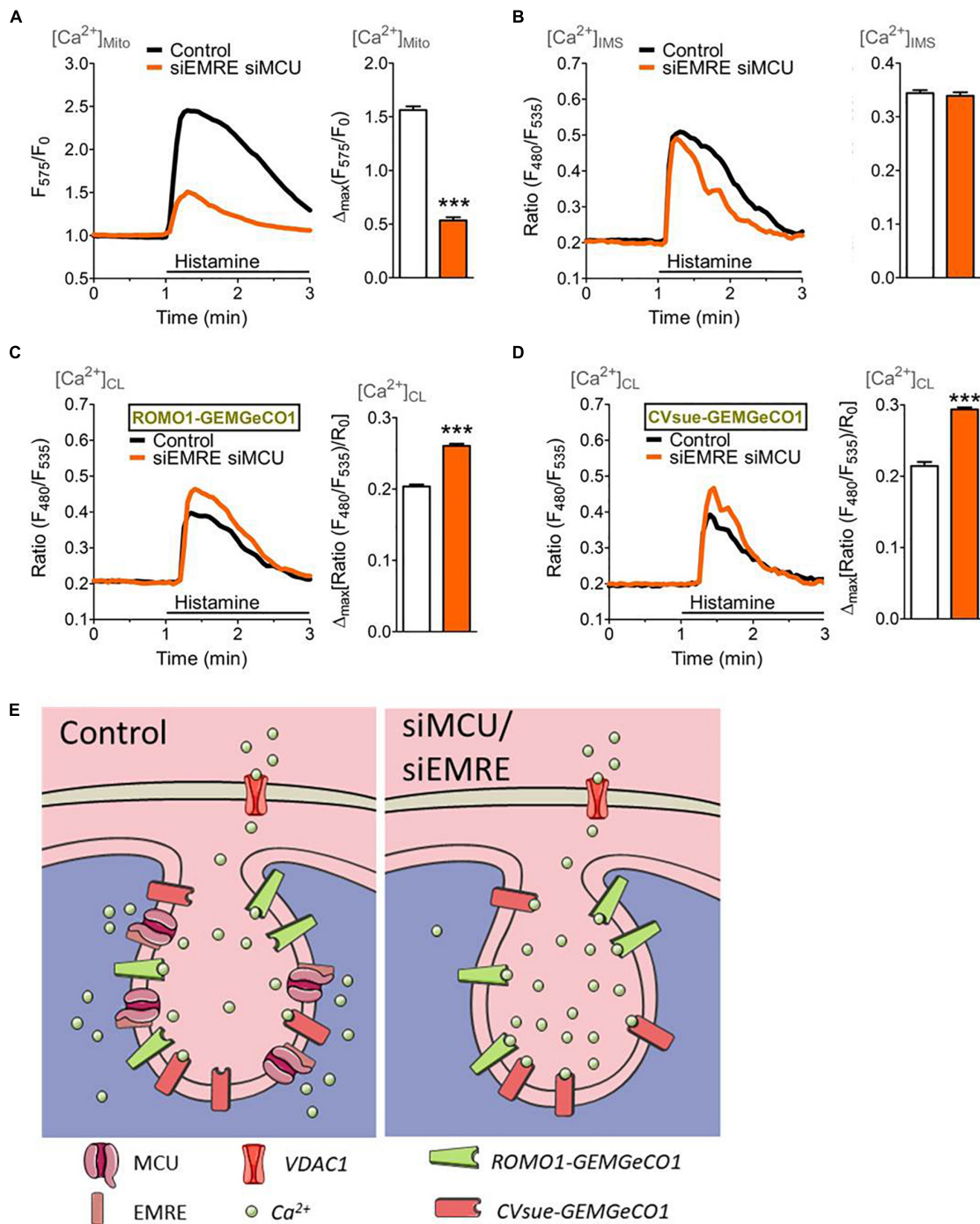
In this study we identified specific sequences that allow the distinct targeting of genetically encoded  $\text{Ca}^{2+}$  sensors for (simultaneous) sub-mitochondrial  $\text{Ca}^{2+}$  measurements. We aimed to establish such biosensors for sub-mitochondrial  $\text{Ca}^{2+}$  measurements in order to allow the examination of spatial, sub-organellar  $\text{Ca}^{2+}$  kinetics that will foster our attempts in investigating mitochondrial  $\text{Ca}^{2+}$  homeostasis. Besides the identification of suitable signal sequences, targeting was assessed using super-resolution structural-illumination microscopy (SIM), and a comparative characterization of the very  $\text{Ca}^{2+}$  sensitivity was performed. Hence, our work also provides initial (simultaneous) measurements where we applied the new sub-mitochondrial  $\text{Ca}^{2+}$  sensors for analyses of the  $\text{Ca}^{2+}$  kinetics upon given intracellular  $\text{Ca}^{2+}$  signals and, thus, tested the suitability of these new  $\text{Ca}^{2+}$  sensors to reveal distinct sub-mitochondrial  $\text{Ca}^{2+}$  signals under various conditions of altered mitochondrial  $\text{Ca}^{2+}$  signaling.

So far, only few attempts to target fluorescent indicators to these very sub-mitochondrial regions were successful. In an early study, the cDNA of glycerolphosphate dehydrogenase (GPD) was fused to HA1-tagged aequorin to study  $[\text{Ca}^{2+}]_{\text{IMS}}$  (Pinton et al., 1998) or  $[\text{H}^+]_{\text{IMS}}$  (Porcelli et al., 2005), but at that time the authors did not determine the exact sub-mitochondrial localization. In a more recent work specific IMS- or CL-targeted pH sensors were introduced and employed on the investigation of mitoflashes within various mitochondrial regions (Rosselin et al., 2017). However, in the present work we seek for signaling sequences from proteins that are directly involved in  $\text{Ca}^{2+}$  ion signaling and of those the localization has been previously undoubtedly proven. We pictured the localization sequence of MICU1 as very promising approach as it not only includes the important polybasic region between the amino acids 99 to 110. By fusing either the ratiometric green GEMGeCO1 (Zhao et al., 2011) or the intensimetric red CARGeCO1 (Wu et al., 2013) with the C-terminal side of amino acids 1 to 140 from MICU1 we achieved an excellent targeting of the probes exclusively in the IMS but not the CL or mitochondrial matrix. Our approach for targeting  $\text{Ca}^{2+}$  sensors exclusively into the cristae was successful when using the recently identified proteins referred to as complex V subunit e (CVsue) and reactive oxygen species modulator 1 (ROMO1) that has been shown to localize exclusively in the CL (Norton et al., 2014; Rieger et al., 2014; Cogliati et al., 2016). Our findings show that displacing the ROS-sensitive cysteines

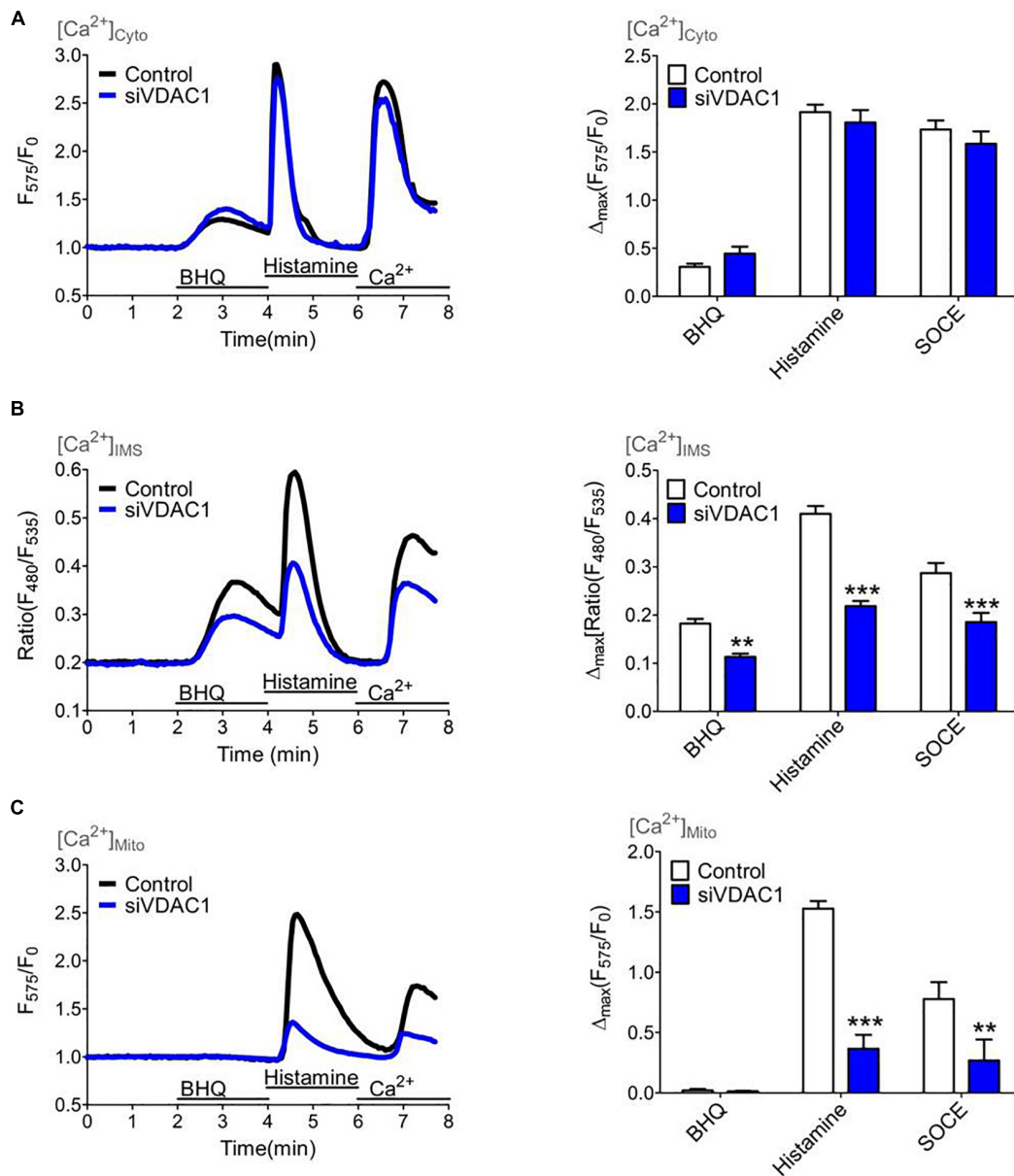


**FIGURE 3 |** Simultaneous measurements of the sub-mitochondrial  $\text{Ca}^{2+}$  sensors with the cytosol and mitochondrial matrix. **(A)** Scheme representing targeting of  $\text{MICU1}^{1-140}$ -GEMGeCO1, CVsue-GEMGeCO1, and ROMO1-GEMGeCO1  $\text{Ca}^{2+}$  indicators within specific sub-mitochondrial regions. Dark gray region indicates intermembrane space (IMS) and light gray area the cristae lumen (CL). Simultaneous  $\text{Ca}^{2+}$  imaging of  $\text{MICU1}^{1-140}$ -GEMGeCO1 **(B,C)**, CVsue-GEMGeCO1 **(D,E)** and ROMO1-GEMGeCO1 **(F,G)** (green curves) with either CARGeCO1 (blue curve; **B,D,F**) or mt-CARGeCO1 (red curve; **C,E,G**) co-expressing single HeLa cells treated with 100  $\mu\text{M}$  histamine in the absence of extracellular  $\text{Ca}^{2+}$  and upon subsequent store-operated  $\text{Ca}^{2+}$  entry. Simultaneous measurements allow kinetical comparisons of the  $\text{Ca}^{2+}$  signals in the various (sub-)compartments.





**FIGURE 4 |** Mitochondrial (sub-)compartmental  $\text{Ca}^{2+}$  signaling upon knockdown of the pore-forming units of the mitochondrial  $\text{Ca}^{2+}$  uniporter complex, MCU and EMRE. HeLa cells were co-transfected with GeCO1  $\text{Ca}^{2+}$  sensors either targeted in the mitochondrial matrix (A), the IMS and (B) the CL targeted with either CVsue (C) or ROMO1 (D), and specific siRNAs against EMRE and MCU (siEMRE siMCU, orange curves and bars) or scrambled control siRNAs (Control, black curves, and white bars). Cells were stimulated with 100  $\mu\text{M}$  histamine in the absence of extracellular  $\text{Ca}^{2+}$ . (A) Average mitochondrial  $\text{Ca}^{2+}$  signals over time measured with mt-CARGeCO1 (left panel) and statistical evaluation (right panel) of maximal  $\Delta$  intensities upon siEMRE siMCU ( $n = 7$ ) vs. Control ( $n = 8$ ). (B) Average  $[\text{Ca}^{2+}]_{\text{IMS}}$  curves of IMS-GeCO1 expressing cells (left panel) and bars (right panel) representing maximal  $\Delta$  ratios in Control ( $n = 9$ ) and siEMRE siMCU ( $n = 8$ ). (C) Average  $\text{Ca}^{2+}$  signals within the CL recorded from CVsue-GeCO1 expressing HeLa cells (left panel) and statistical analysis (right panel) of Control ( $n = 9$ ) in comparison to siEMRE siMCU ( $n = 9$ ). (D) Average  $[\text{Ca}^{2+}]_{\text{CL}}$  traces of ROMO1-GeCO1 expressing cells (left panel) and bars (right panel) representing maximal ratiometric fluorescence changes for Control ( $n = 11$ ) and siEMRE siMCU ( $n = 10$ ). \*\*\* $P < 0.001$  vs. Control. (E) Illustration of cristae localized  $\text{Ca}^{2+}$  indicators (ROMO1-GeCO1 or CVsue-GeCO1) sensing  $\text{Ca}^{2+}$  upon  $\text{IP}_3$ -mediated  $\text{Ca}^{2+}$  mobilization within the cristae lumen under control (left panel) or under ablation of mitochondrial  $\text{Ca}^{2+}$  uptake proteins (siEMRE siMCU, right panel).



**FIGURE 5 |** Mitochondrial (sub-)compartmental  $\text{Ca}^{2+}$  signaling upon knockdown of VDAC1 that controls the  $\text{Ca}^{2+}$  transfer through the outer mitochondrial membrane (OMM). HeLa cells were treated with either a siRNA against VDAC1 (siVDAC1, blue curves and bars) or a scrambled Control siRNA (Control, black curves and white bars) and  $\text{Ca}^{2+}$  imaging (A–C) was performed over time by consecutive application of 15  $\mu\text{M}$  BHQ and 100  $\mu\text{M}$  histamine in the absence of extracellular  $\text{Ca}^{2+}$  following a readdition of extracellular  $\text{Ca}^{2+}$  to highlight store-operated  $\text{Ca}^{2+}$  entry. (A) Average cytosolic  $\text{Ca}^{2+}$  curves (left panel) and statistical analysis for Control ( $n = 11$ ) and for siVDAC1 ( $n = 11$ ) of maximal  $\text{Ca}^{2+}$  elevations during treatment with either 15  $\mu\text{M}$  BHQ, 100  $\mu\text{M}$  histamine or re-addition of 2 mM  $\text{Ca}^{2+}$  (SOCE) (right panel). (B) Average curves of  $[\text{Ca}^{2+}]_{\text{IMS}}$  (left panel) and statistical evaluation of maximal  $\Delta$  ratio signals (right panel) for Control ( $n = 19$ ) versus siVDAC1 ( $n = 19$ ). (C) Average curves reflecting mitochondrial  $\text{Ca}^{2+}$  signals (left panel) and bar graph (right panel) showing maximal normalized  $\Delta$  intensities for Control ( $n = 17$ ) and siVDAC1 ( $n = 10$ ). \*\* $P < 0.01$  and \*\*\* $P < 0.001$  vs. Control.

of ROMO1 to serines at positions 15, 27, 42, and 79, and C-terminal fusion with the N-terminus of the  $\text{Ca}^{2+}$  sensors did not affect the proteins distinct CL localization, thus, this approach successfully provided us a strategy to localize ( $\text{Ca}^{2+}$ ) sensors exclusively to the CL.

In course of the functional testing of the newly targeted GEMGeCO1  $\text{Ca}^{2+}$  sensors the ratiometric behavior upon

changes in spatial  $\text{Ca}^{2+}$  was verified for all localizations. However, the ratio amplitude within the IMS was found to be approximately 1.5-fold higher than that obtained in the CL. One explanation for such reduced amplitude would be either a reduced  $\text{Ca}^{2+}$  accumulation within the CL. Alternatively, the fluorescence dynamic of GEMGeCO1 might be most likely reduced in the CL because of the acidic

environment (Rosselin et al., 2017). By combining distinctively targeted ratiometric green fluorescent ratiometric GEMGeCO1 (Zhao et al., 2011) with differently targeted red intensiometric CARGeCO1 (Wu et al., 2013) we established simultaneous measurements of the  $\text{Ca}^{2+}$  signals of two distinct sub-mitochondrial compartments. The kinetical analysis of the various  $\text{Ca}^{2+}$  signals upon intracellular  $\text{Ca}^{2+}$  release revealed a tight and almost instant coupling between the cytosol and the intermembrane space, thus, indicating that  $\text{Ca}^{2+}$  transfer through the OMM is very rapid and does not represent a speed-limiting process. Such process is known for the mitochondrial  $\text{Ca}^{2+}$  uniporter complex that is essentially activated upon  $\text{Ca}^{2+}$ -triggered rearrangement of MICU1 that also requires rather high  $\text{Ca}^{2+}$  concentrations ( $>4 \mu\text{M}$ ) to get initiated (Waldeck-Weiermair et al., 2015). However, the kinetics of mitochondrial  $\text{Ca}^{2+}$  uptake complex (MCUC) is much lower than that in any other mitochondrial sub-compartment, thus indicated some further processes necessary for MCUC activation. This assumption is further supported by the findings that upon a slow  $\text{Ca}^{2+}$  release by SERCA inhibition or when  $\text{Ca}^{2+}$  flux through the OMM is reduced by knockdown of VDAC1, no or only very small matrix  $\text{Ca}^{2+}$  signals occur despite the  $\text{Ca}^{2+}$  signals in the IMS is much less affected. Our findings that the prevention of MCUC by knockdown of MCU and EMRE did not affect the  $\text{Ca}^{2+}$  signal in the intermembrane space but considerable increased  $\text{Ca}^{2+}$  accumulation in the CL point to an active contribution of the cristae to mitochondrial  $\text{Ca}^{2+}$  homeostasis.

Altogether, in the present work we have successfully targeted well-known  $\text{Ca}^{2+}$  sensors to sub-compartments of the mitochondria and established simultaneous measurements of two distinct locations. Hence, the newly targeted  $\text{Ca}^{2+}$  sensors described herein have been approved to be suitable for analyses of sub-mitochondrial  $\text{Ca}^{2+}$  signaling and mitochondrial  $\text{Ca}^{2+}$  homeostasis, thus, providing suitable tools to discriminate between malfunction of OMM and/or IMM  $\text{Ca}^{2+}$  import e.g., during generation of neurodegenerative disease and will foster our understanding on mitochondrial  $\text{Ca}^{2+}$  homeostasis in future work.

## DATA AVAILABILITY STATEMENT

The raw data supporting the conclusions of this manuscript will be made available by the authors, without undue reservation, to any qualified researcher.

## REFERENCES

- Alberio, T., Mammucari, C., D'Agostino, G., Rizzuto, R., and Fasano, M. (2014). Altered dopamine homeostasis differentially affects mitochondrial voltage-dependent anion channels turnover. *Biochim. Biophys. Acta Mol. Basis Dis.* 1842, 1816–1822. doi: 10.1016/j.bbdis.2014.06.033
- Arif, T., Amsalem, Z., and Shoshan-Barmatz, V. (2019). Metabolic reprogramming via silencing of mitochondrial VDAC1 expression encourages differentiation of cancer cells. *Mol. Ther. Nucleic Acids* 17, 24–37. doi: 10.1016/j.omtn.2019.05.003

## AUTHOR CONTRIBUTIONS

JR-M, MD, CK, EE, HB, SB, and MW-W performed design and construction of sensors. JR-M, CK, and MW-W performed cloning and delivered plasmid material. MW-W and GZ performed imaging experiments and data analysis. CM-S performed qRT-PCR experiments including analysis. BG performed super-resolution SIM experiments and analysis. MW-W together with RM, BG, and WG supervised the project, performed data interpretation and wrote the manuscript. All authors discussed the results and commented on the manuscript at all stages.

## FUNDING

This work was funded by the Austrian Science Fund (FWF), DKplus W1226-B18 and P28529-B27. JR-M, SB, HB, and MD are doctoral fellows within the doctoral program Molecular Medicine (MolMed) at the Medical University of Graz. BG was supported by Nikon Austria and he as well as GZ and CK are doctoral fellows within the doctoral program Metabolic and Cardiovascular Disease (MCD) (FWF, DKplus W1226-B18) at the Medical University of Graz. Microscopic equipment is part of the Nikon-Center of Excellence, Graz that is supported by the Austrian infrastructure program (HRSM 2013/2014), Nikon Austria Inc., and BioTechMed. The funders had no role in study design, data collection and analysis, decision to publish, or preparation of the manuscript.

## ACKNOWLEDGMENTS

We thank Anna Schreilechner BSc. for her excellent technical assistance and the scientific advisory board of Next Generation Fluorescence Imaging (NGFI) GmbH (<https://www.ngfi.eu/>), a spin-off company of the Medical University of Graz.

## SUPPLEMENTARY MATERIAL

The Supplementary Material for this article can be found online at: <https://www.frontiersin.org/articles/10.3389/fncel.2019.00449/full#supplementary-material>

- Baradaran, R., Wang, C., Siliciano, A. F., and Long, S. B. (2018). Cryo-EM structures of fungal and metazoan mitochondrial calcium uniporters. *Nature* 559, 580–584. doi: 10.1038/s41586-018-0331-8
- Baughman, J. M., Perocchi, F., Girgis, H. S., Plovanich, M., Belcher-Timme, C. A., Sancak, Y., et al. (2011). Integrative genomics identifies MCU as an essential component of the mitochondrial calcium uniporter. *Nature* 476, 341–345. doi: 10.1038/nature10234
- Berridge, M. J., Bootman, M. D., and Roderick, H. L. (2003). Calcium signalling: dynamics, homeostasis and remodelling. *Nat. Rev. Mol. Cell Biol.* 4, 517–529. doi: 10.1038/nrm1155

- Britti, E., Delaspre, F., Tamarit, J., and Ros, J. (2018). Mitochondrial calcium signalling and neurodegenerative diseases. *Neuronal Signal.* 2:NS20180061. doi: 10.1042/ns20180061
- Burgstaller, S., Bischof, H., Gensch, T., Stryeck, S., Gottschalk, B., Ramadani-Muja, J., et al. (2019). pH-Lemon, a fluorescent protein-based pH reporter for acidic compartments. *ACS Sensors* 4, 883–891. doi: 10.1021/acssensors.8b01599
- Camara, A. K. S., Zhou, Y. F., Wen, P. C., Tajkhorshid, E., and Kwok, W. M. (2017). Mitochondrial VDAC1: a key gatekeeper as potential therapeutic target. *Front. Physiol.* 8:460. doi: 10.3389/fphys.2017.00460
- Cárdenas, C., Miller, R. A., Smith, I., Bui, T., Molgó, J., Müller, M., et al. (2010). Essential regulation of cell bioenergetics by constitutive InsP3Receptor  $\text{Ca}^{2+}$  transfer to mitochondria. *Cell* 142, 270–283. doi: 10.1016/j.cell.2010.06.007
- Cogliati, S., Enriquez, J. A., and Scorrano, L. (2016). Mitochondrial cristae: where beauty meets functionality. *Trends Biochem. Sci.* 41, 261–273. doi: 10.1016/j.tibs.2016.01.001
- De Stefani, D., Bononi, A., Romagnoli, A., Messina, A., Pinto, V., De, et al. (2011). VDAC1 selectively transfers apoptotic  $\text{Ca}^{2+}$  signals to mitochondria. *Cell Death Differ.* 19, 267–273. doi: 10.1038/cdd.2011.92
- Frey, T. G., and Mannella, C. A. (2000). The internal structure of mitochondria. *Trends Biochem. Sci.* 25, 319–324. doi: 10.1016/S0968-0004(00)01609-1
- Gautier, C. A., Erpapazoglou, Z., Mouton-Liger, F., Muriel, M. P., Cormier, F., Bigou, S., et al. (2016). The endoplasmic reticulum-mitochondria interface is perturbed in PARK2 knockout mice and patients with PARK2 mutations. *Hum. Mol. Genet.* 25, 2972–2984. doi: 10.1093/hmg/ddw148
- Gellerich, F. N., Gizatullina, Z., Nguyen, H. P., Trumbeckaite, S., Vielhaber, S., Seppet, E., et al. (2008). Impaired regulation of brain mitochondria by extramitochondrial  $\text{Ca}^{2+}$  in transgenic huntington disease rats. *J. Biol. Chem.* 283, 30715–30724. doi: 10.1074/jbc.M70955200
- Gottschalk, B., Klec, C., Leitinger, G., Bernhart, E., Rost, R., Madreiter-sokolowski, C., et al. (2019). MICU1 controls cristae junction and spatially anchors mitochondrial  $\text{Ca}^{2+}$  uniporter complex. *Nat. Commun.* 10:3732. doi: 10.1038/s41467-019-11692-x
- Gottschalk, B., Klec, C., Waldeck-Weiermair, M., Malli, R., and Graier, W. F. (2018). Intracellular  $\text{Ca}^{2+}$  release decelerates mitochondrial cristae dynamics within the junctions to the endoplasmic reticulum. *Pflugers Arch.* 470, 1193–1203. doi: 10.1007/s00424-018-2133-0
- Grosskreutz, J., Van Den Bosch, L., and Keller, B. U. (2010). Calcium dysregulation in amyotrophic lateral sclerosis. *Cell Calcium* 47, 165–174. doi: 10.1016/j.ceca.2009.12.002
- Herrmann, J. M. (2010). Ups delivery to the intermembrane space of mitochondria: a novel affinity-driven protein import pathway. *EMBO J.* 29, 2859–2860. doi: 10.1038/emboj.2010.189
- Kamer, K. J., and Mootha, V. K. (2014). MICU1 and MICU2 play nonredundant roles in the regulation of the mitochondrial calcium uniporter. *EMBO Rep.* 15, 299–307. doi: 10.1002/embr.201337946
- MacAskill, A. F., Atkin, T. A., and Kittler, J. T. (2010). Mitochondrial tracking and the provision of energy and calcium buffering at excitatory synapses. *Eur. J. Neurosci.* 32, 231–240. doi: 10.1111/j.1460-9568.2010.07345.x
- Mandal, A., Pinter, K., and Drerup, C. M. (2018). Analyzing neuronal mitochondria in vivo using fluorescent reporters in Zebrafish. *Front. Cell Dev. Biol.* 6:144. doi: 10.3389/fcell.2018.00144
- Norton, M., Ng, A. C. H., Baird, S., Dumoulin, A., Shutt, T., Mah, N., et al. (2014). ROMO1 is an essential redox-dependent regulator of mitochondrial dynamics. *Sci. Signal.* 7:ra10. doi: 10.1126/scisignal.2004374
- Petrungaro, C., Zimmermann, K. M., Küttner, V., Fischer, M., Dengiel, J., Bogeski, I., et al. (2015). The  $\text{Ca}^{2+}$ -dependent release of the Mia40-Induced MICU1-MICU2 dimer from MCU regulates mitochondrial  $\text{Ca}^{2+}$  uptake. *Cell Metab.* 22, 721–733. doi: 10.1016/j.cmet.2015.08.019
- Pinton, P., Brini, M., Bastianutto, C., Tuft, R. A., Pozzan, T., and Rizzuto, R. (1998). New light on mitochondrial calcium. *Biofactors* 8, 243–253. doi: 10.1002/biof.5520080312
- Pivovarova, N. B., and Andrews, S. B. (2010). Calcium-dependent mitochondrial function and dysfunction in neurons. *FEBS J.* 277, 3622–3636. doi: 10.1111/j.1742-4658.2010.07754.x
- Porcelli, A. M., Ghelli, A., Zanna, C., Pinton, P., Rizzuto, R., and Rugolo, M. (2005). pH difference across the outer mitochondrial membrane measured with a green fluorescent protein mutant. *Biochem. Biophys. Res. Commun.* 326, 799–804. doi: 10.1016/j.bbrc.2004.11.105
- Rieger, B., Junge, W., and Busch, K. B. (2014). Lateral pH gradient between OXPHOS complex IV and F(0)F(1) ATP-synthase in folded mitochondrial membranes. *Nat. Commun.* 5:3103. doi: 10.1038/ncomms4103
- Rosselin, M., Santo-Domingo, J., Bermont, F., Giacomello, M., and Demaurex, N. (2017). L-OPA1 regulates mitoflash biogenesis independently from membrane fusion. *EMBO Rep.* 18, 451–463. doi: 10.15252/embr.201642931
- Rugarli, E. I., and Langer, T. (2012). Mitochondrial quality control: a matter of life and death for neurons. *EMBO J.* 31, 1336–1349. doi: 10.1038/emboj.2012.38
- Sancak, Y., Markhard, A. L., Kitami, T., Kovács-bogdán, E., Kamer, K. J., Udeshi, N. D., et al. (2013). EMRE is an essential component. *Science* 147, 1379–1382. doi: 10.1126/science.1242993
- Shoshan-Barmatz, V., Krelm, Y., and Shtenfer-Kuzmine, A. (2018). VDAC1 functions in  $\text{Ca}^{2+}$  homeostasis and cell life and death in health and disease. *Cell Calcium* 69, 81–100. doi: 10.1016/j.ceca.2017.06.007
- Shoshan-Barmatz, V., and Mizrachi, D. (2012). VDAC1: from structure to cancer therapy. *Front. Oncol.* 2:164. doi: 10.3389/fonc.2012.00164
- Smilansky, A., Dangoor, L., Nakdimon, I., Ben-Hail, D., Mizrachi, D., and Shoshan-Barmatz, V. (2015). The voltage-dependent anion channel 1 mediates amyloid  $\beta$  toxicity and represents a potential target for Alzheimer disease therapy. *J. Biol. Chem.* 290, 30670–30683. doi: 10.1074/jbc.M115.691493
- Szabadkai, G., Bianchi, K., Várnai, P., De Stefani, D., Wieckowski, M. R., Cavagna, D., et al. (2006). Chaperone-mediated coupling of endoplasmic reticulum and mitochondrial  $\text{Ca}^{2+}$  channels. *J. Cell Biol.* 175, 901–911. doi: 10.1083/jcb.200608073
- Szymański, J., Janikiewicz, J., Michalska, B., Patalas-Krawczyk, P., Perrone, M., Ziolkowski, W., et al. (2017). Interaction of mitochondria with the endoplasmic reticulum and plasma membrane in calcium homeostasis, lipid trafficking and mitochondrial structure. *Int. J. Mol. Sci.* 18, 1–24. doi: 10.3390/ijms18071576
- van Vliet, A. R., Verfaillie, T., and Agostinis, P. (2014). New functions of mitochondria associated membranes in cellular signaling. *Biochim. Biophys. Acta Mol. Cell Res.* 1843, 2253–2262. doi: 10.1016/j.bbamcr.2014.03.009
- Waldeck-Weiermair, M., Malli, R., Parichatanond, W., Gottschalk, B., Madreiter-Sokolowski, C. T., Klec, C., et al. (2015). Rearrangement of MICU1 multimers for activation of MCU is solely controlled by cytosolic  $\text{Ca}^{2+}$ . *Sci. Rep.* 5, 1–10. doi: 10.1038/srep15602
- Wang, L., Yang, X., Li, S., Wang, Z., Liu, Y., Feng, J., et al. (2014). Structural and mechanistic insights into MICU1 regulation of mitochondrial calcium uptake. *EMBO J.* 33, 594–604. doi: 10.1002/emboj.201386523
- Weisthal, S., Keinan, N., Ben-Hail, D., Arif, T., and Shoshan-Barmatz, V. (2014).  $\text{Ca}^{2+}$ -mediated regulation of VDAC1 expression levels is associated with cell death induction. *Biochim. Biophys. Acta Mol. Cell Res.* 1843, 2270–2281. doi: 10.1016/j.bbamcr.2014.03.021
- Wu, J., Liu, L., Matsuda, T., Zhao, Y., Rebane, A., Drobizhev, M., et al. (2013). Improved orange and red  $\text{Ca}^{2+}$  indicators and photophysical considerations for optogenetic applications. *ACS Chem. Neurosci.* 4, 963–972. doi: 10.1021/cn400012b
- Zhao, Y., Araki, S., Wu, J., Teramoto, T., Chang, Y. F., Nakano, M., et al. (2011). An expanded palette of genetically encoded  $\text{Ca}^{2+}$  indicators. *Science* 333, 1888–1891. doi: 10.1126/science.1208592 doi: 10.1126/science.1208592

**Conflict of Interest:** The authors declare that the research was conducted in the absence of any commercial or financial relationships that could be construed as a potential conflict of interest.

Copyright © 2019 Waldeck-Weiermair, Gottschalk, Madreiter-Sokolowski, Ramadani-Muja, Ziomek, Klec, Burgstaller, Bischof, Depaoli, Eroglu, Malli and Graier. This is an open-access article distributed under the terms of the Creative Commons Attribution License (CC BY). The use, distribution or reproduction in other forums is permitted, provided the original author(s) and the copyright owner(s) are credited and that the original publication in this journal is cited, in accordance with accepted academic practice. No use, distribution or reproduction is permitted which does not comply with these terms.





# Fluorescent Biosensors for Neurotransmission and Neuromodulation: Engineering and Applications

Anna V. Leopold<sup>1</sup>, Daria M. Shcherbakova<sup>2</sup> and Vladislav V. Verkhusha<sup>1,2\*</sup>

<sup>1</sup> Medicum, Faculty of Medicine, University of Helsinki, Helsinki, Finland, <sup>2</sup> Department of Anatomy and Structural Biology, Gruss-Lipper Biophotonics Center, Albert Einstein College of Medicine, Bronx, NY, United States

## OPEN ACCESS

### Edited by:

Shai Berlin,  
Technion Israel Institute  
of Technology, Israel

### Reviewed by:

Markus Rothmel,  
RWTH Aachen University, Germany  
Terence Hébert,  
McGill University, Canada  
David Sulzer,  
Columbia University, United States

### \*Correspondence:

Vladislav V. Verkhusha  
vladislav.verkhusha@einstein.yu.edu

### Specialty section:

This article was submitted to  
Cellular Neurophysiology,  
a section of the journal  
Frontiers in Cellular Neuroscience

**Received:** 15 July 2019

**Accepted:** 08 October 2019

**Published:** 23 October 2019

### Citation:

Leopold AV, Shcherbakova DM  
and Verkhusha VV (2019) Fluorescent  
Biosensors for Neurotransmission  
and Neuromodulation: Engineering  
and Applications.  
Front. Cell. Neurosci. 13:474.  
doi: 10.3389/fncel.2019.00474

Understanding how neuronal activity patterns in the brain correlate with complex behavior is one of the primary goals of modern neuroscience. Chemical transmission is the major way of communication between neurons, however, traditional methods of detection of neurotransmitter and neuromodulator transients in mammalian brain lack spatiotemporal precision. Modern fluorescent biosensors for neurotransmitters and neuromodulators allow monitoring chemical transmission *in vivo* with millisecond precision and single cell resolution. Changes in the fluorescent biosensor brightness occur upon neurotransmitter binding and can be detected using fiber photometry, stationary microscopy and miniaturized head-mounted microscopes. Biosensors can be expressed in the animal brain using adeno-associated viral vectors, and their cell-specific expression can be achieved with Cre-recombinase expressing animals. Although initially fluorescent biosensors for chemical transmission were represented by glutamate biosensors, nowadays biosensors for GABA, acetylcholine, glycine, norepinephrine, and dopamine are available as well. In this review, we overview functioning principles of existing intensimetric and ratiometric biosensors and provide brief insight into the variety of neurotransmitter-binding proteins from bacteria, plants, and eukaryotes including G-protein coupled receptors, which may serve as neurotransmitter-binding scaffolds. We next describe a workflow for development of neurotransmitter and neuromodulator biosensors. We then discuss advanced setups for functional imaging of neurotransmitter transients in the brain of awake freely moving animals. We conclude by providing application examples of biosensors for the studies of complex behavior with the single-neuron precision.

**Keywords:** GPCR, GltI, GABA, glutamate, dopamine, serotonin, norepinephrine, neural circuit

## INTRODUCTION

Neurotransmitters and neuromodulators are chemicals, which are crucial for signal transmission in neuronal circuits. Neurotransmitters are released by the axon of the presynaptic neuron and excite, like glutamate, or inhibit, like  $\gamma$ -aminobutyric acid (GABA), the adjacent neurons in a sub-second timescale. Neurotransmitters are stored in vesicles in presynaptic terminals and are

released into the synaptic cleft in response to an action potential (**Figure 1A**; Klein et al., 2019). Neuromodulators are diffusing chemicals that modulate activity of the groups of neurons and can act not only on fast but also on slow timescales (**Figures 1B,C**). However, even classical fast neurotransmitters, such as glutamate, may not necessarily act as point-to-point transmitters; and diffusion of neurotransmitters from the synaptic cleft to the extracellular space is sufficient to activate non-synaptic receptors at a significant distance. This type of neurotransmission is called volumetric transmission (Taber and Hurley, 2014).

Neurotransmitters act on ionotropic and metabotropic receptors. Ionotropic receptors are ion channels whose activity is directly modulated by neurotransmitters. As an example, glutamate interaction with its ionotropic receptors (iGluRs) at the plasma membrane of the post-synaptic neurone leads to opening of channel pores, cation influx and membrane depolarization (**Figure 1C**; Traynelis et al., 2010). Metabotropic receptors are G-protein-coupled receptors (GPCRs) and their activation by neurotransmitters leads to indirect modulation of ion channels activity via activation of G-protein signaling (Nadim and Bucher, 2014).

Neuromodulators act mostly through G-protein-coupled receptors (**Figure 1C**; Nadim and Bucher, 2014; Avery and Krichmar, 2017), however, clear distinction between neurotransmitters and neuromodulators is problematic, as far as many classical neuromodulators may act through ionotropic receptors. For example, acetylcholine acts mostly as point-to-point neurotransmitter at neuromuscular junctions and in peripheral nervous system but as neuromodulator in central nervous system (Picciotto et al., 2012).

While neurotransmission leads to the fast excitation or inhibition of the post-synaptic neurons, neuromodulation results in the alteration of synaptic efficacy and in the changes of synaptic dynamics. Action of neuromodulators can change the rates of depression and facilitation at synapses, allowing synaptic dynamics as well as strength to vary (Nadim and Bucher, 2014). In the nervous system neuromodulators regulate switching of brain states, with the examples of serotonin controlling mood and norepinephrine controlling sleep and arousal (Avery and Krichmar, 2017).

All neurotransmitters and neuromodulators are essential to cognition and behavior (Nadim and Bucher, 2014; Avery and Krichmar, 2017). The correlation of chemical transmission in animal brain with its complex behavior can be studied using modern fluorescent biosensors. These biosensors provide high spatiotemporal precision for the visualization of fast neurotransmitter transients in neural circuits in brains of behaving animals (Brunert et al., 2016; Xie et al., 2016; McGirr et al., 2017; Sun et al., 2018; Tanaka et al., 2018; Feng et al., 2019; Marvin et al., 2019).

Fluorescent proteins (FPs) are essential part of modern biosensors. There are two major approaches of using FPs in biosensors. The first approach employs Förster resonance energy transfer (FRET) between two FPs (Li et al., 2016). FRET occurs when a donor FP is excited by light and non-radiatively transfers the excitation energy to the nearby chromophore, an acceptor. The second approach employs circular permutants

of FPs (cpFPs) (Wang et al., 2018). Circular permutation involves rearrangement of the parts of the original FP that retains the protein secondary structure. Certain regions in cpFPs tolerate insertion of other proteins; and conformational changes in the insert profoundly influence the fluorescence intensity. Moreover, circular permutants alter the relative orientation of the chromophore to a fusion partner, which is exploited in the optimization of FRET-based biosensors by inserting cpFPs.

Fluorescent biosensors can be delivered to the animal brain using viral vectors and detected in behaving animals by fiber photometry, including multi-channel fiber photometry (Guo et al., 2015), stationary two-photon (2P) excitation microscopy (Svoboda and Yasuda, 2006), and miniaturized head-mounted microscopes (Aharoni et al., 2019). Imaging of neurotransmitter transients in response to visual, audio or olfactory stimuli can be performed in restrained animals, however, head-mounted wireless miniaturized microscopes allow imaging of biosensors in the brain of freely moving animals (Liberti et al., 2017).

In this review, we firstly summarize available fluorescent biosensors for neurotransmitters and neuromodulators. We then outline a biosensor engineering workflow and provide the basic design principles for the modern biosensors. Next, we overview detection and functional imaging techniques that allow recording neurotransmitter and neuromodulator transients in animals. We then discuss how the biosensors enable monitoring brain function with high spatiotemporal precision and how they can be combined with common optogenetic tools for all-optical electrophysiology assays. Lastly, we outline avenues for engineering and applications of future biosensors for neurotransmitters and neuromodulators.

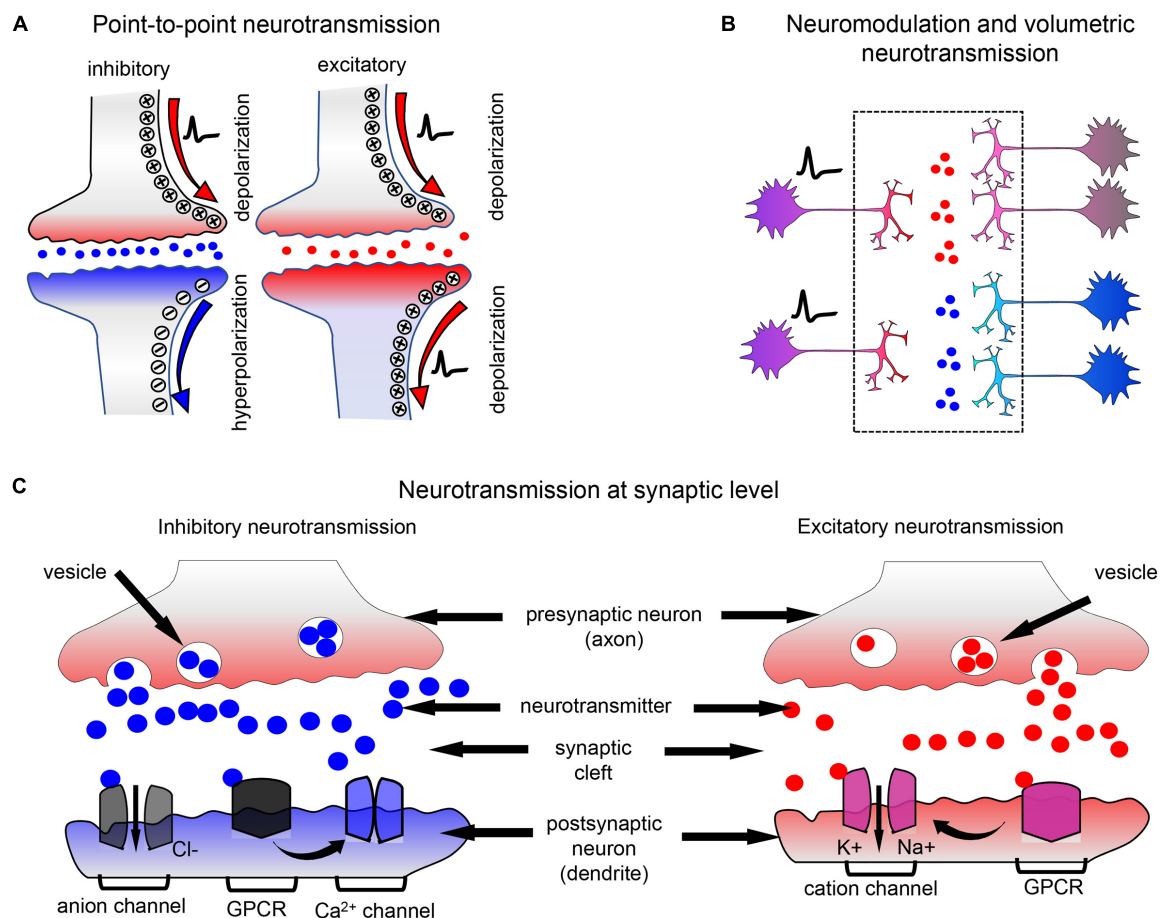
For biosensors of neural activity, such as genetically encoded membrane voltage and calcium indicators, we refer our readers to the recent reviews (Chen et al., 2017; Bando et al., 2019; Kannan et al., 2019; Piatkevich et al., 2019).

## GENERAL DESIGNS OF BIOSENSORS FOR CHEMICAL TRANSMISSION

To develop fluorescent biosensor for neurotransmitter or neuromodulator, a FRET pair of FPs or a cpFP is combined with a respective binding protein, called a sensing domain. In FRET-based biosensors a ratio between fluorescence intensities of the FRET donor and FRET signal changes upon neurotransmitter binding, therefore they are referred as ratiometric biosensors. In single-FP-based biosensors, fluorescence at single wavelength changes upon neurotransmitter binding, therefore they are referred as intensimetric biosensors (Lindenburg and Merckx, 2014; Chen et al., 2017). Currently, two types of sensing domains are used for engineering of both ratiometric and intensimetric biosensors.

First, periplasmic-binding proteins (PBPs) that interact with neurotransmitters are used. PBPs possess so-called Venus Flytrap Domain (VFTD), which changes its conformation upon binding neurotransmitter. VFTD is a bilobal protein, which remains “open” in the inactive state and “closes” upon ligand binding (**Figure 2**; Kunishima et al., 2000; Pin et al., 2003). At the





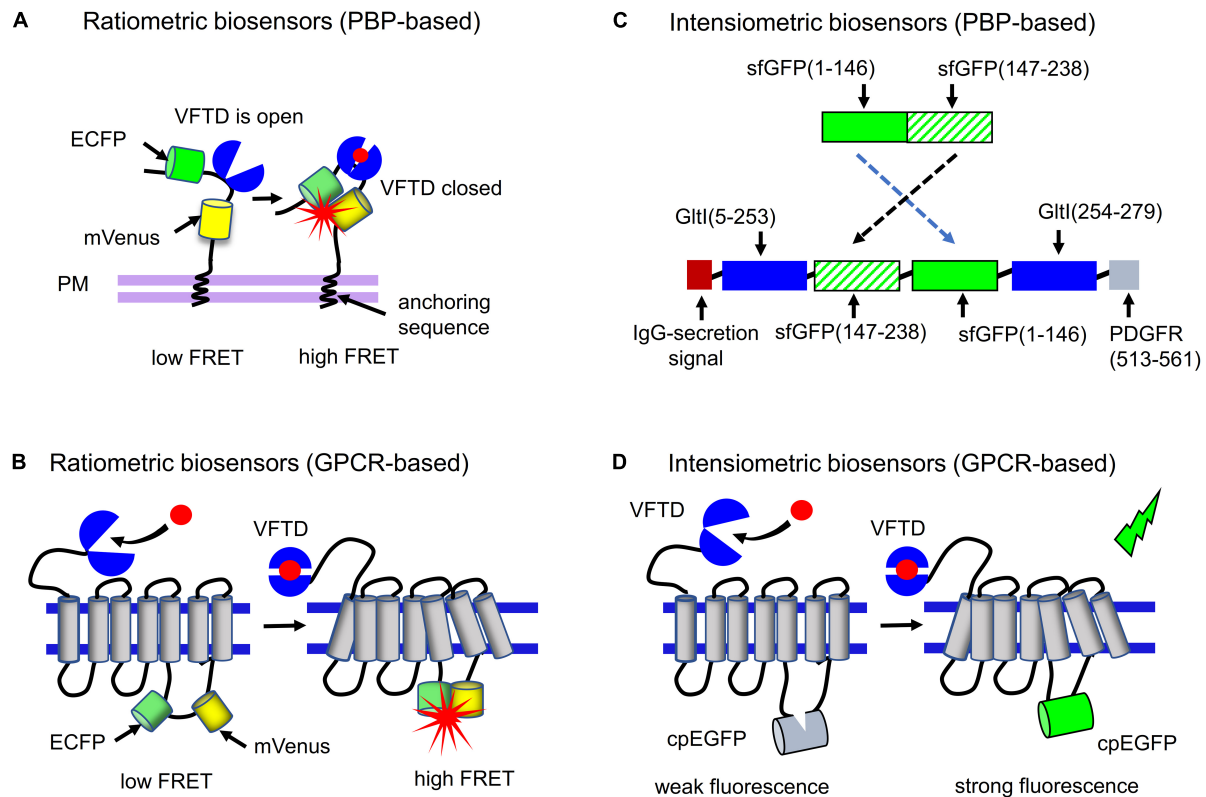
**FIGURE 1 |** Neurotransmission and neuromodulation principles. **(A)** In local neurotransmission, neurotransmitters packed in vesicles are released into the synaptic cleft and interact with the ionotropic receptors of neurotransmitters, which are typically ion channels. The interaction causes receptor with inhibitory or excitatory neurotransmitter channel to open to negatively or positively charged ions. The post-synaptic neuron is inhibited (blue) or excited (red). Neurotransmitters released by a presynaptic neuron act only on the single post-synaptic neuron and, after interaction with ionotropic receptors, are rapidly destroyed in the synaptic cleft. **(B)** In neuromodulation and volumetric transmission, neuromodulators released by a single neuron act simultaneously on the groups of neurons, modulating their synaptic strength. **(C)** Neurotransmission at synaptic level: on the left: the inhibitory neurotransmitter is released in the synaptic cleft and activates anion channels and GPCR receptors. Activation of GPCR receptors by the inhibitory neurotransmitters, such as GABA, negatively regulates calcium channels. On the right: the excitatory neurotransmitter is released in the synaptic cleft and activates cation channels and relevant GPCR receptors.

moment only three PBP proteins, such as GltI from *Escherichia coli*, Atu2422 from *Agrobacterium tumefaciens*, and Pf622 from *Pseudomonas fluorescens* are used in the neurotransmitter biosensors (Table 1). In PBP-based biosensors VFTD domain is inserted into the FRET pair (Figure 2A; Chen et al., 2017) or, on the contrary, cpFP is inserted into the flexible region of VFTD domain (Figure 2C; Marvin et al., 2013). Upon neurotransmitter binding, VFTD domain changes its structure from “open” to “closed” and that results in the either FRET between fluorescent proteins or restoration of the cpFP fluorescence, if cpFP is used.

Glutamate, acetylcholine, serotonin and GABA binding-proteins were discovered in organisms lacking nervous systems and even in unicellular organisms (Venter et al., 1988; Hoyle, 2011; Elphick et al., 2018). Bacteria use neurotransmitter-recognizing motifs presented by PBPs (Moussatova et al., 2008) in ATP binding cassette (ABC) transporters (Wilkins, 2015), with an example of several glutamine, L-histidine, glycine,

and arginine-binding transporters (Moussatova et al., 2008). Moreover, the family of plant glutamate-receptor like proteins might become a source of neurotransmitter-binding motifs. Proteins of this family bind GABA and various amino acids, such as glycine and glutamate (Forde and Roberts, 2014). AtGAT1, a high-affinity GABA transporter in *Arabidopsis thaliana* may also present a valuable scaffold for engineering of GABA biosensors (Meyer et al., 2006). Dopamine/norepinephrine transporter (SMDAT) (Larsen et al., 2011), as well as transporters of serotonin and norepinephrine (Ribeiro and Patocka, 2013), were found in human parasite trematode *Schistosoma mansoni*.

Second, GPCRs are used for the development of neurotransmitter and neuromodulator biosensors. GPCRs are membrane-spanning proteins, which change their conformation upon binding of neurotransmitters or neuromodulators and activate downstream signaling (Niswender and Conn, 2010). In this type of biosensors the activation state of GPCR is



**FIGURE 2 |** Ratiometric and intensimetric biosensors. **(A)** FRET-based biosensors in which PBP proteins are used as neurotransmitter-sensing domains. A PBP is inserted between FRET pair of FPs, such as ECFP and mVenus. Upon PBP interaction with neurotransmitter the FRET efficiency between FPs changes, which can be detected. **(B)** FRET-based biosensors in which GPCR receptors are used as neurotransmitter-sensing domains. A FRET pair consisting of ECFP and mVenus is inserted in the third intracellular loop of the respective GPCR. Upon interaction of the receptor with neurotransmitter FRET between two FPs changes. **(C)** Example of the PBP-based intensimetric biosensor is shown. Circular permutant of superfolder GFP (sfGFP) between positions 146–147 is inserted into GltI protein, resulting in the SF-iGluSnFR glutamate biosensor (Marvin et al., 2018). N-terminal IgG-secretion signal ensures transport of the biosensor to extracellular space, while C-terminal transmembrane domain of PDGFR receptor anchors the biosensor to the plasma membrane **(D)** Example of the GPCR-A-based intensimetric biosensor is shown. Circularly permuted EGFP (cpEGFP) is inserted into the third intracellular loop of GPCR having the VFTD domain at the N-terminus. After binding neurotransmitter or neuromodulator, the conformation of GPCR changes that results in enhancement of cpEGFP fluorescence.

detected. Neurotransmitters and neuromodulators mostly interact with GPCRs of the A group (GPCR-A), with the exception of glutamate and GABA, which interact with the GPCRs of the C group (GPCR-C), such as metabotropic glutamate receptors and GABA receptors. GPCR-C receptors possess the large N-terminal domain, which is structurally similar to the VFTD of PBPs. Similar to VFTDs of GltI and Atu2422, the VFTD of GPCR-C remains “open” in the inactive state and “closes” upon neurotransmitter binding (Figure 2B). Second and third intracellular loops of GPCR-C receptors form the cavity, responsible for the G-protein recognition (Pin et al., 2003). The GPCR-A group comprises all other receptors of neurotransmitters and neuromodulators, including catecholamine aminergic receptors,  $\beta$ -adrenergic receptors, histamine H1 receptor and muscarinic acetylcholine receptors (Katritch et al., 2013). As opposed to GPCR-C receptors, GPCR-A receptors have the longer intracellular third domain (it is the longest intracellular domain in these receptors, while in GPCR-Cs the second domain is the longest) and do not have VFTD domain.

In both GPCR-A- and GPCR-C-based neurotransmitter biosensors, a FRET pair of FPs (Figure 2B) or a cpFP (Figure 2D) is inserted in a third intracellular loop of the receptor (Sun et al., 2018; Wang et al., 2018; Feng et al., 2019). Upon neurotransmitter binding to the extracellular part of the GPCR, the receptor conformational changes are transferred to the intracellular part, causing the FRET changes between FPs or the recovery of cpFP fluorescence.

Below we describe the modern biosensors for neurotransmitters and neuromodulators, which are compatible with the studies of chemical transients in the brain of behaving animals.

## BIOSENSORS FOR GLUTAMATE

Glutamate is the most abundant excitatory neurotransmitter in the mammalian nervous system. Concentration of glutamate is tightly regulated by the number of transporters and glutamate-degrading enzymes, preventing the glutamate excitotoxicity

**TABLE 1 |** Modern biosensors for neurotransmitters and neuromodulators.

<b>FRET-based biosensors</b>	<b>FRET pair</b>	<b>Relative change of FRET ratio, <math>\Delta R/R</math> (%)</b>	<b><math>K_d</math> (<math>\mu M</math>)</b>	<b>Conditions used to measure <math>\Delta R/R</math> and <math>K_d</math></b>	<b>Substance (neurotransmitter or neuromodulator)</b>	<b>Template for sensing domain</b>	<b><i>In vivo</i> use</b>	<b>References</b>
SuperGluSnFR	ECFP-Citrine	44	2.5	Cultured neurons, 1P microscopy	Glutamate	GltI	Not tested	Hires et al., 2008
M1-cam5	ECFP-EYFP	10	Not determined	HEK293 cells, 1P microscopy	Acetylcholine	M1mAChR		Markovic et al., 2012
GlyFS	EGFP-Venus	20	20	Brain slices, 2P microscopy	Glycine	Atu2422 (AYW mutant)		Zhang et al., 2018
<b>Single-FP-based biosensors</b>	<b>Circularly permuted FP</b>	<b>Relative change of fluorescence, <math>\Delta F/F</math> (%)</b>	<b><math>K_d</math> (<math>\mu M</math>)</b>	<b>Conditions used to measure <math>\Delta F/F</math> and <math>K_d</math></b>	<b>Substance (neurotransmitter or neuromodulator)</b>	<b>Template for sensing domain</b>	<b><i>In vivo</i> use</b>	<b>References</b>
iGluSnFR	cpGFP	103	4.9	Cultured neurons, 1P microscopy	Glutamate	GltI	Imaging of dendritic spines	Marvin et al., 2013
SF-iGluSnFR A184V	sfGFP	69	0.6					Marvin et al., 2018
SF-iGluSnFR S72A		250	34					
SF-Azurite-iGluSnFR	Azurite	66	46					
SF-Venus-iGluSnFR	Venus	66	2					
SF-mTurquoise2-iGluSnFR	mTurquoise	90	41					
iGABASnFR	sfGFP	250	9	Purified protein, fluorimeter	GABA	Pf622	Imaging of single neurons	Marvin et al., 2019
iGlu <sub>f</sub>	EGFP	100	137	HEK293 cells, stopped-flow	Glutamate	GltI	Not tested	Helassa et al., 2018
iGlu <sub>u</sub>		170	600					
R-iGluSnFR1	mApple	-33	11	Purified protein, fluorimeter				Wu et al., 2018
R-ncp-iGluSnFR1			0.9					
GACH	EGFP	90	2	HEK293 cells, 1P microscopy	Acetylcholine	M <sub>3</sub> R	Imaging of single neurons	Jing et al., 2018
GRAB <sub>NE1m</sub>		230	1.9		Norepinephrine	$\alpha$ 2AR	Aggregated fluorescence signal	Feng et al., 2019
GRAB <sub>NE1h</sub>		150	0.093					
Nb80-GFP		Not determined	Not determined	Not applicable		$\beta$ 2AR/Nb80	Not tested	Irannejad et al., 2013
OR-sensor	EGFP	Not determined	Not determined	Not applicable	Activation of $\mu$ and $\delta$ ORs	$\mu$ and $\delta$ ORs/Nb33	Not tested	Stoeber et al., 2018
iATPSnFR	spGFP	150	630	Cultured neurons, 1P microscopy	ATP	$\epsilon$ subunit of FOF1 ATPase from <i>Bacillus</i> PS3	Imaging of single astrocytes	Lobas et al., 2018
dLight1.1	EGFP	230	0.33	HEK293 cells, 1P microscopy	Dopamine	DRD1 (inserted into the ICL3)	Aggregated fluorescence signal	Patriarchi et al., 2018
dLight1.2		340	0.77					
DA1m		90	0.13			DRD2 (inserted into the ICL3)		Sun et al., 2018
DA1h			0.01					

(Zhou and Danbolt, 2014). Glutamate is released not only by neurons but also by glial cells (Harada et al., 2015). As it has been mentioned, glutamate-binding proteins are found in all kingdoms of life (Pin et al., 2003; Ribeiro and Patocka, 2013; Forde and Roberts, 2014). Some of these proteins, such as GltI, are similar to extracellular VFTD domains of mammalian GPCR-C receptors of glutamate and GABA (Figure 2A).

The first glutamate ratiometric biosensor was based on the GltI inserted between the ECFP-mVenus FRET pair of proteins (Okumoto et al., 2005). It was later improved by replacing mVenus with EYFP and systematic screening for the highest glutamate sensitivity. This resulted in SuperGluSnFR biosensor (Table 1) that exhibits 44% change in FRET/donor ratio upon glutamate binding (Hires et al., 2008).

Later, an intensimetric glutamate sensor, iGluSnFR, was engineered by inserting of cpEGFP in GltI (Figure 2C; Marvin et al., 2013). Although iGluSnFR was shown to work *in vivo*, it has some limitations including slow readout of glutamate dynamics in synapses and inability to detect sparse glutamate release (Marvin et al., 2018). iGluSnFR was recently improved by developing two fast glutamate biosensors iGlu<sub>u</sub> and iGlu<sub>f</sub> (Helassa et al., 2018). Reducing the GltI affinity to glutamate enabled increasing rate of its dissociation in iGlu<sub>u</sub> and iGlu<sub>f</sub>. Another family of glutamate biosensors was developed by replacing cpEGFP in iGluSnFR with circularly permuted superfolder GFP (fGFP) (Marvin et al., 2013). Moreover, iGluSnFR affinity to glutamate was changed by mutating GltI in the ligand-binding center. This resulted in two biosensors, SF-iGluSnFRS72A and SF-iGluSnFRA184V, with the reduced and enhanced affinity to glutamate, respectively. To develop multicolor SF-iGluSnFR biosensors, Marvin et al. (2018) introduced in the cpsfGFP chromophore mutations from spectrally-shifted GFP variants, such as mAzurite, mTurquoise2 and mVenus, resulting in the blue, cyan and yellow SF-GluSnFRA184V variants, respectively.

To shift intensimetric glutamate biosensors toward red spectral range, cpEGFP in iGluSnFR was replaced with circularly permuted mApple red FP, resulting in R-iGluSnFR1 and R-ncp-iGluSnFR1 biosensors (Wu et al., 2018). Although R-iGluSnFR1 exhibits the high glutamate affinity and dynamic range (Table 1; Wu et al., 2018), it demonstrates the fluorescence decrease upon glutamate binding, as opposed to the glutamate biosensors based on the GFP variants. It makes R-iGluSnFR1 rather similar to “turn-off” quantum dots used in neurotransmitter research, which lose fluorescence upon neurotransmitter binding (Ankireddy and Kim, 2015). Red fluorescent biosensors for glutamate which respond to glutamate binding with fluorescence increase are still waiting to be developed.

## GABA BIOSENSORS

While glutamate is the primary excitatory neurotransmitter in the brain, GABA is the main inhibitory neurotransmitter. GABA interacts with the GPCR-C receptors. While the earlier GABA

biosensors were “semisynthetic” (Masharina et al., 2012; Lecat-Guillet et al., 2017), recently, a fully genetically encoded GABA biosensor was developed (Marvin et al., 2019).

The first GABA semisynthetic biosensor, called GABA-Sniff (Masharina et al., 2012), is based on the GABA<sub>B</sub> receptor in which VFTD is N-terminally fused to the CLIP and SNAP tag peptide sequences. The SNAP and CLIP tags interact with the synthetic fluorophores forming a FRET pair. Moreover, in the GABA-Sniff an antagonist of GABA, CGP71783, occupies a cleft between the lobes of the VFTD. When the cleft is occupied by CGP71783, FRET between synthetic fluorophores is weak; however, when GABA displaces CGP71783 the FRET enhances (Masharina et al., 2012). Another semisynthetic biosensor reports conformational changes in the heterodimeric GABA<sub>B</sub> receptor that consist of GB1 and GB2 subunits. Similarly to GABA-Sniff, in the GABA<sub>B</sub> receptor-based biosensor the SNAP and ACP peptide tags are used. These tags are attached to VFTDs of the different GABA<sub>B</sub> subunits. Fluorescein and Lumi4-Tb fluorophores bind the SNAP and ACP tags, respectively (Masharina et al., 2012; Lecat-Guillet et al., 2017).

The semisynthetic biosensors need adding of fluorophores, which complicates their use *in vivo*. Recently, a GABA-recognizing Pf622 protein from non-sequenced *Pseudomonas fluorescens* strain was used to engineer an intensimetric GABA biosensor, named iGABASnFR. In iGABASnFR, cpsfGFP is inserted into the Pf622 protein. As the membrane-anchoring sequences iGABASnFR utilizes an N-terminal immunoglobulin secretion signal and a C-terminal transmembrane domain of the platelet-derived growth factor receptor (PDGFR) (Marvin et al., 2019). Similarly to SF-iGluSnFR biosensor, iGABASnFR demonstrated good membrane localization, however, its response to neurotransmitter release was almost 10-fold smaller than of SF-iGluSnFR. In hippocampal acute slices, iGABASnFR detected GABA release caused by electric stimulation of *stratum radiatum* with sufficient signal-to-noise ratio. Yet, reliable recording of GABA release from individual synapses using iGABASnFR was challenging, whereas release of glutamate at individual synapses was easily detectable with SF-iGluSnFR.

## ACETYLCHOLINE BIOSENSORS

Acetylcholine acts as fast point-to-point neurotransmitter in the peripheral nervous system and in neuromuscular junctions and as neuromodulator acting on the groups of neurons in the central nervous system. It is responsible for the adaptive behavior and coordinates responses of neuronal circuits in many brain areas (Picciotto et al., 2012). As a neuromodulator, acetylcholine influences neuronal excitability, synaptic transmission and synaptic plasticity. Moreover, acetylcholine coordinates firing of groups of neurons (Picciotto et al., 2012). It acts through the nicotinic receptors (nAChR), which are non-selective cationic channels, and muscarinic receptors (mAChR), which are GPCRs (Markovic et al., 2012) coupled to either Gq proteins (M1, M2, and M5 subtypes) activating phospholipase C or Gi/o proteins (M2 and M4 subtypes) inhibiting adenylate cyclase (Wess, 2003;



Picciotto et al., 2012). Acetylcholine can act as inhibitory and excitatory neuromodulator, depending on the localization and type of muscarinic receptors. Action of acetylcholine on presynaptic mAChRs (M2/M4) is inhibitory whereas action on post-synaptic muscarinic receptors (M1/M5) is activatory (Picciotto et al., 2012). Action of acetylcholine on nicotinic ionotropic receptors in the brain is mostly neuromodulatory because nAChRs predominantly participate in coordination of neuronal firing (Picciotto et al., 2012).

M1-mAChR was used to develop the first genetically encoded acetylcholine biosensor. A FRET-based acetylcholine biosensor was engineered by inserting ECFP and EYFP into the third intracellular loop of the mouse M1-mAChR receptor. The resulting biosensor, called M1-cam5, retained the ability to stimulate downstream signaling of M1-mAChR (Markovic et al., 2012).

mAChRs were also used to develop intensimetric biosensors. For this, the longest third intracellular loop of mAChRs was replaced with the shorter third intracellular loop from the  $\beta_2$  adrenergic receptor, and cpEGFP was inserted in it, following random mutagenesis of the N- and C-termini of cpEGFP. After the first round of mutagenesis Jing et al. (2018) identified several best clones producing up to ~70% fluorescence increase upon acetylcholine binding. The mutations from the found clones were rationally combined and the best biosensor variant was called GACH2.0 (Jing et al., 2018). In contrast to ratiometric M1-cam5 biosensor (Markovic et al., 2012) GACH2.0 exhibits weak coupling to downstream G-protein intracellular signaling, likely due to the replacement of mAChR third intracellular loop with the respective intracellular loop of the  $\beta_2$  adrenergic receptor.

Recently, the acetylcholine synthesis pathway was described in unicellular eukaryotes *Acanthamoeba* sp. (Baig et al., 2018). Earlier, a mAChR1 homolog was identified in *Acanthamoeba castellanii* (Baig and Ahmad, 2017). Likely, these unicellular eukaryotes can become a source of acetylcholine-binding domains for the development of novel acetylcholine biosensors.

## DOPAMINE BIOSENSORS

Dopamine is primarily involved in the reward behavior, control of movement, emotion and cognition. Dysfunction of dopaminergic system is the cause of several mental disorders including Parkinsonism and autism spectrum disorder. Dopamine interacts with D1 and D2-like GPCR receptors. The important difference between D1 and D2-like receptors is their action on the production of the secondary messenger cAMP. Due to the coupling to the different types of G-proteins they either activate (D1) or inhibit (D2) cAMP production (Klein et al., 2019).

Existing methods of dopamine measurements are not well suited to detect changes of dopamine with both high spatial and high temporal precision during complex animal behavior. The widely used for dopamine measurements fast-scan cyclic voltammetry allows to measure longitudinal changes of dopamine in single recording locations, however, this technique is invasive and restricts animals (Rodeberg et al., 2017).

Despite high temporal resolution of cyclic voltammetry, its spatial resolution is low and does not allow visualization of dopamine release from single neurons. Use of false fluorescent neurotransmitters (FFN) allows to visualize dopamine release with a single-neuron precision (Sames et al., 2013). However, it requires intracranial infusion of FFN, and is not applicable for longitudinal measurements (Dunn et al., 2018). In contrast, a genetically encoded biosensor for dopamine allows to measure dopamine transients in mice, zebrafish and flies with a high spatiotemporal precision for months (Patriarchi et al., 2018; Sun et al., 2018).

To engineer the intensimetric dopamine biosensor Sun et al. (2018). inserted cpEGFP in the third intracellular loop of several human dopamine receptors. Among them, a D1-cpEGFP chimera appeared to be the most promising. Changing the position of cpEGFP insertion and mutagenesis of linker residues led to the development of two biosensor variants, DA1m and DA1h. Both variants demonstrated rapid (~60 ms for DA1m and ~140 ms for DA1h) fluorescence increase in response to dopamine. A reversibility of the response was demonstrated by treatment with dopamine antagonist. Dopamine biosensors DA1m and DA1h (also called together GRAB<sub>DA</sub>) were orthogonal to the cell signaling and did not activate GPCR downstream pathways (Sun et al., 2018).

In another dopamine biosensor family, called dLight1, cpEGFP was inserted in the human D1 receptor (Patriarchi et al., 2018). The initial variant, which was obtained by inserting cpEGFP into the third loop of D1, showed a fluorescence decrease in response to dopamine. To engineer a positive-response biosensor Patriarchi et al. (2018) screened a library of the D1-based mutants in HEK293 cells to select a dLight1.1 variant, which exhibited the highest fluorescence increase in response to dopamine. An additional Phe129 mutation in the GPCR part of dLight1.1 resulted in a dLight1.2 variant with even higher dynamic range (Patriarchi et al., 2018).

Similar to GRAB<sub>DA</sub> family, dLight1 biosensors do not interfere with G-protein signaling and, unlike natural D1 receptor, do not stimulate cAMP synthesis. Thus, the conversion of D1 to fluorescent biosensors blocked its ability to bind G-protein and trigger signaling (Patriarchi et al., 2018). Moreover, neither GRAB<sub>DA</sub> nor dLight1 biosensors exhibit internalization, which is inherent to dopamine receptors (Sun et al., 2018).

## SENSING NOREPINEPHRINE SIGNALING

Norepinephrine, also known as noradrenalin, is a neurotransmitter that participates in the memory consolidation of emotionally arousing experiences (Cahill and Alkire, 2003). Norepinephrine is released by several brainstem nuclei including locus coeruleus (LC, a nucleus in the pons of brainstem) and is important for modulation of forebrain function. Release of norepinephrine by LC is associated with waking in both the cortex and hippocampus (Borodovitsyna et al., 2017).

Norepinephrine interacts with three types of adrenergic GPCR receptors, such as  $\alpha_1$ ,  $\alpha_2$  and  $\beta_1$ . Receptors  $\alpha_1$  and  $\beta_1$  activate

phospholipase C and adenylyl cyclase whereas  $\alpha 2$  mostly exerts inhibitory effect on cell signaling via suppression of adenylyl cyclase activity (Ramos and Arnsten, 2007).

To develop an intensimetric biosensor for norepinephrine Feng et al. (2019) inserted cpEGFP in the third intracellular loop of several adrenergic receptors including  $\alpha 2$ AR. Among all tested constructs,  $\alpha 2$ AR-cpEGFP preserved the membrane trafficking and, therefore, was selected for further optimization. The systematic truncation of the linker regions surrounding cpEGFP resulted in the family of norepinephrine biosensors (Table 1) consisting of GRAB<sub>NE1m</sub> and GRAB<sub>NE1h</sub> (Feng et al., 2019).

In another approach, a conformation-specific single-domain nanobody was proposed to probe activation of  $\beta 2$ -adrenoceptor. The nanobody Nb80 recognizes  $\beta 2$ AR only in its activated form, so that upon activation of  $\beta 2$ AR the Nb80-EGFP fusion translocates from the cytoplasm to the plasma membrane. However, this type of translocation biosensors is difficult to implement *in vivo* (Irannejad et al., 2013).

All adrenergic receptors interact not only with norepinephrine but also with structurally similar epinephrine (Ramos and Arnsten, 2007). Thus, the development of norepinephrine-specific GPCR-based biosensor seems problematic if not impossible (Feng et al., 2018).

Bacteria are also able to sense norepinephrine. An example of bacterial receptor of norepinephrine is the histidine kinase QseC from enterohemorrhagic *E. coli* strain. It was shown that a response of QseC to norepinephrine was blocked by norepinephrine antagonists (Clarke et al., 2006). Moreover, a homology modeling revealed the presence of typical for histidine kinases periplasmic signal-recognition domain, which is responsible for the norepinephrine binding (Clarke et al., 2006). Likely, use of this sensing domain as norepinephrine-binding template could result in the development of novel norepinephrine biosensors, similar to GltI-based biosensors for glutamate.

## OPIOID BIOSENSOR

Opioid receptors are GPCRs that are activated by endogenous opioid peptides and exogenous compounds. They play a key role in pain management, drug abuse and mood disorders. There are three major subtypes of opioid receptors, such as  $\delta$ ,  $\mu$ , and  $\kappa$  (Shang and Filizola, 2015). Signaling of opioid GPCRs is not limited to the cell plasma membrane but to other cellular compartments (Irannejad et al., 2013) including endosomes and Golgi membranes (Eichel and von Zastrow, 2018). Studying opioid receptor signaling from different cellular locations was problematic because of the lack of relevant biosensors. To overcome this, Stoeber et al. (2018) developed a nanobody-based fluorescent biosensor. For that they selected a nanobody, which recognized only activated opioid receptors, and fused it to EGFP (Stoeber et al., 2018). This biosensor, called OR-sensor, allowed to detect difference between activation of opioid receptors by endogenous peptides and exogenous compounds, such as drugs. It was found that the peptide agonists produce a

specific activation pattern initiated at the plasma membrane and propagated to endosomes after receptor internalization whereas drugs produce a different activation pattern by additionally causing opioid receptor activation in Golgi apparatus (Stoeber et al., 2018).

## ATP BIOSENSORS

The function of the number of cellular metabolites depends on their location. An example is ATP, which is universal intracellular energy source and also a key purinergic signal that mediates cell-to-cell communication both in and between organs. Thus, targeting ATP biosensors to extracellular space allow to detect purinergic transmission (Burnstock, 2006).

This approach was implemented with an ATeam ratiometric biosensor for ATP. ATeam family of intracellular biosensors was the first developed by an Imamura group (Conley et al., 2017). These biosensors are composed of an  $\epsilon$  subunit from a bacterial FoF1-ATP synthase that is inserted between ECFP and EYFP. ATP binding induces a conformational change that increases FRET between the ECFP donor and EYFP acceptor. Targeting ATeam3.10 using an immunoglobulin K leader sequence and a transmembrane anchor domain from the PDGFR to a surface of the plasma membrane turns it into an extracellular biosensor.

Similarly, an  $\epsilon$  subunit of FOF1-ATPase from *Bacillus* PS3 was used to develop an intensimetric biosensor iATPSnFR. In this biosensor, cpEGFP is inserted between two  $\alpha$ -helices of the  $\epsilon$  subunit using two amino acid linkers from each side with expectation that conformational changes of the  $\epsilon$  subunit might affect fluorescence. Both linkers were extensively mutated to maximize ATP-dependent fluorescence changes. To optimize expression of biosensor variants on the surface of HEK293 cells, EGFP was replaced with sfGFP and additionally mutated to reduce biosensor dimerization. The resulting iATPSnFR ATP biosensor exhibited efficient cell surface trafficking and 25%  $\Delta F/F$  (Lobas et al., 2018).

## BIOSENSOR FOR GLYCINE

Glycine acts as inhibitory neurotransmitter through ionotropic glycine receptors and as co-agonist of excitatory glutamate receptors of the NMDAR subtype. Recently, the first FRET-based glycine biosensor GlyFS was developed. For this, Zhang et al. (2018) used the Atu2422 protein from *Agrobacterium tumefaciens*. Atu2422 binds glycine, serine and GABA; however, rational design of the Atu2422 binding site allowed to significantly increase its specificity to glycine. A glycine-specific mutant of Atu2422, called AYW, was inserted between EGFP and mVenus FPs. The ratiometric response of this initial EGFP-AYW-mVenus construct to glycine was only 4%. To enhance it, Zhang et al. (2018) truncated the flexible linker between the AYW and EGFP and introduced a rigid (EAAAK)<sub>4</sub> linker between AYW and mVenus. These modifications led to the increase of the dynamic range to 28%. Further elongation of the rigid linker caused the decrease of FRET efficiency. The



resulting GlyFS biosensor was applied to detection of glycine transients in hippocampal acute slices. Since targeting of the GlyFS to the cell surface using immunoglobulin K leader sequence was ineffective, the biotin-streptavidin interaction was utilized. For that, acute brain slices were biotinylated, and the purified from expressing bacteria GlyFS biosensor with streptavidin was injected into the slices. Likely, use of the alternative membrane surface targeting peptides could result in the GlyFS delivery to the cell surface. Also, further engineering of glycine-binding AYW core could result in the development of an intensimetric glycine biosensor, as exemplified by use of GltI in both FRET and single-FP biosensors for glutamate (Table 1).

## WORKFLOW FOR ENGINEERING OF BIOSENSORS FOR NEUROTRANSMITTERS

Modern biosensors for glutamate, GABA, acetylcholine, dopamine and glycine (Table 1) provide examples of the successful development of biosensors. Based on their engineering steps, we provide below the general workflow for development of biosensors for neurotransmitters and neuromodulators. The workflow consists of 4 steps outlined in Figure 3.

Step 1, an appropriate neurotransmitter or neuromodulator binding protein should be chosen. It can be VFTD or GPCR. As it was showed in engineering of biosensors for GABA (Marvin et al., 2019) and glycine (Zhang et al., 2018), a specificity of the selected sensing protein can become a problem. Natural Atu2422 protein binds both GABA and glycine, so that it is not possible to immediately use it for a biosensor specific to one of these neurotransmitters. Therefore, Zhang et al. (2018) mutated amino acid residues in the ligand-binding center of Atu2422 that resulted in a glycine-specific Atu2422 mutant, named AYW (Figure 3). Atu2422 sensing domain has been considered for GABA biosensor too, however, its low specificity prompted Marvin et al. (2019) to search for other GABA-binding proteins. That search resulted in the identification of Pf622 that interacts with GABA only (Marvin et al., 2019).

Step 2, the selected specific neurotransmitter or neuromodulator binding protein can be fused with either a cpFP or a FRET pair of monomeric FPs. For ratiometric FRET-based biosensors, this VFTD-containing sensing PBP is inserted between two FPs. For intensimetric biosensors, the cpFP is inserted in a flexible part of the VFTD-containing PBP, such as GltI in iGluSnFr (Marvin et al., 2013) or Pf622 in iGABASnFr (Marvin et al., 2019) biosensors. For both ratiometric and intensimetric GPCR-based biosensors, an insertion-point for FRET pair or cpFP is the same; it is the third intracellular loop that undergoes the most pronounced conformational changes upon GPCR activation.

Step 3, to efficiently report neurotransmitter changes several properties of the biosensor prototype obtained in the previous step should be improved. Fusing the neurotransmitter or neuromodulator binding protein with FRET pair or cpFP usually results in a biosensor variant with low dynamic range

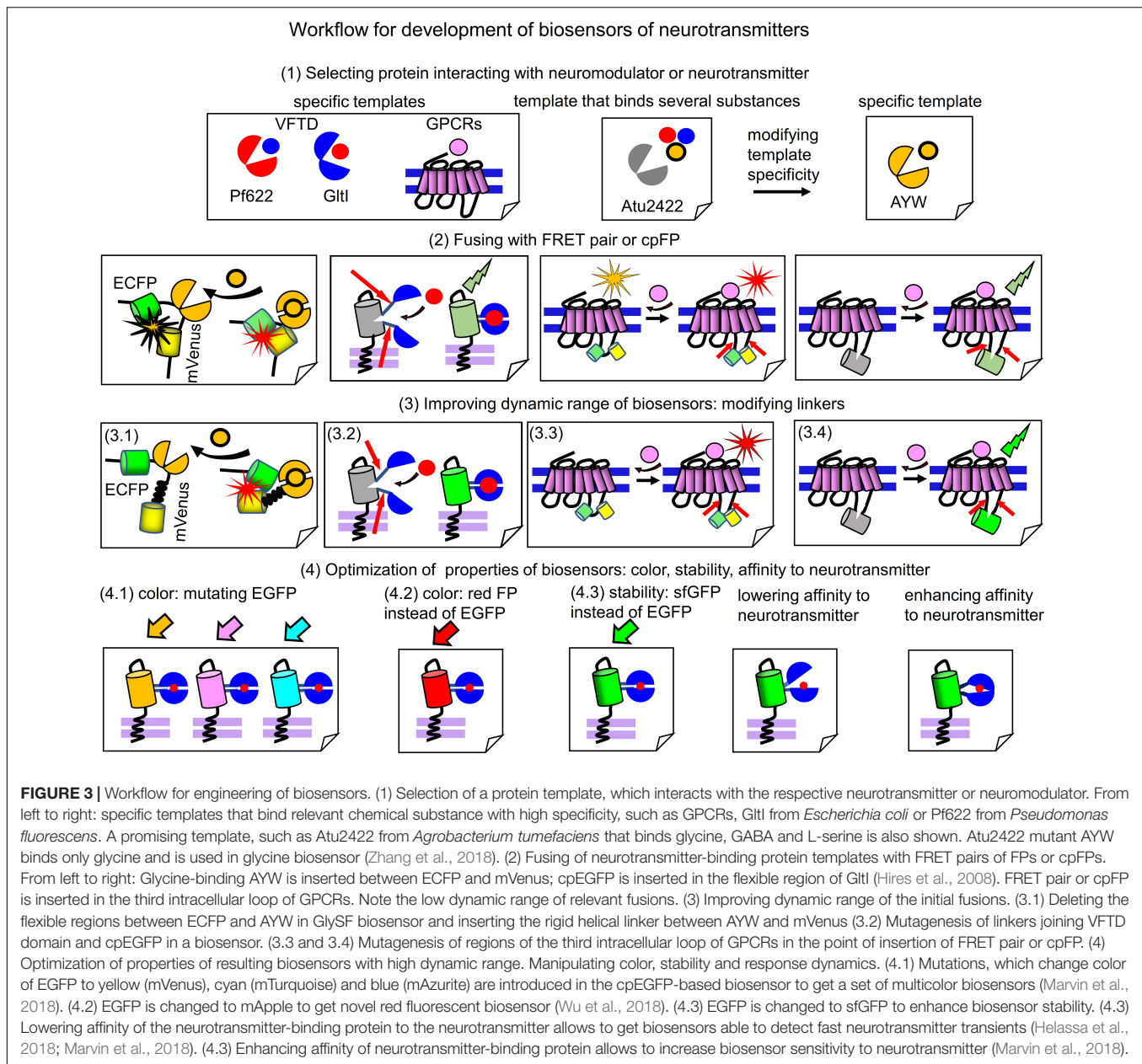
of FRET or fluorescence intensity changes upon binding the relevant substance. To improve dynamic range, a length and a composition of the linkers connecting FPs with the neurotransmitter-sensing domain (either VFTD or GPCR) should be modified by length and contents using either structure-based or random mutagenesis. For FRET-biosensors the linkers should provide an efficient separation of FPs in the non-bound state and optimally position FPs for high FRET in the bound state. For example, in GlySF glycine biosensor replacement of the flexible linker between AYW and FPs with the rigid helical linker (EAAAK)<sub>4</sub> resulted in the sevenfold increase of dynamic range (Zhang et al., 2018). In other cases linkers were either subjected to random mutagenesis followed by screening, as in the dopamine biosensors (Feng et al., 2018; Patriarchi et al., 2018) or modified by stepwise deletions of amino acid residues, as in the acetylcholine biosensor (Jing et al., 2018).

Step 4, the resulting biosensors with high dynamic range can be subjected to several types of optimizations to improve parameters, such as color, stability, affinity and rate. Many intensimetric biosensors contain circular permutants of GFP, which can be changed to other FPs. For example, the cpsfGFP-based glutamate biosensor SF-iGluSnFR was converted into blue, cyan and yellow biosensors (Marvin et al., 2018) by introducing chromophore-modifying mutations in cpsfGFP (Figure 3). Changing cpEGFP in iGluSnFR to cpmApple resulted in the red glutamate biosensors R-iGluSnFR1 and R-ncpiGluSnFR1 (Wu et al., 2018). An ability of biosensor to monitor fast dynamics of neurotransmitter in synaptic cleft can be improved by manipulating of binding affinity to neurotransmitter in the sensing protein by mutating a ligand-binding site of the respective VFTD. For example, the decrease of affinity resulted in the development of fast glutamate biosensors, such as iGlu (Helassa et al., 2018) and SF-iGluSnFR/S72A (Marvin et al., 2018).

## APPLICATION OF NEUROTRANSMITTER BIOSENSORS IN VIVO

Correlation of real-time neuronal activity with corresponding psychophysiological activities is one of the primary goals of neuroscience (Alivisatos et al., 2013). Since chemical transmission is the major communication pathway between neurons, precise detection of chemical transmission in neural circuits is required for achieving this goal. Chemical point-to-point transmission occurs extremely fast: depolarization of the post-synaptic neuron occurs within hundreds of milliseconds after glutamate release in the synaptic cleft. Chemical transmission underlies both unconscious and conscious behavior. Experimental objects perform complex psychophysiological tasks in 50–200 ms whereas perception of conscious experience requires 0.5–2 s (Korf and Gramsbergen, 2007).

Traditional molecular imaging methods, such as magnetic resonance imaging (MRI), proton MR spectroscopy (HMRS), and positron emission tomography (PET), has insufficient spatiotemporal resolution to efficiently visualize these fast events



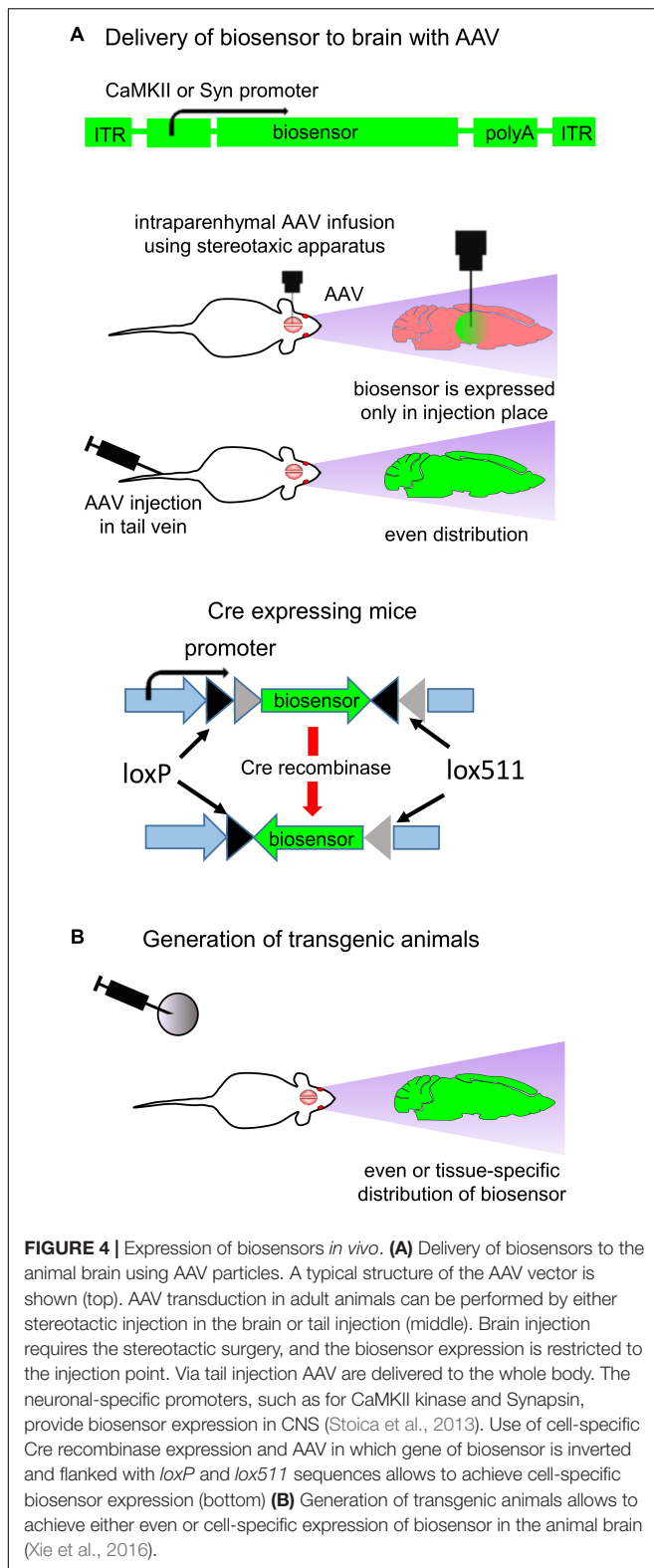
of chemical transmission. For example, PET has temporal resolution of few minutes and spatial resolution of few millimeters (Liang et al., 2015). Moreover, these techniques do not allow imaging of single neurons and separate neural circuits. However, spatially-precise longitudinal detection of fast neurotransmitter transients in the animal brain can be performed using modern optical techniques.

## Setups for *in vivo* Experiments

Design of *in vivo* experiment with fluorescent biosensors for neurotransmitters and neuromodulators, consists of a transduction of the relevant brain zone with adeno-associated virus (AAV) encoding a biosensor under specific promoters. AAV injection can be performed intravenously via either tail injection

or using stereotactic injection, which requires surgery. Tail injection allows to achieve even AAV distribution in the rodent brain whereas stereotactic injection leads to expression of the neurotransmitter only at the injection place (Figure 4A; Boulaire et al., 2009; Stoica et al., 2013). In the case of tail injection a tissue-specific promoter is important to limit biosensor expression to certain tissue or subset of cells.

Common way to achieve neuron-specific biosensor expression is use of specific promoters, such as human *Synapsin1* (hSyn1) promoter or *CaMKII* promoter (Kugler et al., 2003). *Synapsin1* promoter ensures efficient neuronal targeting without expression in glial cells (Kugler et al., 2003). If expression of biosensor in glial cells is desirable then glial fibrillary acidic protein (GFAP) promoter can be used (Dashkoff et al., 2016).



Some promoters are able to limit transgene expression to one type of neurons only. For example, Hb9 promoter limits biosensor expression to motor neurons (Lukashchuk et al., 2016).

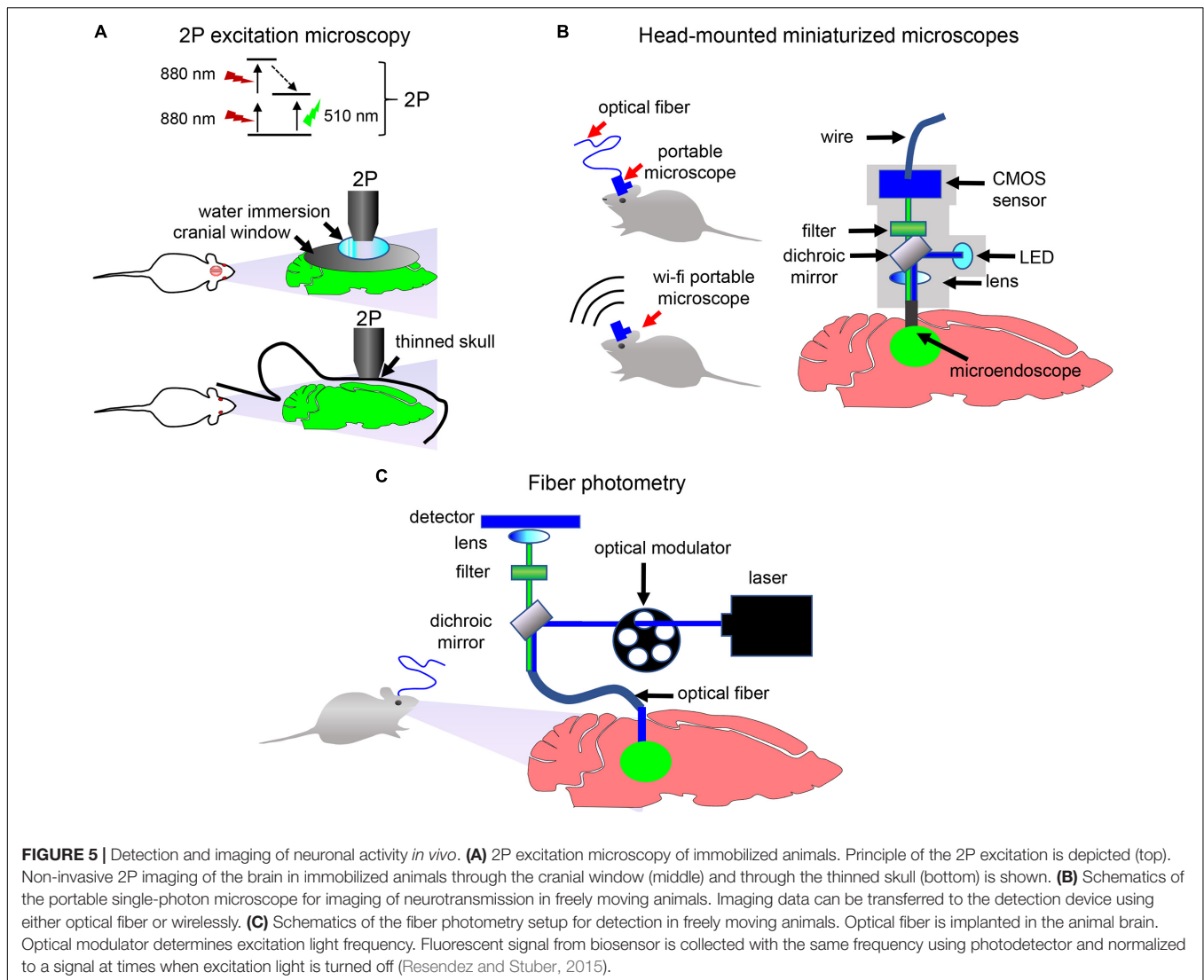
mDlx enhancer placed before the minimal AAV promoter restricts transgene expression to GABAergic neurons (Dimidschstein et al., 2016; Wilson et al., 2017), and *Vglut2* promoter restricts transgene expression to glutamatergic neurons (Borgius et al., 2010). For detailed description of the relevant neuronal-specific promoters we refer readers to several reviews (Shevtsova et al., 2005; Hioki et al., 2007; Delzor et al., 2012; Dashkoff et al., 2016).

Generation of a transgenic animal line is another way to achieve cell-specific biosensor expression in the mammalian brain (Figure 4B; McGirr et al., 2017). Biosensor expression is defined to the specific subset of neurons if mice with cell-specific expression of Cre recombinase are used. In this case, mice are injected with AAV in which the biosensor encoding sequence is inverted and flanked with *loxP* and *lox511* sequences (Figure 4A; bottom). Cre recombinase recognizes the *lox* sequences, excises and inverts the biosensor gene. For example, expressing Cre recombinase under the glutamatergic neurons specific *Vglut2* promoter allows to confine the gene expression to the excitatory glutamatergic neurons (Borgius et al., 2010).

Delivery of biosensor can be followed by the visualization of transmitter-specific events in the brain of behaving animals with 2P microscopy, miniaturized head-mounted microscopes or fiber photometry (Figure 5; Helmchen et al., 2001; Guo et al., 2015; Brunert et al., 2016; Ozbay et al., 2018).

When choosing how image acquisition should be performed, two important issues should be considered. If study is performed in immobilized animals, then imaging can be done using a stationary 2P microscope. The 2P microscopy can be performed via two types of imaging windows. In one type, a thin-skull window technique is used in which the skull is thinned down to a thickness of  $\sim 15 \mu\text{m}$ . In another type, a part of skull is removed and a glass cranial window is placed instead (Figure 5A). Both window techniques have advantages and disadvantages. The thinned-skull window is less invasive and allows immediate chronic imaging after surgery and long imaging intervals. Open-skull window allows imaging of deep brain layers (Yang et al., 2010). Thinned-skull and open-skull window techniques are compared in details in several reviews (Yang et al., 2010; Isshiki and Okabe, 2014).

If detection of neurotransmitter transients in freely behaving animals is desirable, then a miniaturized head-mounted microscope or a fiber photometry can be used (Figures 5B,C). A number of miniaturized devices has been developed by different research groups (Aharoni et al., 2019). While usually a miniaturized microscope is connected with the detection device using an optical fiber, wireless microscopes became recently available too (Liberti et al., 2017). In contrast to single-photon head-mounted microscopes that frequently require invasive brain surgery for inserting optical objectives or prisms in the brain, 2P miniaturized microscopes allow non-invasive deep-brain imaging via thinned skull or, with limited skull surgery, via cranial window (Silva, 2017). Moreover, modern 2P head-mounted microscopes allow high-resolution imaging of cortex with visualization of individual dendrites and dendritic spines (Silva, 2017; Ozbay et al., 2018).



Similarly to miniaturized microscopes, a fiber photometry (**Figure 5C**) enables detection of fluorescence in the brain of freely moving animals. However, it requires implantation of an optical fiber in the animal brain and, opposed to the above microscopy approaches, lacks single-cell resolution. Nevertheless, simplicity of fiber photometry instrumentation and high sensitivity of detection of neuronal activities makes it attractive to researchers (Resendez and Stuber, 2015). Multicolor fiber photometry is also available, allowing readout of several biosensors simultaneously. Moreover, a wireless fiber photometry was recently developed to detect biosensor responses in the brain of non-tethered animals (Lu et al., 2018).

## Examples of Applications of Biosensors for Neurotransmitters

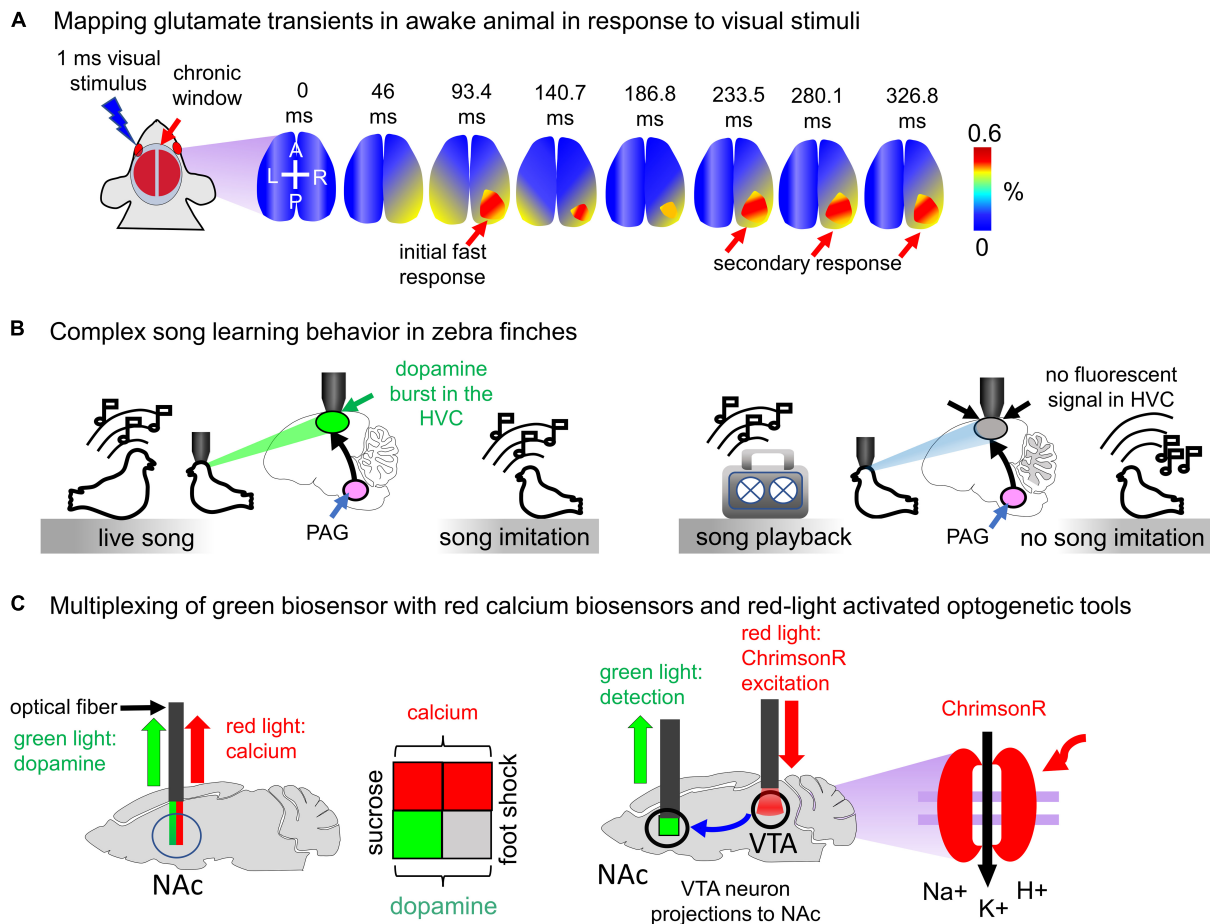
Biosensors for neurotransmitters are used in animals in a wide range of studies, from simple responses to sensory stimuli to complex animal behaviors in models of mood disorders.

## Mapping Neurotransmitter Transients in Cortex of Behaving Animals

Neurotransmitter biosensors allow precise spatiotemporal mapping of neurotransmission in the brain of animals. For example, Xie et al. (2016) used iGluSnFR to determine high-frequency mesoscale intracortical maps. In this study iGluSnFR enabled to resolve temporal features of sensory processing in both anesthetized and awake mice. The fast glutamate transmission events on 13–200 ms timescale in response to sensual stimuli, such as touching whiskers, skin on the fore- and hind limbs, and visual stimuli, were imaged (**Figure 6A**; Xie et al., 2016).

iGluSnFR was also used to localize task-specific glutamate events in the primary motor cortex of mice. iGluSnFR was delivered to the mouse motor cortex using AAV particles, and the brain of mice was imaged in rest and upon running (while head of running mice was fixed). It was found that in the brain of resting mice the repetitive glutamate transients are observed in dendritic spines. Running increased frequency of these events twice over 8 s of running. Extremely high spatiotemporal resolution in





**FIGURE 6 |** Visualization of neurotransmitter transients *in vivo*. **(A)** Mapping glutamate transients in the mouse brain is performed through the chronic cranial window. One millisecond light visual stimulation induces an initial fast response followed by a clearly separated secondary response in awake Emx-CaMKII-iGluSnFR mouse (Xie et al., 2016). **(B)** Complex song learning in zebra finches is outlined. Left: juvenile zebra finch is exposed to the living adult male tutor. The song causes dopamine bursts in the high vocal center (HVC) of the juvenile bird, resulting in song learning. Right: juvenile zebra finch is exposed to the playback of the song. Dopamine bursts in the HVC of juvenile bird are not detected, and consequently, song learning does not occur (Tanaka et al., 2018). **(C)** Spectral multiplexing of green fluorescent dLight1.1 with either red fluorescent jRGECO1a biosensor or channelrhodopsin ChrimsonR activatable with red light. Left: both dopamine and calcium signals are detected in the mouse brain using multicolor fiber photometry. The sucrose application causes both dopamine transients and neuronal activity in the NAc (green and red squares), whereas the foot shock increases calcium but not dopamine transients (gray and red squares). Right: ChrimsonR channelrhodopsin is selectively expressed in the VTA of the mouse brain. Activation of ChrimsonR with red light causes the dopamine release in the NAc. The VTA neuron projections to NAc are shown with the arrow.

this study demonstrates the utility of iGluSnFR for the precise mapping of glutamate release events (Marvin et al., 2013).

### Complex Song Learning in Zebra Finches

Juvenile zebra finches copy songs of the living bird adult tutors only if they interact with them and fail to reproduce songs played to them through a speaker (Figure 6B). To elucidate how juvenile birds detect a difference between the tutor and speaker Tanaka et al. (2018) expressed intensimetric dopamine biosensor GRAB<sub>DA1h</sub> in the neurons of high vocal center (HVC) and imaged dopamine transients using 2P microscopy. He has found that only interaction with the song of live tutor caused dopamine secretion by the neurons of the periaqueductal gray (PAG). Even playback of the song from the recent tutor failed to evoke similar activity. Thus,

the single-FP neurotransmitter biosensor allowed to visualize dopamine transients with the single-neuron precision and to establish connection between dopamine secretion by the PAG neurons and transmission of vocal behaviors from one bird to another (Tanaka et al., 2018).

In the same study the PAG neurons were excited optogenetically using ChR2 channelrhodopsin actuator expressed in the HVC. Interestingly, the excitation of the HVC neurons via ChR2 in combination with playback of the song from the speaker resulted in the successful learning by juvenile birds (Tanaka et al., 2018). Dopamine blockers reduced the effect. However, optogenetic excitation was not combined with the simultaneous analysis of dopamine transients because ChR2 is excited by the same light used for visualization of EGFP-based biosensors.

## Multiplexing of dLight1.1 With Red-Light Excited Probes

The availability of red fluorescent calcium biosensors and red-shifted channelrhodopsins provides possibility either to simultaneously detect neurotransmitter transients and neuron activity or to combine optogenetic excitation of certain neurons with detection of neurotransmitters released by their terminals. Patriarchi et al. (2018) combined visualization of dopamine transients with calcium imaging using jRGECO1a red biosensor. It has been shown that mice consuming water containing sucrose (reward) show both dopamine and calcium peaks in the nucleus accumbens (NAc) region. However, mice subjected to foot shock demonstrated only calcium spikes in the NAc (**Figure 6C**; Patriarchi et al., 2018).

In the same study dLight1.1 was combined with the red-light excited channelrhodopsin ChrimsonR (**Figure 6C**). Dopaminergic neurons in the ventral tegmental area (VTA) send projections to the NAc. dLight1.1 was delivered in the mouse brain using AAV particles, and ChrimsonR was selectively expressed in the VTA. Photostimulation of neurons in the VTA enabled detection of individual peaks of dopamine transients in the NAc region.

## Imaging Neurotransmission in Animal Behavioral Models

Dysregulation of neurotransmission underlies the number of brain diseases, making the biosensors useful in various animal models of human neuropsychiatric disorders. The animal models of human CNS disorders proved their effectiveness in studies of Parkinsonism (Blesa and Przedborski, 2014), major depressive disorder (Morozova et al., 2016; Zorkina et al., 2019), autism (Chesselet, 2005) and many others reviewed elsewhere (Keifer and Summers, 2016).

For example, the glutamate intensimetric biosensor iGluSnFR was used to study antidepressant activities of ketamine (McGirr et al., 2017). Transgenic mice expressing iGluSnFR (**Figure 4B**) were subjected to social defeat model of depression and then treated with ketamine. Glutamate transients were imaged non-invasively using the thin-skull window technique. Longitudinal tracking of iGluSnFR signal revealed that social defeat caused the network-wide glutamate functional hyperconnectivity in animals whereas injection of ketamine reduces this effect.

In another study, the GRAB<sub>DA</sub> biosensor for dopamine was applied to detect endogenous dopamine release during Pavlovian conditioning in immobilized and freely moving mice (Feng et al., 2018). The water-restricted mice were trained to associate a brief auditory cue with reward (a drop of water). Monitoring fluorescence changes of GRAB<sub>DA</sub> in these trained animals allowed to visualize dopamine release in response to the reward-predictive cue (sound). Also, the dopamine biosensor was used to study dopamine dynamics during naturally rewarding social behaviors, such as courtship and mating. It was confirmed that introduction of the sexually receptive mouse female into the home cage of the male promoted dopamine release during mating.

Moreover, given the important role of dopaminergic transmission in reward and pleasure behavior (Bressan and Crippa, 2005) it will be advantageous to apply dopamine biosensors in animal models of depression, similarly to iGluSnFR.

## CONCLUSION

Recently developed fluorescent biosensors for glutamate, dopamine, acetylcholine, adrenaline and GABA allow to detect neuronal activity *in vivo* with high spatiotemporal precision. Single-FP-based intensimetric biosensors represent the most useful group of the biosensors because they are monochromic and have the higher dynamic range than FRET-based, thus, enabling spectral multiplexing with other biosensors or optogenetic tools and imaging of neuronal activity *in vivo*, respectively.

In spite of many advantages, there are two major limitations of the biosensors for neurotransmitters and neuromodulators. One limitation is that these biosensors may influence dynamics of neurotransmitters and neuromodulators in the brain by binding them. The similar problem and possible ways of its resolution were recently described for calcium biosensors (McMahon and Jackson, 2018). The other limitation is related to use of the biosensors in the human brain. Although nervous system is considered immunologically tolerant, but expression of proteins from bacteria and invertebrates may cause immunological response. Currently, expression of bacterial channelrhodopsins is restricted to human eyes in vision restoration (Baker and Flannery, 2018). However, heterologous expression of bacterial proteins may become a subject of immunogenicity (Maimon et al., 2018).

We foresee the following future directions in the development and applications of biosensors for chemical transmission.

First, the major characteristics of the existing fluorescent biosensors, such as selectivity, stability, sensitivity, kinetics, reversibility and dynamic range (Shang and Filizola, 2015), will be enhanced and optimized for specific applications in the mammalian brain.

Second, the availability of the neurotransmitter- and neuromodulator-binding proteins in unicellular and multicellular organisms, including diverse bacterial ABC-transporters (Moussatova et al., 2008), GABA-binding malate transporters in plants (Ramesh et al., 2015), and monoamine-binding transporters in worms (Ribeiro and Patocka, 2013), allows to anticipate that they will be used as molecular templates to engineer novel biosensors. Likely, search of these templates can be alleviated using machine learning approaches, such as deep learning. Machine learning is based on computer algorithms, which are able to learn automatically to distinguish between various datasets, for example, between two sets of images (Majaj and Pelli, 2018). Deep machine learning is based on complex multi-layered artificial neural networks (Miotto et al., 2018; Mehta et al., 2019). Deep learning approaches are already used to predict interaction of a chemical substance, like drug, with a target protein. Likely, deep learning approaches for prediction of drug-target interactions (Anusuya et al., 2018; Lee et al., 2019)



and to annotate protein functions (Sureyya Rifaioğlu et al., 2019) can be adapted to predict interaction of neurotransmitters or neuromodulators with proteins with unknown function. Thus, novel specific neurotransmitter-binding proteins can be found while limitations derived from use of GPCRs or finite number of bacterial proteins used in biosensor engineering could be overcome. Use of deep learning for identification of such proteins *in silico* will reduce laborious and time-consuming search for neurotransmitter-binding proteins *in vitro*.

Third, the available biosensors have fluorescence readout mainly in the green range of light spectrum, with few exceptions in the red range. We anticipate that more red and, moreover, far-red and near-infrared fluorescent biosensors for neurotransmitters will be developed based on the modern red (Shcherbakova et al., 2015), far-red and near-infrared FPs (Chernov et al., 2017; Oliinyk et al., 2017; Shcherbakova et al., 2018). Far-red and near-infrared light is less cytotoxic, penetrates animal tissues deeper, and exhibits less scattering. Moreover, far-red and near-infrared biosensors will allow cross-talk free simultaneous use of common optogenetic tools and major calcium biosensors.

Fourth, we hypothesize that processing of the data obtained in imaging experiments will benefit from deep learning methods. Neurotransmitter and neuromodulator biosensors allow *in vivo* detection of large neural populations during weeks with single-neuron and single-spike resolution, similar to calcium biosensors (Pnevmatikakis, 2019). Several deep learning-based techniques for calcium imaging (Stringer and Pachitariu, 2019) can be adopted for processing of data obtained in experiments with neurotransmitter imaging. For example, an artificial neural network STNeuroNet was recently used to identify and segment active neurons expressing calcium biosensor (Soltanian-Zadeh et al., 2019). Likely, the similar technologies will be applied for analysis of large datasets of neurotransmitter and neuromodulator imaging.

## REFERENCES

- Aharoni, D., Khakh, B. S., Silva, A. J., and Golshani, P. (2019). All the light that we can see: a new era in miniaturized microscopy. *Nat. Methods* 16, 11–13. doi: 10.1038/s41592-018-0266-x
- Alivisatos, A. P., Andrews, A. M., Boyden, E. S., Chun, M., Church, G. M., Deisseroth, K., et al. (2013). Nanotools for neuroscience and brain activity mapping. *ACS Nano* 7, 1850–1866. doi: 10.1021/nn4012847
- Andersen, R. A., Kellis, S., Klaes, C., and Aflalo, T. (2014). Toward more versatile and intuitive cortical brain-machine interfaces. *Curr. Biol.* 24, R885–R897. doi: 10.1016/j.cub.2014.07.068
- Ankireddy, S. R., and Kim, J. (2015). Selective detection of dopamine in the presence of ascorbic acid via fluorescence quenching of InP/ZnS quantum dots. *Int. J. Nanomedicine* 10, 113–119. doi: 10.2147/IJN.S88388
- Anusuya, S., Keshervani, M., Priya, K. V., Vimala, A., Shanmugam, G., Velmurugan, D., et al. (2018). Drug-target interactions: prediction methods and applications. *Curr. Protein Pept. Sci.* 19, 537–561. doi: 10.2174/1389203718666161108091609
- Avery, M. C., and Krichmar, J. L. (2017). Neuromodulatory systems and their interactions: a review of models, theories, and experiments. *Front. Neural Circuits* 11:108. doi: 10.3389/fncir.2017.00108
- Baig, A. M., and Ahmad, H. R. (2017). Evidence of a M1-muscarinic GPCR homolog in unicellular eukaryotes: featuring *Acanthamoeba* spp bioinformatics 3D-modelling and experimentations. *J. Recept. Signal Transduct. Res.* 37, 267–275. doi: 10.1080/10799893.2016.1217884
- Baig, A. M., Rana, Z., Tariq, S., Lalani, S., and Ahmad, H. R. (2018). Traced on the timeline: discovery of acetylcholine and the components of the human cholinergic system in a primitive unicellular eukaryote *Acanthamoeba* spp. *ACS Chem. Neurosci.* 9, 494–504. doi: 10.1021/acschemneuro.7b00254
- Baker, C. K., and Flannery, J. G. (2018). Innovative optogenetic strategies for vision restoration. *Front. Cell Neurosci.* 12:316. doi: 10.3389/fncel.2018.00316
- Bando, Y., Sakamoto, M., Kim, S., Ayzenshtat, I., and Yuste, R. (2019). Comparative evaluation of genetically encoded voltage indicators. *Cell Rep.* 26, 802.e4–813.e4. doi: 10.1016/j.celrep.2018.12.088
- Blesa, J., and Przedborski, S. (2014). Parkinson's disease: animal models and dopaminergic cell vulnerability. *Front. Neuroanat.* 8:155. doi: 10.3389/fnana.2014.00155
- Borgius, L., Restrepo, C. E., Leao, R. N., Saleh, N., and Kiehn, O. (2010). A transgenic mouse line for molecular genetic analysis of excitatory glutamatergic neurons. *Mol. Cell Neurosci.* 45, 245–257. doi: 10.1016/j.mcn.2010.06.016
- Borodovitsyna, O., Flamini, M., and Chandler, D. (2017). Noradrenergic modulation of cognition in health and disease. *Neural Plast.* 2017:6031478. doi: 10.1155/2017/6031478
- Boulaire, J., Balani, P., and Wang, S. (2009). Transcriptional targeting to brain cells: engineering cell type-specific promoter containing cassettes for enhanced transgene expression. *Adv. Drug Deliv. Rev.* 61, 589–602. doi: 10.1016/j.addr.2009.02.007

Fifth and last, much wider implementation of biosensors for neurotransmitters and neuromodulators for mapping of brain activity can be anticipated. Correlation between brain activities and behavior makes possible prediction of motor or cognitive functions out of imaging data (Li et al., 2019). Data obtained by imaging of fluorescent biosensors for neurotransmitters and neuromodulators in animal brain can also be used to predict motor and cognitive function in animal models. For example, calcium imaging data recorded by 2P microscopy in rodent brain were used to predict features of upcoming movement (forelimb reach) in mice. For that, the authors collected calcium imaging signal from motor cortex while mice were performing a two-dimensional lever reaching task. Obtained calcium imaging data were used to train deep learning model to predict forelimb movement direction in mice. This deep learning model was then used to determine the motion direction based on imaging of calcium in the motor cortex (Li et al., 2019). We hypothesize that this approach can be expanded to the prediction of motion direction out of neurotransmitter and neuromodulator biosensor imaging. Such data can be further applied in the field of brain-computer interface (Andersen et al., 2014; Li et al., 2019).

## AUTHOR CONTRIBUTIONS

All authors contributed to the writing and reviewing of the manuscript.

## FUNDING

This work was supported by the grants GM122567 (VV) and EY030705 (DS) from the US National Institutes of Health, and 322226 (VV) from the Academy of Finland.

- Bressan, R. A., and Crippa, J. A. (2005). The role of dopamine in reward and pleasure behaviour—review of data from preclinical research. *Acta Psychiatr. Scand. Suppl.* 427, 14–21. doi: 10.1111/j.1600-0447.2005.00540.x
- Brunert, D., Tsuno, Y., Rothermel, M., Shipley, M. T., and Wachowiak, M. (2016). Cell-type-specific modulation of sensory responses in olfactory bulb circuits by serotonergic projections from the raphe nuclei. *J. Neurosci.* 36, 6820–6835. doi: 10.1523/JNEUROSCI.3667-15.2016
- Burnstock, G. (2006). Historical review: ATP as a neurotransmitter. *Trends Pharmacol. Sci.* 27, 166–176. doi: 10.1016/j.tips.2006.01.005
- Cahill, L., and Alkire, M. T. (2003). Epinephrine enhancement of human memory consolidation: interaction with arousal at encoding. *Neurobiol. Learn. Mem.* 79, 194–198. doi: 10.1016/s1074-7427(02)00036-9
- Chen, Z., Truong, T. M., and Ai, H. W. (2017). Illuminating brain activities with fluorescent protein-based biosensors. *Chemosensors* 5:32. doi: 10.3390/chemosensors5040032
- Chernov, K. G., Redchuk, T. A., Omelina, E. S., and Verkhusha, V. V. (2017). Near-infrared fluorescent proteins, biosensors, and optogenetic tools engineered from phytochromes. *Chem. Rev.* 117, 6423–6446. doi: 10.1021/acs.chemrev.6b00700
- Chesselet, M. F. (2005). Animal models of neurological disorders. *NeuroRx* 2:395. doi: 10.1602/neurorx.2.3.395
- Clarke, M. B., Hughes, D. T., Zhu, C., Boedeker, E. C., and Sperandio, V. (2006). The QseC sensor kinase: a bacterial adrenergic receptor. *Proc. Natl. Acad. Sci. U.S.A.* 103, 10420–10425. doi: 10.1073/pnas.0604343103
- Conley, J. M., Radhakrishnan, S., Valentino, S. A., and Tantama, M. (2017). Imaging extracellular ATP with a genetically-encoded, ratiometric fluorescent sensor. *PLoS One* 12:e0187481. doi: 10.1371/journal.pone.0187481
- Dashkoff, J., Lerner, E. P., Truong, N., Klickstein, J. A., Fan, Z., Mu, D., et al. (2016). Tailored transgene expression to specific cell types in the central nervous system after peripheral injection with AAV9. *Mol. Ther. Methods Clin. Dev.* 3:16081. doi: 10.1038/mtm.2016.81
- Delzor, A., Dufour, N., Petit, F., Guillermier, M., Houitte, D., Auregan, G., et al. (2012). Restricted transgene expression in the brain with cell-type specific neuronal promoters. *Hum. Gene Ther. Methods* 23, 242–254. doi: 10.1089/hgtb.2012.073
- Dimidschstein, J., Chen, Q., Tremblay, R., Rogers, S. L., Saldi, G. A., Guo, L., et al. (2016). A viral strategy for targeting and manipulating interneurons across vertebrate species. *Nat. Neurosci.* 19, 1743–1749. doi: 10.1038/nn.4430
- Dunn, M., Henke, A., Clark, S., Kovalyova, Y., Kempadoo, K. A., Karpowicz, R. J., et al. (2018). Designing a norepinephrine optical tracer for imaging individual noradrenergic synapses and their activity in vivo. *Nat. Commun.* 9:2838. doi: 10.1038/s41467-018-05075-x
- Eichel, K., and von Zastrow, M. (2018). Subcellular organization of GPCR Signaling. *Trends Pharmacol. Sci.* 39, 200–208. doi: 10.1016/j.tips.2017.11.009
- Elphick, M. R., Mirabeau, O., and Larhammar, D. (2018). Evolution of neuropeptide signalling systems. *J. Exp. Biol.* 221(Pt 3):jeb151092. doi: 10.1242/jeb.151092
- Feng, J., Zhang, C., Lischinsky, J., Jing, M., Zhou, J., Wang, H., et al. (2018). A genetically encoded fluorescent sensor for rapid and specific *in vivo* detection of norepinephrine. *bioRxiv [Preprint]*. 449546. doi: 10.1101/449546
- Feng, J., Zhang, C., Lischinsky, J. E., Jing, M., Zhou, J., Wang, H., et al. (2019). A genetically encoded fluorescent sensor for rapid and specific *in vivo* detection of norepinephrine. *Neuron* 102, 745.e8–761.e8. doi: 10.1016/j.neuron.2019.02.037
- Forde, B. G., and Roberts, M. R. (2014). Glutamate receptor-like channels in plants: a role as amino acid sensors in plant defence? *F1000Prime Rep.* 6:37. doi: 10.12703/P6-37
- Guo, Q., Zhou, J., Feng, Q., Lin, R., Gong, H., Luo, Q., et al. (2015). Multi-channel fiber photometry for population neuronal activity recording. *Biomed. Opt. Express* 6, 3919–3931. doi: 10.1364/BOE.6.003919
- Harada, K., Kamiya, T., and Tsuboi, T. (2015). Gliotransmitter release from astrocytes: functional, developmental, and pathological implications in the brain. *Front. Neurosci.* 9:499. doi: 10.3389/fnins.2015.00499
- Helassa, N., Durst, C. D., Coates, C., Kerruth, S., Arif, U., Schulze, C., et al. (2018). Ultrafast glutamate sensors resolve high-frequency release at Schaffer collateral synapses. *Proc. Natl. Acad. Sci. U.S.A.* 115, 5594–5599. doi: 10.1073/pnas.1720648115
- Helmchen, F., Fee, M. S., Tank, D. W., and Denk, W. (2001). A miniature head-mounted two-photon microscope: high-resolution brain imaging in freely moving animals. *Neuron* 31, 903–912. doi: 10.1016/s0896-6273(01)00421-4
- Hioki, H., Kameda, H., Nakamura, H., Okunomiya, T., Ohira, K., Nakamura, K., et al. (2007). Efficient gene transduction of neurons by lentivirus with enhanced neuron-specific promoters. *Gene Ther.* 14, 872–882. doi: 10.1038/sj.gt.3302924
- Hires, S. A., Zhu, Y., and Tsien, R. Y. (2008). Optical measurement of synaptic glutamate spillover and reuptake by linker optimized glutamate-sensitive fluorescent reporters. *Proc. Natl. Acad. Sci. U.S.A.* 105, 4411–4416. doi: 10.1073/pnas.0712008105
- Hoyle, C. H. (2011). Evolution of neuronal signalling: transmitters and receptors. *Auton. Neurosci.* 165, 28–53. doi: 10.1016/j.autneu.2010.05.007
- Irannejad, R., Tomshine, J. C., Tomshine, J. R., Chevalier, M., Mahoney, J. P., Steyaert, J., et al. (2013). Conformational biosensors reveal GPCR signalling from endosomes. *Nature* 495, 534–538. doi: 10.1038/nature12000
- Isshiki, M., and Okabe, S. (2014). Evaluation of cranial window types for *in vivo* two-photon imaging of brain microstructures. *Microscopy* 63, 53–63. doi: 10.1093/jmicro/dft043
- Jing, M., Zhang, P., Wang, G., Feng, J., Mesik, L., Zeng, J., et al. (2018). A genetically encoded fluorescent acetylcholine indicator for *in vitro* and *in vivo* studies. *Nat. Biotechnol.* 36, 726–737. doi: 10.1038/nbt.4184
- Kannan, M., Vasan, G., and Pieribone, V. A. (2019). Optimizing strategies for developing genetically encoded voltage indicators. *Front. Cell Neurosci.* 13:53. doi: 10.3389/fncel.2019.00053
- Katritch, V., Cherezov, V., and Stevens, R. C. (2013). Structure-function of the G protein-coupled receptor superfamily. *Annu. Rev. Pharmacol. Toxicol.* 53, 531–556. doi: 10.1146/annurev-pharmtox-032112-135923
- Keifer, J., and Summers, C. H. (2016). Putting the “Biology” Back into “Neurobiology”: the strength of diversity in animal model systems for neuroscience research. *Front. Syst. Neurosci.* 10:69. doi: 10.3389/fnsys.2016.00069
- Klein, M. O., Battagello, D. S., Cardoso, A. R., Hauser, D. N., Bittencourt, J. C., and Correa, R. G. (2019). Dopamine: functions, signaling, and association with neurological diseases. *Cell Mol. Neurobiol.* 39, 31–59. doi: 10.1007/s10571-018-0632-3
- Korf, J., and Gramsbergen, J. B. (2007). Timing of potential and metabolic brain energy. *J. Neurochem.* 103, 1697–1708. doi: 10.1111/j.1471-4159.2007.04909.x
- Kugler, S., Kilic, E., and Bahr, M. (2003). Human synapsin 1 gene promoter confers highly neuron-specific long-term transgene expression from an adenoviral vector in the adult rat brain depending on the transduced area. *Gene Ther.* 10, 337–347. doi: 10.1038/sj.gt.3301905
- Kunishima, N., Shimada, Y., Tsuji, Y., Sato, T., Yamamoto, M., Kumasaka, T., et al. (2000). Structural basis of glutamate recognition by a dimeric metabotropic glutamate receptor. *Nature* 407, 971–977. doi: 10.1038/35039564
- Larsen, M. B., Fontana, A. C., Magalhaes, L. G., Rodrigues, V., and Mortensen, O. V. (2011). A catecholamine transporter from the human parasite *Schistosoma mansoni* with low affinity for psychostimulants. *Mol. Biochem. Parasitol.* 177, 35–41. doi: 10.1016/j.molbiopara.2011.01.006
- Lecat-Guillet, N., Monnier, C., Rovira, X., Kniazeff, J., Lamarque, L., Zwier, J. M., et al. (2017). FRET-based sensors unravel activation and allosteric modulation of the GABAB receptor. *Cell Chem. Biol.* 24, 360–370. doi: 10.1016/j.chembiol.2017.02.011
- Lee, I., Keum, J., and Nam, H. (2019). DeepConv-DTI: prediction of drug-target interactions via deep learning with convolution on protein sequences. *PLoS Comput. Biol.* 15:e1007129. doi: 10.1371/journal.pcbi.1007129
- Li, C., Chan, D. C. W., Yang, X., Ke, Y., and Yung, W. H. (2019). Prediction of forelimb reach results from motor cortex activities based on calcium imaging and deep learning. *Front. Cell Neurosci.* 13:88. doi: 10.3389/fncel.2019.00088
- Li, G., Kong, W., Zhao, M., Lu, S., Gong, P., Chen, G., et al. (2016). A fluorescence resonance energy transfer (FRET) based “Turn-On” nanofluorescence sensor using a nitrogen-doped carbon dot-hexagonal cobalt oxyhydroxide nanosheet architecture and application to alpha-glucosidase inhibitor screening. *Biosens. Bioelectron.* 79, 728–735. doi: 10.1016/j.bios.2015.12.094
- Liang, R., Broussard, G. J., and Tian, L. (2015). Imaging chemical neurotransmission with genetically encoded fluorescent sensors. *ACS Chem. Neurosci.* 6, 84–93. doi: 10.1021/cn500280k
- Liberti, W. A., Perkins, L. N., Leman, D. P., and Gardner, T. J. (2017). An open source, wireless capable miniature microscope system. *J. Neural Eng.* 14:045001. doi: 10.1088/1741-2552/aa6806

- Lindenburg, L., and Merckx, M. (2014). Engineering genetically encoded FRET sensors. *Sensors* 14, 11691–11713. doi: 10.3390/s140711691
- Lobas, M., Nagai, J., Kronschrager, M. T., Borden, P., Marvin, J. S., Looger, L. L., et al. (2018). A genetically encoded single-wavelength sensor for imaging cytosolic and cell surface ATP. *bioRxiv [Preprint]*. 385484. doi: 10.1101/385484
- Lu, L., Gutruf, P., Xia, L., Bhatti, D. L., Wang, X., Vazquez-Guardado, A., et al. (2018). Wireless optoelectronic photometers for monitoring neuronal dynamics in the deep brain. *Proc. Natl. Acad. Sci. U.S.A.* 115, E1374–E1383. doi: 10.1073/pnas.1718721115
- Lukashchuk, V., Lewis, K. E., Coldicott, I., Grierson, A. J., and Azzouz, M. (2016). AAV9-mediated central nervous system-targeted gene delivery via cisterna magna route in mice. *Mol. Ther. Methods Clin. Dev.* 3:15055. doi: 10.1038/mtm.2015.55
- Maimon, B. E., Diaz, M., Revol, E. C. M., Schneider, A. M., Leaker, B., Varela, C. E., et al. (2018). Optogenetic peripheral nerve immunogenicity. *Sci. Rep.* 8:14076. doi: 10.1038/s41598-018-32075-0
- Majaj, N. J., and Pelli, D. G. (2018). Deep learning-using machine learning to study biological vision. *J. Vis.* 18:2. doi: 10.1167/18.13.2
- Markovic, D., Holdich, J., Al-Sabah, S., Mistry, R., Krasel, C., Mahaut-Smith, M. P., et al. (2012). FRET-based detection of M1 muscarinic acetylcholine receptor activation by orthosteric and allosteric agonists. *PLoS One* 7:e29946. doi: 10.1371/journal.pone.0029946
- Marvin, J. S., Borghuis, B. G., Tian, L., Cichon, J., Harnett, M. T., Akerboom, J., et al. (2013). An optimized fluorescent probe for visualizing glutamate neurotransmission. *Nat. Methods* 10, 162–170. doi: 10.1038/nmeth.2333
- Marvin, J. S., Scholl, B., Wilson, D. E., Podgorski, K., Kazempour, A., Muller, J. A., et al. (2018). Stability, affinity, and chromatic variants of the glutamate sensor iGluSnFR. *Nat. Methods* 15, 936–939. doi: 10.1038/s41592-018-0171-3
- Marvin, J. S., Shimoda, Y., Magloire, V., Leite, M., Kawashima, T., Jensen, T. P., et al. (2019). A genetically encoded fluorescent sensor for in vivo imaging of GABA. *Nat. Methods* 16, 763–770. doi: 10.1038/s41592-019-0471-2
- Masharina, A., Reymond, L., Maurel, D., Umezawa, K., and Johnsson, K. (2012). A fluorescent sensor for GABA and synthetic GABA(B) receptor ligands. *J. Am. Chem. Soc.* 134, 19026–19034. doi: 10.1021/ja306320s
- McGirr, A., LeDue, J., Chan, A. W., Xie, Y., and Murphy, T. H. (2017). Cortical functional hyperconnectivity in a mouse model of depression and selective network effects of ketamine. *Brain* 140, 2210–2225. doi: 10.1093/brain/awx142
- McMahon, S. M., and Jackson, M. B. (2018). An inconvenient truth: calcium sensors are calcium buffers. *Trends Neurosci.* 41, 880–884. doi: 10.1016/j.tins.2018.09.005
- Mehta, P., Wang, C. H., Day, A. G. R., Richardson, C., Bukov, M., Fisher, C. K., et al. (2019). A high-bias, low-variance introduction to machine learning for physicists. *Phys. Rep.* 810, 1–124. doi: 10.1016/j.physrep.2019.03.001
- Meyer, A., Eskandari, S., Grallath, S., and Rentsch, D. (2006). AtGAT1, a high affinity transporter for gamma-aminobutyric acid in *Arabidopsis thaliana*. *J. Biol. Chem.* 281, 7197–7204. doi: 10.1074/jbc.M510766200
- Miotto, R., Wang, F., Wang, S., Jiang, X., and Dudley, J. T. (2018). Deep learning for healthcare: review, opportunities and challenges. *Brief. Bioinform.* 19, 1236–1246. doi: 10.1093/bib/bbx044
- Morozova, A., Zubkov, E., Strekalova, T., Kekelidze, Z., Storozeva, Z., Schroeter, C. A., et al. (2016). Ultrasound of alternating frequencies and variable emotional impact evokes depressive syndrome in mice and rats. *Prog. Neuropsychopharmacol. Biol. Psychiatry* 68, 52–63. doi: 10.1016/j.pnpbp.2016.03.003
- Moussatova, A., Kandt, C., O'Mara, M. L., and Tieleman, D. P. (2008). ATP-binding cassette transporters in *Escherichia coli*. *Biochim. Biophys. Acta* 1778, 1757–1771. doi: 10.1016/j.bbame.2008.06.009
- Nadim, F., and Bucher, D. (2014). Neuromodulation of neurons and synapses. *Curr. Opin. Neurobiol.* 29, 48–56. doi: 10.1016/j.conb.2014.05.003
- Niswender, C. M., and Conn, P. J. (2010). Metabotropic glutamate receptors: physiology, pharmacology, and disease. *Annu. Rev. Pharmacol. Toxicol.* 50, 295–322. doi: 10.1146/annurev.pharmtox.011008.145533
- Okumoto, S., Looger, L. L., Micheva, K. D., Reimer, R. J., Smith, S. J., and Frommer, W. B. (2005). Detection of glutamate release from neurons by genetically encoded surface-displayed FRET nanosensors. *Proc. Natl. Acad. Sci. U.S.A.* 102, 8740–8745. doi: 10.1073/pnas.0503274102
- Oliynyk, O. S., Chernov, K. G., and Verkhusha, V. V. (2017). Bacterial phytochromes, cyanobacteriochromes and allophycocyanins as a source of near-infrared fluorescent probes. *Int. J. Mol. Sci.* 18:1691. doi: 10.3390/ijms18081691
- Ozbay, B. N., Futia, G. L., Ma, M., Bright, V. M., Gopinath, J. T., Hughes, E. G., et al. (2018). Three dimensional two-photon brain imaging in freely moving mice using a miniature fiber coupled microscope with active axial-scanning. *Sci. Rep.* 8:8108. doi: 10.1038/s41598-018-26326-3
- Patriarchi, T., Cho, J. R., Merten, K., Howe, M. W., Marley, A., Xiong, W. H., et al. (2018). Ultrafast neuronal imaging of dopamine dynamics with designed genetically encoded sensors. *Science* 360:eaat4422. doi: 10.1126/science.aat4422
- Piatkevich, K. D., Murdock, M. H., and Subach, F. V. (2019). Advances in engineering and application of optogenetic indicators for neuroscience. *Appl. Sci.* 9:562. doi: 10.3390/app9030562
- Picciotto, M. R., Higley, M. J., and Mineur, Y. S. (2012). Acetylcholine as a neuromodulator: cholinergic signaling shapes nervous system function and behavior. *Neuron* 76, 116–129. doi: 10.1016/j.neuron.2012.08.036
- Pin, J. P., Galvez, T., and Prezeau, L. (2003). Evolution, structure, and activation mechanism of family 3/C G-protein-coupled receptors. *Pharmacol. Ther.* 98, 325–354. doi: 10.1016/s0163-7258(03)00038-x
- Pneumatikakis, E. A. (2019). Analysis pipelines for calcium imaging data. *Curr. Opin. Neurobiol.* 55, 15–21. doi: 10.1016/j.conb.2018.11.004
- Ramesh, S. A., Tyerman, S. D., Xu, B., Bose, J., Kaur, S., Conn, V., et al. (2015). GABA signalling modulates plant growth by directly regulating the activity of plant-specific anion transporters. *Nat. Commun.* 6:7879. doi: 10.1038/ncomms8879
- Ramos, B. P., and Arnsten, A. F. (2007). Adrenergic pharmacology and cognition: focus on the prefrontal cortex. *Pharmacol. Ther.* 113, 523–536. doi: 10.1016/j.pharmthera.2006.11.006
- Resendez, S. L., and Stuber, G. D. (2015). In vivo calcium imaging to illuminate neurocircuit activity dynamics underlying naturalistic behavior. *Neuropsychopharmacology* 40, 238–239. doi: 10.1038/npp.2014.206
- Ribeiro, P., and Patočka, N. (2013). Neurotransmitter transporters in schistosomes: structure, function and prospects for drug discovery. *Parasitol. Int.* 62, 629–638. doi: 10.1016/j.parint.2013.06.003
- Rodeberg, N. T., Sandberg, S. G., Johnson, J. A., Phillips, P. E., and Wightman, R. M. (2017). Hitchhiker's guide to voltammetry: acute and chronic electrodes for in vivo fast-scan cyclic voltammetry. *ACS Chem. Neurosci.* 8, 221–234. doi: 10.1021/acscchemneuro.6b00393
- Sames, D., Dunn, M., Karpowicz, R. J. Jr., and Sulzer, D. (2013). Visualizing neurotransmitter secretion at individual synapses. *ACS Chem. Neurosci.* 4, 648–651. doi: 10.1021/cn4000956
- Shang, Y., and Filizola, M. (2015). Opioid receptors: structural and mechanistic insights into pharmacology and signaling. *Eur. J. Pharmacol.* 763(Pt B), 206–213. doi: 10.1016/j.ejphar.2015.05.012
- Shcherbakova, D. M., Shemetov, A. A., Kaberniuk, A. A., and Verkhusha, V. V. (2015). Natural photoreceptors as a source of fluorescent proteins, biosensors, and optogenetic tools. *Annu. Rev. Biochem.* 84, 519–550. doi: 10.1146/annurev-biochem-060614-034411
- Shcherbakova, D. M., Stepanenko, O. V., Turoverov, K. K., and Verkhusha, V. V. (2018). Near-infrared fluorescent proteins: multiplexing and optogenetics across scales. *Trends Biotechnol.* 36, 1230–1243. doi: 10.1016/j.tibtech.2018.06.011
- Shevtsova, Z., Malik, J. M., Michel, U., Bahr, M., and Kugler, S. (2005). Promoters and serotypes: targeting of adeno-associated virus vectors for gene transfer in the rat central nervous system in vitro and in vivo. *Exp. Physiol.* 90, 53–59. doi: 10.1113/expphysiol.2004.028159
- Silva, A. J. (2017). Miniaturized two-photon microscope: seeing clearer and deeper into the brain. *Light Sci. Appl.* 6:e17104. doi: 10.1038/lsa.2017.104
- Soltanian-Zadeh, S., Sahingur, K., Blau, S., Gong, Y., and Farsiu, S. (2019). Fast and robust active neuron segmentation in two-photon calcium imaging using spatiotemporal deep learning. *Proc. Natl. Acad. Sci. U.S.A.* 116, 8554–8563. doi: 10.1073/pnas.1812995116
- Stoeber, M., Jullie, D., Lobingier, B. T., Laeremans, T., Steyaert, J., Schiller, P. W., et al. (2018). A genetically encoded biosensor reveals location bias of opioid drug action. *Neuron* 98, 963.e5–976.e5. doi: 10.1016/j.neuron.2018.04.021

- Stoica, L., Ahmed, S. S., Gao, G., and Sena-Esteves, M. (2013). Gene transfer to the CNS using recombinant adeno-associated virus. *Curr. Protoc. Microbiol.* Chapter 14:Unit14D.5. doi: 10.1002/9780471729259.mc14d05s29
- Stringer, C., and Pachitariu, M. (2019). Computational processing of neural recordings from calcium imaging data. *Curr. Opin. Neurobiol.* 55, 22–31. doi: 10.1016/j.conb.2018.11.005
- Sun, F., Zeng, J., Jing, M., Zhou, J., Feng, J., Owen, S. F., et al. (2018). A genetically encoded fluorescent sensor enables rapid and specific detection of dopamine in flies, fish, and mice. *Cell* 174, 481.e19–496.e19. doi: 10.1016/j.cell.2018.06.042
- Sureyya Rifaioglu, A., Dogan, T., Jesus Martin, M., Cetin-Atalay, R., and Atalay, V. (2019). DEEPred: automated protein function prediction with multi-task feed-forward deep neural networks. *Sci. Rep.* 9:7344. doi: 10.1038/s41598-019-43708-3
- Svoboda, K., and Yasuda, R. (2006). Principles of two-photon excitation microscopy and its applications to neuroscience. *Neuron* 50, 823–839. doi: 10.1016/j.neuron.2006.05.019
- Taber, K. H., and Hurley, R. A. (2014). Volume transmission in the brain: beyond the synapse. *J. Neuropsychiatry Clin. Neurosci.* 26:iv. doi: 10.1176/appi.neuropsych.13110351
- Tanaka, M., Sun, F., Li, Y., and Mooney, R. (2018). A mesocortical dopamine circuit enables the cultural transmission of vocal behaviour. *Nature* 563, 117–120. doi: 10.1038/s41586-018-0636-7
- Traynelis, S. F., Wollmuth, L. P., McBain, C. J., Menniti, F. S., Vance, K. M., Ogden, K. K., et al. (2010). Glutamate receptor ion channels: structure, regulation, and function. *Pharmacol. Rev.* 62, 405–496. doi: 10.1124/pr.109.002451
- Venter, J. C., di Porzio, U., Robinson, D. A., Shreeve, S. M., Lai, J., Kerlavage, A. R., et al. (1988). Evolution of neurotransmitter receptor systems. *Prog. Neurobiol.* 30, 105–169. doi: 10.1016/0301-0082(88)90004-4
- Wang, H., Jing, M., and Li, Y. (2018). Lighting up the brain: genetically encoded fluorescent sensors for imaging neurotransmitters and neuromodulators. *Curr. Opin. Neurobiol.* 50, 171–178. doi: 10.1016/j.conb.2018.03.010
- Wess, J. (2003). Novel insights into muscarinic acetylcholine receptor function using gene targeting technology. *Trends Pharmacol. Sci.* 24, 414–420. doi: 10.1016/S0165-6147(03)00195-0
- Wilkens, S. (2015). Structure and mechanism of ABC transporters. *F1000Prime Rep.* 7:14. doi: 10.12703/P7-14
- Wilson, D. E., Smith, G. B., Jacob, A. L., Walker, T., Dimidschstein, J., Fishell, G., et al. (2017). GABAergic Neurons in ferret visual cortex participate in functionally specific networks. *Neuron* 93, 1058.e4–1065.e4. doi: 10.1016/j.neuron.2017.02.035
- Wu, J., Abdelfattah, A. S., Zhou, H., Ruangkittisakul, A., Qian, Y., Ballanyi, K., et al. (2018). Genetically encoded glutamate indicators with altered color and topology. *ACS Chem. Biol.* 13, 1832–1837. doi: 10.1021/acscchembio.7b01085
- Xie, Y., Chan, A. W., McGirr, A., Xue, S., Xiao, D., Zeng, H., et al. (2016). Resolution of high-frequency mesoscale intracortical maps using the genetically encoded glutamate sensor iGluSnFR. *J. Neurosci.* 36, 1261–1272. doi: 10.1523/JNEUROSCI.2744-15.2016
- Yang, G., Pan, F., Parkhurst, C. N., Grutzendler, J., and Gan, W. B. (2010). Thinned-skull cranial window technique for long-term imaging of the cortex in live mice. *Nat. Protoc.* 5, 201–208. doi: 10.1038/nprot.2009.222
- Zhang, W. H., Herde, M. K., Mitchell, J. A., Whitfield, J. H., Wulff, A. B., Vongsouthi, V., et al. (2018). Monitoring hippocampal glycine with the computationally designed optical sensor GlyFS. *Nat. Chem. Biol.* 14, 861–869. doi: 10.1038/s41589-018-0108-2
- Zhou, Y., and Danbolt, N. C. (2014). Glutamate as a neurotransmitter in the healthy brain. *J. Neural Transm.* 121, 799–817. doi: 10.1007/s00702-014-1180-8
- Zorkina, Y. A., Zubkov, E. A., Morozova, A. Y., Ushakova, V. M., and Chekhonin, V. P. (2019). The comparison of a new ultrasound-induced depression model to the chronic mild stress paradigm. *Front. Behav. Neurosci.* 13:146. doi: 10.3389/fnbeh.2019.00146

**Conflict of Interest:** The authors declare that the research was conducted in the absence of any commercial or financial relationships that could be construed as a potential conflict of interest.

Copyright © 2019 Leopold, Shcherbakova and Verkhusha. This is an open-access article distributed under the terms of the Creative Commons Attribution License (CC BY). The use, distribution or reproduction in other forums is permitted, provided the original author(s) and the copyright owner(s) are credited and that the original publication in this journal is cited, in accordance with accepted academic practice. No use, distribution or reproduction is permitted which does not comply with these terms.





# Engineering Photoactivatability in Genetically Encoded Voltage and pH Indicators

Sungmoo Lee<sup>1</sup>, Yoon-Kyu Song<sup>2,3</sup> and Bradley J. Baker<sup>1,4\*</sup>

<sup>1</sup>Center for Functional Connectomics, Brain Science Institute, Korea Institute of Science and Technology, Seoul, South Korea, <sup>2</sup>Program in Nano Science and Technology, Graduate School of Convergence Science and Technology, Seoul National University, Seoul, South Korea, <sup>3</sup>Advanced Institutes of Convergence Technology, Suwon, South Korea, <sup>4</sup>Division of Bio-Medical Science and Technology, KIST School, University of Science and Technology (UST), Seoul, South Korea

Genetically-encoded indicators of neuronal activity enable the labeling of a genetically defined population of neurons to optically monitor their activities. However, researchers often find difficulties in identifying relevant signals from excessive background fluorescence. A photoactivatable version of a genetically encoded calcium indicator, sPA-GCaMP6f is a good example of circumventing such an obstacle by limiting the fluorescence to a region of interest defined by the user. Here, we apply this strategy to genetically encoded voltage (GEVI) and pH (GEPI) indicators. Three photoactivatable GEVI candidates were considered. The first one used a circularly-permuted fluorescent protein, the second design involved a Förster resonance energy transfer (FRET) pair, and the third approach employed a pH-sensitive variant of GFP, ecliptic pHluorin. The candidate with a variant of ecliptic pHluorin exhibited photoactivation and a voltage-dependent fluorescence change. This effort also yielded a pH-sensitive photoactivatable GFP that varies its brightness in response to intracellular pH changes.

**Keywords:** voltage indicator, photoactivatable, GEVI, pH sensor, ecliptic pHluorin, PA-GFP, PA-Bongwoori-R3, PA-ecliptic pHluorin

## OPEN ACCESS

### Edited by:

Shai Berlin,  
Technion Israel Institute of  
Technology, Israel

### Reviewed by:

Takashi Tominaga,  
Tokushima Bunri University, Japan  
Matthias Prigge,  
Leibniz Institute for Neurobiology  
(LG), Germany

### \*Correspondence:

Bradley J. Baker  
bradley.baker19@gmail.com

**Received:** 14 August 2019

**Accepted:** 10 October 2019

**Published:** 29 October 2019

### Citation:

Lee S, Song Y-K and Baker BJ  
(2019) Engineering Photoactivatability  
in Genetically Encoded Voltage and  
pH Indicators.  
*Front. Cell. Neurosci.* 13:482.  
doi: 10.3389/fncel.2019.00482

## INTRODUCTION

Genetically encoded fluorescent sensors often suffer from extensive background fluorescence (Lin and Schnitzer, 2016; Bayguinov et al., 2017; Song et al., 2017; Nakajima and Baker, 2018). Confining the expression to naturally sparse cell types such as parvalbumin positive or somatostatin positive interneurons can alleviate the dense expression issue (Lou et al., 2016; Marshall et al., 2016). Co-injecting a Cre recombinase virus together with a floxed virus that contains a gene of interest can provide a sparse expression pattern but this necessitates an optimization step for each virus sample (Xu et al., 2012). Using a destabilized Cre recombinase was reported to induce sparse labeling in cortical layers 2/3 (Sando et al., 2013; Harris et al., 2014; Madisen et al., 2015). Utilizing this method to achieve a Förster resonance energy transfer (FRET) type genetically encoded voltage (GEVI) expression involved the generation of triple transgenic mice to acquire the desired level of sparseness in cortical pyramidal cells (Song et al., 2017; Quicke et al., 2019). However, sparse labeling is a stochastic approach that is difficult to control. Approaches that empower the experimenter to define the circuits that optically respond would be a welcome addition to the imaging toolbox.

Optically activating fluorophores in a region of interest may address this issue (Berlin et al., 2015). Photoactivation of fluorescent proteins enables optical labeling of a defined region (Lukyanov et al., 2005). As such, the rationally designed, photoactivatable GFP (PA-GFP) has been a useful tool since its development (Patterson and Lippincott-Schwartz, 2002; Betzig et al., 2006). This FP exhibited fluorescence when excited at 470 nm only after photoactivation at 413 nm. The photoactivatable genetically-encoded calcium indicator (sPA-GCaMP6f) reported by Berlin et al. (2015) demonstrated the usefulness of it in studying calcium dynamics of neuronal cells. Besides from the photoactivatable version, two green to red photoconvertible genetically encoded calcium indicators were previously reported (Hoi et al., 2013; Fosque et al., 2015). However, since the observation of intracellular calcium transients is an indirect measure of neuronal depolarization (Lin and Schnitzer, 2016; Storace et al., 2016), having a photoactivatable GEVI (PA-GEVI) would be a valuable addition. A photoconvertible voltage indicator was previously reported (Abdelfattah et al., 2016). This GEVI exhibited a change in emission from green to red upon a 400 nm wavelength excitation. The only photoactivatable GEVI reported to date is a microbial rhodopsin voltage indicator with voltage-dependent near-infrared fluorescence requiring intense and simultaneous dual excitation for the photoactivation enhancement and epifluorescence imaging (Adam et al., 2019).

A genetically encoded pH indicator (GEPI) is useful in studying network activity of the brain slice as well as synaptic transmission at the cellular level (Lin and Schnitzer, 2016). Previously, Miesenböck et al. (1998) and Sankaranarayanan et al. (2000) imaged vesicle release dependent pH changes by using pH-sensitive GFPs. Additionally, Raimondo et al. (2012, 2013, 2016) used a ratiometric pH-sensitive GFP to optically study activity-dependent acidification of both neurons and astrocytes in hippocampal slices (Bizzarri et al., 2006; Raimondo et al., 2012, 2016). Therefore, the development of an optically activatable pH indicator would be a useful asset to the optical imaging toolset.

In this article, we describe the design strategies and experimental results of developing photoactivatable voltage and pH indicators. Based on the rationales used for the development of the original PA-GFP and the photoactivatable GCaMP, three candidate PA-GEVIs were developed. These candidates include a circularly permuted FP, a FRET pair, and a pH-sensitive fluorescent protein. One of the candidates, PA-Bongwoori-R3 demonstrated a voltage-dependent fluorescence change only after photoactivation. The fluorescent protein in PA-Bongwoori-R3 is also pH-sensitive. Since the optical bio-sensor field lacks a photoactivatable, genetically encoded pH indicator (Lukyanov et al., 2005; Lippincott-Schwartz and Patterson, 2009; Chudakov et al., 2010), a voltage insensitive variant of the pH-sensitive GFP, PA-ecliptic pHluorin was developed. When this cytoplasmic photoactivatable pH indicator was expressed in mammalian cells, it had changes in fluorescence intensity for varying intracellular pH values that were difficult to measure before photoactivation.

## MATERIALS AND METHODS

### Gene Constructs Design and Cloning

Two versions of photoactivatable ASAP1 (St-Pierre et al., 2014) were prepared. ASAP1 with three photoactivatable mutations (ASAP1-PATM; Berlin et al., 2015) was generated by two separate gene cloning steps. L163F and T164S mutations (correspond to L64F and T65S mutations in the original PA-GFP) were first introduced by polymerase chain reaction (PCR) using SM067A and SM067B primers. Then the T59H mutation that corresponds to the T203H mutation in PA-GFP construct was substituted in by PCR using SM068A and SM068B primers. A PCR with SM070 and SM071Xho1 primers was conducted to cut and paste the whole ASAP1-PATM insert into pcDNA3.1(+) backbone vector. A second type of photoactivatable ASAP1 was generated by switching the OPT (optimum) variant of circularly permuted superfolder GFP (cpsfGFP-OPT) in ASAP1 into a photoactivatable circularly permuted GFP from the short superfolder photoactivatable GCaMP6f (ssPA-GCaMP6f; Berlin et al., 2015). The synthesized gene fragment had Nhe1 and Xho1 restriction sites to facilitate cloning (Integrated DNA technologies, Coralville, IA, USA; **Supplementary Data S1**). Restriction digest was carried out with the two enzymes to cut and paste the synthesized gene fragment and it was then ligated into the pcDNA3.1(+) backbone vector to acquire ASAP1-ssPA version.

A FRET version PA-GEVI was prepared by mutating Nabi 2.242 developed by Sung et al. (2015). The original Nabi 2.242 has Clover and mRuby2 as a FRET pair. To replace Clover with PA-GFP, a 1,279 base pair long gene fragment that includes a Nhe1 site, PA-GFP, and an Apa1 site was synthesized (Integrated DNA Technologies, Coralville, IA, USA; **Supplementary Data S1**) and cloned into the Nabi 2.242 vector (Sung et al., 2015). Another set of PCR was conducted to produce PA-Nabi2.242 where SM100A and SM100B primers were used to introduce PA-Nabi2.242 into the pcDNA3.1(+) backbone vector.

Photoactivatable Bongwoori-R3 (PA-Bongwoori-R3) was prepared by replacing Bongwoori-R3's (Lee et al., 2017) fluorophore with a mutated ecliptic pHluorin (**Supplementary Data S1**, Miesenböck et al., 1998). T203H and A227D mutations were introduced in the synthesized gene fragment to confer photoactivatability and voltage-sensitivity to the original ecliptic pHluorin. BamH1 and Xho1 restriction sites were used for cloning into the Bongwoori-R3 gene construct. A voltage-sensitive but non-photoactivatable version (ecliptic-Bongwoori-R3\_A227D) and a photoactivatable but non-voltage-sensitive version (PA-Bongwoori-R3\_T203H\_D227A) were generated by PCR with SM105A and SM105B, and SM106A and SM106B primers, respectively. A cytoplasmic version of photoactivatable GFP (pPA-GFP-N1) was purchased from Addgene, USA (#11909).

A cytoplasmic version of photoactivatable ecliptic pHluorin was generated by a simple one-step PCR with SM103 and SM013 to acquire the ecliptic pHluorin part from PA-Bongwoori-R3\_T203H\_D227A. The polymerized insert was

cut and ligated back into pcDNA3.1(+) backbone vector resulting in photoactivatable ecliptic pHluorin D227A (PA-ecliptic pHluorin).

All primers are listed in **Supplementary Table S1**. The sequences of newly generated gene constructs were verified commercially (Cosmogenetech, South Korea).

## Cell Culture and Transfection

Human Embryonic Kidney 293 (HEK 293) cells were cultured and transfected following the methods described in Lee et al. (2017) with a few modifications. The cells were maintained in Dulbecco's Modified Eagle Medium (DMEM; Gibco, USA) with 10% (v/v) Fetal Bovine Serum (Gibco, USA) and kept in a CO<sub>2</sub> incubator (MCO-20AIC, Sanyo, Japan) at 37°C and 5% CO<sub>2</sub> level throughout the culture. For a transient transfection with a plasmid DNA construct, the HEK 293 cells were detached by using 0.25% trypsin-EDTA solution (Gibco, USA) and seeded onto poly-D-lysine (Sigma-Aldrich, USA) coated coverslips (10 mm diameter and 0.08–0.13 mm thickness, Ted Pella, USA). For transfection, 1  $\mu$ L of a lipofection reagent (Lipofectamine 2000, Life Technologies, USA) was pre-mixed with 100 ng of the plasmid DNA molecules for each of the coverslip and incubated in the CO<sub>2</sub> incubator overnight.

## Photoactivation and Imaging

A 385 nm light-emitting diode [bandwidth (FWHM): 10 nm] placed in a 4-wavelength LED housing (LED4D242, Thorlabs, USA) was used for photoactivation of all photoactivatable variants. To find a photoactivatable optical sensor expressing cell and for photoactivation with the 385 nm LED, a filter cube consisting of a 385/23 nm excitation filter (FF01-386/23-25, Semrock, USA), a 495 nm dichroic mirror (FF495-Di03, Semrock, USA) and a 520/35 nm emission filter (FF01-520/35, Semrock, USA) was used. After photoactivation, a 470 nm LED [bandwidth (FWHM): 25 nm] delivered excitation light to green fluorophores in the specimen. A 4-channel LED driver and its software (DC4100, Thorlabs, USA) were used to control the LEDs. Protocols for simultaneous voltage imaging and electrophysiology experiments were as described in Lee et al. (2017). The high-speed CCD camera (Neuro CCD, RedShirtImaging, Decatur, GA, USA) and the camera software NeuroPlex (RedShirtImaging, Decatur, GA, USA) were used to acquire images. For photoactivation at 385 nm and epifluorescence imaging at 470 nm, the LEDs were modulated at their full intensities. The intensities of 385 nm and 470 nm were 2.7 mW/mm<sup>2</sup> and 5.3 mW/mm<sup>2</sup>, respectively. Before the photoactivation, the 385 nm LED was used at its 10% intensity to locate transfected cells while preventing unintended photoactivation.

To locate a cell expressing the FRET sensors (PA-Nabi 2. 242), a 565 nm LED [bandwidth (FWHM): 104 nm], a 561/14 nm excitation filter (FF01-561/14, Semrock, USA), a 561 nm dichroic mirror (Di02-R561, Semrock, USA) and a 609/54 nm emission filter (FF01-609/54, Semrock, USA) were used. For the imaging of a FRET pair, an image splitter (Optosplit 2, Cairn, UK) was placed between the high-speed CCD camera and the c-mount port of the microscope to divide the CCD sensor

into two halves for simultaneous imaging of green (ET 520/40, Chroma, USA) and red (ET 645/75, Chroma, USA) fluorescence. For FRET imaging, the 470 nm LED light was filtered by a 475/23 nm excitation filter (FF01-475/23-25, Semrock, USA). For imaging of Nabi 2.242, a 75 W Xenon arc lamp (Osram, Germany) was used (lamp housing from Cairn, UK).

For pH imaging experiments of PA-GFP and PA-ecliptic pHluorin, and Gramicidin D (Sigma-Aldrich) was applied to transfected cells at 50  $\mu$ M to perforate their cell membranes for 20 min at 34°C. The Gramicidin was prepared and stored as described previously (Kang and Baker, 2016). After the photoactivation, each bath solution with a different pH was perfused into the patching chamber for at least 20 min to induce pH-dependent fluorescence change of the photoactivatable probe. The strongly buffered bath solution (100 mM NaCl, 3 mM KCl, 0.5 mM MgCl<sub>2</sub>, 1 mM CaCl<sub>2</sub>, 3 mM Glucose and 100 mM HEPES) was prepared following the description in Kang and Baker (Kang and Baker, 2016) and used to change intracellular pH level. A scientific CCD camera (128  $\times$  128 pixels, Neuro CCD, RedShirtImaging, Decatur, GA, USA) was used to measure pH sensitivities of the fluorescent proteins.

## Analyses

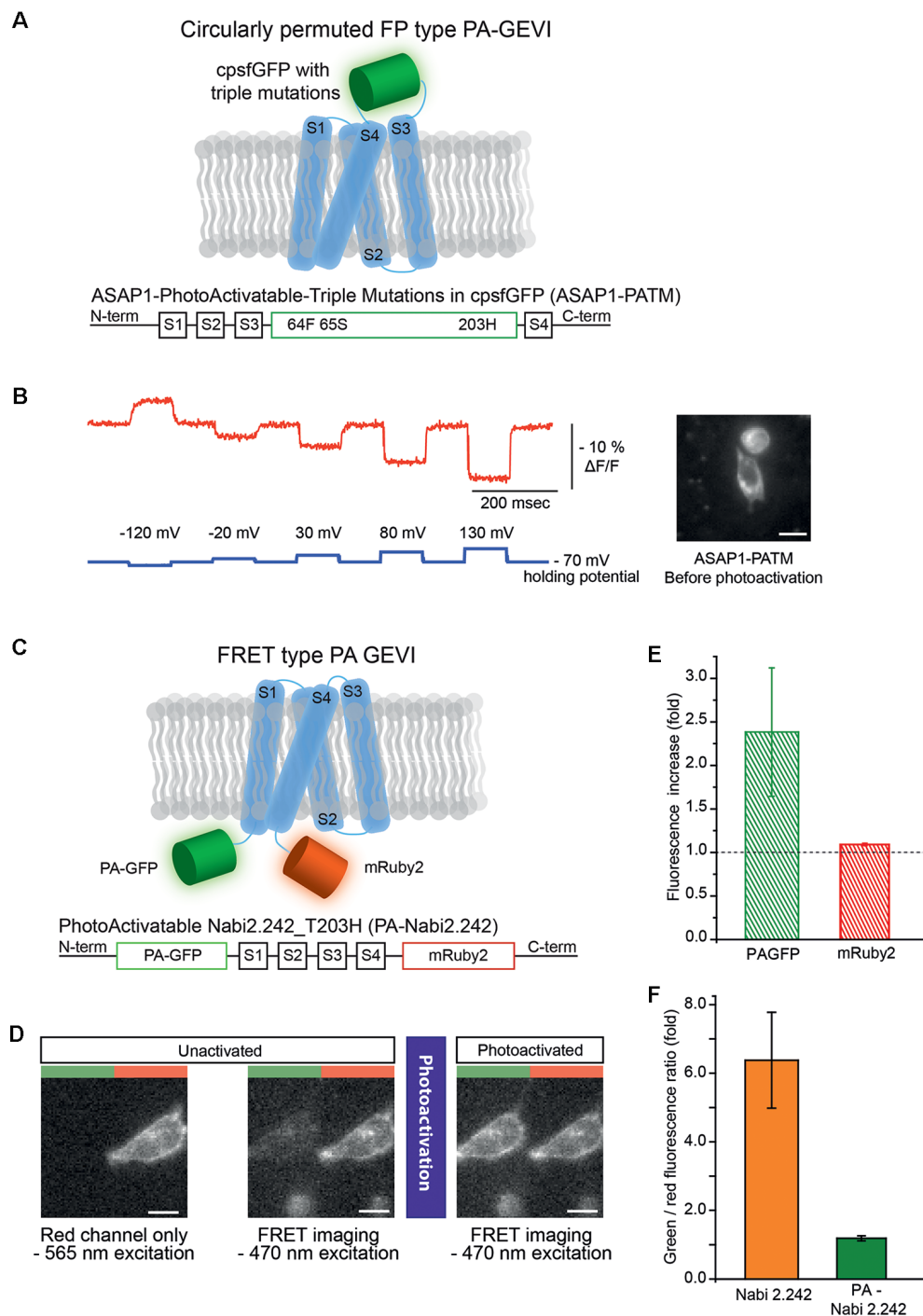
As described earlier in Lee et al. (2017), fluorescence traces from selected pixels were derived from NeuroPlex software (RedShirtImaging, Decatur, GA, USA). Calculation of averaged  $\Delta F/F$  values and statistics of means for comparison were conducted in Origin 9.0 (OriginLab, Northampton, MA, USA) and Microsoft Office—Excel 2016 (Microsoft, USA).

## RESULTS

### Engineering a Circularly Permuted FP Type GEVI

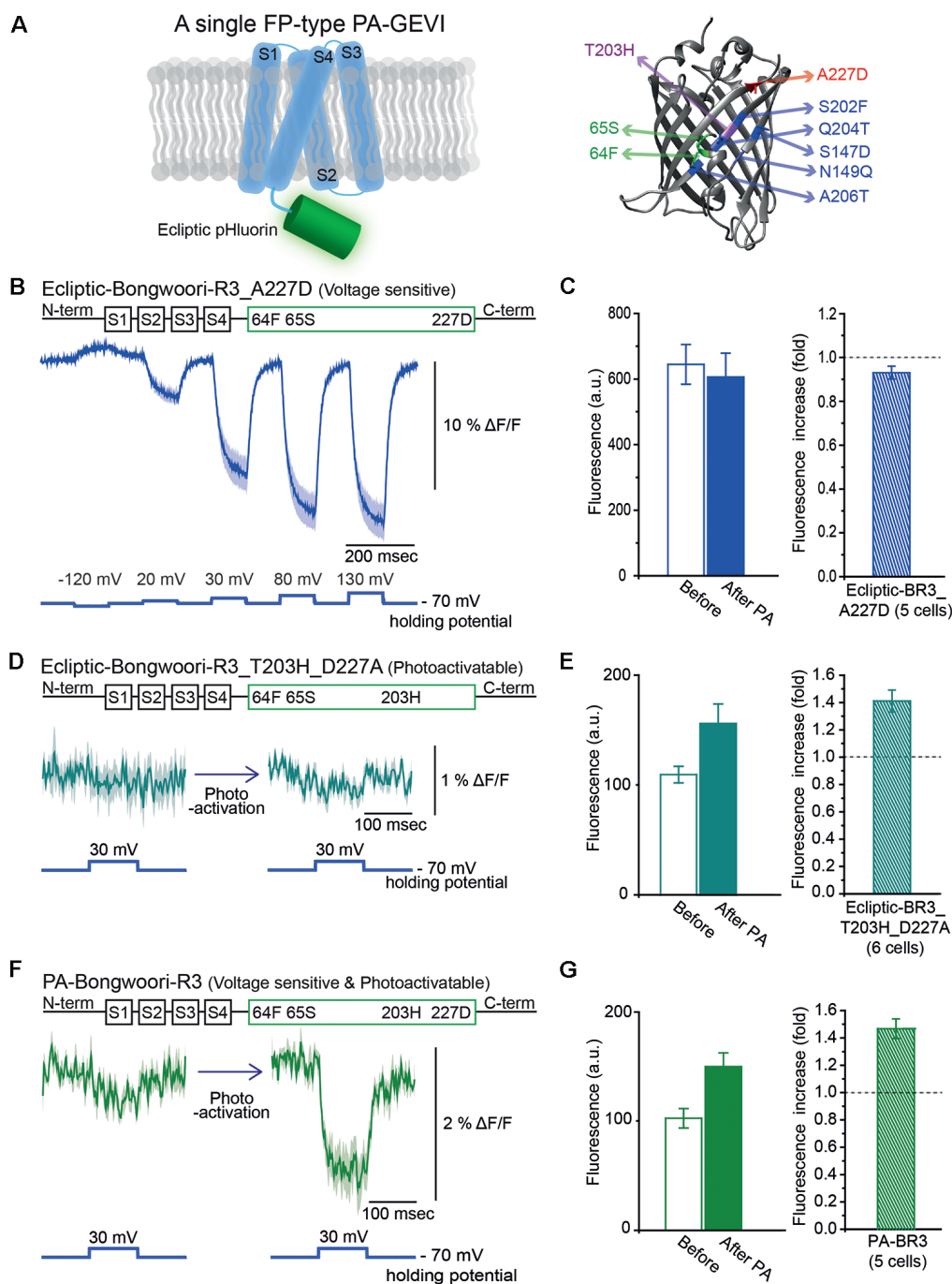
The photoactivatable GFP (PA-GFP) developed by Patterson and Lippincott-Schwartz (2002) had four mutations in comparison to eGFP. The L64F and T65S mutations recovered the 390 nm absorbance peak that originally existed in wild-type GFP (wtGFP; The amino acid residue numbers indicate GFP residues only). The T203H mutation maximized the contrast of the two absorbance bands so the FP could stay dim during 470 nm excitation until it was activated by 390 nm light. The V163 residue was mutated to alanine to improve protein folding at 37°C as an alternative to the F64L mutation in eGFP.

Two photoactivatable voltage indicator candidates were designed based on the rationale described above (**Figures 1A,C**). First, a photoactivatable version of ASAP1 (St-Pierre et al., 2014) which is a genetically-encoded voltage indicator with a voltage-sensing domain and a circularly permuted GFP was generated. The three mutations from PA-GFP, F64L, S65T and T203H, were introduced into the GEVI's FP and named as ASAP1-PATM (**Figure 1A**, bottom). The V163A mutation that was previously used to improve protein folding was already present in ASAP1. Another photoactivatable variant of ASAP1 was prepared by using a photoactivatable circularly permuted GFP engineered by Berlin et al. (2015) for the



**FIGURE 1 |** Photoactivatable versions of ASAP1 and Nabi 2.242. **(A)** Schematics of photoactivatable ASAP1-PATM (top) and the gene construct design (bottom). The voltage-sensing domain is depicted in light blue. **(B)** A representative voltage-dependent fluorescence change of the unactivated ASAP1-PATM. The inset on the right shows an HEK 293 cell expressing ASAP1-PATM before photoactivation. **(C)** Schematics of photoactivatable Nabi 2.242 (PA-Nabi 2.242; top) and its gene construct design (bottom). **(D)** Images acquired by a CCD camera before (left/middle) and after photoactivation (right). The left half of each image represents FRET donor (green) channel and the right half is the FRET acceptor (red) channel. **(E)** The increase in fluorescence after photoactivation for PA-GFP and mRuby2. **(F)** The ratio between FRET donor (green) and FRET acceptor (red) fluorescence calculated for the original non-photoactivatable Nabi 2.242 (Clover/mRuby2 brightness ratio) and PA-Nabi 2.242 (photoactivated PA-GFP/mRuby2 brightness ratio), respectively. For the fluorescence imaging of Nabi 2.242, a Xenon arc lamp was used. The photoactivation time for PA-Nabi 2.242 cells varied for 30 s (cell1), 10 s (cell2), and 20 s (cell3). Scale bar is 20  $\mu$ m.





**FIGURE 2 |** Engineering of Photoactivatable Bongwoori-R3 and verification of its photoactivatability and voltage sensitivity. **(A)** A schematic design of Bongwoori-R3 with an ecliptic pHluorin (left). Key mutations of photoactivatable ecliptic pHluorin compared to wild-type GFP (right). Residues in green (65S and 64F) contribute to the wild-type dual absorbance bands. The T203H mutation is responsible for photoactivatability. The A227D mutation confers voltage-sensitivity. Mutations depicted in blue color (S147D, N149Q, S202F, Q204T and A206T) are characteristic residues for ecliptic pHluorin compared to wtGFP. Protein Data Bank ID: 1GFL. **(B)** Gene construct design of ecliptic-Bongwoori-R3 with the A227D mutation (top) and the voltage-dependent fluorescence change imaged from HEK 293 cells expressing the variant (bottom). Traces from three cells were analyzed. **(C)** Raw fluorescence intensity values imaged before and after photoactivation (left). The ratio of the fluorescence change is on the right. The number of cells analyzed was five. **(D)** Gene construct design (top) and response to a 100 mV voltage pulse (bottom) of ecliptic-Bongwoori-R3\_T203H\_D227A. **(E)** The raw fluorescence intensities before and after photoactivation (left). The increase ratio after photoactivation (right). Six cells were analyzed. **(F)** PA-Bongwoori-R3 responding to a 100 mV membrane depolarization. **(G)** The fluorescence intensities before and after photoactivation (left). The increase ratio of fluorescence intensity after photoactivation (right). Five PA-Bongwoori-R3 expressing cells were analyzed. The shaded area in the traces and error bars denote standard error of the mean. The protein structure image in **(A)** was from Protein Data Bank ID: 1GFL. Further modifications were made with UCSF Chimera 1.13.1 software.

development of their photoactivatable calcium indicators. The FP part of ASAP1 was substituted with the short superfolder photoactivatable circularly permuted GFP (sPA-cpGFP). This candidate was named ASAP1-ssPA.

ASAP1-ssPA transfected HEK 293 cells were imaged with both 385 nm and 470 nm excitation light. Very weak green fluorescence was observed indicating poor expression of the probe (**Supplementary Figure S1**). Conversely, ASAP1 with the three photoactivatable mutations (ASAP1-PATM) expressed well in the plasma membrane (**Figure 1B**, inset). The photoactivatable ASAP1 showed bright green fluorescence even before the photoactivation with 385 nm light. In its non-photoactivated state, this GEVI responded well to voltage steps (**Figure 1B**). The response in the non-photoactivated state diminished the value of this probe as a photoactivatable optical sensor.

## Engineering a GEVI With a FRET Pair

A photoactivatable GEVI with a FRET pair was also generated. Nabi 2.242 is a FRET-based GEVI (Sung et al., 2015) that consists of the FPs, Clover, the FRET donor and, mRuby2, the FRET acceptor (Lam et al., 2012). Originally, Nabi 2.242 responds to a depolarizing voltage pulse with a decrease in the FRET donor and an increase in the acceptor fluorescence. Since the photoactivated PA-GFP had excitation and emission spectra similar to Clover (Patterson and Lippincott-Schwartz, 2002; Lam et al., 2012), it was substituted as the FRET donor (**Figure 1C**).

To verify the expression in HEK 293 cells, mRuby2 was excited with a 565 nm LED which kept the photoactivatable FRET donor inactive (**Figure 1D**, left). The image from the FRET acceptor channel clearly showed red fluorescence mainly from the plasma membrane of the cell. Subsequent FRET imaging with a 470 nm LED showed weak green and red fluorescence indicating a basal level of FRET before photoactivation (**Figure 1D**, middle). After photoactivation of the FRET donor, the PA-GFP emission was increased about 2-fold (**Figure 1D**, right and **Figure 1E**) but the FRET acceptor showed only 10% increase in its red fluorescence (**Figure 1E**). The green to red fluorescence ratios of the original non-photoactivatable Nabi 2.242 (Clover/mRuby2) and PA-Nabi 2.242 (photoactivated PA-GFP/mRuby2) were analyzed to compare the relative brightness of Clover and photoactivated PA-GFP (**Figure 1F**). This revealed that the photoactivated PA-GFP was 5-fold dimmer than the original FRET donor FP. There was no detectable voltage-dependent optical signal.

## Development of Photoactivatable Bongwoori-R3 With a Mutated Ecliptic pHluorin

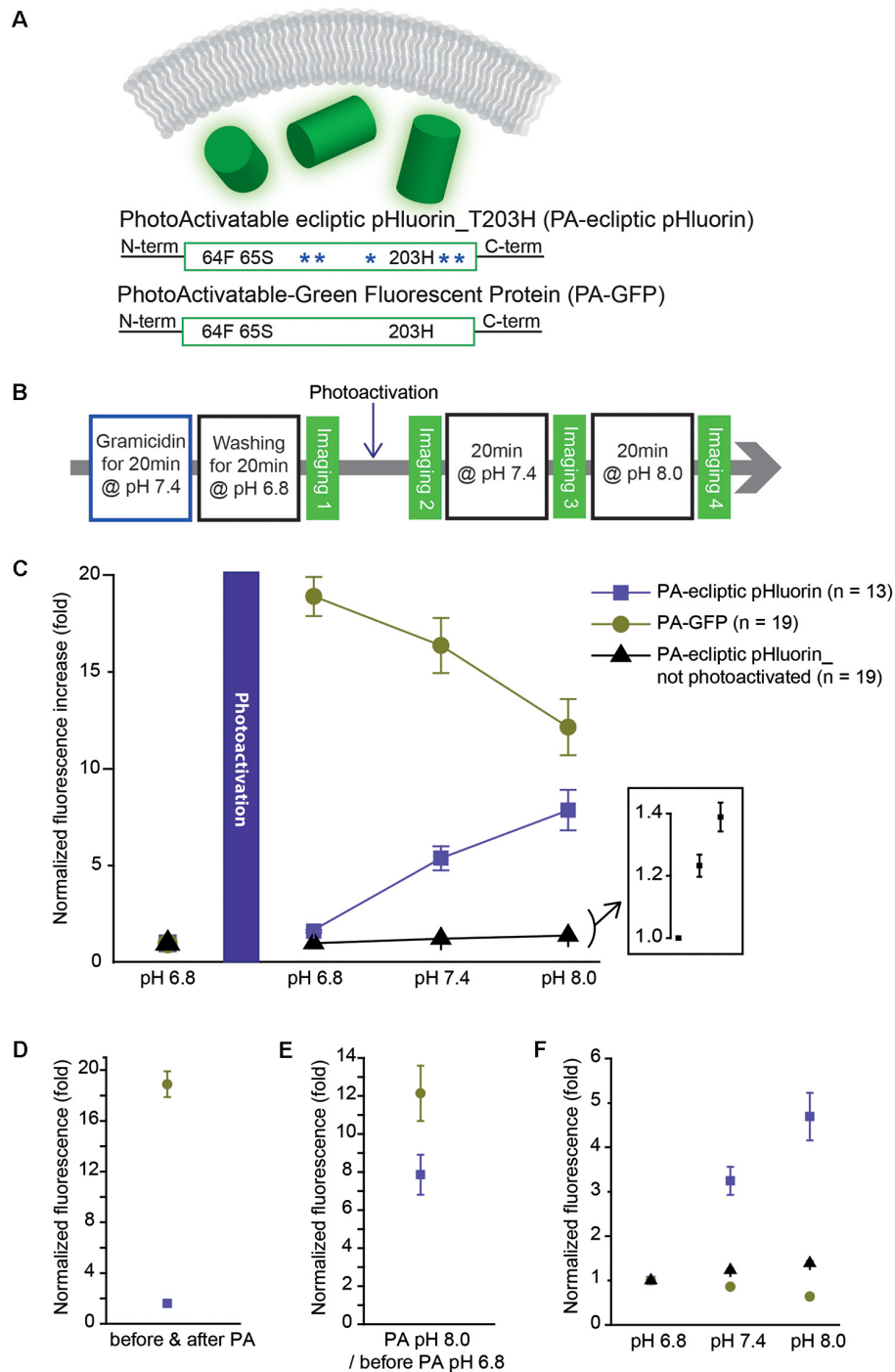
We also tried to develop a photoactivatable version of the GEVI, Bongwoori-R3 (Lee et al., 2017). Bongwoori-R3 uses the FP, super ecliptic pHluorin, to optically report voltage changes. Super ecliptic pHluorin is a modified version of ecliptic pHluorin with diminished 390 nm excitation (Miesenböck et al., 1998; Sankaranarayanan et al., 2000). We, therefore, created a photoactivatable probe with the ecliptic version of the FP

that can be excited with both 390 nm and 470 nm light (**Figure 2A**). The ecliptic FP version of ArcLight has been shown to be voltage-sensitive (Jin et al., 2012; Treger et al., 2015; Platasa et al., 2017). The ecliptic Bongwoori-R3 construct exhibited a voltage-dependent fluorescence change that was smaller and slower than that of the original Bongwoori-R3 (Lee et al., 2017; **Figure 2B**). This variant did not show an increase in fluorescence after photoactivation (**Figure 2C**). The construct consisting of ecliptic-Bongwoori-R3 with the T203H photoactivatable mutation but lacking the A227D mutation that improves the voltage-dependent optical signal was prepared. This construct increased fluorescence upon photoactivation but did not yield a voltage-sensitive optical signal (**Figure 2D**). The photoactivation with 385 nm light improved its brightness by  $1.4 \pm 0.1$  fold (**Figure 2E**).

Subsequently, both the A227D and T203H mutations were introduced into the ecliptic pHluorin version of Bongwoori-R3 to improve voltage sensitivity and confer photoactivatability. This variant of Bongwoori-R3 expressed well in HEK 293 cells. A photoactivation at 385 nm wavelength increased the green fluorescence imaged with 470 nm excitation light about  $1.5 \pm 0.1$ -fold (**Figure 2G**). To examine its voltage-sensitivity, a 100 mV voltage change was induced before and after the photoactivation while imaging at a frame rate of 1,000 Hz. Before photoactivation, only a slight voltage-dependent fluorescence change was observed (**Figure 2F**, left). After photoactivation, a 2%  $\Delta F/F$  was observed during the 100 mV depolarization step. While this signal size is much reduced compared to the original Bongwoori-R3 probe, the fact that the voltage-dependent optical signal can only be detected after photoactivation suggests that the probe may be useful *in vivo* and merits further development. We named this variant PA-Bongwoori-R3.

## Development of Photoactivatable Ecliptic pHluorin and Its pH Sensitivity

The photoactivatable version of Bongwoori-R3 used a variant of a pH-sensitive GFP, ecliptic pHluorin, which is known to get brighter as the pH increases. A photoactivatable GEPI candidate was created by removing the *Ciona Intestinalis* voltage-sensing domain from ecliptic-Bongwoori-R3\_T203H\_D227A. Since it was unnecessary for the probe to sense a voltage change, the 227D mutation in the FP was also removed (**Figure 3A**). The cytoplasmic version of ecliptic pHluorin with T203H (PA-ecliptic pHluorin) and PA-GFP were expressed in HEK 293 cells. The cells were first incubated with an ionophore that makes the cell membrane permeable to external monovalent cations (Gramacidin, Sigma-Aldrich, USA). Next, the cells were washed with a pH 6.8 bath solution with a high buffering capacity (100 mM HEPES) to efficiently change the intracellular pH (**Figure 3B**). Subsequent photoactivation of both PA-ecliptic pHluorin and PA-GFP at the same pH level increased the fluorescence intensity by 1.5 and 18-fold, respectively (**Figures 3C,D**). As the pH of the bath solution was changed from 6.8 to 7.4, PA-ecliptic pHluorin showed an increase in its fluorescence level as expected from ecliptic pHluorin's pH sensitivity (Miesenböck et al., 1998). At pH 8.0,



**FIGURE 3 |** A photoactivatable optical pH sensor (PA-ecliptic pHluorin) and its pH sensitivity in HEK 293 cells in comparison to PA-GFP. **(A)** Schematics of a cytoplasmic optical pH sensor (top), the photoactivatable ecliptic pHluorin with T203H mutation (middle) and PA-GFP (bottom). The blue asterisks depict pH-sensitive mutations in ecliptic pHluorin. **(B)** Experimental procedure for the photoactivatability and pH sensitivity tests. **(C)** Fluorescence intensities measured at each pH level normalized to the fluorescence read-out at pH 6.8 before photoactivation. For the non-photoactivated PA-ecliptic pHluorin experiment (black dots), the photoactivation step shown in **(B)** was omitted. The inset shows PA-ecliptic pHluorin's sensitivity at pH 6.8, 7.4, and 8.0 from the no photoactivation experiment. **(D)** Comparison of photoactivatability of PA-GFP (dark green dots) and PA-ecliptic pHluorin (violet dots) at pH 6.8 (normalized to non-photoactivated states at pH 6.8). **(E)** Fluorescence intensities of PA-GFP (dark green dots) and PA-ecliptic pHluorin (violet dots) at photoactivated pH 8.0 normalized to non-photoactivated states at pH 6.8. **(F)** Fluorescence intensities of PA-GFP (dark green dots) and PA-ecliptic pHluorin (violet dots: photoactivated/black dots: non-photoactivated) normalized to their values at pH 6.8 after photoactivation to only show their pH sensitivities. Error bars are standard error of the mean (SEM). The number of cells analyzed were 13 cells (PA-ecliptic pHluorin), 19 cells (PA-GFP) and 19 cells (PA-ecliptic pHluorin\_non-photoactivated).

PA-ecliptic pHluorin exhibited a further increase in green emission that was  $7.9 \pm 1.0$  fold brighter compared to its non-activated state at pH 6.8 (**Figure 3E**). The non-pH sensitive FP, PA-GFP, only showed decreased fluorescence levels as the bath solution was changed to basic pH. Photoactivation did not confer pH sensitivity. As a control experiment, non-photoactivated PA-ecliptic pHluorin was also tested at different pH levels. Although the fluorescence from these cells remained dim, the FP was slightly sensitive to pH changes (**Figure 3C**, inset). **Figure 3F** summarizes pH sensitivities from the three experiments.

## DISCUSSION

The addition of PA-GFP to the palette of fluorescent proteins led to the development of photoactivated localization microscopy (PALM) that realized single molecule imaging below the diffraction limit in a biological sample (Patterson and Lippincott-Schwartz, 2002; Betzig et al., 2006; Lippincott-Schwartz and Patterson, 2009). The wtGFP has some intrinsic degree of photoactivation due to its characteristic dual excitation bands at 397 nm and 475 nm. Before photoactivation, its chromophore stays in the protonated (neutral) state. Illumination with near 400 nm light is thought to shift the neutral state into the anionic state by deprotonating the chromophore. In this activated state, the excitation at 470 nm becomes dominant. PA-GFP has the T203H mutation that improves the 470 nm excitation upon photoactivation with 400 nm light from 3-fold (wtGFP) to 100-fold (PA-GFP) when measured using purified protein preparations (Patterson and Lippincott-Schwartz, 2002). In order to utilize the advantage of photoactivatable fluorescent proteins for the efficient and controllable fluorescence imaging of voltage and pH, several photoactivatable GEVI candidates and one photoactivatable GEPI were rationally designed and generated. Except for ASAP1-ssPA, all candidates expressed well in HEK 293 cells and showed an increase in fluorescence upon photoactivation. The ASAP1-PATM was bright enough to resolve induced voltage pulses even before photoactivation. However, it would be more useful if the increase in fluorescence level after photoactivation is large enough to make the activated cells easily distinguishable from non-activated cells.

The 385 nm LED light used to photoactivate all the photoactivatable variants in this work was measured to be  $2.7 \text{ mW/mm}^2$  in intensity. As this light intensity was both low and slightly off centered from the typical 400–405 nm light used for illuminating a photoactivatable GFP, the increase after photoactivation may improve if a stronger 400–405 nm light source is used.

The FRET version of the GEVI, PA-Nabi 2.242 was prepared by replacing the bright green FP, Clover, by PA-GFP. This construct failed to show a voltage-dependent FRET signal. Several properties affect FRET efficiency. The distance between the chromophores of donor and acceptor, the spectral overlap between the donor's emission and the acceptor's excitation bands, and the relative orientation of the donor and acceptor dipoles all contribute to the FRET efficiency (Tsien, 1998;

Campbell, 2009). Both PA-GFP and Clover are variants of GFP and the construction of PA-Nabi 2.242 was a simple substitution of PA-GFP for Clover. The emission maxima of the two FPs (photoactivated PA-GFP and Clover) are 517 nm and 515 nm, respectively. A comparison of the emission spectra suggests the overlap with the mRuby2's excitation spectrum was similar for both FRET donors. The quantum yields of photoactivated PA-GFP and Clover are 0.79 and 0.76, respectively (Lukyanov et al., 2005; Lam et al., 2012). However, the extinction coefficients for photoactivated PA-GFP and Clover were measured to be 17,400 and 111,000  $\text{M}^{-1} \text{ cm}^{-1}$  (Patterson and Lippincott-Schwartz, 2002; Lam et al., 2012). As the intrinsic brightness of a fluorophore is determined by extinction coefficient multiplied by quantum yield, Clover is far brighter than the photoactivated PA-GFP. The brightness of photoactivated PA-GFP was measured to be 0.42-fold of eGFP (Lukyanov et al., 2005). Clover is about 2.5-fold brighter than eGFP (Lam et al., 2012). A rough extrapolation of the two values would suggest that the photoactivated PA-GFP is about 5–6-fold dimmer than Clover. A similar difference was seen in our result as well (**Figure 1F**). Although PA-Nabi 2.242 was not promising, having a red-shifted FP as both a FRET acceptor and a guide to locate nicely transfected cells without accidentally activating photoactivatable GFP molecules merits continued exploration.

Photoactivatable Bongwoori-R3 and its derivatives nicely demonstrated the functions of the voltage sensing mutation (A227D) and the photoactivatable mutation (T203H). The voltage-sensitive but non-photoactivatable version, ecliptic-Bongwoori-R3\_A227D, had a small voltage-dependent fluorescence change without photoactivation. However, the  $\Delta F/F$  for a 100 mV depolarization of the plasma membrane was decreased to less than 50% of the original Bongwoori-R3. Jin et al. (2012) also tested both ecliptic pHluorin and super ecliptic pHluorin containing the A227D mutation. According to their report, both variants showed about 18%  $\Delta F/F$  for a 100 mV depolarization. Further linker length optimization for the super ecliptic pHluorin A227D version resulted in the development of ArcLight. Since it is well-known that both linker length and composition affect the voltage-dependent fluorescence signal (Jung et al., 2015; Piao et al., 2015; Lee et al., 2017; Yi et al., 2018), the same may improve PA-Bongwoori-R3 variants' optical signals. Combining the two distinct mutations successfully accomplished a photoactivatable GEVI. With the optical setup that was used in this work, PA-Bongwoori-R3 expressing cells responded to a voltage pulse only after they were photoactivated. As these cells stay in a dim state before the activation, even the modest  $\Delta F/F$  change could be useful (**Figure 2F**).

The intensity of PA-Bongwoori-R3 after photoactivation showed less than a 2-fold increase. This was about 50-fold weaker than that previously reported for PA-GFP (Patterson and Lippincott-Schwartz, 2002). Although the 100-fold increase from the original report was measured from purified proteins embedded in a polyacrylamide gel, PA-Bongwoori-R3's photoactivation increase was modest. This may suggest that the mutations in the photoactivatable ecliptic pHluorin A227D



hindered proper photoactivation. Another possibility could be the weak 385 nm LED light used to photoactivate the molecules. The small 2%  $\Delta F/F$  per 100 mV of PA-Bongwoori-R3 could also be improved through the optimization of linker length.

The regulation of intracellular proton concentration is involved in synaptic vesicle release and network excitability (Sankaranarayanan et al., 2000; Raimondo et al., 2012, 2013, 2016; Lin and Schnitzer, 2016). Optical measurement of intracellular pH changes is important since other means to measure pH such as microelectrodes are limited due to their size (Raimondo et al., 2013). The presynaptic terminal of a neuron, the pH level in the synaptic vesicle lumen is maintained near pH 5.5 and increases to pH 7.3 upon the vesicle opening into the synaptic cleft (Anderson and Orci, 1988; Nelson, 1992; Lin and Schnitzer, 2016). Ecliptic pHluorin is only weakly fluorescent at pH 5.5 and becomes brighter at pH 7.3 (Miesenböck et al., 1998). The pH-sensitivity of PA-ecliptic pHluorin should be useful for studying pH changes in the cytoplasm (Figure 3C). Non-photoactivated PA-ecliptic pHluorin was still pH-sensitive but its brightness at pH 8.0 increased by about 1.5-fold compared to the photoactivated state which had an 8-fold increase in fluorescence.

The key finding of this report is that the voltage-sensing mutation, A227D, and the photoactivatable mutation, T203H, were applicable to the development of photoactivatable voltage and pH sensors. Further optimization of photoactivation for both PA-Bongwoori-R3 and PA-ecliptic pHluorin may enable the optical resolution of both high speed and low speed *in vivo* neuronal activity.

## DATA AVAILABILITY STATEMENT

The datasets generated for this study are available on request to the corresponding author.

## REFERENCES

- Abdelfattah, A. S., Rancic, V., Rawal, B., Ballanyi, K., and Campbell, R. E. (2016). Ratiometric and photoconvertible fluorescent protein-based voltage indicator prototypes. *Chem. Commun.* 52, 14153–14156. doi: 10.1039/c6cc06810c
- Adam, Y., Kim, J. J., Lou, S., Zhao, Y., Xie, M. E., Brinks, D., et al. (2019). Voltage imaging and optogenetics reveal behaviour-dependent changes in hippocampal dynamics. *Nature* 569, 413–417. doi: 10.1038/s41586-019-1166-7
- Anderson, R. G., and Orci, L. (1988). A view of acidic intracellular compartments. *J. Cell Biol.* 106, 539–543. doi: 10.1083/jcb.106.3.539
- Bayguinov, P. O., Ma, Y., Gao, Y., Zhao, X., and Jackson, M. B. (2017). Imaging voltage in genetically defined neuronal subpopulations with a Cre recombinase-targeted hybrid voltage sensor. *J. Neurosci.* 37, 9305–9319. doi: 10.1523/JNEUROSCI.1363-17.2017
- Berlin, S., Carroll, E. C., Newman, Z. L., Okada, H. O., Quinn, C. M., Kallman, B., et al. (2015). Photoactivatable genetically encoded calcium indicators for targeted neuronal imaging. *Nat. Methods* 12, 852–858. doi: 10.1038/nmeth.3480
- Betzig, E., Patterson, G. H., Sougrat, R., Lindwasser, O. W., Olenych, S., Bonifacio, J. S., et al. (2006). Imaging intracellular fluorescent proteins at nanometer resolution. *Science* 313, 1642–1645. doi: 10.1126/science.1127344
- Bizzarri, R., Arcangeli, C., Arosio, D., Ricci, F., Faraci, P., Cardarelli, F., et al. (2006). Development of a novel GFP-based ratiometric excitation and

## AUTHOR CONTRIBUTIONS

SL designed experiments, performed experiments, analyzed data, created figures and wrote the manuscript. Y-KS analyzed data and co-wrote the manuscript. BB designed experiments, analyzed data, and co-wrote the manuscript.

## FUNDING

Research reported in this publication was supported by the National Institute of Neurological Disorders and Stroke of the National Institutes of Health under Award Number U01NS099691 (USA). The content is solely the responsibility of the authors and does not necessarily represent the official views of the National Institutes of Health. This study was also funded by the Korea Institute of Science and Technology (KIST) grants 2E29180 and 2E27850. SL was supported by Global Ph.D. Fellowship program (NRF-2013H1A2A1033344) of the National Research Foundation (NRF), Ministry of Education (South Korea). The research was also supported by Basic Science Research Program (NRF-2015R1D1A1A01060569) through the National Research Foundation of Korea (NRF), Ministry of Education.

## ACKNOWLEDGMENTS

We would like to thank Lawrence B. Cohen for critically reviewing the manuscript.

## SUPPLEMENTARY MATERIAL

The Supplementary Material for this article can be found online at: <https://www.frontiersin.org/articles/10.3389/fncel.2019.00482/full#supplementary-material>.

- emission pH indicator for intracellular studies. *Biophys. J.* 90, 3300–3314. doi: 10.1529/biophysj.105.074708
- Campbell, R. E. (2009). Fluorescent-protein-based biosensors: modulation of energy transfer as a design principle. *Anal. Chem.* 81, 5972–5979. doi: 10.1021/ac802613w
- Chudakov, D. M., Matz, M. V., Lukyanov, S., and Lukyanov, K. A. (2010). Fluorescent proteins and their applications in imaging living cells and tissues. *Physiol. Rev.* 90, 1103–1163. doi: 10.1152/physrev.00038.2009
- Fosque, B. F., Sun, Y., Dana, H., Yang, C. T., Ohyama, T., Tadross, M. R., et al. (2015). Labeling of active neural circuits *in vivo* with designed calcium integrators. *Science* 347, 755–760. doi: 10.1126/science.1260922
- Harris, J. A., Hirokawa, K. E., Sorensen, S. A., Gu, H., Mills, M., Ng, L. L., et al. (2014). Anatomical characterization of Cre driver mice for neural circuit mapping and manipulation. *Front. Neural Circuits* 8:76. doi: 10.3389/fncir.2014.00076
- Hoi, H., Matsuda, T., Nagai, T., and Campbell, R. E. (2013). Highlightable Ca<sup>2+</sup> indicators for live cell imaging. *J. Am. Chem. Soc.* 135, 46–49. doi: 10.1021/ja310184a
- Jin, L., Han, Z., Platasa, J., Woollorton, J. R., Cohen, L. B., and Pieribone, V. A. (2012). Single action potentials and subthreshold electrical events imaged in neurons with a fluorescent protein voltage probe. *Neuron* 75, 779–785. doi: 10.1016/j.neuron.2012.06.040

- Jung, A., Garcia, J. E., Kim, E., Yoon, B. J., and Baker, B. J. (2015). Linker length and fusion site composition improve the optical signal of genetically encoded fluorescent voltage sensors. *Neurophotonics* 2:021012. doi: 10.1117/1.nph.2.2.021012
- Kang, B. E., and Baker, B. J. (2016). Pado, a fluorescent protein with proton channel activity can optically monitor membrane potential, intracellular pH, and map gap junctions. *Sci. Rep.* 6:23865. doi: 10.1038/srep23865
- Lam, A. J., St-Pierre, F., Gong, Y., Marshall, J. D., Cranfill, P. J., Baird, M. A., et al. (2012). Improving FRET dynamic range with bright green and red fluorescent proteins. *Nat. Methods* 9, 1005–1012. doi: 10.1038/nmeth.2171
- Lee, S., Geiller, T., Jung, A., Nakajima, R., Song, Y. K., and Baker, B. J. (2017). Improving a genetically encoded voltage indicator by modifying the cytoplasmic charge composition. *Sci. Rep.* 7:8286. doi: 10.1038/s41598-017-08731-2
- Lin, M. Z., and Schnitzer, M. J. (2016). Genetically encoded indicators of neuronal activity. *Nat. Neurosci.* 19, 1142–1153. doi: 10.1038/nn.4359
- Lippincott-Schwartz, J., and Patterson, G. H. (2009). Photoactivatable fluorescent proteins for diffraction-limited and super-resolution imaging. *Trends Cell Biol.* 19, 555–565. doi: 10.1016/j.tcb.2009.09.003
- Lou, S., Adam, Y., Weinstein, E. N., Williams, E., Williams, K., Parot, V., et al. (2016). Genetically targeted all-optical electrophysiology with a transgenic Cre-dependent optopatch mouse. *J. Neurosci.* 36, 11059–11073. doi: 10.1523/jneurosci.1582-16.2016
- Lukyanov, K. A., Chudakov, D. M., Lukyanov, S., and Verkhusha, V. V. (2005). Innovation: photoactivatable fluorescent proteins. *Nat. Rev. Mol. Cell Biol.* 6, 885–891. doi: 10.1038/nrm1741
- Madisen, L., Garner, A. R., Shimaoka, D., Chuong, A. S., Klapoetke, N. C., Li, L., et al. (2015). Transgenic mice for intersectional targeting of neural sensors and effectors with high specificity and performance. *Neuron* 85, 942–958. doi: 10.1016/j.neuron.2015.02.022
- Marshall, J. D., Li, J. Z., Zhang, Y., Gong, Y., St-Pierre, F., Lin, M. Z., et al. (2016). Cell-type-specific optical recording of membrane voltage dynamics in freely moving mice. *Cell* 167, 1650–1662.e15. doi: 10.1016/j.cell.2016.11.021
- Miesenböck, G., De Angelis, D. A., and Rothman, J. E. (1998). Visualizing secretion and synaptic transmission with pH-sensitive green fluorescent proteins. *Nature* 394, 192–195. doi: 10.1038/28190
- Nakajima, R., and Baker, B. J. (2018). Mapping of excitatory and inhibitory postsynaptic potentials of neuronal populations in hippocampal slices using the GEVI, ArcLight. *J. Phys. D Appl. Phys.* 51:504003. doi: 10.1088/1361-6463/aae2e3
- Nelson, N. (1992). Structure and function of V-ATPases in endocytic and secretory organelles. *J. Exp. Biol.* 172, 149–153.
- Patterson, G. H., and Lippincott-Schwartz, J. (2002). A photoactivatable GFP for selective photolabeling of proteins and cells. *Science* 297, 1873–1877. doi: 10.1126/science.1074952
- Piao, H. H., Rajakumar, D., Kang, B. E., Kim, E. H., and Baker, B. J. (2015). Combinatorial mutagenesis of the voltage-sensing domain enables the optical resolution of action potentials firing at 60 Hz by a genetically encoded fluorescent sensor of membrane potential. *J. Neurosci.* 35, 372–385. doi: 10.1523/JNEUROSCI.3008-14.2015
- Platasa, J., Vasan, G., Yang, A., and Pieribone, V. A. (2017). Directed evolution of key residues in fluorescent protein inverses the polarity of voltage sensitivity in the genetically encoded indicator ArcLight. *ACS Chem. Neurosci.* 8, 513–523. doi: 10.1021/acschemneuro.6b00234
- Quicke, P., Song, C., McKimm, E. J., Milosevic, M. M., Howe, C. L., Neil, M., et al. (2019). Single-neuron level one-photon voltage imaging with sparsely targeted genetically encoded voltage indicators. *Front. Cell. Neurosci.* 13:39. doi: 10.3389/fncel.2019.00039
- Raimondo, J. V., Irkle, A., Wefelmeyer, W., Newey, S. E., and Akerman, C. J. (2012). Genetically encoded proton sensors reveal activity-dependent pH changes in neurons. *Front. Mol. Neurosci.* 5:68. doi: 10.3389/fnmol.2012.00068
- Raimondo, J. V., Joyce, B., Kay, L., Schlagheck, T., Newey, S. E., Srinivas, S., et al. (2013). A genetically-encoded chloride and pH sensor for dissociating ion dynamics in the nervous system. *Front. Cell. Neurosci.* 7:202. doi: 10.3389/fncel.2013.00202
- Raimondo, J. V., Tomes, H., Irkle, A., Kay, L., Kellaway, L., Markram, H., et al. (2016). Tight coupling of astrocyte pH dynamics to epileptiform activity revealed by genetically encoded pH sensors. *J. Neurosci.* 36, 7002–7013. doi: 10.1523/JNEUROSCI.0664-16.2016
- Sando, R. III., Baumgaertel, K., Pieraut, S., Torabi-Rander, N., Wandless, T. J., Mayford, M., et al. (2013). Inducible control of gene expression with destabilized Cre. *Nat. Methods* 10, 1085–1088. doi: 10.1038/nmeth.2640
- Sankaranarayanan, S., De Angelis, D., Rothman, J. E., and Ryan, T. A. (2000). The use of pHluorins for optical measurements of presynaptic activity. *Biophys. J.* 79, 2199–2208. doi: 10.1016/S0006-3495(00)76468-X
- Song, C., Do, Q. B., Antic, S. D., and Knöpfel, T. (2017). Transgenic strategies for sparse but strong expression of genetically encoded voltage and calcium indicators. *Int. J. Mol. Sci.* 18:E1461. doi: 10.3390/ijms18071461
- Storage, D., Sepehri Rad, M., Kang, B., Cohen, L. B., Hughes, T., and Baker, B. J. (2016). Toward better genetically encoded sensors of membrane potential. *Trends Neurosci.* 39, 277–289. doi: 10.1016/j.tins.2016.02.005
- St-Pierre, F., Marshall, J. D., Yang, Y., Gong, Y., Schnitzer, M. J., and Lin, M. Z. (2014). High-fidelity optical reporting of neuronal electrical activity with an ultrafast fluorescent voltage sensor. *Nat. Neurosci.* 17, 884–889. doi: 10.1038/nn.3709
- Sung, U., Sepehri-Rad, M., Piao, H. H., Jin, L., Hughes, T., Cohen, L. B., et al. (2015). Developing fast fluorescent protein voltage sensors by optimizing FRET interactions. *PLoS One* 10:e0141585. doi: 10.1371/journal.pone.0141585
- Treger, J. S., Priest, M. F., and Bezanilla, F. (2015). Single-molecule fluorimetry and gating currents inspire an improved optical voltage indicator. *Elife* 4:e10482. doi: 10.7554/elife.10482
- Tsien, R. Y. (1998). The green fluorescent protein. *Annu. Rev. Biochem.* 67, 509–544. doi: 10.1146/annurev.biochem.67.1.509
- Xu, N. L., Harnett, M. T., Williams, S. R., Huber, D., O'Connor, D. H., Svoboda, K., et al. (2012). Nonlinear dendritic integration of sensory and motor input during an active sensing task. *Nature* 492, 247–251. doi: 10.1038/nature11601
- Yi, B., Kang, B. E., Lee, S., Braubach, S., and Baker, B. J. (2018). A dimeric fluorescent protein yields a bright, red-shifted GEVI capable of population signals in brain slice. *Sci. Rep.* 8:15199. doi: 10.1038/s41598-018-33297-y

**Conflict of Interest:** The authors declare that the research was conducted in the absence of any commercial or financial relationships that could be construed as a potential conflict of interest.

Copyright © 2019 Lee, Song and Baker. This is an open-access article distributed under the terms of the Creative Commons Attribution License (CC BY). The use, distribution or reproduction in other forums is permitted, provided the original author(s) and the copyright owner(s) are credited and that the original publication in this journal is cited, in accordance with accepted academic practice. No use, distribution or reproduction is permitted which does not comply with these terms.



# Biosensors Show the Pharmacokinetics of S-Ketamine in the Endoplasmic Reticulum

Kallol Bera<sup>1</sup>, Aron Kamajaya<sup>1</sup>, Amol V. Shivange<sup>1</sup>, Anand K. Muthusamy<sup>1,2</sup>, Aaron L. Nichols<sup>1,2</sup>, Philip M. Borden<sup>3</sup>, Stephen Grant<sup>2</sup>, Janice Jeon<sup>1</sup>, Elaine Lin<sup>1</sup>, Ishak Bishara<sup>1</sup>, Theodore M. Chin<sup>1</sup>, Bruce N. Cohen<sup>1</sup>, Charlene H. Kim<sup>1</sup>, Elizabeth K. Unger<sup>4</sup>, Lin Tian<sup>4</sup>, Jonathan S. Marvin<sup>3</sup>, Loren L. Looger<sup>3</sup> and Henry A. Lester<sup>1\*</sup>

<sup>1</sup>Division of Biology and Biological Engineering, California Institute of Technology, Pasadena, CA, United States, <sup>2</sup>Division of Chemistry and Chemical Engineering, California Institute of Technology, Pasadena, CA, United States, <sup>3</sup>Janelia Research Campus, Howard Hughes Medical Institute, Ashburn, VA, United States, <sup>4</sup>Department of Biochemistry and Molecular Medicine, University of California, Davis, Davis, CA, United States

## OPEN ACCESS

### Edited by:

Shai Berlin,  
Technion Israel Institute of  
Technology, Israel

### Reviewed by:

Kenji Hashimoto,  
Chiba University, Japan  
Randy Franklin Stout,  
New York Institute of Technology,  
United States

### \*Correspondence:

Henry A. Lester  
lester@caltech.edu

**Received:** 19 August 2019

**Accepted:** 22 October 2019

**Published:** 12 November 2019

### Citation:

Bera K, Kamajaya A, Shivange AV, Muthusamy AK, Nichols AL, Borden PM, Grant S, Jeon J, Lin E, Bishara I, Chin TM, Cohen BN, Kim CH, Unger EK, Tian L, Marvin JS, Looger LL and Lester HA (2019) Biosensors Show the Pharmacokinetics of S-Ketamine in the Endoplasmic Reticulum. *Front. Cell. Neurosci.* 13:499. doi: 10.3389/fncel.2019.00499

The target for the “rapid” (<24 h) antidepressant effects of S-ketamine is unknown, vitiating programs to rationally develop more effective rapid antidepressants. To describe a drug’s target, one must first understand the compartments entered by the drug, at all levels—the organ, the cell, and the organelle. We have, therefore, developed molecular tools to measure the subcellular, organellar pharmacokinetics of S-ketamine. The tools are genetically encoded intensity-based S-ketamine-sensing fluorescent reporters, iSKetSnFR1 and iSKetSnFR2. In solution, these biosensors respond to S-ketamine with a sensitivity, S-slope =  $\Delta(F/F_0)/(\Delta[S\text{-ketamine}])$  of 0.23 and 1.9/ $\mu\text{M}$ , respectively. The iSKetSnFR2 construct allows measurements at <0.3  $\mu\text{M}$  S-ketamine. The iSKetSnFR1 and iSKetSnFR2 biosensors display >100-fold selectivity over other ligands tested, including R-ketamine. We targeted each of the sensors to either the plasma membrane (PM) or the endoplasmic reticulum (ER). Measurements on these biosensors expressed in Neuro2a cells and in human dopaminergic neurons differentiated from induced pluripotent stem cells (iPSCs) show that S-ketamine enters the ER within a few seconds after appearing in the external solution near the PM, then leaves as rapidly after S-ketamine is removed from the extracellular solution. In cells, S-slopes for the ER and PM-targeted sensors differ by <2-fold, indicating that the ER [S-ketamine] is less than 2-fold different from the extracellular [S-ketamine]. Organelles represent potential compartments for the engagement of S-ketamine with its antidepressant target, and potential S-ketamine targets include organellar ion channels, receptors, and transporters.

**Keywords:** antidepressants, organelles, green fluorescent protein, protein engineering and design, periplasmic binding proteins (PBPs), inside-out pharmacology, iSKetSnFR1, iSKetSnFR2

## INTRODUCTION

Despite half a century of research and improvement, antidepressant drugs do not work optimally. Although selective serotonin reuptake inhibitor antidepressants help appreciable numbers of patients, their benefits appear too slowly (2–6 weeks) after treatment has begun. In contrast, administration of a single, relatively small (subanesthetic) dose of racemic ketamine for ~1 h partially relieves depression in <1 day; this relief continues for several days post-administration (Berman et al., 2000). In some preclinical studies, R-ketamine has more potent and lasting antidepressant action than S-ketamine (Hashimoto, 2019). Recently, the US FDA approved inhaled S-ketamine for treatment-resistant depression.

However, because higher doses of S-ketamine have adverse effects, developing antidepressants that act similarly to S-ketamine may be a better strategy than using S-ketamine itself. To enable developing better rapidly acting antidepressants, one must first understand the mechanism of S-ketamine action, including the molecular target.

Most investigators emphasize the hypothesis that S-ketamine exerts its antidepressant effects by binding to an N-Methyl-D-aspartate (NMDA) receptor subtype (MacDonald et al., 1991; Blanpied et al., 1997; Preskorn et al., 2008; Autry et al., 2011; Emnett et al., 2013; Gideons et al., 2014; Miller et al., 2014; Johnson et al., 2015). Other articles suggest the following receptor, channel, or transporter targets for ketamine:  $\alpha 3\beta 2$  nicotinic receptors (nAChRs; Lee et al., 2012),  $\alpha 4\beta 2$  nAChRs (Buisson and Bertrand, 1998),  $\alpha 7$  nAChRs (Coates and Flood, 2001; Moaddel et al., 2013), dopamine D2 receptors (Kapur and Seeman, 2001, 2002; Seeman and Kapur, 2003), HCN1 channels (Chen et al., 2009), 5-HT<sub>2</sub> receptors (Frohlich and Van Horn, 2014), or 5-HT<sub>3</sub> receptors (Yamakura et al., 2000). Most contemporary psychiatric drugs have well-established receptor, channel, or transporter targets. In contrast, the “target” for the antidepressant actions of S-ketamine is poorly understood.

We comment similarly that downstream signaling pathways are poorly understood. Suggested pathways include mechanistic target of rapamycin (mTOR; Zoncu et al., 2011; Moaddel et al., 2013; Miller et al., 2014), eukaryotic elongation factor 2 (EEF2) kinase (Autry et al., 2011; Gideons et al., 2014; Adaikkan et al., 2018), serine/threonine kinase glycogen synthase kinase-3 (GSK-3; Beurel et al., 2011; Liu et al., 2013), calcium/calmodulin-dependent protein kinase II (CaMKII; Adaikkan et al., 2018), brain-derived neurotrophic factor (BDNF; Lepack et al., 2014), Kir4.1-containing transport vesicles (Stenovec et al., 2019), and G-protein translocation to/from lipid rafts (Wray et al., 2018). These molecules are thought to participate in enhancements of glutamatergic (Zanos et al., 2018), cholinergic, or GABAergic (Widman and McMahon, 2018) transmission (Ren et al., 2016). Finally, we comment similarly about brain regions and nuclei. Most studies focus on hippocampus and cortex; but ketamine also blocks bursting in the lateral habenula (Yang et al., 2018).

If one does not know the target for a drug, then an appropriate step is to seek that target in all compartments that contain

the drug, and to measure how long the drug remains in each compartment. A previous report shows that a ketamine analog enters cells (Emnett et al., 2016). This report presents the first quantitative, dynamically resolved measurements of S-ketamine in an organelle: the endoplasmic reticulum (ER).

To conduct these experiments, we executed a research strategy resembling our previous report for nicotine (Shivange et al., 2019). We developed a genetically encoded fluorescent biosensor for S-ketamine. We targeted the biosensor to either the plasma membrane (PM) or the ER. We then performed fluorescence measurements to dynamically report the S-ketamine concentration in each compartment.

## MATERIALS AND METHODS

### Directed Evolution of iSKetSnFR Proteins Using Bacterial-Expressed Protein Assays

Starting with the iNicSnFR biosensor constructs (Shivange et al., 2019), we constructed and measured ~3,000 mutants, in iterative rounds of site-saturated mutagenesis (SSM). We utilized the Quikchange mutagenesis protocol (Agilent), including a mixture of three primers, creating 22 unique codons encoding the 20 canonical amino acids (Kille et al., 2013). The 22-codon procedure yields an estimated >96% residue coverage for a collection of 96 randomly chosen clones.

A Tecan Spark M10 96-well fluorescence plate reader (equipped with appropriate filters) was used to measure resting and S-ketamine-induced fluorescence ( $F_0$  and  $\Delta F$ , respectively). Bacterial lysates were tested with excitation at 485 nm and emission at 535 nm. Promising clones were amplified and sequenced. The most sensitive construct in each round of SSM was used as a template for the next round of SSM.

### Measurements on Purified iSKetSnFR Constructs

Biosensors selected for further study were purified with the His<sub>6</sub> sequence included in the bacterial expression vector (Shivange et al., 2019). Proteins were purified by immobilization in phosphate-buffered saline (PBS), pH 7.4, and elution in an imidazole gradient (10–200 mM). Proteins were concentrated by centrifugation through a 30 kDa cut off column, and by dialysis against PBS. The dialyzed protein was quantified using a nanodrop spectrofluorometer, and 50 or (preferably) 100 nM was used in dose-response studies to characterize responses to various ligands. Dose-response relations for ligands were conducted with the plate reader. The pH-dependent dose-response studies with purified iSKetSnFR constructs were performed using 3× PBS buffers.

### Expression in Mammalian Cells

We constructed two variants of the iSKetSnFR1 and iSKetSnFR2 biosensors for expression in mammalian cells. The plasma membrane (\_PM) and endoplasmic reticulum (\_ER) variants were constructed by a circular polymerase extension cloning procedure. For iSKetSnFR1\_PM and iSKetSnFR2\_PM, we cloned the bacterial constructs into pCMV(MinDis), a variant of pDisplay (Invitrogen, Carlsbad, CA, USA) lacking the



hemagglutinin tag (Marvin et al., 2013). We modified the previous transmembrane domain (Shivange et al., 2019) as follows. We replaced the terminal KKPR of the PDGF receptor (a putative ER retention motif) with KYLQKRRERRRQ (a p14 Golgi export motif) and ENANSFCYENEVAL (a putative Kir2.X ER export motif). To generate iSketSnFR1\_ER and iSketSnFR2\_ER, we replaced the 14 C-terminal amino acids (QVDEQKLISEEDLN, including the Myc tag) with an ER retention motif, QTAEKDEL (Shivange et al., 2019).

We conducted cDNA transfection experiments on iSketSnFR1\_PM, iSketSnFR2\_PM, iSketSnFR1\_ER, and iSketSnFR2\_ER in Neuro2a cells. Neuro2a cells were purchased from ATCC<sup>1</sup> and cultured according to ATCC protocols. For chemical transfection, we utilized either Lipofectamine 2000 or Lipofectamine 3000, following the manufacturer's recommended protocol. Cells were incubated in the transfection medium for 24 h and then in growth media for ~24 h before imaging.

## Expression in Dopaminergic Neurons Differentiated From Human Induced Pluripotent Stem Cells (iPSCs)

Fujifilm CDI<sup>2</sup> (formerly named Cellular Dynamics International, Madison WI, USA), furnished iCell DopaNeurons. These are human dopaminergic neurons differentiated from induced pluripotent stem cells (iPSCs). The supplier has measured that 89% of the cells are positive for tyrosine hydroxylase by fluorescence-activated cell sorting. The iCell DopaNeurons were maintained in 95% BrainPhys Neuronal medium (STEMCELL Technologies<sup>3</sup>), 2% iCell Neural Supplement B (CDI), 1% iCell Nervous System Supplement (CDI), 0.1% of 1 mg/ml laminin (Sigma), 1% N-2 Supplement 100× (Thermo Fisher Scientific, Waltham, MA, USA) and supplemented with penicillin and streptomycin. iCell DopaNeurons were maintained on dishes for 17–24 days before imaging. Glass bottoms of the 35-mm imaging dishes (MatTek<sup>4</sup>) were coated with ~0.07% poly(ethyleneimine) solution and incubated at 37°C for 1 h. Dishes were rinsed with PBS, then rinsed with water and air-dried overnight. Glass bottoms were then coated with 80 µg/ml laminin solution for 30 min at 37°C before cells were plated. We confirmed that ≥40% of the cells stained for TH by immunocytochemistry using a previously described assay (Srinivasan et al., 2016).

Cultured iCell DopaNeurons were transfected after either 13 or 21 days in culture using the Viafect kit (Promega, Cat. #E4981) at 4:1 transfection reagent (µl): DNA (µg) ratio. The transfection mixture was prepared in 100 µl OptiMEM (Thermo Fisher Scientific, Waltham, MA, USA) containing 4 µl of Viafect transfection reagent and 1 µg of cDNA. The mixture was incubated for 10–15 min, then added directly to fresh maintenance medium in the culture dish. Transfection medium was removed after 24 h and cells incubated for 48–72 h further before imaging.

## Time-Resolved Fluorescence Measurements in Live Mammalian Cells

We find that signals with the iSketSnFR constructs have brightness similar to those of the previous iNicSnFR cpGFP-based biosensors for nicotine (Shivange et al., 2019), but the dynamic range is somewhat lower for the iKetSnFRs. Datasets were taken on an Olympus IX-81 microscope, in widefield epifluorescence mode. Images were acquired at 3–4 frames/s with a back-illuminated EMCCD camera (iXon DU-897, Andor Technology USA, South Windsor, CT, USA; Pantoja et al., 2009), controlled by Andor IQ2 or IQ3 software. Fluorescence measurements at  $\lambda_{\text{ex}} = 470$  nm have been described (Shivange et al., 2019). We also installed a second LED for excitation at 405 nm. The epifluorescence cube was previously described (Srinivasan et al., 2011). The 40× lens proved most convenient for imaging several adjacent cells and was relatively insensitive to modest drift of the focus. PM-directed constructs were measured with a region of interest (ROI) that included only the cell periphery.

Solutions were delivered from elevated reservoirs by gravity flow, through solenoid valves (Automate Scientific, Berkeley, CA, USA), then through tubing fed into a manifold, at a rate of 1–2 ml/min. Experiments were performed with HBSS buffer, except that iPSC-derived neurons were studied in PBS plus D-glucose (5.56 mM), MgCl<sub>2</sub> (0.49 mM), MgSO<sub>4</sub> (0.4 mM), KCl (5.33 mM), and CaCl<sub>2</sub> (1.26 mM). Other details have been described (Shivange et al., 2019). As usual in fluorescence imaging experiments, we excluded data from the brightest cells, because these may have fluorescent impurities or aggregates that produce a rapidly bleaching baseline. Data analysis procedures included subtraction of blank (extracellular) areas and corrections for baseline drifts.

## Confocal Fluorescence Imaging

For laser scanning confocal fluorescence imaging, Neuro2a cells were transfected with iSketSnFR1\_PM, iSketSnFR2\_PM, iSketSnFR1\_ER, or iSketSnFR2\_ER (0.5 µg) with the aid of either Lipofectamine 2000 or Lipofectamine 3000, using the manufacturer's recommended protocol. The images were acquired with a Zeiss LSM 710 laser-scanning confocal microscope, equipped with a 63× NA 1.4 objective lens. HBSS was used to wash and replace the growth medium in the dishes before imaging. GFP illumination was at 488 nm, observed through a 495–550 nm band-pass filter.

## The S-Slope

We introduce a convenient metric to summarize progress in evolving increasingly sensitive fluorescent biosensors for drugs. The metric, the S-slope, is especially appropriate for low drug concentrations because it corresponds to the relationship between [drug] and  $\Delta F$  at the beginning of the dose-response relation. We define the S-slope for use with intensity-based drug biosensors:

$$\text{S-slope} = \Delta \left( \frac{F}{F_0} \right) / (\Delta [\text{drug}]).$$

We state the S-slope in units of  $\mu\text{M}^{-1}$ .

<sup>1</sup>www.attc.org

<sup>2</sup>fujifilmcdi.com

<sup>3</sup>www.stemcell.com

<sup>4</sup>www.mattek.com

This article uses the S-slope for measurements on S-ketamine biosensors in bacterial lysates, with purified proteins, and expressed in cells. For measurements with bacterial lysates and with purified proteins, it is usually possible to construct a complete dose-response relation with a Hill coefficient close to 1. In this case, we calculated (as in **Figure 2A** below),

$$\text{S-slope} = \frac{\Delta F_{\max}}{F_0} / EC_{50}$$

## Reagents

All solvents purchased were of analytical grade and used without further purification. S-ketamine HCl was purchased from Sigma-Aldrich (St. Louis, MO, USA; Cat. #K1884, CAS #33643-47-9). We purchased R-ketamine HCl from Cayman Chemicals (Ann Arbor, MI, USA; Cat. #16519, CAS#33795-24-3).

## Data Analysis

Image movie files, spectral data, and dose-response data were analyzed further and presented with general-purpose software. These programs include ImageJ2 (Rueden et al., 2017), Excel (Microsoft), and Origin (OriginLab). All the sequencing analyses used Benchling.

## RESULTS

### Development of iSKetSnFR1 and iKetSnFR2

We tested S-ketamine and R-ketamine (**Figure 1**) against iNicSnFR1, iNicSnFR2, and iNicSnFR3a, as well as against 12 other biosensors in the series that led to the iNicSnFRs (Shivange et al., 2019). We found no detectable fluorescence increase activated by S-ketamine, at concentrations <100  $\mu\text{M}$ .

For further insights, we computationally docked S-ketamine into the structure of iNicSnFR1 (PDB file 6EFR), and several computationally mutated variants (**Supplementary Figure S1**). In the highest-ranked results, the predicted distances between the S-ketamine N atom and the aromatic groups are too great to form a cation- $\pi$  interaction of the type suggested by docking, structural, and mutational studies for the iNicSnFR series with nicotine, acetylcholine, and varenicline (Shivange et al., 2019).

These observations, while heuristic and not definitive, suggested that we mutate the aromatic residues.

When we applied SSM to the Tyr357 position, we found S-ketamine responses, but only for a Gly residue at position 357 ( $\Delta F/F_0 \sim 0.12$  at 1  $\mu\text{M}$ ). While insufficiently sensitive for systematic measurements, this construct (AK1) provided an entry for further SSM experiments.

After we identified AK1, further rounds of SSM (retaining the Gly357 codon) led to improvements by mutations at and near the ligand site, including positions 10, 436, and 457. The iKetSnFR1 construct has an S-slope of  $0.32 \mu\text{M}^{-1}$ , nearly equal to that of nicotine for iNicSnFR3a and iNicSnFR3b (Shivange et al., 2019). Thus, *in vitro*, one expects a response to 1  $\mu\text{M}$  S-ketamine of  $\Delta F/F_0 = 0.32$ . The actual recorded data in cells were in this range (see below). The development series has culminated in iKetSnFR2, which has an S-slope of  $1.87 \mu\text{M}^{-1}$  (**Figure 2**).

We note the presence of the Phe436Trp mutation (referred to the original OpuBC periplasmic binding protein). One conformer of the Trp side chain can fit into the vacancy left by the absence of a side chain at Gly357. This combination may re-establish a cation- $\pi$  interaction with the nitrogen of ketamine; further structural analysis would test this hypothesis.

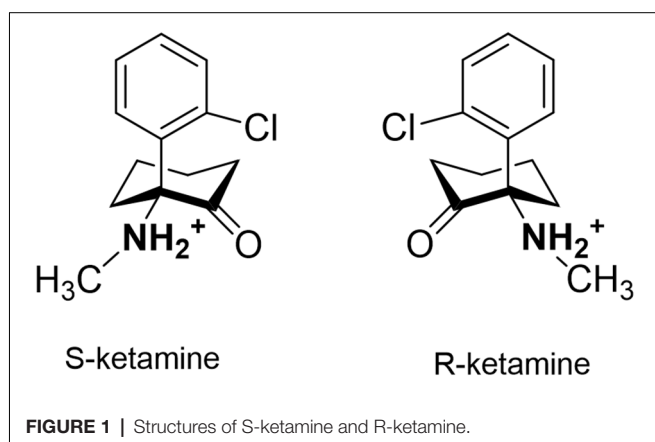
We also note the substantial increased sensitivity for the Met10 codon (from AK7 to iKetSnFR2). We have no explicit structural explanation for the effectiveness of this mutation.

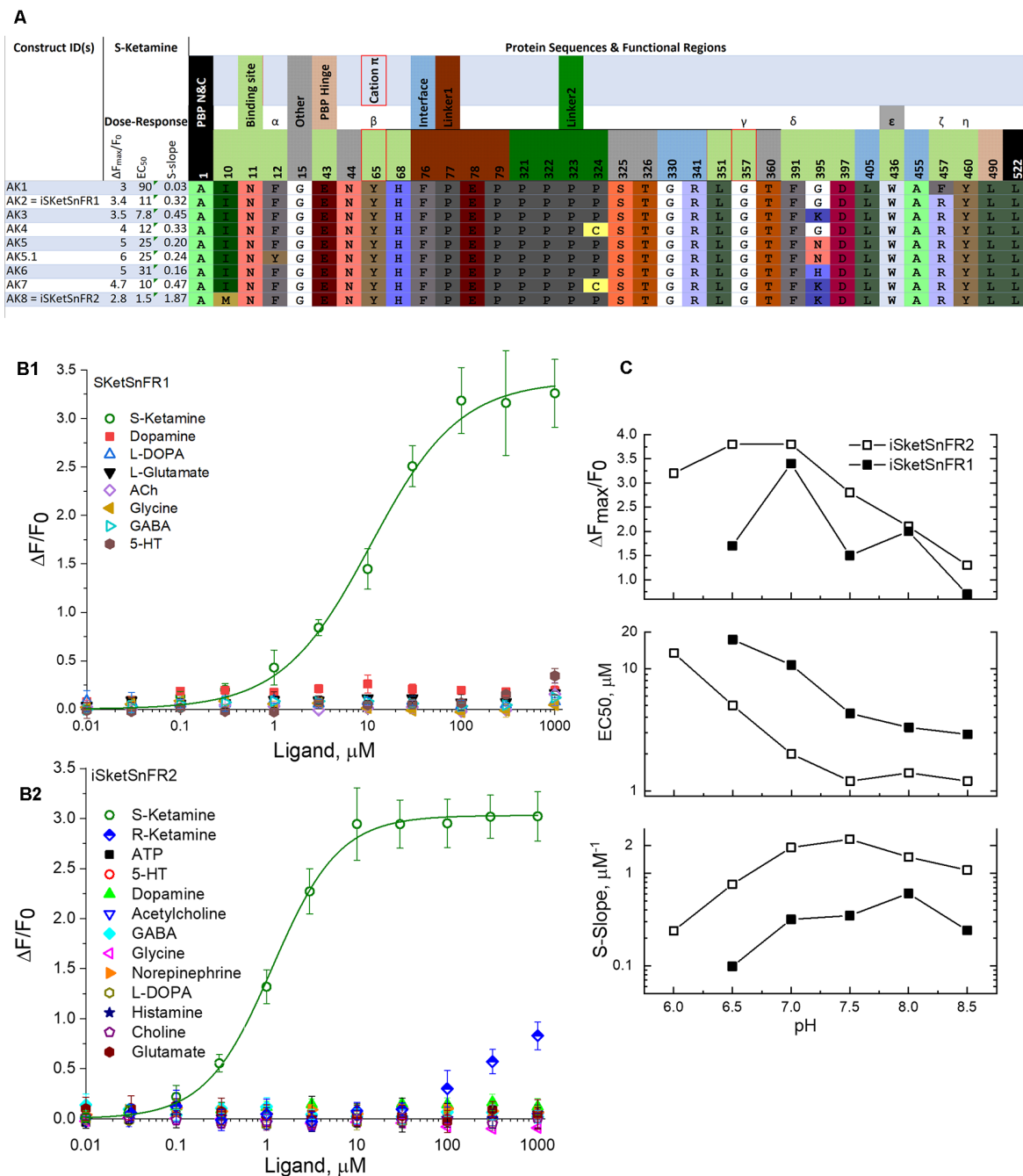
### pH Dependence of iKetSnFRs

Studies of the pH dependence on the GCaMP family provide a mechanistic background for other biosensors that use cpGFP. In the inactive conformation of cpGFP, the fluorophore has a pKa of 8–9, and a second at a higher, only approximately characterized pH. At neutral pH, the fluorophore is almost fully protonated, decreasing the absorption in the band centered at  $\lambda_{\text{ex}} \sim 485 \text{ nm}$  (Barnett et al., 2017). In the active form, the pKa is  $\sim 7$ , so that some of the fluorophore molecules are deprotonated. This allows absorption and fluorescence (Barnett et al., 2017). Possibly both the pH dependence of the biosensor and that of the ligand affect measurements with iKetSnFR1 and iKetSnFR2.

Therefore, in the pH range from 6 to 8.5, we determined the  $\Delta F$  dose-response relations of iKetSnFR1 and iKetSnFR2 using excitation at  $\lambda_{\text{ex}} = 485 \text{ nm}$  (**Figure 2C**). The greatest S-slope occurs at pH 7.0–8.5, resulting from maximal  $\Delta F_{\max}/F_0$  at pH 6.5–7 and an  $EC_{50}$  that decreases monotonically with pH. Both those trends resemble results with the iNicSnFR family (Shivange et al., 2019). For measurements at  $\lambda_{\text{ex}} = 400 \text{ nm}$ , see **Figure 7** below and **Supplementary Figure S2**.

The permanently charged nicotine analog, N'-methylnicotinium, previously provided additional insights for the iNicSnFR family (Shivange et al., 2019). The analogous S-ketamine derivative, N,N-dimethyl-S-ketamine, did not produce robust activation of the iKetSnFR constructs, vitiating experiments to study the possible role of charge at the nitrogen atom. This is consistent with but does not prove a reduced role for cation- $\pi$  interactions between S-ketamine and the biosensor. Regardless of the underlying





**FIGURE 2 |** Sequences, dose-response relations, and pH dependence of iSkeSnFR1, iSkeSnFR2 and related proteins. **(A)** Sequences of eight iKetSnFRs studied. The names iSkeSnFR1 and iSkeSnFR2 correspond to AK2 and AK8. Functional regions of the biosensor protein are shown as stippled cells above the sequences. Regions highlighted include those surrounding the ligand ("binding site"), the interface between the PBP and the cpGFP moiety, the two linker sequences leading from the PBP to the cpGFP, and vice versa, and the PBP hinge. The N- and C-terminal amino acids are also shown. The numbering corresponds to PDB entry 6EFR (Shivange et al., 2019). The cpGFP moiety, not shown, runs from codon 80 to 320. Greek letters denote aromatic groups that were candidates for cation- $\pi$  interactions with the N-atom of the ligand (Shivange et al., 2019), and red borders denote those with the strongest evidence. The residues shown were mutated in this study or in a previous study that generated iNicSnFR biosensors. The background colors for amino acids, similar to those in Jmol, have no chemical meaning but are chosen to provide a wide, distinguishing range of colors. There is no correspondence between the background color of the stippled entries and the background color for the codons. **(B1)** Dose-response relations for purified iSkeSnFR1, studied for various ligands at pH 7.0, 3 $\times$  phosphate-buffered saline (PBS; Shivange et al., 2019). The data for S-ketamine have been fitted to the Hill equation,  $\Delta F_{max}/F_0 = 3.4 \pm 0.1$  and  $EC_{50} = 10.7 \pm 1.5 \mu M$ , Hill coefficient ( $n_H$ ) =  $0.91 \pm 0.09$ .

(Continued)

**FIGURE 2 | Continued**

The other seven ligands tested yielded responses that were too small for systematic study. **(B2)** Dose-response relations for purified iSketSnFR2, studied for various ligands at pH 7.0, 3× PBS (Shivange et al., 2019). The data for S-ketamine have been fitted to the Hill equation,  $\Delta F_{\max}/F_0 = 3.0 \pm 0.3$  and  $EC_{50} = 1.16 \pm 0.6 \mu\text{M}$ , Hill coefficient ( $n_H$ ) =  $1.18 \pm 0.07$ . The other 12 ligands tested yielded responses that were too small for systematic study. **(C)** Dose-response parameters at varying pH values between 6.0 and 8.5, for S-ketamine at purified iSketSnFR1 and iSketSnFR2. Data are included for curve fits that gave  $n_H$  values between 0.75 and 1.2 and  $EC_{50}$  values < 50  $\mu\text{M}$ . The plots show that iSketSnFR2 has the most favorable S-slope at all pH values studied, because of both its lower  $EC_{50}$  and its higher  $\Delta F_{\max}/F_0$ .

mechanism, the data suggest that the pH dependence of iSketSnFR1 and of iSketSnFR2 is dominated by that of the cpGFP moiety rather than by that of the weakly basic ligand, S-ketamine.

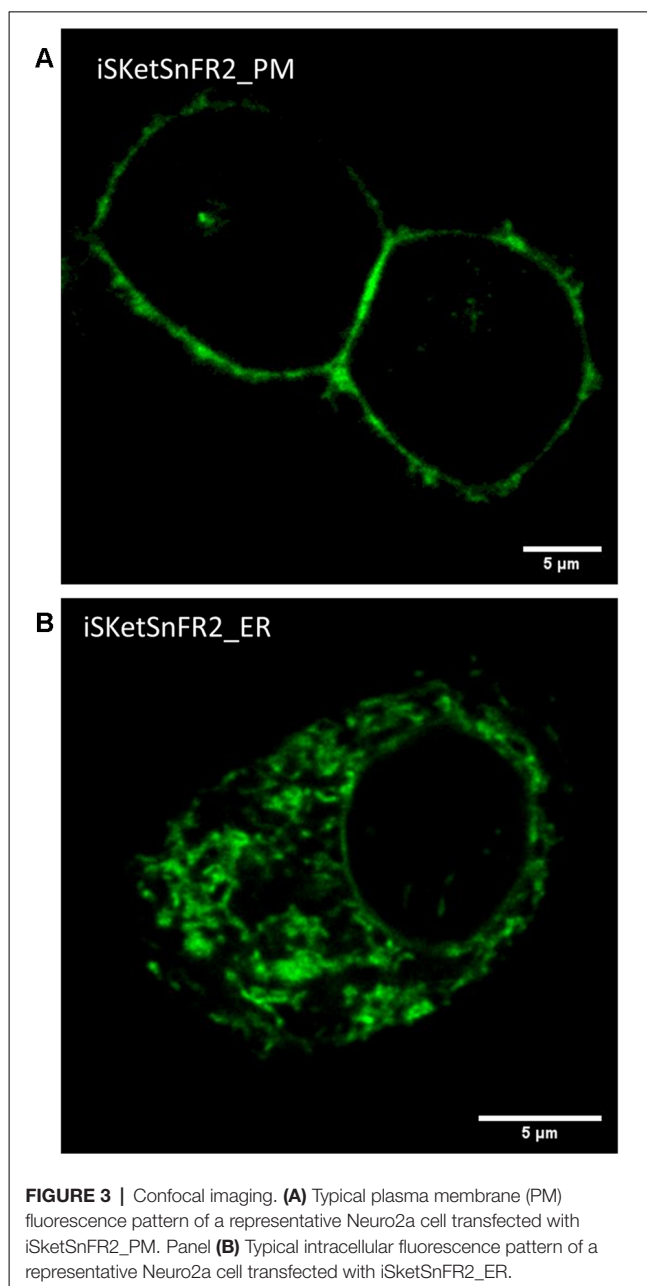
### The \_PM and \_ER Constructs Reach the Intended Organelles

We examined the subcellular localization of the iSketSnFR2\_PM and iSketSnFR2\_ER constructs, using confocal microscopy (**Figure 3**). The iSketSnFR2\_PM construct shows the expected localization at the cell periphery (**Figure 3A**). The iSketSnFR2\_ER construct shows the expected intracellular localization, including the nuclear lamina (**Figure 3B**). Neuro2a cells are not ideal for distinguishing among organelles, and it is possible that some fluorescence arises from localization in both the ER and Golgi. For both the iSketSnFR2\_PM and iSketSnFR2\_ER constructs, we noted clear increases in fluorescence when we added 1.5  $\mu\text{M}$  S-ketamine. We described this increase systematically in the specialized, time-resolved, albeit lower-resolution imaging experiments presented below. Similar images were obtained for iSketSnFR1\_PM and iSketSnFR1\_ER.

### Time-Resolved Responses to S-Ketamine in Live Cells

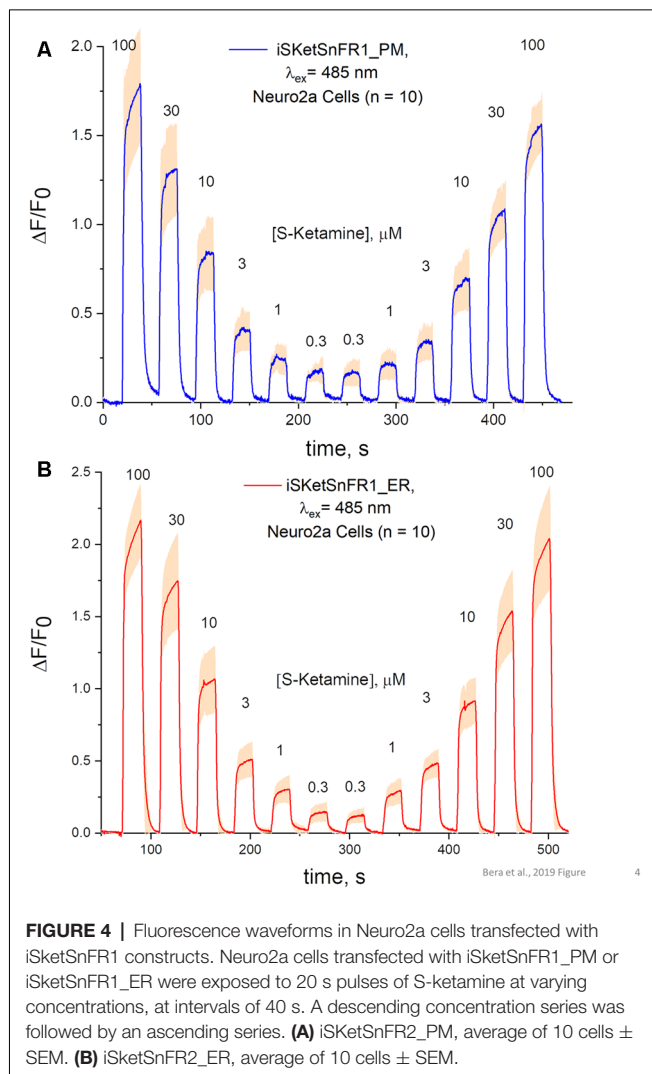
The S-slope of iSketSnFR1 for S-ketamine roughly equals that of nicotine for iNicSnFR3a and iNicSnFR3b. As expected from this similarity, iSketSnFR1 provided meaningful time-resolved dose-response relations for S-ketamine, at concentrations >1  $\mu\text{M}$  (**Figure 4**). Transfected Neuro2a cells readily displayed  $\Delta F$  within a few seconds after the external solution was switched to one containing S-ketamine; and the fluorescence decreased to baseline within a few seconds after the external solution was switched to a ketamine-free solution. The half-maximal concentration of S-ketamine is  $\sim 10 \mu\text{M}$ , near the concentration measured with purified protein.

The rapid antidepressant effects of S-ketamine occur after peak blood plasma concentrations of 0.2–1  $\mu\text{M}$ , and free brain concentration of S-ketamine may be similar (Lester et al., 2012; Janssen Research and Development, 2019). Although the Hill coefficient near unity implies that measurement at [S-ketamine] >1  $\mu\text{M}$  can be linearly extrapolated to provide meaningful insights for lower [S-ketamine], we sought direct measurements at the pharmacologically relevant [S-ketamine]. Our most powerful and sensitive tool for such a study is



iSketSnFR2, with its S-slope of  $1.9 \mu\text{M}^{-1}$  at purified protein. Transfected Neuro2a cells readily displayed measurable  $\Delta F$  within a few seconds after the external solution was switched to an S-ketamine solution; and the fluorescence decreased to baseline within a few seconds after the external solution was switched to a ketamine-free solution (**Figure 5**). We plotted data for [S-ketamine]  $\leq 1 \mu\text{M}$ , which is less than the  $EC_{50}$  measured with purified iSketSnFR2 protein. This ensures that our measurements remain on the linear part of a conventional dose-response relation. Summarizing our experiments on cells expressing targeted iSketSnFR2 constructs for [S-ketamine] <1  $\mu\text{M}$ , iSketSnFR2\_PM displayed an S-slope =  $0.42 \pm 0.14 \mu\text{M}^{-1}$  (mean  $\pm$  SD, 25 total cells from

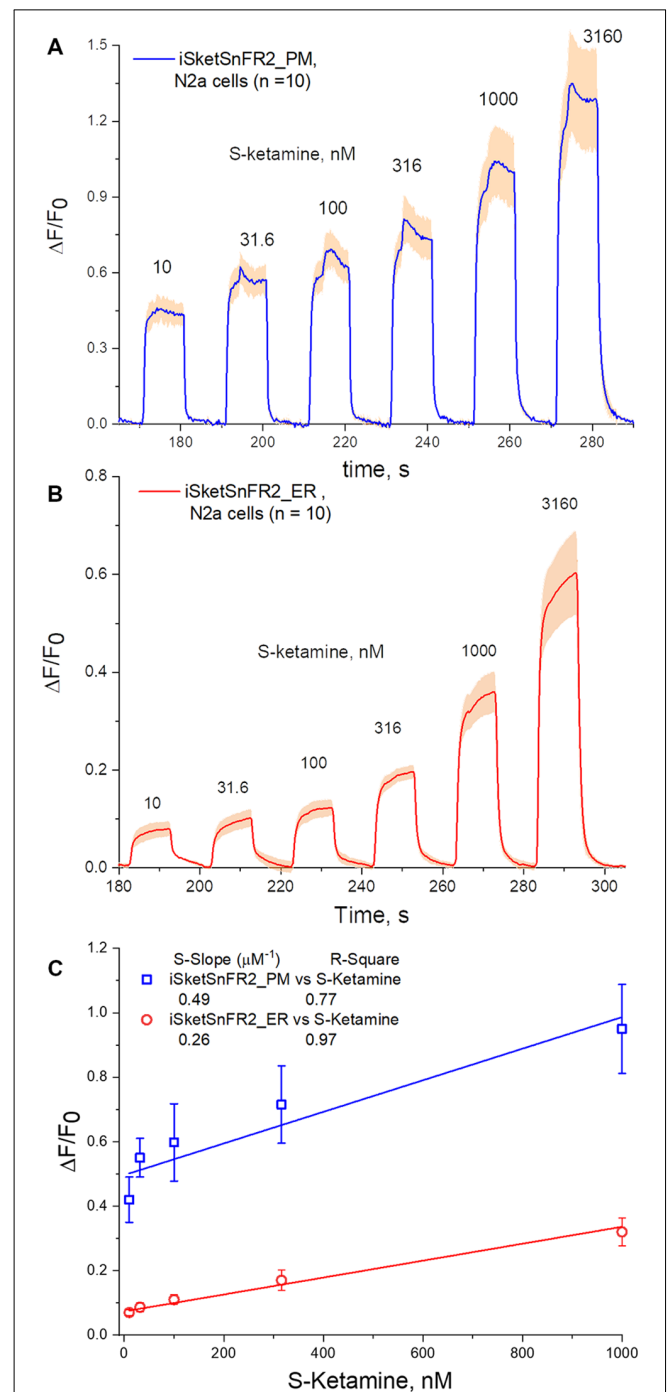




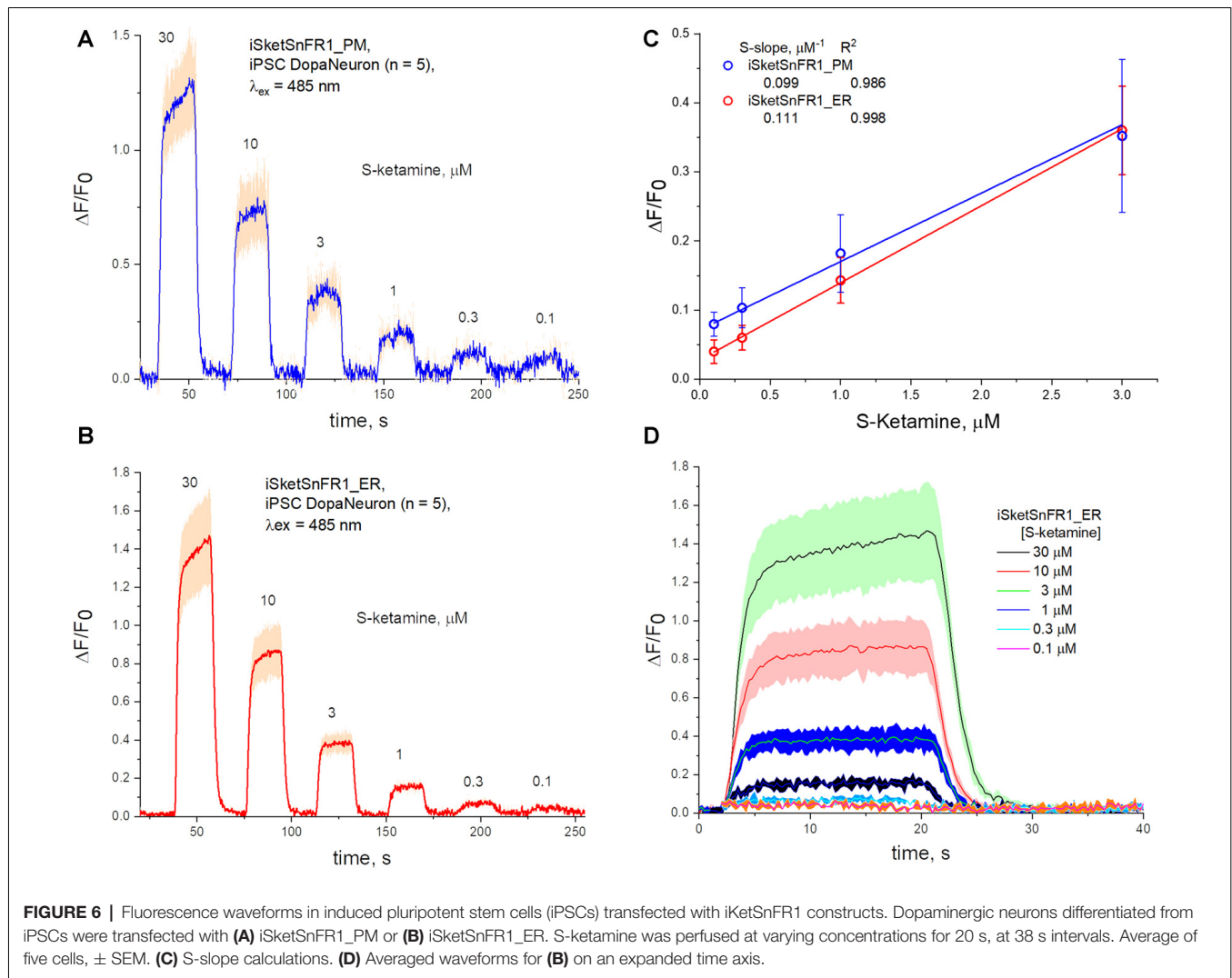
two independent transfections) and iSketSnFR\_ER displayed an S-slope =  $0.29 \pm 0.04 \mu\text{M}^{-1}$  (mean  $\pm$  SD, 25 total cells from two independent transfections). These S-slopes do not differ significantly.

### Time-Resolved Responses to S-Ketamine in iPSC-Derived Dopaminergic Neurons

We also studied iPSCs differentiated to become dopaminergic neurons (Shivange et al., 2019) and transfected with either iSketSnFR1\_PM or iSketSnFR1\_ER. In these cells, responses to S-ketamine appeared and decreased within just a few seconds after jumps in the extracellular S-ketamine concentration (Figure 6), resembling the results in Neuro2a cells. Responses increased linearly with concentration when we applied S-ketamine at concentrations  $<$  the  $\text{EC}_{50}$  (Figure 6). The experimentally determined S-slope for iSketSnFR1\_PM was  $0.1 \mu\text{M}^{-1}$ , or  $\sim 4$ -fold lower than the value measured for iSketSnFR2\_PM in Neuro2a cells. Importantly, iSketSnFR1\_ER constructs in iPSCs displayed an S-slope only slightly greater than that of the iSketSnFR1\_PM construct.



S-slopes measured for PM and ER constructs in cells are several fold lower than for purified iSketSnFR proteins, as also observed for iNicSnFR constructs (Shivange et al.,



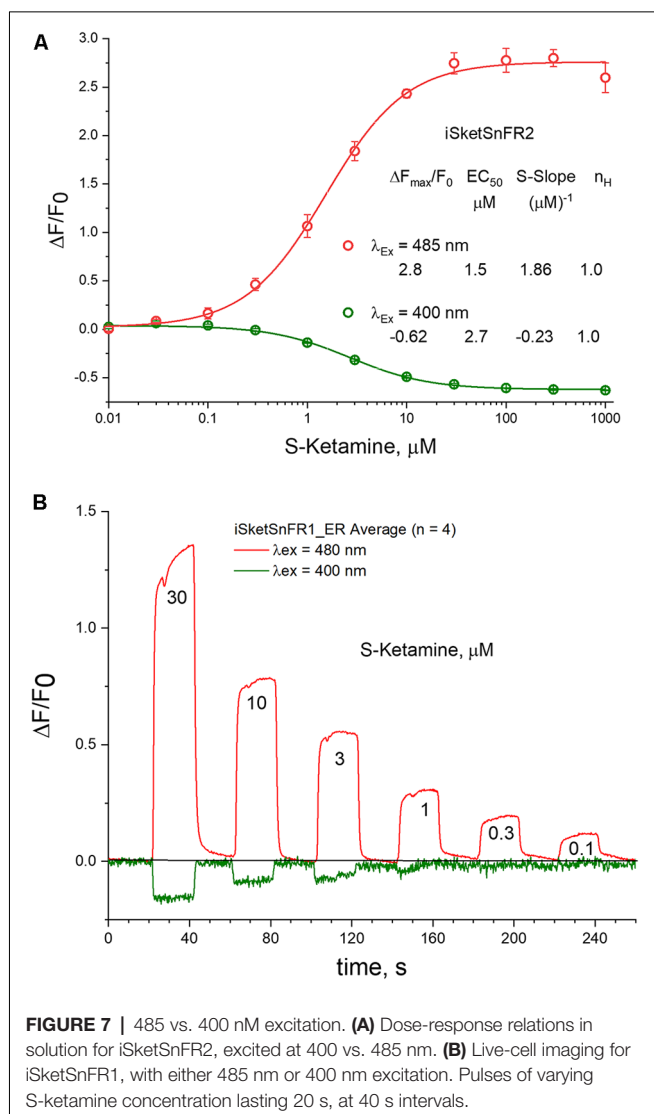
2019). Furthermore, S-slopes measured in cells for iSketSnFR2 constructs are  $\sim$ 2- to 4-fold higher than for iSketSnFR1, rather than 5.8-fold higher as measured for the purified biosensor proteins. Both these differences presumably arise because cellular experiments have appreciable contributions to  $F_0$  from other fluorescent molecules. Further experiments with various optical arrangements and with various cell types are required. The major conclusion is that, for two cell types and for two iSketSnFR biosensor proteins, the ER S-ketamine concentration follows the extracellular concentration, within a few seconds and within 2-fold.

### Excitation at 400 nm vs. 485 nm

Previous studies indicate that cpGFP-based sensors can also provide information when excited at 400 nm (Barnett et al., 2017). In tests at pH 7, we found that the  $EC_{50}$  is not markedly different at 400 and 485 nm, as though measurements are detecting a common binding and conformational change event (Figure 7A). The S-slope at pH 7 is  $-0.23$ , some 7-fold lower than at 485 nm (and opposite in sign). With iSketSnFR1\_ER,

we tested whether one can monitor S-ketamine entry into the ER at  $\lambda_{ex} = 400$  nm, even though the lower S-slope produces a lower signal-to-noise ratio. As shown in Figure 7B, this is possible, but only at [S-ketamine] in the higher range of the dose-response relation.

In measurements on purified iSketSnFR2, we compared the pH sensitivity for measurements at  $\lambda_{ex} = 400$  nm and at  $\lambda_{ex} = 485$  nm. We confirmed that the  $EC_{50}$  for S-ketamine does remain approximately equal when tested at  $\lambda_{ex} = 400$  nm vs. 485 nm, increasing at lower pH (compare Figure 2C vs. Supplementary Figure S2). A similar trend was previously noted for iNicSnFR3a. This trend is opposite to the expectation for a response limited only by the fraction of protonated ligand in the solution (Shivange et al., 2019). Therefore, we restate the previous suggestion that the pH dependence of S-ketamine measurements with iSketSnFR sensors is dominated by the pH sensitivity of the biosensor protein, not of the S-ketamine ligand. Because of this sensitivity, the [S-slope] for  $\lambda_{ex} = 400$  nm becomes quite small at pH  $< 7$ , never exceeding 0.3 even for iSketSnFR2 (Supplementary Figure S2).



## DISCUSSION

### S-Ketamine in Organelles

As pointed out in the “Introduction” section, in the absence of well-established information about a drug’s target, one needs to know which compartments a drug enters, how quickly, and at what concentrations. The present study establishes that S-ketamine enters the ER within a few seconds after appearing near cells, then leaves within a few seconds after S-ketamine is removed from the extracellular space. The S-ketamine concentration in the ER is less than 2-fold different from that in the extracellular solution. These conclusions arise from data on two biosensor constructs (iSketSnFR1, iSketSnFR2) and on two cell types (Neuro2a and human dopaminergic neurons differentiated from iPSCs).

A previous report shows that ketamine enters cells (Emnett et al., 2016). The pharmacological role of entry into organelles may differ between nicotine and S-ketamine; the former was studied in a previous article on ER permeation (Shivange et al.,

2019). For nicotine, the ER is a major compartment relevant for pharmacological chaperoning and upregulation—the early stages of nicotine dependence (Henderson and Lester, 2015). For S-ketamine, if target engagement occurs in an organelle rather than on the PM, that organelle is still unknown. The sigma-1 receptor, a binding site for both R-ketamine and S-ketamine, occurs in the ER (Su, 2019).

Other organelles should also be considered as possible compartments for target engagement by S-ketamine. In 1974, it was first pointed out that weak bases accumulate, perhaps by factors of 100, in lysosomes and other acidic compartments (de Duve et al., 1974). In one suggestion, the relevant compartment(s) for S-ketamine are acidic vesicles (Lester et al., 2015; Stenovec et al., 2019). Uncertainties about the relevant acidic vesicles imply that the relevant pH is between 4.5 (lysosomes) and 5.5 (synaptic vesicles). Further uncertainties about ketamine permeability in the charged state allow for a wide range of intraluminal [S-ketamine] (Trapp et al., 2008). Therefore, it will be important to study intraluminal S-ketamine concentration directly.

The pharmacokinetic literature points out that lysosomes (pH ~4.5), representing just ~1% of a cell’s volume, would accumulate as much weakly basic drug as the entire cytoplasm (Smith et al., 2012). Antipsychotic drugs, which are also weak bases, accumulate in synaptic vesicles (pH ~5.5), and their release by pre-synaptic action potentials has both pre- and post-synaptic consequences (Trapp et al., 2008; Tischbirek et al., 2012; Tucker et al., 2015; Walters and Levitan, 2019). The present data provide the foundation for modifications of iSketSnFR1 and iSketSnFR2 that also function in acidic vesicles.

### Other Candidate Ketamine Analogs and Metabolites

Candidate rapidly acting antidepressants include R-ketamine, as well as metabolites such as (2R, 6R)-hydroxynorketamine (HNK) and (2S, 6S)-HNK. Scopolamine also has rapid antidepressant actions (Wohleb et al., 2016). Biosensors tested in our experiments do respond, though quite weakly, to several of these compounds (Supplementary Figure S3). In previous experiments, the iNicSnFR series was “evolved” from initial biosensors characterized by an S-slope of  $\sim 10^{-5}$  (Shivange et al., 2019). The strategy we describe could conceivably be extended to these ligands.

### Technical Considerations for Drug Biosensors

We comment on developing “iDrugSnFRs,” biosensors for synthetic and endogenous drugs. To some extent, the considerations differ from biosensors for endogenous neurotransmitters. For comparisons among intensity-based biosensors such as PBP-based or G protein-coupled receptor (GPCR)-based constructs, this article emphasizes the S-slope, a single metric that summarizes the beginning of the dose-response relation. The S-slope is simply  $\Delta F_{\max}/F_0$  divided by the  $EC_{50}$ . The S-slope has dimensions,  $\mu M^{-1}$ . Use of the S-slope has the following advantages.

(1) In our experience with isolated cells and *in vivo* systems, two factors usually render it desirable to follow the time course of relatively low drug concentrations. First, the pharmacological half-maximal dose is often less than the  $EC_{50}$  that characterizes the fluorescence. The S-slope describes sensitivity in the appropriate concentration range. Second, a full dose-response relation, in organelles of live cells, can be complicated if higher drug concentrations inhibit transporters, short-circuit proton gradients, or saturate buffers.

(2) An increased S-slope [pedantically, an increased (S-slope)] denotes an increased sensitivity. Interference by other drugs or neurotransmitters (again, at rather low concentrations) can be simply stated as the ratio of the S-slopes. This is an useful comparison if either  $EC_{50}$ , or  $\Delta F_{max}/F_0$ , or both vary among ligands. In the case of iSketSnFR1 and iSketSnFR2, all other ligands we measured have  $\Delta F$  responses so low that an S-slope can be approximately determined only by extrapolation at higher concentrations (Supplementary Figure S3). R-ketamine, another ligand of interest which gives detectable responses at concentrations  $>100 \mu M$ , has an S-slope at least 100-fold lower than S-ketamine at iSketSnFR2.

This article shows that S-slope comparisons between data on purified proteins have some predictive value. However, the S-slopes in cells, between iSketSnFR1 and iSketSnFR2, differed by smaller factors than those measured with purified protein, presumably because in cells, endogenous fluorescent molecules increase the  $F_0$  values.

(3) Use of a single parameter allows one to estimate the lowest analyte concentration observable, especially if one has characterized the fluorescence measurements in one's imaging instruments. In isolated cells, which have favorable fluorescence properties, we find that our instruments allow  $\Delta F/F_0$  values of 0.1 to be resolved readily. Therefore, an S-slope of 0.3, 1, 3, or 10 (Shivange et al., 2019) allows measurements as low as  $\sim 0.3 \mu M$ ,  $\sim 0.1 \mu M$ , 10 nM, or 3 nM, respectively.

(4) Use of the S-slope is more general than the previous metric,  $\Delta F/F_0$  at 1  $\mu M$  ligand (Shivange et al., 2019). As noted above, this generality allows ready extensions to experiments that use only sub-micromolar concentrations of drugs. The S-slope can also be applied to decreases in fluorescence, for instance at 400 nm excitation (Figure 7). Because fluorescence cannot become less than zero,  $\Delta F/F_0$  can never become more negative than  $-1$ . However,  $EC_{50}$  can become so small that S-slope values become more negative than  $-1 \mu M^{-1}$ .

Use of the S-slope does require simplifications that occur with both PBP-based and GPCR-based fluorescent biosensors. These simplifications may not occur with less direct sensors such as those that measure Ca fluxes (Ding et al., 2019) or gene activation (Bick et al., 2017). One simplification appropriate to both PBP-based and GPCR-based biosensors: the Hill slope is near unity, so that responses  $<$  the  $EC_{50}$  remain linear with the [drug].

Straightforward choices based solely on the S-slope are possible because here, as in Shivange et al. (2019), the binding and conformational changes are rapid enough to eliminate concerns caused by the response of the sensor itself. However, very low  $K_d$  would depart from this experience. In the simplest view, the

equilibrium  $EC_{50}$  ( $K_d$ ) is a ratio of two (possibly composite) kinetic steps, characterized phenomenologically as  $K_d = k_{off}/k_{on}$ . In our experience,  $k_{on}$  values for OpuBC-based biosensors are  $\sim 10^7/M/s$  (Shivange et al., 2019). Therefore,  $K_d$  values  $< 10^{-7} M$  (100 nM) are accompanied by  $k_{off} < 1/s$ . Such values would produce a "lag" of  $>1 s$  between the drug concentration and the fluorescence response.

An important final assumption is that *in vitro* and *in vivo* measurements occur at the same pH. The S-slope does vary with pH, because both its numerator and denominator vary with pH (Figure 2C, Supplementary Figure S2; Barnett et al., 2017; Shivange et al., 2019). We would like to extend the iDrugSnFR measurements to acidic organelles. With PBP-GFP-based iDrugSnFRs, this is not yet possible: the S-slope approaches zero.

## Prospects for Developing Improved Rapidly Acting Antidepressants

Knowing that S-ketamine enters organelles will not in itself develop a new  $\sim 24 h$  antidepressant drug. Nonetheless, such data can help test whether novel mechanisms, such as action on intra-organellar targets and subcellular pharmacokinetics, must be considered in developing such drugs. Researchers may wish to test the subcellular pharmacokinetics, targets, compartment of target engagement, and downstream signaling events of other candidate drugs as rapidly acting antidepressants.

## DATA AVAILABILITY STATEMENT

The datasets generated for this study are available on request to the corresponding author.

## AUTHOR CONTRIBUTIONS

KB, AK, AS, PB, IB, TC, AM, SG, CK and JM: performed experiments. KB, AK, AS, AM, AN, JJ, EL, BC, JM and HL: analysis. BC, JM, LL and HL: research direction. EU and LT: constructs. AN, BC, KB, EL, LL and HL: manuscript preparation and revision. LL, KB and HL: funding.

## FUNDING

This research was supported by grants from US National Institutes of Health (GM123582, MH120823, DA046122, NS090604, NS013522, MH107056), the California Institute for Regenerative Medicine (EDUC2-08398), the Brain and Behavior Research Foundation (NARSAD), the Della Martin Foundation, the Howard Hughes Medical Institute, the Caltech  $Ca^{2+}$  program, Caltech SURF donors David and Karen Rossum, and the Mistletoe Foundation.

## ACKNOWLEDGMENTS

Jacob P. Keller: advice on pH and tubing. Laura Luebbert: help with experiments. Luke L. Lavis: synthesis of N,N-dimethyl-S-ketamine. Michael Maher: advice on ketamine.



Anindya Bhattacharya: advice on ketamine. Daniel Wagenaar: construction of LED light sources. Lauren M. Barnett: advice on photochemistry. Eric R. Schreiter: biosensors. Jonathan Wang: technical help. Margaret Jefferies and Purnima Deshpande: excellent lab management at Janelia and Caltech.

## REFERENCES

- Adaikkan, C., Taha, E., Barrera, I., David, O., and Rosenblum, K. (2018). Calcium/calmodulin-dependent protein kinase II and eukaryotic elongation factor 2 kinase pathways mediate the antidepressant action of ketamine. *Biol. Psychiatry* 84, 65–75. doi: 10.1016/j.biopsych.2017.11.028
- Autry, A. E., Adachi, M., Nosyreva, E., Na, E. S., Los, M. F., Cheng, P. F., et al. (2011). NMDA receptor blockade at rest triggers rapid behavioural antidepressant responses. *Nature* 475, 91–95. doi: 10.1038/nature10130
- Barnett, L. M., Hughes, T. E., and Drobizhev, M. (2017). Deciphering the molecular mechanism responsible for GCaMP6m's  $\text{Ca}^{2+}$ -dependent change in fluorescence. *PLoS One* 12:e0170934. doi: 10.1371/journal.pone.0170934
- Berman, R. M., Cappiello, A., Anand, A., Oren, D. A., Heninger, G. R., Charney, D. S., et al. (2000). Antidepressant effects of ketamine in depressed patients. *Biol. Psychiatry* 47, 351–354. doi: 10.1016/s0006-3223(99)00230-9
- Beurel, E., Song, L., and Jope, R. S. (2011). Inhibition of glycogen synthase kinase-3 is necessary for the rapid antidepressant effect of ketamine in mice. *Mol. Psychiatry* 16, 1068–1070. doi: 10.1038/mp.2011.47
- Bick, M. J., Greisen, P. J., Morey, K. J., Antunes, M. S., La, D., Sankaran, B., et al. (2017). Computational design of environmental sensors for the potent opioid fentanyl. *Elife* 6:e28909. doi: 10.7554/elifesciences.28909
- Blanpied, T. A., Boeckman, F. A., Aizenman, E., and Johnson, J. W. (1997). Trapping channel block of NMDA-activated responses by amantadine and memantine. *J. Neurophysiol.* 77, 309–323. doi: 10.1152/jn.1997.77.1.309
- Buisson, B., and Bertrand, D. (1998). Open-channel blockers at the human  $\alpha 4\beta 2$  neuronal nicotinic acetylcholine receptor. *Mol. Pharmacol.* 53, 555–563. doi: 10.1124/mol.53.3.555
- Chen, X., Shu, S., and Bayliss, D. A. (2009). HCN1 channel subunits are a molecular substrate for hypnotic actions of ketamine. *J. Neurosci.* 29, 600–609. doi: 10.1523/JNEUROSCI.3481-08.2009
- Coates, K. M., and Flood, P. (2001). Ketamine and its preservative, benzethonium chloride, both inhibit human recombinant  $\alpha 7$  and  $\alpha 4\beta 2$  neuronal nicotinic acetylcholine receptors in *Xenopus* oocytes. *Br. J. Pharmacol.* 134, 871–879. doi: 10.1038/sj.bjp.0704315
- de Duve, C., de Barsey, T., Poole, B., Trouet, A., Tulkens, P., and Van Hoof, F. (1974). Commentary. Lysosomotropic agents. *Biochem. Pharmacol.* 23, 2495–2531. doi: 10.1016/0006-2952(74)90174-9
- Ding, K., Han, Y., Seid, T. W., Buser, C., Karigo, T., Zhang, S., et al. (2019). Imaging neuropeptide release at synapses with a genetically engineered reporter. *Elife* 8:e46421. doi: 10.7554/elifesciences.46421
- Emmett, C., Li, H., Jiang, X., Benz, A., Boggiano, J., Conyers, S., et al. (2016). A clickable analogue of ketamine retains NMDA receptor activity, psychoactivity, and accumulates in neurons. *Sci. Rep.* 6:38808. doi: 10.1038/srep38808
- Emmett, C. M., Eisenman, L. N., Taylor, A. M., Izumi, Y., Zorumski, C. F., and Mennerick, S. (2013). Indistinguishable synaptic pharmacodynamics of the N-methyl-D-aspartate receptor channel blockers memantine and ketamine. *Mol. Pharmacol.* 84, 935–947. doi: 10.1124/mol.113.089334
- Frohlich, J., and Van Horn, J. D. (2014). Reviewing the ketamine model for schizophrenia. *J. Psychopharmacol.* 28, 287–302. doi: 10.1177/0269881113512909
- Gideons, E. S., Kavalali, E. T., and Monteggia, L. M. (2014). Mechanisms underlying differential effectiveness of memantine and ketamine in rapid antidepressant responses. *Proc. Natl. Acad. Sci. U S A* 111, 8649–8654. doi: 10.1073/pnas.1323920111
- Hashimoto, K. (2019). Rapid-acting antidepressant ketamine, its metabolites and other candidates: a historical overview and future perspective. *Psychiatry Clin. Neurosci.* 73, 613–627. doi: 10.1111/pcn.12902
- Henderson, B. J., and Lester, H. A. (2015). Inside-out neuropharmacology of nicotinic drugs. *Neuropharmacol.* 96, 178–193. doi: 10.1016/j.neuropharm.2015.01.022
- Janssen Research and Development. (2019). *Esketamine Nasal Spray for Patients with Treatment-resistant Depression*. Available online at: <https://www.fda.gov/media/121377/download>. Accessed August 15, 2019.
- Johnson, J. W., Glasgow, N. G., and Povysheva, N. V. (2015). Recent insights into the mode of action of memantine and ketamine. *Curr. Opin. Pharmacol.* 20, 54–63. doi: 10.1016/j.coph.2014.11.006
- Kapur, S., and Seeman, P. (2001). Ketamine has equal affinity for NMDA receptors and the high-affinity state of the dopamine D2 receptor. *Biol. Psychiatry* 49, 954–957. doi: 10.1016/s0006-3223(01)01110-6
- Kapur, S., and Seeman, P. (2002). NMDA receptor antagonists ketamine and PCP have direct effects on the dopamine D<sub>2</sub> and serotonin 5-HT<sub>2</sub> receptors—implications for models of schizophrenia. *Mol. Psychiatry* 7, 837–844. doi: 10.1038/sj.mp.4001093
- Kille, S., Acevedo-Rocha, C. G., Parra, L. P., Zhang, Z. G., Opperman, D. J., Reetz, M. T., et al. (2013). Reducing codon redundancy and screening effort of combinatorial protein libraries created by saturation mutagenesis. *ACS Synth. Biol.* 2, 83–92. doi: 10.1021/sb300037w
- Lee, R. H., Tseng, T. Y., Wu, C. Y., Chen, P. Y., Chen, M. F., Kuo, J. S., et al. (2012). Memantine inhibits  $\alpha 3\beta 2$ -nAChRs-mediated nitroergic neurogenic vasodilation in porcine basilar arteries. *PLoS One* 7:e40326. doi: 10.1371/journal.pone.0040326
- Lepack, A. E., Fuchikami, M., Dwyer, J. M., Banasr, M., and Duman, R. S. (2014). BDNF release is required for the behavioral actions of ketamine. *Int. J. Neuropsychopharmacol.* 18:pyu033. doi: 10.1093/ijnp/pyu033
- Lester, H. A., Lavis, L. D., and Dougherty, D. A. (2015). Ketamine inside neurons? *Am. J. Psychiatry* 172, 1064–1066. doi: 10.1176/appi.ajp.2015.14121537
- Lester, H. A., Miwa, J. M., and Srinivasan, R. (2012). Psychiatric drugs bind to classical targets within early exocytotic pathways: therapeutic effects. *Biol. Psychiatry* 72, 905–915. doi: 10.1016/j.biopsych.2012.05.020
- Liu, R. J., Fuchikami, M., Dwyer, J. M., Lepack, A. E., Duman, R. S., and Aghajanian, G. K. (2013). GSK-3 inhibition potentiates the synaptogenic and antidepressant-like effects of subthreshold doses of ketamine. *Neuropsychopharmacology* 38, 2268–2277. doi: 10.1038/npp.2013.128
- MacDonald, J. F., Bartlett, M. C., Mody, I., Pappapill, P., Reynolds, J. N., Salter, M. W., et al. (1991). Actions of ketamine, phencyclidine and MK-801 on NMDA receptor currents in cultured mouse hippocampal neurones. *J. Physiol.* 432, 483–508. doi: 10.1113/jphysiol.1991.sp018396
- Marvin, J. S., Borghuis, B. G., Tian, L., Cichon, J., Harnett, M. T., Akerboom, J., et al. (2013). An optimized fluorescent probe for visualizing glutamate neurotransmission. *Nat. Methods* 10, 162–170. doi: 10.1038/nmeth.2333
- Miller, O. H., Yang, L., Wang, C. C., Hargroder, E. A., Zhang, Y., Delpire, E., et al. (2014). GluN2B-containing NMDA receptors regulate depression-like behavior and are critical for the rapid antidepressant actions of ketamine. *Elife* 3:e03581. doi: 10.7554/elifesciences.03581
- Moaddel, R., Abdrakhmanova, G., Kozak, J., Jozwiak, K., Toll, L., Jimenez, L., et al. (2013). Sub-anesthetic concentrations of (R,S)-ketamine metabolites inhibit acetylcholine-evoked currents in  $\alpha 7$  nicotinic acetylcholine receptors. *Eur. J. Pharmacol.* 698, 228–234. doi: 10.1016/j.ejphar.2012.11.023
- Pantoja, R., Rodriguez, E. A., Dibas, M. I., Dougherty, D. A., and Lester, H. A. (2009). Single-molecule imaging of a fluorescent unnatural amino acid incorporated into nicotinic receptors. *Biophys. J.* 96, 226–237. doi: 10.1016/j.bpj.2008.09.034
- Preskorn, S. H., Baker, B., Kolluri, S., Menniti, F. S., Krams, M., and Lenden, J. W. (2008). An innovative design to establish proof of concept of the antidepressant effects of the NR2B subunit selective N-methyl-D-aspartate antagonist, CP-101,606, in patients with treatment-refractory major depressive disorder. *J. Clin. Psychopharmacol.* 28, 631–637. doi: 10.1097/JCP.0b013e31818a6cea

## SUPPLEMENTARY MATERIAL

The Supplementary Material for this article can be found online at: <https://www.frontiersin.org/articles/10.3389/fncel.2019.00499/full#supplementary-material>.

- Ren, Z., Pribiag, H., Jefferson, S. J., Shorey, M., Fuchs, T., Stellwagen, D., et al. (2016). Bidirectional homeostatic regulation of a depression-related brain state by  $\gamma$ -aminobutyric acidergic deficits and ketamine treatment. *Biol. Psychiatry* 80, 457–468. doi: 10.1016/j.biopsych.2016.02.009
- Rueden, C. T., Schindelin, J., Hiner, M. C., DeZonia, B. E., Walter, A. E., Arena, E. T., et al. (2017). ImageJ2: ImageJ for the next generation of scientific image data. *BMC Bioinformatics* 18:529. doi: 10.1186/s12859-017-1934-z
- Seeman, P., and Kapur, S. (2003). Anesthetics inhibit high-affinity states of dopamine D2 and other G-linked receptors. *Synapse* 50, 35–40. doi: 10.1002/syn.10221
- Shivange, A. V., Borden, P. M., Muthusamy, A. K., Nichols, A. L., Bera, K., Bao, H., et al. (2019). Determining the pharmacokinetics of nicotinic drugs in the endoplasmic reticulum using biosensors. *J. Gen. Physiol.* 151, 738–757. doi: 10.1085/jgp.201812201
- Smith, D., Allerton, C., Kalgutkar, A., van de Waterbeemd, H., and Walker, D. (2012). *Pharmacokinetics and Metabolism in Drug Design*. Weinheim: Wiley VCH.
- Srinivasan, R., Henley, B. M., Henderson, B. J., Indersmitten, T., Cohen, B. N., Kim, C. H., et al. (2016). Smoking-relevant nicotine concentration attenuates the unfolded protein response in Dopaminergic neurons. *J. Neurosci.* 36, 65–79. doi: 10.1523/JNEUROSCI.2126-15.2016
- Srinivasan, R., Pantoja, R., Moss, F. J., Mackey, E. D. W., Son, C., Miwa, J., et al. (2011). Nicotine upregulates  $\alpha 4\beta 2$  nicotinic receptors and ER exit sites via stoichiometry-dependent chaperoning. *J. Gen. Physiol.* 137, 59–79. doi: 10.1085/jgp.201010532
- Stenovec, M., Božič, M., Pirnat, S., and Zorec, R. (2019). Astroglial mechanisms of ketamine action include reduced mobility of Kir4.1-carrying vesicles. *Neurochem. Res.* doi: 10.1007/s11064-019-02744-1
- Su, T.-P. (2019). Non-canonical targets mediating the action of drugs of abuse: cocaine at the Sigma-1 receptor as an example. *Front. Neurosci.* 13:761. doi: 10.3389/fnins.2019.00761
- Tischbirek, C. H., Wenzel, E. M., Zheng, F., Huth, T., Amato, D., Trapp, S., et al. (2012). Use-dependent inhibition of synaptic transmission by the secretion of intravesicularly accumulated antipsychotic drugs. *Neuron* 74, 830–844. doi: 10.1016/j.neuron.2012.04.019
- Trapp, S., Rosania, G. R., Horobin, R. W., and Kornhuber, J. (2008). Quantitative modeling of selective lysosomal targeting for drug design. *Eur. Biophys. J.* 37, 1317–1328. doi: 10.1007/s00249-008-0338-4
- Tucker, K. R., Block, E. R., and Levitan, E. S. (2015). Action potentials and amphetamine release antipsychotic drug from dopamine neuron synaptic VMAT vesicles. *Proc. Natl. Acad. Sci. U S A* 112, E4485–E4494. doi: 10.1073/pnas.1503766112
- Walters, S. H., and Levitan, E. S. (2019). Vesicular antipsychotic drug release evokes an extra phase of dopamine transmission. *Schizophr. Bull.* doi: 10.1093/schbul/sbz085
- Widman, A. J., and McMahon, L. L. (2018). Disinhibition of CA1 pyramidal cells by low-dose ketamine and other antagonists with rapid antidepressant efficacy. *Proc. Natl. Acad. Sci. U S A* 115, E3007–E3016. doi: 10.1073/pnas.1718883115
- Wohleb, E. S., Wu, M., Gerhard, D. M., Taylor, S. R., Picciotto, M. R., Alreja, M., et al. (2016). GABA interneurons mediate the rapid antidepressant-like effects of scopolamine. *J. Clin. Invest.* 126, 2482–2494. doi: 10.1172/jci85033
- Wray, N. H., Schappi, J. M., Singh, H., Senese, N. B., and Rasenick, M. M. (2018). NMDAR-independent, cAMP-dependent antidepressant actions of ketamine. *Mol. Psychiatry* doi: 10.1038/s41380-018-0083-8
- Yamakura, T., Chavez-Noriega, L. E., and Harris, R. A. (2000). Subunit-dependent inhibition of human neuronal nicotinic acetylcholine receptors and other ligand-gated ion channels by dissociative anesthetics ketamine and dizocilpine. *Anesthesiology* 92, 1144–1153. doi: 10.1097/0000542-200004000-00033
- Yang, Y., Cui, Y., Sang, K., Dong, Y., Ni, Z., Ma, S., et al. (2018). Ketamine blocks bursting in the lateral habenula to rapidly relieve depression. *Nature* 554, 317–322. doi: 10.1038/nature25509
- Zanos, P., Moaddel, R., Morris, P. J., Riggs, L. M., Highland, J. N., Georgiou, P., et al. (2018). Ketamine and ketamine metabolite pharmacology: insights into therapeutic mechanisms. *Pharmacol. Rev.* 70, 621–660. doi: 10.1124/pr.117.015198
- Zoncu, R., Efeyan, A., and Sabatini, D. M. (2011). mTOR: from growth signal integration to cancer, diabetes and ageing. *Nat. Rev. Mol. Cell Biol.* 12, 21–35. doi: 10.1038/nrm3025

**Conflict of Interest:** LT is the founder of Seven Biosciences.

The remaining authors declare that the research was conducted in the absence of any commercial or financial relationships that could be construed as a potential conflict of interest.

Copyright © 2019 Bera, Kamajaya, Shivange, Muthusamy, Nichols, Borden, Grant, Jeon, Lin, Bishara, Chin, Cohen, Kim, Unger, Tian, Marvin, Looger and Lester. This is an open-access article distributed under the terms of the Creative Commons Attribution License (CC BY). The use, distribution or reproduction in other forums is permitted, provided the original author(s) and the copyright owner(s) are credited and that the original publication in this journal is cited, in accordance with accepted academic practice. No use, distribution or reproduction is permitted which does not comply with these terms.



# Live-Cell Assays for Cell Stress Responses Reveal New Patterns of Cell Signaling Caused by Mutations in Rhodopsin, $\alpha$ -Synuclein and TDP-43

Kevin M. Harlen<sup>1\*</sup>, Elizabeth C. Roush<sup>1</sup>, Joseph E. Clayton<sup>2</sup>, Scott Martinka<sup>1</sup> and Thomas E. Hughes<sup>1\*</sup>

<sup>1</sup>Montana Molecular, Bozeman, MT, United States, <sup>2</sup>BioTek Instruments Inc., Winooski, VT, United States

## OPEN ACCESS

### Edited by:

Shai Berlin,  
Technion Israel Institute of  
Technology, Israel

### Reviewed by:

Rafael Linden,  
Federal University of  
Rio de Janeiro, Brazil  
Takashi Kawashima,  
Weizmann Institute of Science, Israel

### \*Correspondence:

Kevin M. Harlen  
kevin.harlen@gmail.com  
Thomas E. Hughes  
thughes@montanamolecular.com

**Received:** 01 August 2019

**Accepted:** 19 November 2019

**Published:** 18 December 2019

### Citation:

Harlen KM, Roush EC, Clayton JE,  
Martinka S and Hughes TE  
(2019) Live-Cell Assays for Cell  
Stress Responses Reveal New  
Patterns of Cell Signaling Caused by  
Mutations in Rhodopsin,  $\alpha$ -Synuclein  
and TDP-43.  
*Front. Cell. Neurosci.* 13:535.  
doi: 10.3389/fncel.2019.00535

Many neurodegenerative diseases induce high levels of sustained cellular stress and alter a number of cellular processes. To examine how different mutations associated with neurodegenerative disease affect cell stress and signaling, we created live-cell assays for endoplasmic reticulum (ER)-mediated cell stress and second messenger signaling. We first examined neurodegenerative mutations associated with direct ER stress by exploring the effect of rhodopsin mutations on ER stress and  $\text{Ca}^{2+}$  signaling. The rhodopsin P23H mutation, the most common mutation in autosomal dominant Retinitis Pigmentosa (RP), produced increased ER stress levels compared to wild type (WT) rhodopsin. Moreover, this increase in cell stress correlated with blunted  $\text{Ca}^{2+}$  signaling in a stress-dependent manner. Analysis of single-cell  $\text{Ca}^{2+}$  signaling profiles revealed unique  $\text{Ca}^{2+}$  signaling responses exist in cells expressing WT or P23H rhodopsin, consistent with the idea that second messenger signaling is affected by cell stress. To explore the use of the ER-stress biosensor in neurodegenerative diseases that may not have a direct effect on ER-mediated cell stress, we examined how various mutants of  $\alpha$ -synuclein and TDP-43 affected ER stress. Mutants of both  $\alpha$ -synuclein and TDP-43 associated with Parkinson's disease (PD) and Amyotrophic lateral sclerosis (ALS) demonstrated increased ER stress compared to WT proteins. To examine the effect of  $\alpha$ -synuclein and TDP-43 mutants on cellular signaling, we created a second live-cell assay to monitor changes in cAMP signaling during expression of various forms of  $\alpha$ -synuclein and TDP-43. The increased cell stress caused by expression of the mutant proteins was accompanied by changes in phosphodiesterase activity. Both HEK293T and SH-SY5Y cells expressing these proteins displayed a shift towards increased cAMP degradation rates, likely due to increased phosphodiesterase activity. Together these data illustrate how biosensors for cellular stress and signaling can provide nuanced, new views of neurodegenerative disease processes.

**Keywords:** neurodegeneration, Parkinson's disease, unfolded protein response, retinitis pigmentosa, cAMP,  $\text{Ca}^{2+}$ , biosensor, ER stress

## INTRODUCTION

Genetically-encoded fluorescent biosensors are powerful tools that have provided new views of how circuits in the brain operate, and how cells and networks of cells process and respond to stimuli (Chen et al., 2017). Many of these biosensors detect small molecule analytes, like  $\text{Ca}^{2+}$ , cyclic AMP (cAMP) and diacylglycerol (Zhao et al., 2011; Tewson et al., 2012, 2016; Broussard et al., 2014) that change in concentration during cell signaling events. Biosensors of this type are used to monitor events such as G-protein coupled receptor (GPCR) activation or neuronal  $\text{Ca}^{2+}$  signaling. Because they are protein-based, biosensors can be targeted to distinct sub-populations of cells or to specific organelles and subcellular domains (Moore et al., 2016; Pendin et al., 2017), and can be systemically delivered by viral vectors. These features have popularized genetically-encoded biosensors, especially those for  $\text{Ca}^{2+}$  and cAMP (Castro et al., 2014), for use in both *in vitro* as well as *in vivo* models (Chen et al., 2017). Another type of genetically encoded biosensor targets changes to the state of the cell. For example, biosensors for apoptosis (Xu et al., 1998), cell cycle state (Sakaue-Sawano et al., 2008), autophagy (Katayama et al., 2011), and cell stress (Iwawaki et al., 2004; Roy et al., 2017) have been developed to detect broad changes to cellular states. However, these two classes of biosensors are often used in separate assays to examine unique outcomes of either change in cell state or signaling. We reasoned that combining biosensors for cell state with those for cell signaling could provide new insights as to how changes in cell state, such as cell stress, alter cellular signaling.

Neurodegenerative disorders, such as Parkinson's disease (PD), Amyotrophic lateral sclerosis (ALS), and the degenerative blinding disease Retinitis Pigmentosa (RP) all involve cellular stress and occur over the course of many years. Each disease is also linked to changes in second messenger signaling. In RP, rod photoreceptors slowly degrade over time, eventually degrading the cone photoreceptors as well, leading to photoreceptor cell death and blindness (Hartong et al., 2006; Ferrari et al., 2011; Koch et al., 2015). The most common mutation associated with RP is the autosomal dominant P23H mutation within the rhodopsin gene (Ferrari et al., 2011). This rhodopsin mutation is accompanied by changes in  $\text{Ca}^{2+}$  and cyclic GMP (cGMP) signaling, along with increased cell stress triggered by the unfolded protein response (UPR; Arango-Gonzalez et al., 2014; Shinde et al., 2016). In Parkinson's and ALS, unique subpopulations of neurons experience prolonged cell stress before eventually dying (Bosco et al., 2011; Taylor et al., 2016; Maiti et al., 2017). Parkinson's and ALS are characterized by the accumulation of misfolded proteins throughout the cell. However, there is also evidence that the modulation of second messenger signaling levels mediated through GPCR activity may influence disease progression (Xu et al., 2012; Mittal et al., 2017). Furthermore, inhibition of phosphodiesterase activity, which is responsible for the breakdown of cAMP and cGMP, has been demonstrated to preserve dopaminergic neurons in models of PD (Morales-Garcia et al., 2011). Thus, accumulating evidence suggests that

changes in both cell stress and signaling are associated with multiple neurodegenerative diseases.

Imagine the neuron suffering under the load of a misfolded protein for years on end. Which stress pathways are activated and how does it compensate for the stress? Does it still respond to its environment appropriately? Can it still sense the same neurotransmitters and neuromodulators in the same way? Does it still respond to drugs in the same way that the healthy, surrounding cells do? To answer these questions live-cell assays conducted in models of neurodegeneration must be developed. Genetically-encoded biosensors represent useful tools for the development of these assays because of their ability to monitor cellular function in real-time. Multiple biosensors can also be paired to monitor different cellular activities and pathways simultaneously, providing details of cellular function that cannot be assessed by simply monitoring cell death.

Endoplasmic reticulum (ER) stress is associated with multiple neurodegenerative diseases including RP, Parkinson's, and ALS (Shinde et al., 2016; Remondelli and Renna, 2017) and occurs well before cell death, making it an important live-cell assay target. We created an ER-stress biosensor that can be combined with biosensors for second messengers. We then monitored, either simultaneously or orthogonally, changes in cell stress levels and the effects on cellular signaling. To analyze these signaling changes we created two assays. We first examined how the expression of mutant rhodopsin affects ER-stress and  $\text{Ca}^{2+}$  signaling. We show that a blunted  $\text{Ca}^{2+}$  signaling response accompanies increased ER stress in cells expressing the rhodopsin P23H mutant. Next, using mutants of  $\alpha$ -synuclein and TAR DNA binding protein (TDP-43) we created a second live-cell assay that reveals how cAMP signaling is altered under ER stress brought on by expression of these neurodegenerative associated proteins. Together, these results demonstrate the usefulness of live-cell assays utilizing unique genetically-encoded fluorescent biosensors as models to study neurodegenerative disease.

## MATERIALS AND METHODS

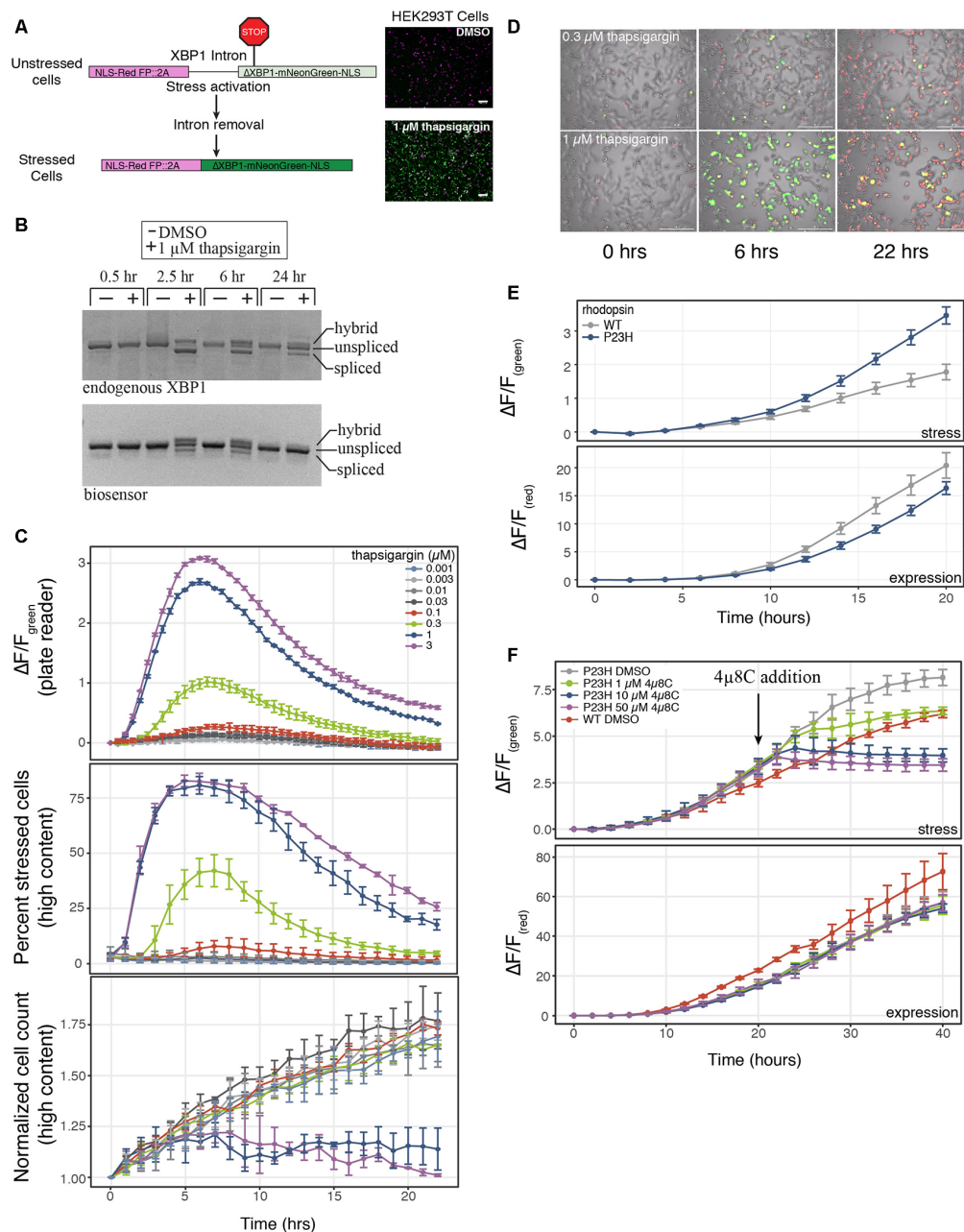
### Biosensor Construction

The ER-stress biosensor was modified from Iwawaki et al. (2004). mNeonGreen was placed downstream of the XBP1 sequence and splice site. SantakaRFP (ATUM FPB-58-609) was placed upstream of the XBP1 sequence (Figure 1A). The SantakaRFP and XBP1-mNeonGreen sequences were separated by a self-cleaving 2A peptide sequence. For the R-GECO-cell stress biosensor SantakaRFP was replaced with R-GECO1.2 (Wu et al., 2013; Figure 3A). Cloning was done using In-Fusion HD cloning (Takara 638911). R-GECO (U0600R), R-cADDIs (U0200R) and bPAC (V0100N) were obtained from Montana Molecular.

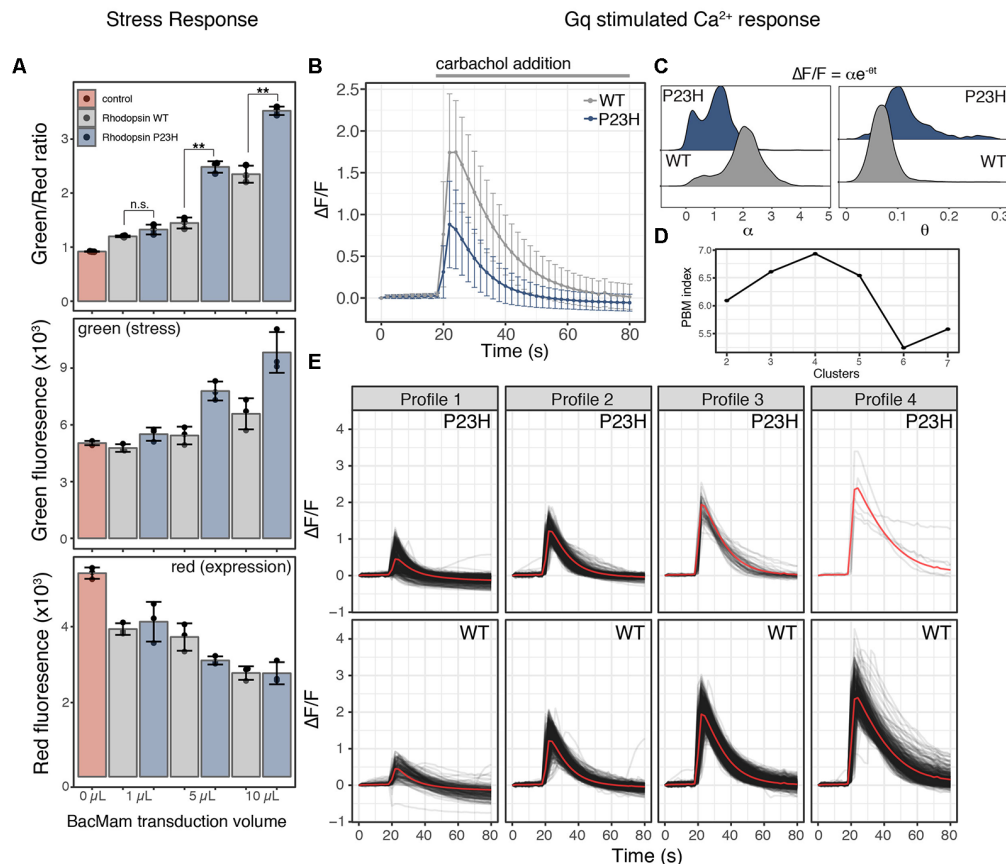
### Chemicals

Sodium butyrate (B5887), valproic acid (P4543), and carbachol (C4382) were obtained from Millipore Sigma. Thapsigargin (10522) and 4 $\mu$ 8C (22110) were obtained from Cayman Chemical.





**FIGURE 1 |** A genetically-encoded fluorescent biosensor to detect endoplasmic reticulum (ER)-mediated cell stress. **(A)** Schematic of the two-color cell stress biosensor. The biosensor is polycistronic transcript consisting of a nuclear targeted constitutively expressed red fluorescent protein followed by a self-cleaving 2A peptide and a stress-induced nuclear targeted green fluorescent protein (mNeonGreen) fused to a portion of the XBP1 protein ( $\Delta$ XBP1-mNeonGreen). Activation of ER stress through the IRE1 $\alpha$ -XBP1 pathway splices out a portion of the XBP1 mRNA, shifting mNeonGreen into frame. Top: unstressed cells; bottom: stressed cells treated with 1  $\mu$ M thapsigargin. Scale bar = 100  $\mu$ m. **(B)** Reverse-transcription polymerase chain reaction (RT-PCR) agarose gel of the splicing status of either endogenous or biosensor XBP1 transcripts over 24 h. Cells were treated with either DMSO or 1  $\mu$ M thapsigargin. Three bands are present, unspliced XBP1, spliced XBP1 and a hybrid band of spliced and unspliced transcripts (Chalmers et al., 2017). **(C)** HEK293T cells were transduced with the cell stress biosensor and treated with increasing amounts of thapsigargin. Top: the fold change ( $\Delta F/F$ ) in green fluorescence was calculated over 22 h, measured every 30 min on a plate reader. Middle: the percent of stressed cells per image was calculated every hour on a high content imager. Bottom: the normalized cell count per image was calculated every hour on a high content imager. Data are plotted as mean  $\pm$  SD,  $N = 3$  wells per condition. **(D)** Overlay of phase, red fluorescence, and green fluorescence images of HEK293 cells transduced with the cell stress biosensor and treated with 0.3  $\mu$ M and 1  $\mu$ M thapsigargin. Images acquired at 0, 6 and 22 h after treatment, scale bar = 200  $\mu$ m. **(E)** HEK293T cells were transfected with the cell stress biosensor and either wild type (WT) or mutant P23H rhodopsin. The fold change in green and red fluorescence ratio is plotted over 20 h. Fold change in stress response ( $\Delta F/F_{\text{green}}$ ) and expression ( $\Delta F/F_{\text{red}}$ ) is shown. Data are plotted as mean  $\pm$  SD,  $N = 3$  wells per condition. **(F)** After 20 h the cells from (E) were treated with increasing amounts of the IRE1 $\alpha$  inhibitor 4 $\mu$ 8C or DMSO. The fold change in stress response ( $\Delta F/F_{\text{green}}$ ) and expression ( $\Delta F/F_{\text{red}}$ ) were monitored for an additional 20 h.



**FIGURE 2 |** Mutant P23H rhodopsin elicits ER-mediated cell stress and alters  $\text{Ca}^{2+}$  signaling. **(A)** HEK293T cells transduced with the cell stress biosensor and either no protein (control), wild type (WT) rhodopsin or P23H rhodopsin. After 24 h the green, red, and green/red fluorescence ratio were analyzed. Data are plotted as mean  $\pm$  SD,  $N = 3$  wells per condition, \*\* $P$ -value  $< 0.01$ , n.s. = not significant. **(B)** Average profiles of the fold change in cytoplasmic  $\text{Ca}^{2+}$  in cells expressing the R-GECO  $\text{Ca}^{2+}$  biosensor and transduced with 5  $\mu\text{L}$  WT or P23H rhodopsin during stimulation with 30  $\mu\text{M}$  carbachol. Data are plotted as the mean  $\pm$  SD of two wells and 2,125 cells for WT and two wells and 1,023 cells for P23H. **(C)**  $\text{Ca}^{2+}$  signaling profiles from individual cells in **(B)** expressing WT or P23H rhodopsin were fit to equation  $\Delta F/F = \alpha e^{-\theta t}$ , where  $\Delta F/F$  is the fold change in fluorescence,  $\alpha$  is the signaling amplitude,  $\theta$  is the exponential decay rate, and  $t$  is time in seconds. Density plots of the values for  $\alpha$  and  $\theta$  from each cell are shown for WT and P23H expressing cells. **(D)** PBM index score of  $\text{Ca}^{2+}$  signaling profile clusters in WT and P23H rhodopsin expressing cells. A maximum at four clusters indicates  $\text{Ca}^{2+}$  signaling profiles can be best segmented into four distinct profiles. **(E)** Individual  $\text{Ca}^{2+}$  responses from each cell in **(B)** were analyzed and separated into four distinct profiles based on the PBM index score from **(D)**. Each black line represents a single cell; the red line represents the mean response of each profile.

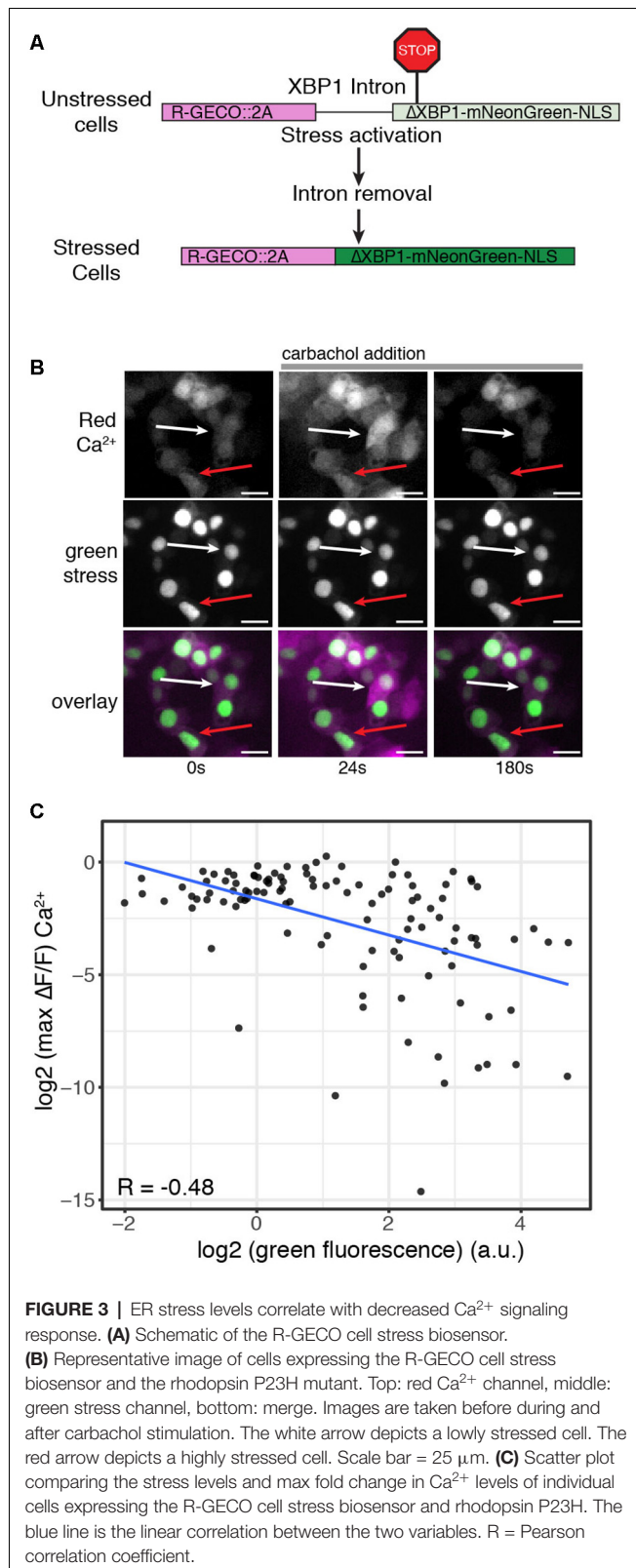
## Cell Culture

HEK293T cells were obtained from ATCC (CRL-11268) and cultured in T-75 flasks at  $37^{\circ}\text{C}$  and 5%  $\text{CO}_2$  in EMEM media (ATCC 30-2003) containing  $1 \times$  Penicillin-Streptomycin (Thermo Fisher Scientific 15140122), supplemented with 10% fetal bovine serum (FBS). SH-SY5Y cells were obtained from ATCC (CRL-2266) and cultured the same as the HEK293T cells except DMEM (ATCC 30-2002) which was used as the base media. For plate reader, experiments cells were cultured in Fluorobrite DMEM (Thermo Fisher Scientific A1896701) containing 4 mM Glutamax (35050061) and 10% FBS (Figure 1), or the media was replaced with DPBS (Figures 2–6). For imaging media was replaced with DPBS containing calcium and magnesium (Thermo Fisher Scientific SH30264.01). For all experiments cells were subcultured at 70–90% confluence and plated onto

96-well poly-D lysine coated microplates (Greiner Bio-One 82050-806).

## Gene Expression

Plasmid transfections were done using Lipofectamine 2000 (Thermo Fisher Scientific 11668019) according to the manufacturer's instructions. Briefly, 0.4  $\mu\text{L}$  of Lipofectamine 2000 per 100 ng of plasmid DNA was added to Opti-Mem reduced serum media (Thermo Fisher Scientific 31985088) to create a final volume of 100  $\mu\text{L}$ . After incubation at room temperature for 20 min all 100  $\mu\text{L}$  of the transfection mix was mixed with 100  $\mu\text{L}$  of HEK293T cells and plated onto a single well of a 96-well microtiter plate. For all transfection experiments, 100 ng of either the cell stress biosensor or the R-GECO-cell stress biosensor plasmids were delivered along with 100 ng of WT or mutant P23H rhodopsin plasmid per



27,000 cells. Four hours later the media was exchanged for 150  $\mu\text{l}$  of Fluorobrite DMEM media. For viral transduction experiments, the following BacMam viruses were used: cell stress

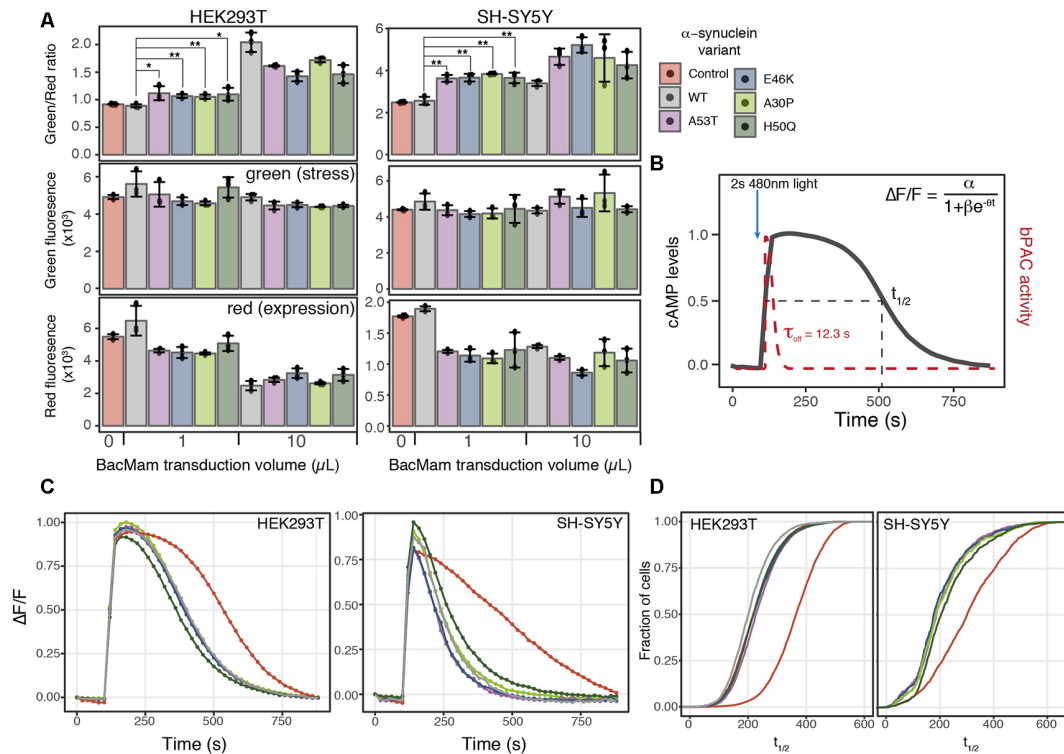
biosensor ( $2 \times 10^{10}$  viral genes (VG)/ml), R-GECO ( $3.1 \times 10^{10}$  VG/ml), bPAC ( $1.18 \times 10^{11}$  VG/ml), R-cADDIs ( $5.06 \times 10^{10}$  VG/ml), rhodopsin,  $\alpha$ -synuclein, and TDP-43 viral titers listed in **Table 1**. For experiments comparing WT and mutant versions of rhodopsin,  $\alpha$ -synuclein, and TDP-43 the viral volume was matched to the titer of the WT protein in the case of rhodopsin and TDP-43 and the A53T mutant of  $\alpha$ -synuclein. For all experiments using BacMam 25  $\mu\text{l}$  of biosensor was transduced per 48,000 cells. When bPAC was used it was transduced at 5  $\mu\text{l}$  per 48,000 cells. For HEK293T cells all transductions were conducted in the presence of 2 mM sodium butyrate and for SH-SY5Y cells all transductions were conducted in the presence of 6 mM valproic acid. After 24 h incubation, the cells were analyzed for cell stress,  $Ca^{2+}$  signaling, or cAMP degradation.

## RT-qPCR

Two wells of a 96-well plate containing 48,000 HEK293T (96,000 total) cells were transduced with either 1 or 10  $\mu\text{l}$  of BacMam virus indicated in **Table 1**. Cells were then incubated for 24 h followed by RNA isolation using *Quick-RNA* Microprep Kit (Zymo Research R1050). cDNA was generated using the M-MLV Reverse Transcriptase kit (Promega M1701) according to the manufacturer's instructions. Quantitative polymerase chain reaction (qPCR) was conducted using Syber select master mix for CFX (Thermo Fisher Scientific 4472942).

## Plate Reader, Imaging and Image Analysis

For the long-term plate reader analyses in **Figure 1**, cells were transfected as described above with the addition of 25 mM HEPES (Thermo Fisher Scientific 15630080) to the media. Cells were analyzed for 20–40 h on a BMG CLARIOstar (**Figure 1C**) or BioTek SynergyMX (**Figures 1E,F**) plate reader, heated to 37°C. Reads with excitation/emission of 485/528 and 558/603 with 20 nm bandpass were taken every 30 min. Data are plotted every 2 h for clarity. High content analysis (**Figures 1C,D**) was conducted on the Lionheart FX Automated Microscope (BioTek Instruments) at 37°C and 5%  $\text{CO}_2$ . HEK293 cells were transduced with 10  $\mu\text{l}$  of the cell stress biosensor per well in Fluorobrite DMEM containing 6 mM valproic acid and plated onto 96-well plates. Twenty-four hours after plating, increasing concentrations of thapsigargin was added to the cells and cells were imaged every hour using a 10 $\times$  objective and the following filter sets, red fluorescence: 531 Ex, 593 Em LED filter cube, green fluorescence: 469 Ex, 525 Em LED filter cube. Images for **Figure 2** were collected on a Zeiss Axiovert 200 using an Olympus UPlanFL 10 $\times$ /0.30 lens and a Teledyne Qimaging 2000R CCD camera. Images were taken every 2 s exciting for 200 ms with a 1A 560 nm LED (Thorlabs DC4100) with a 556/20 Semrock excitation filter and a 617/70 Semrock emission filter. Images for **Figure 3** were acquired on an Olympus IX81 using an Olympus UPlanSApo 20 $\times$ /0.75 lens and a Hamamatsu C9100 EM-CCD camera. Images were acquired every 2 s exciting for 200 ms with a 1A Halogen Exfo X-cite series 120 lamp using the same excitation and emission filters. For all bPAC-RcADDIs imaging in **Figures 4–6**, the Zeiss Axiovert with the 10 $\times$  lens was used. Images were acquired every 20 s using a 100 ms exposure and the 556/20 Semrock excitation filter. After 100 s,



**FIGURE 4 |**  $\alpha$ -synuclein expression induces ER-mediated cell stress and alters PDE activity. **(A)** HEK293T or SH-SY5Y cells were transduced with the cell stress biosensor and either no other virus (control) or 1 or 10  $\mu\text{L}$  of WT  $\alpha$ -synuclein or one of four  $\alpha$ -synuclein mutants. The green, red, and green/red ratio fluorescence were measured after 24 h of expression. Individual data points are plotted and bars represent the mean, error bars represent the standard deviation of  $N = 3$  wells. **(B)** Schematic of optical PDE activity assay. Cells were transduced with the red fluorescent cAMP biosensor R-cADDi and the blue light-activated adenylyl cyclase bPAC. Baseline cAMP levels were monitored prior to bPAC activation to raise cAMP levels. A 2-s pulse of blue light activates bPAC to raise cAMP. bPAC activity decays rapidly and cAMP levels were monitored for 15 min at which point cAMP levels return to baseline. cAMP degradation profiles were fit with the following logistic function  $\Delta F/F = \alpha / (1 + \beta e^{-\theta t})$  for cAMP half-life calculation where  $\Delta F/F$  is the change in fluorescence,  $\alpha$  is the maximum cAMP level,  $\beta e^{-\theta}$  is the exponential decay rate, and  $t$  is time in seconds. **(C)** Average cAMP degradation profiles in HEK293T and SH-SY5Y cells expressing different variants of  $\alpha$ -synuclein or control cells not over-expressing any form  $\alpha$ -synuclein. For HEK293T cells  $N = 3$  wells per sample, control = 4,047 cells, WT = 3,882 cells, A53T = 3,385 cells, E46K = 3,431 cells, A30P = 3,700 cells, H50Q = 3,455 cells. For SH-SY5Y cells  $N = 3$  wells per sample, control = 2,697 cells, WT = 2,427 cells, A53T = 2,775, E46K = 1,462 cells, A30P = 1,902 cells, H50Q = 2,209 cells. **(D)** Cumulative distribution functions plotted for the distribution of cAMP half-lives ( $t_{1/2}$ ) determined from the individual cells analyzed in **(C)**. \* $P$ -value < 0.05, \*\* $P$ -value < 0.01.

the sample was pulsed with blue light for 2 s using a 1A 470 nm LED and a 470/20 Semrock excitation filter. Following this, pulse images were acquired every 20 s as before the pulse. All image analysis was conducted using CellProfiler (McQuinn et al., 2018). Raw images and CellProfiler scripts are available in the supplemental materials.

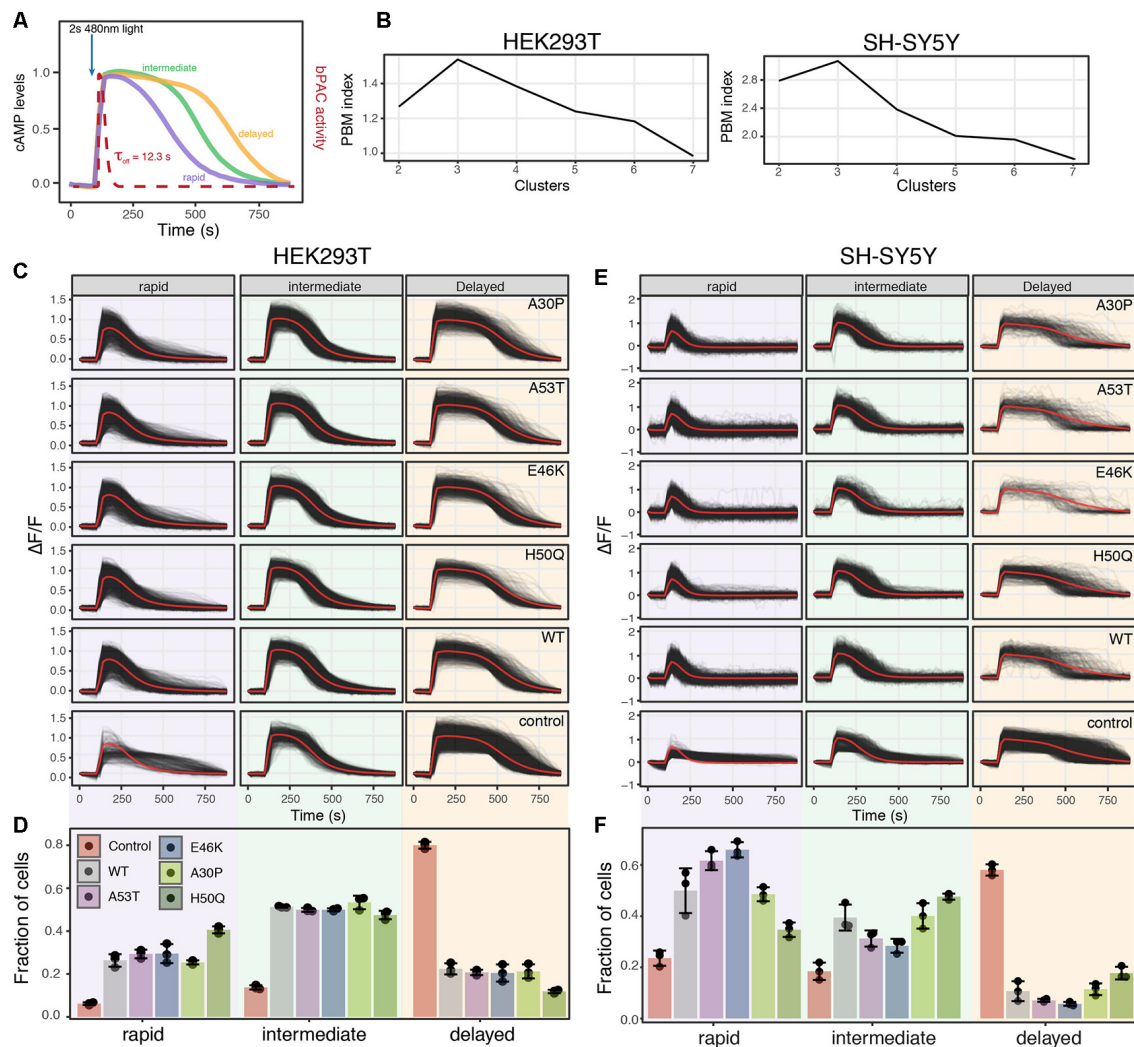
## Statistical Analysis

Where applicable, data are reported as mean  $\pm$  SD of at least three replicates. Either the fold change ( $\Delta F/F$ ) in fluorescence or the percent stressed cells was used to determine cell stress response.  $\Delta F/F$  refers to the fold change in green fluorescence induced by activation of the stress sensor. Percent stressed cells is calculated by dividing the number of cells that display both green and red fluorescence by the total number of cells expressing red fluorescence within a single image. The percent stressed cell analysis was used to analyze high content data in **Figure 1**. For image analysis in **Figures 2–6**, individual cells from

two or three images were analyzed, with the total number of wells and cells listed for each experiment in the figure legends.  $P$ -values were determined using two-tailed equal variance  $t$ -tests.  $\text{Ca}^{2+}$  signaling and cAMP degradation profile analysis was conducted in R<sup>1</sup> using the TSrepr package (Laurinec, 2018). Data were first filtered for a positive increase in cAMP levels after bPAC stimulation by removing cells displaying a  $\Delta F/F$  of less than 0.2. The number of cAMP degradation profiles was determined using the PBM index (Pakhira et al., 2004), identifying the number of clusters that had highest PBM index score. Calculation of the  $\text{Ca}^{2+}$  signaling amplitude and decay were conducted in R. Data from each cell was fit to the following exponential equation,  $\Delta F/F = \alpha e^{-\theta t}$ , where  $\Delta F/F$  is the fold change in fluorescence,  $\alpha$  is the signaling amplitude,  $\theta$  is the exponential decay rate, and  $t$  is time in seconds. The distribution of values for  $\alpha$  and  $\theta$  in cells expressing WT and P23H rhodopsin

<sup>1</sup>www.r-project.org





**FIGURE 5 |** Analysis of PDE activity from individual cells reveals distinct PDE activity profiles. **(A)** Schematic of PDE activity profiles from individual cells revealed three distinct cAMP decay profiles, rapid, intermediate, and delayed. **(B)** PBM index score of cAMP degradation profile clusters in HEK293T and SH-SY5Y cells. Data from control cells or cells expressing WT or a mutant variant of  $\alpha$ -synuclein were merged for analysis. A maximum at three clusters indicates cAMP degradation profiles can be best segmented into three distinct profiles for both HEK293T and SH-SY5Y cells. **(C)** Individual cAMP degradation profiles from control HEK293T cells and HEK293T cells expressing WT or a mutant variant of  $\alpha$ -synuclein. Each black line represents a single cell; the red line represents the mean response of each profile.  $N = 3$  wells per sample, control = 4,047 cells, WT = 3,882 cells, A53T = 3,385 cells, E46K = 3,431 cells, A30P = 3,700 cells, H50Q = 3,455 cells. **(D)** Bar plot of the fraction of cells in each profile for control and  $\alpha$ -synuclein variants from the profiles determined in **(C)**.  $N = 3$  wells for each condition. Individual data points are plotted along with the mean bar and error bars representing the standard deviation. Panels **(E, F)** same as in **(C, D)** but for SH-SY5Y cells.  $N = 3$  wells per sample, control = 2,697 cells, WT = 2,427 cells, A53T = 2,775, E46K = 1,462 cells, A30P = 1,902 cells, H50Q = 2,209 cells.

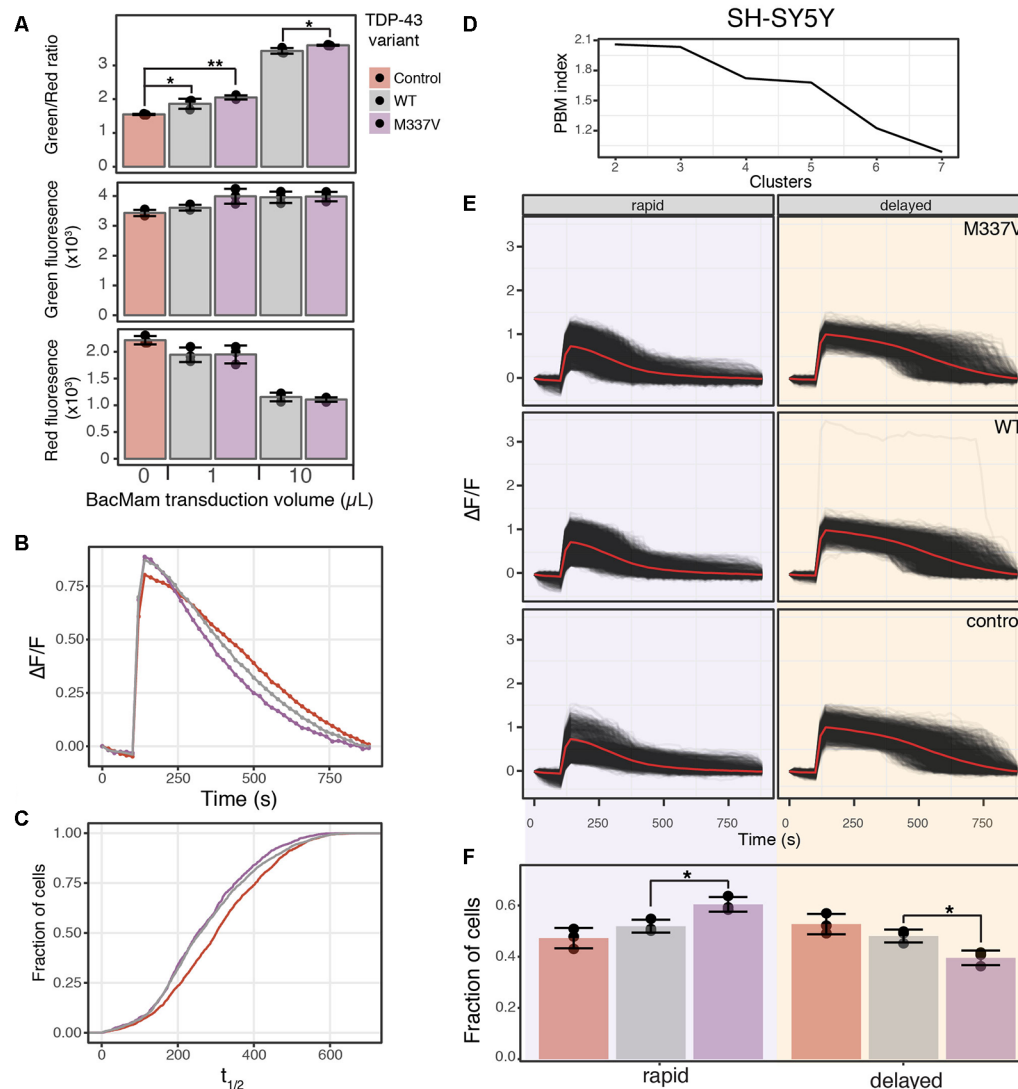
were then plotted. cAMP average profiles for each sample were calculated by average individual cAMP signaling profiles from each cell from three biological replicate images. cAMP half-lives were calculated by first fitting each cAMP degradation profile to following logistic function,  $\Delta F/F = \alpha/(1+\beta e^{-\theta t})$ , where  $\Delta F/F$  is the change in fluorescence,  $\alpha$  is the maximum cAMP level,  $\beta e^{-\theta}$  is the exponential decay rate, and  $t$  is time in seconds. The  $t_{1/2}$  was then calculated for each cell from three biological replicate images. The cumulative distribution function of  $t_{1/2}$  values from each sample was then calculated in R and compared between samples. Note, for both  $\text{Ca}^{2+}$  and cAMP analysis,

the equations were fit to the data after carbachol or bPAC stimulation, respectively.

## RESULTS

### A Genetically-Encoded Reversible Biosensor to Detect Cell Stress

To assay cellular stress responses, we created a genetically encoded live-cell biosensor to detect an ER-mediated stress response through the IRE1 $\alpha$ -XBP1 arm of the UPR. Versions of



**FIGURE 6 |** TDP-43 expression induces cell stress and increases cAMP degradation rate. **(A)** SH-SY5Y cells were transduced with the cell stress biosensor and either no other virus (control), 1 or 10  $\mu$ L of WT or M337V TDP-43 virus. The green, red and green/red ratio fluorescence was measured after 24 h of expression. Individual data points are plotted and bars represent the mean, error bars represent the standard deviation of  $N = 3$  wells. **(B)** Average cAMP degradation profiles in SH-SY5Y cells expressing different variants of TDP-43 or control cells.  $N = 3$  wells per sample, control = 2,697 cells, WT = 3,352 cells, M337V = 3,023 cells. **(C)** Cumulative distribution functions plotted for the distribution of cAMP half-lives ( $t_{1/2}$ ) determined from the individual cells analyzed in **(B)**. To determine  $t_{1/2}$  cAMP, data from each cell were fit to the following equation  $\Delta F/F = \alpha/(1 + \beta e^{-\alpha t})$  with the same parameters as **Figure 4B**. **(D)** PBM index score of cAMP degradation profile clusters in SH-SY5Y cells. Data from control cells or cells expressing WT or M337V versions of TDP-43 were merged for analysis. A maximum at two clusters indicates cAMP degradation profiles can be best segmented into two distinct profiles. **(E)** Individual cAMP degradation profiles from control cells and cells expressing WT or M337V TDP-43. Each black line represents a single cell; the red line represents the mean response of each profile. Well and cell number are the same as **(B)**. **(F)** Bar plot of the fraction of cells in each profile for control and TDP-43 variants from the profiles determined in **(E)**.  $N = 3$  wells for each condition. Individual data points are plotted along with the mean bar and error bars representing the standard deviation. \* $P$ -value < 0.05, \*\* $P$ -value < 0.01.

this type of biosensor have been previously described (Iwawaki et al., 2004; Roy et al., 2017), however, we sought to modify the sensor to adapt it for use in both imaging and plate reader-based assays. Upon detection of misfolded proteins within the lumen of the ER, IRE1 $\alpha$  is activated and carries out an unconventional cytoplasmic splicing of the XBP1 transcript. This splicing leads to a frame shift in the XBP1 open reading frame, creating a functional transcription factor which in turn

activates a host of stress response genes (Grootjans et al., 2016). Similar to previous versions of this biosensor, we co-opted this splicing event to shift into frame a bright green fluorescent protein, mNeonGreen (**Figure 1A**). Also in line with previous XBP1-based biosensors we either removed or maintained key sequence features of the XBP1 protein and fused this sequence to the mNeonGreen portion of the biosensor (Yanagitani et al., 2009; Peschek et al., 2015). These sequence features were either

**TABLE 1** | mRNA transcripts per cell for WT and mutant versions of the genes used in this study.

Protein	Mutation	Viral Titer (VG/ml)	Transduced virus ( $\mu$ l)	mRNA transcripts per cell	**TPM HEK293	Transcripts per cell HEK293	**TPM SH-SY5Y	Transcripts per cell SH-SY5Y
Rhodopsin	WT	$6.73 \times 10^{10}$	1	118.82	*5,592.8	1,118.56	0	0
			10	1,547.71				
			10	2,103.75				
$\alpha$ -synuclein	WT	$5.00 \times 10^{10}$	1	29.17	21.9	4.38	16.2	3.24
			10	667.60				
	A53T	$7.66 \times 10^{10}$	1	139.01				
			10	1,067.81				
	A30P	$7.93 \times 10^{10}$	1	82.52				
			10	989.90				
	E46K	$8.57 \times 10^{10}$	1	62.86				
			10	1,147.50				
TDP-43	WT	$8.77 \times 10^{10}$	1	101.65	151	30.2	167.7	33.54
			10	917.29				
			10	45.51				
	M337V	$7.66 \times 10^{10}$	1	58.62				
			10	36.11				
			10	137.77				

All genes were packaged in BacMam and the viral titer was determined as viral genes (VG) per milliliter. mRNA transcripts per cell were determined by qRT-PCR and compared to endogenous expression levels in HEK293T and SH-SY5Y cells. \*For rhodopsin expression data from the retina was used. \*\*Data obtained from Uhlén et al. (2015). TPM, transcripts per million.

added or removed to create a biosensor that displayed similar activation and termination kinetics to the endogenous UPR. We first removed the DNA binding and basic domains of XBP1 as was done in previous versions of this biosensor (Iwawaki et al., 2004). Removing these domains from XBP1 is important as overexpression of full-length XBP1 inhibits the endogenous UPR response (Lee et al., 2003; Iwawaki et al., 2004). We also removed the leucine zipper domain of XBP1 to decrease the stability of the XBP1-mNeonGreen fusion. The leucine zipper domain is important for maintaining stability and expression of spliced XBP1 during the stress response (Uemura et al., 2013). Unspliced XBP1 protein enhances the degradation of the spliced protein. Binding of UBC9 to the leucine zipper domain inhibits this enhanced degradation (Uemura et al., 2013). By removing this domain from the portion of XBP1 that is fused to mNeonGreen, we created a biosensor that was likely sensitive endogenous UPR regulation. We term this modified XBP1-mNeonGreen fusion  $\Delta$ XBP1-mNeonGreen. We also added a constitutively expressed red fluorescent protein upstream of the XBP1 intron to identify cells expressing the biosensor and as an indicator for protein expression levels. A self-cleaving 2A peptide was placed between the red and green fluorescent proteins to uncouple changes in protein expression from changes in ER-mediated cell stress. Finally, we targeted both fluorescent signals to the nucleus for easy image analysis and signal comparison. To test the ability of the biosensor to report on ER-mediated cell stress through the UPR, we compared the endogenous XBP1 splicing status to the biosensor splicing status during treatment with thapsigargin, a SERCA pump inhibitor that activates the IRE1 $\alpha$ -XBP1 pathway. The splicing of the biosensor and the endogenous XBP1 transcript display similar profiles during a 24-h treatment with thapsigargin (Figure 1B). The highest level of spliced endogenous XBP1 transcript is observed between 2 and 6 h after thapsigargin treatment but diminishes within 24 h (van Schadewijk et al., 2012; Figure 1B). Both the splicing of the

biosensor transcript and the stress-related green fluorescence peak between 2 and 6 h of treatment, diminishing after 22–24 h (Figures 1B–D), mimicking the endogenous stress response. Importantly, the cell stress response to thapsigargin is similar whether the stress levels are monitored using the fold change in green fluorescence on a plate reader (Figure 1C, top) or a high content imager using the percent of stressed cells within the well (Figure 1C, middle). Additionally, high content image analysis demonstrates that changes in cell stress occur an order of magnitude prior to changes to cell growth (Figure 1C, middle and bottom) when cells are stressed with thapsigargin. These data indicate that the cell stress biosensor may be more sensitive to detect changes in cellular stress response than assays monitoring cell growth or death.

An important feature of many neurodegenerative diseases is sustained cellular stress often caused by genetic mutations or changes in protein expression (Bosco et al., 2011; Ferrari et al., 2011). We next tested the ability of the cell stress biosensor to detect stress mediated through genetic mutations. We chose to assess a WT and mutant variant of rhodopsin. Rhodopsin is trafficked through the ER to the cell membrane in retinal cells (Deretic and Papermaster, 1991). Mutations in rhodopsin can lead to misfolding of the protein within the ER and are known to cause the progressive blinding disease, RP (Sung et al., 1991). By co-expressing the cell stress biosensor with either WT or a mutant form of rhodopsin known to cause RP, rhodopsin P23H, the effects of the WT and mutant rhodopsin were monitored over 20 h. Rhodopsin P23H not only displayed an increased cell stress response (Figure 1E,  $\Delta F/F_{\text{green stress}}$ ), it also resulted in decreased protein expression (Figure 1E,  $\Delta F/F_{\text{red expression}}$ ). This general decrease in protein expression is a hallmark of the UPR. These data demonstrate the ability of the cell stress biosensor to detect cell stress induced by genetic mutations. Lastly, as the cell stress biosensor may be a useful tool for

assaying compounds that alleviate the cell stress response, we assessed the ability of the IRE1 $\alpha$  inhibitor, 4 $\mu$ 8C to reduce the stress caused by the P23H mutation. After 20 h of expression, increasing doses of 4 $\mu$ 8C were added to cells expressing the P23H mutation and the subsequent changes in stress-related green fluorescence and expression-related red fluorescence were monitored independently (**Figure 1F**). As expected addition of 4 $\mu$ 8C reduced the stress response within 5 h after treatment (**Figure 1F**,  $\Delta F/F_{\text{green}}$  stress), while no change in general protein expression was observed (**Figure 1F**,  $\Delta F/F_{\text{red}}$  expression). Importantly, 1  $\mu$ M of 4 $\mu$ 8C, which has an IC<sub>50</sub> for IRE1 $\alpha$  of 6.8  $\mu$ M, was able to reduce stress levels of the P23H mutant back to those of WT within 20 h of treatment (**Figure 1F**, WT DMSO). These results demonstrate the ability of the cell stress biosensor to detect real-time changes in cell stress responses mediated by genetic components.

## Ca<sup>2+</sup> Signaling Is Affected by ER Stress

Cellular stress responses, including those brought on by ER stress, can lead to a number of changes in cellular physiology. Second messenger signaling is especially sensitive to changes in cell state, thus we sought to explore how ER-mediated cell stress, brought on by the overexpression of WT and mutant P23H rhodopsin, affected intracellular Ca<sup>2+</sup> signaling. We chose to explore Ca<sup>2+</sup> signaling as the ER is the main store of Ca<sup>2+</sup> within the cell, and changes to cytosolic Ca<sup>2+</sup> has been associated with the P23H mutation (Shinde et al., 2016). We first created a modified baculovirus, BacMam, to express the cell stress biosensor along with the WT or mutant forms of rhodopsin. We then transduced HEK293T cells with increasing amounts of WT or mutant rhodopsin BacMam along with BacMam carrying the cell stress biosensor. Analysis of the stress signal, the expression signal, and the green/red ratiometric signal (**Figure 2A**) demonstrated a dose-dependent increase in cell stress mediated by WT and mutant P23H rhodopsin when compared to control HEK293T cells that were not transduced with either rhodopsin construct. The stress response from P23H rhodopsin became distinguishable from the WT stress response at 5  $\mu$ l transduced virus, which corresponds to a similar level of rhodopsin mRNA expression observed in the retina (Table 1, Uhlén et al., 2015).

To determine if the stress response instigated by the P23H mutation affected Ca<sup>2+</sup> signaling we co-transduced 5  $\mu$ l of either WT or P23H rhodopsin BacMam along with the R-GECO Ca<sup>2+</sup> biosensor (Wu et al., 2013) and the human cholinergic receptor muscarinic 1 (hM1) GPCR. Cells expressing either WT or P23H rhodopsin were then stimulated with carbachol to activate a Gq signaling response. Cells were imaged every 2 s before and during carbachol treatment. As shown in **Figure 2B**, the average Ca<sup>2+</sup> response was quite different between the cells expressing WT and P23H rhodopsin. WT cells displayed an average  $\sim$ 1.75-fold change in cytoplasmic Ca<sup>2+</sup> levels whereas P23H cells displayed only an average  $\sim$ 0.8-fold change. Inspection of individual Ca<sup>2+</sup> traces from single cells imaged in **Figure 2B** suggested there may be distinct subpopulations of cells with variable responses to Gq activation. To explore this possibility, single-cell traces for

the WT and P23H data were analyzed for Ca<sup>2+</sup> response. First, each Ca<sup>2+</sup> trace was fit to the following equation  $\Delta F/F = \alpha e^{-\theta t}$  to identify the Ca<sup>2+</sup> amplitude ( $\alpha$ ) and cytoplasmic Ca<sup>2+</sup> clearance rate ( $\theta$ ; **Figure 2C**). Cells expressing WT rhodopsin show two distinct populations of  $\alpha$  values, with larger  $\alpha$  values, indicating a larger Ca<sup>2+</sup> signaling amplitude, dominating the distribution. Cells expressing P23H rhodopsin also display two distinct populations of  $\alpha$  values. However, both populations are shifted to lower  $\alpha$  values, indicating a blunted Ca<sup>2+</sup> signaling amplitude. Also, while a greater portion of cells display larger  $\alpha$  values in the P23H expressing cells, the distribution is much more even between the two states than in WT cells (**Figure 2C**). Analysis of the distribution of values for  $\theta$  from WT cells shows a single narrow distribution, while P23H expressing cells show a broader distribution of  $\theta$  values. P23H cells also display a shift towards higher  $\theta$  values, indicating a more rapid clearance of Ca<sup>2+</sup> from the cytoplasm after hM1 stimulation (**Figure 2C**). The distinct distributions of  $\alpha$  and  $\theta$  from WT and P23H expressing cells support the notion that there may be subpopulations of cells with distinct Ca<sup>2+</sup> signaling dynamics within the larger population of WT and P23H expressing cells. To explore this possibility, all single-cell traces from both the WT and P23H expressing cells were pooled and analyzed for the presence of unique Ca<sup>2+</sup> signaling patterns. To identify the number of distinct Ca<sup>2+</sup> signaling clusters present in the data, we tested the goodness of fit for 2–7 clusters of Ca<sup>2+</sup> signaling profiles. Using the PBM index (Pakhira et al., 2004) to score cluster number, we identified four Ca<sup>2+</sup> response profiles (**Figure 2D**). Two profiles, dominant in the WT cells, displayed increased Ca<sup>2+</sup> responses upon hM1 activation (**Figure 2E**, profiles 3 and 4), resembling a typical Gq response (Tewson et al., 2013). The other two profiles, dominant in the P23H cells, displayed a blunted Ca<sup>2+</sup> response (**Figure 2E**, profiles 1 and 2). However, the presence of profiles 1 and 2 in cells expressing WT rhodopsin suggests that even overexpression of WT rhodopsin elicits altered Ca<sup>2+</sup> signaling along with increased ER stress (**Figures 2A,C,E**).

Analysis of ER-mediated cell stress and individual Ca<sup>2+</sup> profiles suggests variability in Ca<sup>2+</sup> signaling response may be related to varying levels of cellular stress induced by the rhodopsin P23H mutation. To explore this possibility, we created a modified version of the cell stress biosensor where the constitutively expressed red fluorescent protein was replaced with R-GECO (**Figure 3A**). We then co-expressed this version of the biosensor with rhodopsin P23H and hM1 and again activated Gq signaling through carbachol treatment. As seen in **Figure 3B**, cells with higher levels of cell stress had blunted Ca<sup>2+</sup> responses, while those with lower levels of cell stress displayed a more typical Gq Ca<sup>2+</sup> response. Comparing the fold change in Ca<sup>2+</sup> levels upon Gq activation with stress levels revealed a negative correlation between cell stress and Ca<sup>2+</sup> signaling. The higher the levels of cell stress, the more blunted the Gq Ca<sup>2+</sup> response (**Figure 3C**). Together these data demonstrate that Ca<sup>2+</sup> signaling dynamics are affected by ER-mediated cell stress. Moreover, the degree to which Ca<sup>2+</sup> signaling is altered by cellular stress is dependent upon the severity of the cellular stress response.



## **$\alpha$ -Synuclein Overexpression Induces Cell Stress and Alters PDE Activity**

ER stress is also associated with protein folding diseases of proteins that are not directly trafficked through the ER (Scheper and Hoozemans, 2015). To test the ability of the cell stress biosensor to detect indirect ER stress, we created BacMam constructs of WT  $\alpha$ -synuclein ( $\alpha$ -syn) and four  $\alpha$ -syn mutants associated with PD (Maiti et al., 2017). HEK293T and SH-SY5Y cells were co-transduced with BacMam containing the cell stress biosensor and either 1  $\mu$ l or 10  $\mu$ l of BacMam containing either WT or one of the mutant  $\alpha$ -syn genes. SH-SY5Y cells were chosen along with HEK293T cells as they are a neuroblastoma cell line that has become an increasingly useful neuronal model to study not only PD but other neurodegenerative diseases as well (Nonaka et al., 2009; Xicoy et al., 2017; Vasquez et al., 2018). After 24 h of expression both the green fluorescence levels, to monitor stress induction, and the red fluorescence levels, to monitor protein expression, were analyzed using a plate reader. In both HEK293T and SH-SY5Y cells all of the  $\alpha$ -syn mutants displayed increased ER-mediated cellular stress, compared to the WT at both 1  $\mu$ l and 10  $\mu$ l of virus (Figure 4A, green/red ratio). Notably, in both cell lines the  $\alpha$ -syn mutants induced a significant decrease in overall protein expression at 1  $\mu$ l of virus, which is equal to  $\sim 7\times$  overexpression (Figure 4A red, Table 1). Normalizing the green stress fluorescent signal to this overall drop in expression results in significant detection of cell stress in each of the  $\alpha$ -syn mutants. Interestingly, in HEK293T cells at 10  $\mu$ l of the virus, the WT  $\alpha$ -syn induces increased stress levels compared to the mutants, but in SH-SY5Y cells each  $\alpha$ -syn mutant induced greater stress levels than the WT. This result suggests cell type may be an important factor to consider when assessing the effects of  $\alpha$ -syn mutations on cellular responses. Together, these data demonstrate the ability of the cell stress biosensor to detect ER-mediated cell stress induced by genetic mutations affecting proteins in the cytoplasm as well as the ER.

Similarly to the rhodopsin mutant, we postulated that expression of  $\alpha$ -syn variants might alter cellular signaling events along with inducing a stress response. Recent studies have identified phosphodiesterase (PDE) inhibitors as a way to preserve dopaminergic neurons (Morales-Garcia et al., 2011), promote neurogenesis (Morales-Garcia et al., 2015) and rescue Parkinsonian phenotypes (Bartolome et al., 2018). PDEs are key in the regulation of cyclic nucleotide second messenger levels within the cell as they degrade both cAMP and cGMP (Francis et al., 2011). We focused our analysis on cAMP as PDE inhibitor treatment increases cAMP levels within the cells which leads to increased CREB activation and expression of genes promoting neurogenesis (Morales-Garcia et al., 2011). How the regulation of basal levels of cAMP is altered in the disease state and how PDE activity affects cAMP dynamics in Parkinson's models remains unclear. To address how changes in cell stress alter cAMP levels and PDE activity, we created a second live-cell assay to compare cell stress and cAMP signaling. We then assessed the effects of expressing different  $\alpha$ -syn variants on cAMP levels and PDE activity in HEK293T and SH-SY5Y cells.

To remove the need for receptor activation to stimulate cAMP production, we developed a completely optical-based approach to monitor cAMP production and degradation. First, we used a blue light-activated adenylyl cyclase, bPAC (Stierl et al., 2011) to transiently raise cAMP levels within the cell, bypassing the endogenous receptor and adenylyl cyclase. The rapid off rate of bPAC allows direct monitoring of cAMP degradation by PDEs using R-cADDis, a red cAMP biosensor (Figure 4B). We first compared the PDE activity profiles between control cells and cells transduced with 1  $\mu$ l of either WT or mutant  $\alpha$ -syn, the lowest level of overexpression found to increase cellular stress. Initial analysis of cAMP degradation profiles revealed a marked difference in PDE activity in control cells and cells expressing any form of  $\alpha$ -syn (Figure 4C). This trend was independent of the cell type analyzed as both HEK293T and SH-SY5Y cells expressing  $\alpha$ -syn variants displayed similar increased PDE activity. We then determined the cAMP half-life ( $t_{1/2}$ ) in cells expressing different  $\alpha$ -syn variants using the following logistic function,  $\Delta F/F = \alpha/(1+\beta e^{-\theta t})$ . The distribution of cAMP  $t_{1/2}$  from individual cells expressing different  $\alpha$ -syn variants was compared to the distribution of cAMP  $t_{1/2}$  determined from control cells. The cumulative distribution function for each  $\alpha$ -syn variant and the control cells was then calculated and plotted to compare the cAMP  $t_{1/2}$  in both HEK293T and SH-SY5Y cells (Figure 4D). Consistent with the average cAMP degradation profiles, the  $\alpha$ -syn variants displayed a shift towards increased PDE activity compared to control cells.

Taking advantage of the live-cell nature of this PDE activity assays, we inspected individual cAMP degradation profiles from cells expressing different  $\alpha$ -syn variants. Interestingly, we identified multiple profiles of PDE activity within the cells. To identify the number of unique profiles and quantify their abundance in the different  $\alpha$ -syn variants, we again used the PBM index score. In both HEK293T and SH-SY5Y cells, three unique cAMP degradation profiles were observed, rapid, intermediate, and delayed (Figures 5A,B). Overexpression of either WT or mutant forms of  $\alpha$ -syn resulted in drastic changes in the cAMP degradation profile distribution in both cell types. In HEK293T cells, overexpression of any form of  $\alpha$ -syn displayed a shift in cAMP degradation away from the delayed profile towards the rapid and intermediate profiles (Figures 5C,D). Similar shifts towards more rapid cAMP degradation were observed in SH-SY5Y cells as well (Figures 5E,F). These data are consistent with the increased cAMP degradation rates observed in the average profiles and cumulative distribution functions. Interestingly, in SH-SY5Y cells, the A53T and E46K mutations displayed an even greater shift towards the rapid profile when compared to WT  $\alpha$ -syn (Figures 5E,F). The fact that overexpression of WT  $\alpha$ -syn creates a shift towards increased PDE activity, with no observable change in ER-mediated cell stress, suggests that monitoring changes in cAMP degradation may be a more sensitive readout to detect defects in cellular function than ER-mediated cell stress. Or that changes to PDE activity may precede detectable changes in cell stress in overexpression models of WT  $\alpha$ -syn. Notably, overexpression of WT  $\alpha$ -syn has been shown to recapitulate Parkinson's symptoms

(Mochizuki et al., 2006; Chesselet, 2008). Together, these data suggest that in the presence of minimally overexpressed  $\alpha$ -syn variants, cells undergo an ER-mediated cellular stress response and display increased PDE activity. These results are consistent with previous reports that PDE inhibitors can preserve dopaminergic neurons suggesting that cAMP levels play an important role in the progression of PD (Morales-Garcia et al., 2011, 2015).

## TDP-43 Overexpression Increases cAMP Degradation Rate

To determine if these changes in cell stress and cAMP degradation kinetics are unique to  $\alpha$ -syn, we repeated the cell stress assay and optical interrogation of PDE activity using SH-SY5Y cells co-transduced with either WT or the M337V mutant of TDP-43. Overexpression of either WT or M337V versions of TDP-43 resulted in increased cell stress (**Figure 6A**) when compared to control cells at 1  $\mu$ l of transduced virus, which corresponds to  $\sim 1.5\times$  overexpression of TDP-43 in SH-SY5Y cells (**Table 1**). Transduction of 10  $\mu$ l of virus, corresponding to  $\sim 5\times$  overexpression, also resulted in increased cell stress when compared to control cells. Further, when compared to WT, the M337V mutation displayed a significant increase in cell stress at 10  $\mu$ l of transduced virus (**Figure 6A**, 10  $\mu$ l). Analysis of PDE activity again demonstrated a shift towards more rapid cAMP degradation in cells expressing WT or M337V TDP-43 compared to control cells (**Figure 6B**). Plotting the cumulative distribution function of cAMP  $t_{1/2}$  values from individual cells confirmed this shift towards more rapid cAMP degradation in cells expressing TDP-43 variants (**Figure 6C**). However, this shift was diminished compared to the shift observed in SH-SY5Y cells expressing  $\alpha$ -syn variants (compare WT samples in **Figures 4D**, **6C**). These data suggest while TDP-43 overexpression increased PDE activity, it is to a lesser degree than  $\alpha$ -syn overexpression. Lastly, analysis of cAMP degradation profiles by clustering revealed two distinct cAMP degradation patterns, a rapid and a delayed profile (**Figure 6D**). As control cells are analyzed along with cells expressing TDP-43 WT or TDP-43 M337V to determine cluster number, the intermediate profiles identified when comparing control cells to  $\alpha$ -syn variants were segmented into either rapid or delayed profiles. Similarly to  $\alpha$ -syn overexpression, both the WT and the M337V mutant of TDP-43 displayed a shift towards rapid cAMP degradation profiles at 1  $\mu$ l of virus (**Figures 6E,F**), consistent with average cAMP degradation profiles and cumulative distribution functions. The M337V mutant also displayed a significant shift away from the delayed cAMP degradation profile towards the rapid profile when compared to WT TDP-43 (**Figure 6F**). These data are not only consistent with overexpression of TDP-43 increasing PDE activity, but with the notion that detectable changes in cell signaling are observed prior to changes in ER-mediated cell stress when comparing WT and M337V TDP-43 variants. These data, coupled with the similar results for  $\alpha$ -syn, suggest that activation of cell stress and increased PDE activity are a common feature of overexpression of two of the major proteins associated with PD and ALS.

## DISCUSSION

The cell stress biosensor described here builds upon previous attempts to create ER stress biosensors through the IRE1 $\alpha$ -XBP1 pathway (Iwawaki et al., 2004; Roy et al., 2017). The generation of a reversible ER stress biosensor makes it possible to identify the onset as well as the alleviation of cell stress. This feature may prove useful for screening of compounds or genetic mutations that activate ER stress as well those that inhibit the response, using a single assay. The detection of ER stress brought on by a mutation in rhodopsin and the subsequent inhibition of this stress response by blocking IRE1 $\alpha$  splicing activity through the use of 4 $\mu$ 8C is an intriguing example of such an intervention. Moreover, these assays were conducted in HEK293T cells but recapitulated the stress response observed in retinal cells. This type of assay, where both activation and inhibition of a cellular stress response can be detected in an immortalized cell model should prove useful. The genetic nature of these assays will also be useful in moving to *in vivo* models of neurodegeneration. *In vivo* models allow for a broader context for studying disease and having assays that can be deployed in both *in vitro* and *in vivo* models will help transition findings between the two. Thus, future work to optimize and deploy these assays in animal models will be an important next step.

Diseases such as RP, PD and ALS are difficult to study and treat because the assays used to study the effects of these diseases are often endpoint assays monitoring cell death. At this point, the ability to intervene and alter the course of the affected cell is lost. Furthermore, any changes in cell function, such as susceptibility to neurotransmitters and agonists, changes to second messenger regulation, or organelle function are best studied during the disease process. *In vitro* models for neurodegenerative diseases provide a useful platform to study these processes as many different mutations and cellular processes can be examined in a rapid manner. Studies of  $\alpha$ -synuclein in SH-SY5Y cells highlight the usefulness of this *in vitro* system (Emadi et al., 2009; Xin et al., 2015; Xicoy et al., 2017; Vasquez et al., 2018). It is our hope that the biosensors and assays described here can be applied to these models to provide new insights into the changes in cellular function that accompany neurodegenerative-associated mutations. These assays may also provide a strategy to identify pertinent mutations, stress responses, and signaling events to be further assessed using *in vivo* models.

Many neurodegenerative diseases not only display cellular stress responses but changes in cellular signaling events as well (Xu et al., 2012; Shinde et al., 2016). The changes observed in cAMP and Ca<sup>2+</sup> signaling induced by neurodegenerative mutations observed here also raises the question of how affected cells respond to stimuli. Changing the balance and timing of second messenger signaling in the cell may affect the ability of the cell to properly respond to, or transduce, extracellular signals such as neurotransmitters and neuromodulators. This alteration in cellular transduction status may also impact the druggability of cells. For example, a neuron expressing the A53T  $\alpha$ -syn mutation displays an increased cell stress response

and altered cAMP regulation. However, a neighboring cell, where the mutation has not caused build-up of misfolded protein yet, has intact cAMP regulation. If both cells are treated with agonists to the dopamine receptor there will likely be unique signal transduction responses in each cell. These differences are likely to affect how the cell responds or does not respond to the stimuli. These changes are important to consider in the development of drugs targeting these diseased cells. If a cell has lost its ability to transduce certain signals, those receptors, even though present at the cell surface, may no longer be a valid drug target. Indeed, our results suggest that targeting PDE activity may be a more effective method to restore the cellular transduction status. Thus, understanding how multiple stress and signaling pathways converge to affect cellular function in neurodegeneration will be an important step in the search for drugs to combat these diseases.

Finally, while ER-mediated cell stress is an important stress response involved in neurodegenerative disorders, many other cell stress pathways are involved. Proteasome stress, protein aggregation, mitochondrial stress, and oxidative stress have all been associated with neurodegenerative disease (Ciechanover and Kwon, 2017; Tan et al., 2019). Creating and combining genetically-encoded fluorescent biosensors for these pathways with biosensors for cellular signaling would further enhance our understanding of how neurodegenerative diseases disrupt cellular homeostasis and create new avenues for treatment of these diseases.

## REFERENCES

- Arango-Gonzalez, B., Trifunović, D., Sahaboglu, A., Kranz, K., Michalak, S., Farinelli, P., et al. (2014). Identification of a common non-apoptotic cell death mechanism in hereditary retinal degeneration. *PLoS One* 9:e112142. doi: 10.1371/journal.pone.0112142
- Bartolome, F., de la Cueva, M., Pascual, C., Antequera, D., Fernandez, T., Gil, C., et al. (2018). Amyloid  $\beta$ -induced impairments on mitochondrial dynamics, hippocampal neurogenesis and memory are restored by phosphodiesterase 7 inhibition. *Alzheimers Res. Ther.* 10:24. doi: 10.1186/s13195-018-0352-4
- Bosco, D. A., LaVoie, M. J., Petsko, G. A., and Ringe, D. (2011). Proteostasis and movement disorders: Parkinson's disease and amyotrophic lateral sclerosis. *Cold Spring Harb. Perspect. Biol.* 3:a007500. doi: 10.1101/cshperspect.a007500
- Broussard, G. J., Liang, R., and Tian, L. (2014). Monitoring activity in neural circuits with genetically encoded indicators. *Front. Mol. Neurosci.* 7:97. doi: 10.3389/fnmol.2014.00097
- Castro, L. R. V., Guiot, E., Polito, M., Paupardin-Tritsch, D., and Vincent, P. (2014). Decoding spatial and temporal features of neuronal cAMP/PKA signaling with FRET biosensors. *Biotechnol. J.* 9, 192–202. doi: 10.1002/biot.201300202
- Chalmers, F., van Lith, M., Sweeney, B., Cain, K., and Bulleid, N. J. (2017). Inhibition of IRE1 $\alpha$ -mediated XBP1 mRNA cleavage by XBP1 reveals a novel regulatory process during the unfolded protein response. *Wellcome Open Res.* 2:36. doi: 10.12688/wellcomeopenres.11764.2
- Chen, Z., Truong, T. M., and Ai, H.-W. (2017). Illuminating brain activities with fluorescent protein-based biosensors. *Chemosensors* 5:32. doi: 10.3390/chemosensors5040032
- Cheslelet, M.-F. (2008). *In vivo*  $\alpha$ -synuclein overexpression in rodents: a useful model of Parkinson's disease? *Exp. Neurol.* 209, 22–27. doi: 10.1016/j.expneurol.2007.08.006
- Ciechanover, A., and Kwon, Y. T. (2017). Protein quality control by molecular chaperones in neurodegeneration. *Front. Neurosci.* 11:185. doi: 10.3389/fnins.2017.00185
- Deretic, D., and Papermaster, D. S. (1991). Polarized sorting of rhodopsin on post-Golgi membranes in frog retinal photoreceptor cells. *J. Cell Biol.* 113, 1281–1293. doi: 10.1083/jcb.113.6.1281
- Emadi, S., Kasturirangan, S., Wang, M. S., Schulz, P., and Sierks, M. R. (2009). Detecting morphologically distinct oligomeric forms of  $\alpha$ -Synuclein. *J. Biol. Chem.* 284, 11048–11058. doi: 10.1074/jbc.m806559200
- Ferrari, S., Di Iorio, E., Barbaro, V., Ponzin, D., Sorrentino, F. S., and Parmeggiani, F. (2011). Retinitis pigmentosa: genes and disease mechanisms. *Curr. Genomics* 12, 238–249. doi: 10.2174/138920211795860107
- Francis, S. H., Blount, M. A., and Corbin, J. D. (2011). Mammalian cyclic nucleotide phosphodiesterases: molecular mechanisms and physiological functions. *Physiol. Rev.* 91, 651–690. doi: 10.1152/physrev.00030.2010
- Grootjans, J., Kaser, A., Kaufman, R. J., and Blumberg, R. S. (2016). The unfolded protein response in immunity and inflammation. *Nat. Rev. Immunol.* 16, 469–484. doi: 10.1038/nri.2016.62
- Hartong, D. T., Berson, E. L., and Dryja, T. P. (2006). Retinitis pigmentosa. *Lancet* 368, 1795–1809. doi: 10.1016/S0140-6736(06)69740-7
- Iwawaki, T., Akai, R., Kohno, K., and Miura, M. (2004). A transgenic mouse model for monitoring endoplasmic reticulum stress. *Nat. Med.* 10, 98–102. doi: 10.1038/nm970
- Katayama, H., Kogure, T., Mizushima, N., Yoshimori, T., and Miyawaki, A. (2011). A sensitive and quantitative technique for detecting autophagic events based on lysosomal delivery. *Chem. Biol.* 18, 1042–1052. doi: 10.1016/j.chembiol.2011.05.013
- Koch, S. F., Tsai, Y.-T., Duong, J. K., Wu, W.-H., Hsu, C.-W., Wu, W.-P., et al. (2015). Halting progressive neurodegeneration in advanced retinitis pigmentosa. *J. Clin. Invest.* 125, 3704–3713. doi: 10.1172/jci82462
- Laurinec, P. (2018). TSrepr R package: time series representations. *J. Open Source Softw.* 3:577. doi: 10.21105/joss.00577

## DATA AVAILABILITY STATEMENT

All raw images and CellProfiler analysis scripts are available on figshare at: <https://doi.org/10.6084/m9.figshare.9209486>.

## AUTHOR CONTRIBUTIONS

KH and TH designed the experiments and wrote the manuscript. ER conducted RT-qPCR, RT-PCR, viral transductions and cell culture. SM produced BacMam virus. KH conducted cell culture, transfections and transductions, collected imaging data, plate reader data, and analyzed the data. JC conducted high content experiments and analysis.

## FUNDING

This work was supported by the ASEE/NSF Small Business Postdoctoral Research Diversity Fellowship Program, National Science Foundation (NSF) award IIP-1552305 (KH) and The National Institute of Neurological Disorders and Stroke, Small Business Innovation Research grant 1R43NS108817-01 (KH and TH).

## ACKNOWLEDGMENTS

We thank members of Montana Molecular for their input on the project.



- Lee, A.-H., Iwakoshi, N. N., Anderson, K. C., and Glimcher, L. H. (2003). Proteasome inhibitors disrupt the unfolded protein response in myeloma cells. *Proc. Natl. Acad. Sci. U S A* 100, 9946–9951. doi: 10.1073/pnas.1334037100
- Maiti, P., Manna, J., and Dunbar, G. L. (2017). Current understanding of the molecular mechanisms in Parkinson's disease: targets for potential treatments. *Transl. Neurodegener.* 6:28. doi: 10.1186/s40035-017-0099-z
- McQuin, C., Goodman, A., Chernyshev, V., Kametsky, L., Cimini, B. A., Karhohs, K. W., et al. (2018). CellProfiler 3.0: next-generation image processing for biology. *PLoS Biol.* 16:e2005970. doi: 10.1371/journal.pbio.2005970
- Mittal, S., Bjørnevik, K., Im, D. S., Flierl, A., Dong, X., Locascio, J. J., et al. (2017).  $\beta$ 2-Adrenoreceptor is a regulator of the  $\alpha$ -synuclein gene driving risk of Parkinson's disease. *Science* 357, 891–898. doi: 10.1126/science.aaf3934
- Mochizuki, H., Yamada, M., and Mizuno, Y. (2006). Alpha-synuclein overexpression model. *J. Neural Transm. Suppl.* 70, 281–284. doi: 10.1007/978-3-211-45295-0\_44
- Moore, B. S., Stepanchick, A. N., Tewson, P. H., Hartle, C. M., Zhang, J., Quinn, A. M., et al. (2016). Cilia have high cAMP levels that are inhibited by Sonic Hedgehog-regulated calcium dynamics. *Proc. Natl. Acad. Sci. U S A* 113, 13069–13074. doi: 10.1073/pnas.1602393113
- Morales-Garcia, J. A., Alonso-Gil, S., Gil, C., Martinez, A., Santos, A., and Perez-Castillo, A. (2015). Phosphodiesterase 7 inhibition induces dopaminergic neurogenesis in hemiparkinsonian rats. *Stem Cells Transl. Med.* 4, 564–575. doi: 10.5966/sctm.2014-0277
- Morales-Garcia, J. A., Redondo, M., Alonso-Gil, S., Gil, C., Perez, C., Martinez, A., et al. (2011). Phosphodiesterase 7 inhibition preserves dopaminergic neurons in cellular and rodent models of Parkinson disease. *PLoS One* 6:e17240. doi: 10.1371/journal.pone.0017240
- Nonaka, T., Arai, T., Buratti, E., Baralle, F. E., Akiyama, H., and Hasegawa, M. (2009). Phosphorylated and ubiquitinated TDP-43 pathological inclusions in ALS and FTL-D-U are recapitulated in SH-SY5Y cells. *FEBS Lett.* 583, 394–400. doi: 10.1016/j.febslet.2008.12.031
- Pakhira, M. K., Bandyopadhyay, S., and Maulik, U. (2004). Validity index for crisp and fuzzy clusters. *Pattern Recognit.* 37, 487–501. doi: 10.1016/j.patcog.2003.06.005
- Pendin, D., Greotti, E., Lefkimiatis, K., and Pozzan, T. (2017). Exploring cells with targeted biosensors. *J. Gen. Physiol.* 149, 1–36. doi: 10.1085/jgp.201611654
- Peschek, J., Acosta-Alvear, D., Mendez, A. S., and Walter, P. (2015). A conformational RNA zipper promotes intron ejection during non-conventional XBP1 mRNA splicing. *EMBO Rep.* 16, 1688–1698. doi: 10.15252/embr.201540955
- Remondelli, P., and Renna, M. (2017). The endoplasmic reticulum unfolded protein response in neurodegenerative disorders and its potential therapeutic significance. *Front. Mol. Neurosci.* 10:187. doi: 10.3389/fnmol.2017.00187
- Roy, G., Zhang, S., Li, L., Higham, E., Wu, H., Marelli, M., et al. (2017). Development of a fluorescent reporter system for monitoring ER stress in Chinese hamster ovary cells and its application for therapeutic protein production. *PLoS One* 12:e0183694. doi: 10.1371/journal.pone.0183694
- Sakaue-Sawano, A., Kurokawa, H., Morimura, T., Hanyu, A., Hama, H., Osawa, H., et al. (2008). Visualizing spatiotemporal dynamics of multicellular cell-cycle progression. *Cell* 132, 487–498. doi: 10.1016/j.cell.2007.12.033
- Scheper, W., and Hoozemans, J. J. M. (2015). The unfolded protein response in neurodegenerative diseases: a neuropathological perspective. *Acta Neuropathol.* 130, 315–331. doi: 10.1007/s00401-015-1462-8
- Shinde, V., Kotla, P., Strang, C., and Gorbatyuk, M. (2016). Unfolded protein response-induced dysregulation of calcium homeostasis promotes retinal degeneration in rat models of autosomal dominant retinitis pigmentosa. *Cell Death Dis.* 7:e2085. doi: 10.1038/cddis.2015.325
- Stierl, M., Stumpf, P., Udvari, D., Gueta, R., Hagedorn, R., Losi, A., et al. (2011). Light modulation of cellular cAMP by a small bacterial photoactivated adenyl cyclase, bPAC, of the soil bacterium *Beggiatoa*. *J. Biol. Chem.* 286, 1181–1188. doi: 10.1074/jbc.M110.185496
- Sung, C. H., Schneider, B. G., Agarwal, N., Papermaster, D. S., and Nathans, J. (1991). Functional heterogeneity of mutant rhodopsins responsible for autosomal dominant retinitis pigmentosa. *Proc. Natl. Acad. Sci. U S A* 88, 8840–8844. doi: 10.1073/pnas.88.19.8840
- Tan, S. H., Karri, V., Tay, N. W. R., Chang, K. H., Ah, H. Y., Ng, P. Q., et al. (2019). Emerging pathways to neurodegeneration: dissecting the critical molecular mechanisms in Alzheimer's disease, Parkinson's disease. *Biomed. Pharmacother.* 111, 765–777. doi: 10.1016/j.biopha.2018.12.101
- Taylor, J. P., Brown, R. H. Jr., and Cleveland, D. W. (2016). Decoding ALS: from genes to mechanism. *Nature* 539, 197–206. doi: 10.1038/nature20413
- Tewson, P. H., Martinka, S., Shaner, N. C., Hughes, T. E., and Quinn, A. M. (2016). New DAG and cAMP sensors optimized for live-cell assays in automated laboratories. *J. Biomol. Screen.* 21, 298–305. doi: 10.1177/1087057115618608
- Tewson, P. H., Quinn, A. M., and Hughes, T. E. (2013). A multiplexed fluorescent assay for independent second-messenger systems: decoding GPCR activation in living cells. *J. Biomol. Screen.* 18, 797–806. doi: 10.1177/1087057113485427
- Tewson, P., Westenberg, M., Zhao, Y., Campbell, R. E., Quinn, A. M., and Hughes, T. E. (2012). Simultaneous detection of  $\text{Ca}^{2+}$  and diacylglycerol signaling in living cells. *PLoS One* 7:e42791. doi: 10.1371/journal.pone.0042791
- Uemura, A., Taniguchi, M., Matsuo, Y., Oku, M., Wakabayashi, S., and Yoshida, H. (2013). UBC9 regulates the stability of XBP1, a key transcription factor controlling the ER stress response. *Cell Struct. Funct.* 38, 67–79. doi: 10.1247/csf.12026
- Uhlén, M., Fagerberg, L., Hallström, B. M., Lindskog, C., Oksvold, P., Mardinoglu, A., et al. (2015). Proteomics. Tissue-based map of the human proteome. *Science* 347:1260419. doi: 10.1126/science.1260419
- van Schadewijk, A., van't Wout, E. F. A., Stolk, J., and Hiemstra, P. S. (2012). A quantitative method for detection of spliced X-box binding protein-1 (XBP1) mRNA as a measure of endoplasmic reticulum (ER) stress. *Cell Stress Chaperones* 17, 275–279. doi: 10.1007/s12192-011-0306-2
- Vasquez, V., Mitra, J., Perry, G., Rao, K. S., and Hegde, M. L. (2018). An inducible alpha-synuclein expressing neuronal cell line model for Parkinson's disease1. *J. Alzheimers Dis.* 66, 453–460. doi: 10.3233/jad-180610
- Wu, J., Liu, L., Matsuda, T., Zhao, Y., Rebane, A., Drobnitzhev, M., et al. (2013). Improved orange and red  $\text{Ca}^{2+}$  indicators and photophysical considerations for optogenetic applications. *ACS Chem. Neurosci.* 4, 963–972. doi: 10.1021/cn400012b
- Xicoy, H., Wieringa, B., and Martens, G. J. M. (2017). The SH-SY5Y cell line in Parkinson's disease research: a systematic review. *Mol. Neurodegener.* 12:10. doi: 10.1186/s13024-017-0149-0
- Xin, W., Emadi, S., Williams, S., Liu, Q., Schulz, P., He, P., et al. (2015). Toxic oligomeric alpha-synuclein variants present in human Parkinson's disease brains are differentially generated in mammalian cell models. *Biomolecules* 5, 1634–1651. doi: 10.3390/biom5031634
- Xu, X., Gerard, A. L., Huang, B. C., Anderson, D. C., Payan, D. G., and Luo, Y. (1998). Detection of programmed cell death using fluorescence energy transfer. *Nucleic Acids Res.* 26, 2034–2035. doi: 10.1093/nar/26.8.2034
- Xu, Y., Yan, J., Zhou, P., Li, J., Gao, H., Xia, Y., et al. (2012). Neurotransmitter receptors and cognitive dysfunction in Alzheimer's disease and Parkinson's disease. *Prog. Neurobiol.* 97, 1–13. doi: 10.1016/j.pneurobio.2012.02.002
- Yanagitani, K., Imagawa, Y., Iwawaki, T., Hosoda, A., Saito, M., Kimata, Y., et al. (2009). Cotranslational targeting of XBP1 protein to the membrane promotes cytoplasmic splicing of its own mRNA. *Mol. Cell* 34, 191–200. doi: 10.1016/j.molcel.2009.02.033
- Zhao, Y., Araki, S., Wu, J., Teramoto, T., Chang, Y.-F., Nakano, M., et al. (2011). An expanded palette of genetically encoded  $\text{Ca}^{2+}$  indicators. *Science* 333, 1888–1891. doi: 10.1126/science.1208592

**Conflict of Interest:** KH and TH hold a provisional patent filing for cell stress biosensors coupled to cell signaling biosensors. KH, TH, ER, and SM were employed by Montana Molecular. JC was employed by BioTek Instruments Inc.

Copyright © 2019 Harlen, Roush, Clayton, Martinka and Hughes. This is an open-access article distributed under the terms of the Creative Commons Attribution License (CC BY). The use, distribution or reproduction in other forums is permitted, provided the original author(s) and the copyright owner(s) are credited and that the original publication in this journal is cited, in accordance with accepted academic practice. No use, distribution or reproduction is permitted which does not comply with these terms.





# Reversible Loss of Hippocampal Function in a Mouse Model of Demyelination/Remyelination

Aniruddha Das<sup>1</sup>, Chinthasagar Bastian<sup>1</sup>, Lexie Trestan<sup>1</sup>, Jason Suh<sup>1</sup>, Tanujit Dey<sup>2</sup>, Bruce D. Trapp<sup>1,3</sup>, Selva Baltan<sup>1†</sup> and Hod Dana<sup>1,3\*</sup>

<sup>1</sup> Department of Neurosciences, Lerner Research Institute, Cleveland Clinic, Cleveland, OH, United States, <sup>2</sup> Department of Quantitative Health Sciences, Lerner Research Institute, Cleveland Clinic, Cleveland, OH, United States, <sup>3</sup> Department of Molecular Medicine, Cleveland Clinic Lerner College of Medicine, School of Medicine, Case Western Reserve University, Cleveland, OH, United States

## OPEN ACCESS

### Edited by:

Shai Berlin,  
Technion-Israel Institute  
of Technology, Israel

### Reviewed by:

Lorenzo Di Cesare Mannelli,  
University of Florence, Italy  
Maarten H. P. Kole,  
Netherlands Institute for Neuroscience  
(KNAW), Netherlands  
Chao Zhao,  
University of Cambridge,  
United Kingdom

### \*Correspondence:

Hod Dana  
dana@ccf.org

### †Present address:

Selva Baltan,  
Department of Anesthesiology  
and Perioperative Medicine, Oregon  
Health & Science University, Portland,  
OR, United States

### Specialty section:

This article was submitted to  
Cellular Neuropathology,  
a section of the journal  
Frontiers in Cellular Neuroscience

**Received:** 26 September 2019

**Accepted:** 24 December 2019

**Published:** 22 January 2020

### Citation:

Das A, Bastian C, Trestan L,  
Suh J, Dey T, Trapp BD, Baltan S and  
Dana H (2020) Reversible Loss  
of Hippocampal Function in a Mouse  
Model  
of Demyelination/Remyelination.  
Front. Cell. Neurosci. 13:588.  
doi: 10.3389/fncel.2019.00588

Demyelination of axons in the central nervous system (CNS) is a hallmark of multiple sclerosis (MS) and other demyelinating diseases. Cycles of demyelination, followed by remyelination, appear in the majority of MS patients and are associated with the onset and quiescence of disease-related symptoms, respectively. Previous studies in human patients and animal models have shown that vast demyelination is accompanied by wide-scale changes to brain activity, but details of this process are poorly understood. We used electrophysiological recordings and non-linear fluorescence imaging from genetically encoded calcium indicators to monitor the activity of hippocampal neurons during demyelination and remyelination over a period of 100 days. We found that synaptic transmission in CA1 neurons was diminished *in vitro*, and that neuronal firing rates in CA1 and the dentate gyrus (DG) were substantially reduced during demyelination *in vivo*, which partially recovered after a short remyelination period. This new approach allows monitoring how changes in synaptic transmission induced by cuprizone diet affect neuronal activity, and it can potentially be used to study the effects of therapeutic interventions in protecting the functionality of CNS neurons.

**Keywords:** multiple sclerosis, two-photon microscopy, calcium imaging, electrophysiology, cuprizone

## INTRODUCTION

Multiple sclerosis (MS) is an inflammatory demyelinating disease of the central nervous system (CNS) that affects more than 2.3 million patients worldwide (Wallin et al., 2019). For approximately 85% of patients, disease progression begins with a “relapsing-remitting” phase, where symptoms including motor deficits and vision loss that correlate with increased formation of demyelinated lesions detected by magnetic resonance imaging (MRI). Over time, these symptoms resolve into periods of clinical quiescence and partial remyelination of demyelinated axons (Chari, 2007; Goldenberg, 2012). In the majority of MS patients, the disease course eventually transforms from the relapsing-remitting phase to a secondary-progressive phase, where symptoms continually worsen (Mahad et al., 2015). Traditionally, MS was considered to be mainly a white-matter disease, but today it is widely accepted that there is also a critical gray-matter component, including demyelination of the cerebral cortex and deep gray matter (Geurts and Barkhof, 2008). Previous studies have also identified changes in brain activity patterns of MS patients during both the

relapsing-remitting and secondary-progressive forms of the disease, where presumably the reduced activity of MS-affected brain regions is partially compensated for by increased activity in other brain regions (Staffen et al., 2002; Chiaravalloti and DeLuca, 2008).

Studying the relationships between demyelination/remyelination cycles, motor and cognitive deficits, and changes in brain activity patterns requires the use of appropriate animal models and proper experimental methods. A commonly used mouse model for studying demyelination and remyelination is the cuprizone model (Kipp et al., 2009; Vega-Riquer et al., 2019), in which the copper chelator cuprizone is added to the mouse diet, resulting in damage to oligodendrocyte cells in the CNS. Over time, cuprizone causes extensive demyelination in various brain areas, including the hippocampus, corpus callosum, cortex, and cerebral white matter, which is partially reversible upon cessation of cuprizone by returning the animals to normal diet (Skrupuletz et al., 2008; Kipp et al., 2009; Koutsoudaki et al., 2009; Sachs et al., 2014). Interestingly, cuprizone-treated mice, similar to MS patients, were identified as having demyelination-induced reorganization of brain circuitry (Huebner et al., 2017). Moreover, the extensive brain demyelination produced by cuprizone resulted in significantly poorer performance in various behavioral tests, including hippocampus-dependent tasks (Xu et al., 2009). This reduction in performance was reversed upon remyelination (Dutta et al., 2013). Therefore, the cuprizone model seems to capture the demyelination-induced brain-wide activity reorganization that has been identified in MS patients. However, the traditional brain mapping methods used to identify these brain-wide activity changes in living mice were usually functional MRI and electroencephalogram (EEG), which have limited spatial and temporal resolutions that restrict their ability to assess rapid and local changes in brain activity. In order to uncover demyelination-induced effects on single cells and local networks, a method is required that allows micron-scale identification and single action potential (AP) detection *in vivo*.

Substantial improvements in spatiotemporal resolution can be achieved by using non-linear optics to detect brain activity (Svoboda and Yasuda, 2006). Two-photon laser scanning microscopy (TPLSM) of the fluorescence signal from genetically encoded calcium indicators (GECIs) enables monitoring the activity of thousands of individual neurons in the rodent brain with micron-scale resolution and high signal-to-noise ratio (Chen et al., 2013; Dana et al., 2016, 2019). Moreover, state-of-the-art GECIs provide the temporal dynamics and sensitivity that are necessary to allow detection of single APs over time scales of months, mainly by switching to stable transgenic expression strategies (Dana et al., 2014, 2016, 2018, 2019; Madisen et al., 2015; Wekselblatt et al., 2016). Therefore, this approach may enable the exploration of changes in brain activity following demyelination and remyelination with the required sensitivity and accuracy to detect changes in individual neurons over time.

In this study, we combined electrophysiology and TPLSM recording of acute and chronic activity patterns of neurons in the mouse hippocampus before, during, and after mice were fed with cuprizone diet. We identified rapid degeneration of CA1 activity following the initiation of cuprizone diet, which were faster than

expected by the induced demyelination alone, which decreased neuronal activity to ~20% of its pre-cuprizone level. We also found that synaptic transmission in CA1 neurons in response to sustained pre-synaptic stimuli was drastically diminished after the initiation of cuprizone diet. Synaptic transmission and neuronal activity partially recovered upon cessation of cuprizone diet. Thus, our study presents a new experimental approach for studying the effects of toxin-induced changes to brain physiology, such as demyelination and remyelination, on the integrity of individual neurons and neuronal circuits, and it also provides a platform to test the benefits of potential treatment options.

## MATERIALS AND METHODS

All surgical and experimental procedures were conducted in accordance with protocols approved by the Lerner Research Institute, Institutional Animal Care and Use Committee and Institutional Biosafety Committee.

### Hippocampal Slice Electrophysiology

Electrophysiological experiments were performed in the CA1 region of 400  $\mu$ m-thick transverse hippocampal slices as reported previously (Tekkok and Krnjevic, 1995; Provencio et al., 2016). Briefly, a cohort of 46 mice was divided into control ( $n = 18$ , normal diet, daily Rapamycin injections) and experimental groups ( $n = 28$ , cuprizone diet with daily Rapamycin injections). The experimental group was further divided and, synaptic transmission was monitored and quantified beginning at 1 ( $n = 2$ ), 3 ( $n = 9$ ), 4 ( $n = 8$ ), 5 ( $n = 3$ ), and 6 weeks ( $n = 3$ ) of cuprizone diet. A final group consisted of mice on cuprizone diet for 6 weeks, which were then returned to control diet for 6 weeks to remyelinate ( $n = 3$ , 6 W DM + 6 W RM). Synaptic transmission was recorded in a subset of Controls at week 0 ( $n = 8$ ) and beginning at 4 ( $n = 5$ , 4 W C) or 6 weeks ( $n = 5$ , 6 W C) to match the respective experimental groups. Mice were decapitated after anesthesia and brains were immediately removed and placed in ice-cold ( $\pm 4^\circ\text{C}$ ) artificial cerebrospinal fluid (ACSF) containing in mM: 126 NaCl, 3.5 KCl, 1.3  $\text{MgCl}_2$ , 2  $\text{CaCl}_2$ , 1.3  $\text{NaH}_2\text{PO}_4$ , 25  $\text{NaHCO}_3$ , and 10 glucose at pH 7.4. Hippocampi were quickly dissected and sliced with a McIlwain tissue chopper. Transverse slices were then transferred to ACSF solution and were continuously bubbled with 95%  $\text{O}_2$ /5%  $\text{CO}_2$  for at least 1–2 h at room temperature to stabilize.

Individual slices were then transferred and placed on a Haas-type tissue chamber (Warner Instruments, Harvard Apparatus) on a custom mesh (Warner Instruments, Catalog # 99-1129) to avoid air bubble accumulation and were stabilized using a slice holder (Warner Instruments, Cat. # 64-1415). Slices were kept at the interface of a moist humidified gas mixture of 95%  $\text{O}_2$ /5%  $\text{CO}_2$  and warm ACSF (at  $33\text{--}34^\circ\text{C}$ ) bubbled with 95%  $\text{O}_2$ /5%  $\text{CO}_2$  continually at a flow rate of 3–3.5 ml/min. For simultaneous extracellular recordings of afferent volleys (AV) and excitatory post-synaptic potentials (EPSPs), glass microelectrodes with 1-micron tips were pulled (Sutter Instruments, Borosilicate Glass with filament) and filled with 2 M NaCl (resistance

1–2 M $\Omega$ ). Electrode tips were polished using a Micro-Forge (Leica, MF-830, Narishige, Japan) and placed in the CA1 region of stratum radiatum layer to record synaptic transmission. Responses were evoked by stimulation of Schaffer collateral commissural fibers by a custom-designed bipolar tungsten wire electrode (Microprobes Part# PI2ST30.1B3) with 50  $\mu$ s-long pulses at 30-s intervals. After stabilization, synaptic transmission was recorded for at least 30 min as baseline. Changes in synaptic transmission properties were quantified by measuring the peak amplitude of EPSPs, as well as their area (Clampfit 10.7) to account for smaller slower responses. Maximum EPSPs, evoked by 100% of the stimulation amplitude (1 mA), were chosen for these measurements.

## Installation of Hippocampal Windows

For hippocampal window implantation, we slightly modified a previously described procedure (Dombeck et al., 2010; Lee et al., 2019). Thy1-jRGECO1a line 8.31 mice were anesthetized using isoflurane (2.5–3% for induction, 1.5% during surgery) on a 37°C heating pad. Local pain medication (bupivacaine 0.5%) was injected into the craniotomy area before the skin and connective tissue were removed to expose the skull. A circular craniotomy (3.2 mm diameter) was drilled using a hand drill (OMNIDRILL35, World Precision Instruments). The cortex and corpus callosum, but not the alveus above the dorsal part of the hippocampus, were removed by gentle suction with saline using 26G and 28G sharp and blunt needles connected to a vacuum line. After the hippocampus was exposed, it was kept in place by gently pressing a glass coverslip to it (3 mm diameter #1 glass, Warner Instruments) attached to a metal cannula (2.65 mm internal diameter, 3.2 mm outer diameter, 1.8 mm length, New England Small Tube Corp., type 304L stainless steel). The cannula was attached to the skull bone using dental cement (Contemporary Ortho-Jet, Lang Dental). A custom stainless-steel head post was cemented to the skull using the same dental cement.

## Recording of Hippocampal Activity

Seven to fourteen days after the craniotomy surgery, we started monitoring hippocampal activity. The same procedure was followed for all mice before, during, and after the cuprizone diet period. Mice were anesthetized (3% isoflurane) and injected with Chlorprothixene Hydrochloride (IM, 30  $\mu$ l of a 0.33 mg/ml solution, Santa Cruz). Recordings started at least 30 min after injection. Mice were put on a 37°C heating pad in the dark, and isoflurane levels were reduced to 0.5–0.75% prior to recording to bring the mice to a lightly anesthetized state, where they do not move but are sensitive to pain. Spontaneous activity was recorded using 20–120 mW of 1100 nm excitation light (Insight X3, Spectra-Physics) and a resonant-scanner two-photon microscope (512  $\times$  512 pixels, 30 Hz acquisition rate, Bergamo II, Thorlabs). Light intensity was controlled using a Pockels Cell (model 350-105, Conoptics) to maintain similar signal-to-noise ratios across different animals. Data were recorded on a weekly basis from all animals, and each recording session included acquisition of 200 s for each field of view (FOV), 3–5 FOVs from CA1 and 2–4 FOVs from dentate gyrus (DG) for each mouse.

## Data Analysis

Data analysis was performed using custom MATLAB scripts (MathWorks). Every two frames in the recorded time series were averaged to improve the signal-to-noise ratio, reducing the acquisition rate to 15 Hz. Small drifts and movements of the imaged area during the 200 s recording time were corrected with a MATLAB script using the TurboReg plug-in of ImageJ (Thevenaz et al., 1998). Ring-shaped regions of interest (ROI) corresponding to all identifiable somata were selected using a semi-automatic graphical user interface (Chen et al., 2013). Fluorescence signal from all pixels inside of a ROI were averaged to calculate the fluorescence signal ( $F$ ) for every cell. Baseline fluorescence levels ( $F_0$ ) for each ROI were estimated as its  $F$  median value across the 200 s of recording. To estimate AP firing from the fluorescence data, we calculated  $\Delta F/F_0 = (F - F_0)/F_0$  for each cell, and fed it to a published model (Deneux et al., 2016) for extracting AP activity from calcium traces (for accepting the model assumption, a trace of  $1 + \Delta F/F_0$  was used). We fit the model with the following parameters, according to jRGECO1a published characterization (Dana et al., 2016): one AP amplitude of 15%, decay time of 175 ms, and Hill coefficient of 1.9. Saturation level was set to 0.001 and signal drift to 0.03. Noise level was estimated using the model's internal function. The model results were inspected visually for accuracy, and for CA1 data the noise level estimation was increased by 50% to lower the false-positive rate. We identified active cells as cells with at least one identified AP by the AP-extraction model. The average activity was calculated as the total number of APs divided by the recording duration of 200 s. An activity burst was defined as firing of at least five APs within 660 ms.

For calculating the cellular contrast, we averaged all pixels in the ring-shaped ROI (covering the cellular cytosol), and averaged  $5 \times 5$  grid of pixels around the ROI center, corresponding to an area inside the nucleus. The contrast was calculated as the difference between the averaged cytosolic and nucleic signals, divided by the nucleic signal.

## Statistical Analysis

Statistical analysis was performed using MATLAB and R software (version 3.5.1)<sup>1</sup>. We performed four different statistical tests to identify changes in activity across different recording dates and mice. Wilcoxon Rank Sum tests were used to compare changes in median firing rate between two different recording dates from the same mice. Mann-Kendall Trend Tests were used to identify any monotonic trends in median firing rates during the cuprizone diet period (eight recording dates) for individual mice. Paired  $t$ -tests were used to compare changes in median firing rates of cuprizone or control groups across two recording dates. A repeated measures linear mixed effects model (repeated ANOVA test) was performed to determine the interaction of group (cuprizone and control) and time (eight recording dates) on CA1 and DG median activity rates, separately. The level of significance was set to  $P < 0.05$  for all hypothesis testing procedures.

<sup>1</sup><https://cran.r-project.org>

For analysis of *in vitro* hippocampal experiments, all means are reported  $\pm$  SEM and significant differences within a group was assessed by a one-way ANOVA, followed by Bonferroni's test. N denotes animal numbers in the text and parentheses in **Figure 1** indicate slice numbers.

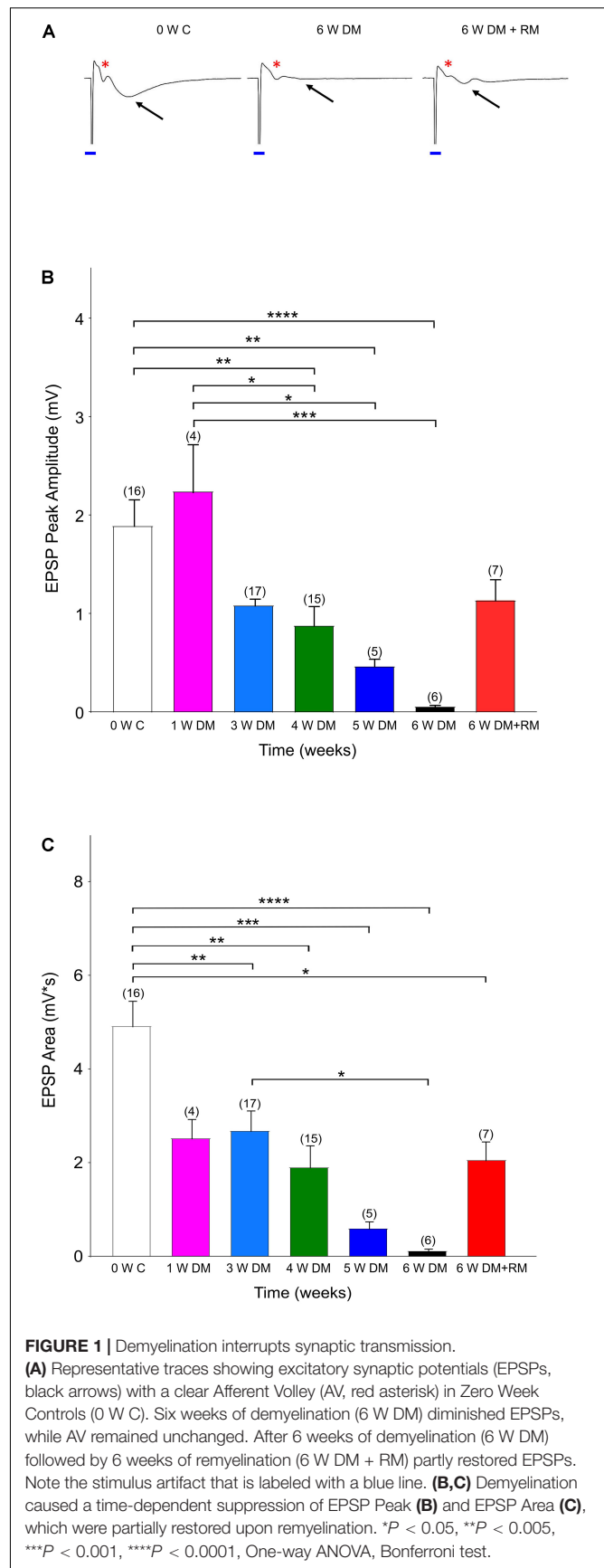
## Mouse Model of Demyelination and Remyelination

After the mice recovered from craniotomy surgery and we recorded at least one imaging session from them (7–14 days after the craniotomy surgery), we switched their diet to include 0.3% cuprizone (TD.140805, Envigo). Mice were provided access to food *ad libitum*. Food pellets were refrigerated and were replaced three times per week to ensure cuprizone efficiency. We continued to monitor hippocampal activity on a weekly basis. After 53 days of cuprizone diet, we identified that activity levels had reached a median level of zero APs (**Figure 2B**) in one of the mice, and we switched the mouse diet back to normal food. Mouse weight was monitored before each recording session (**Supplementary Table 1**). For electrophysiological recording experiments, mice were also injected daily with rapamycin for 12 weeks.

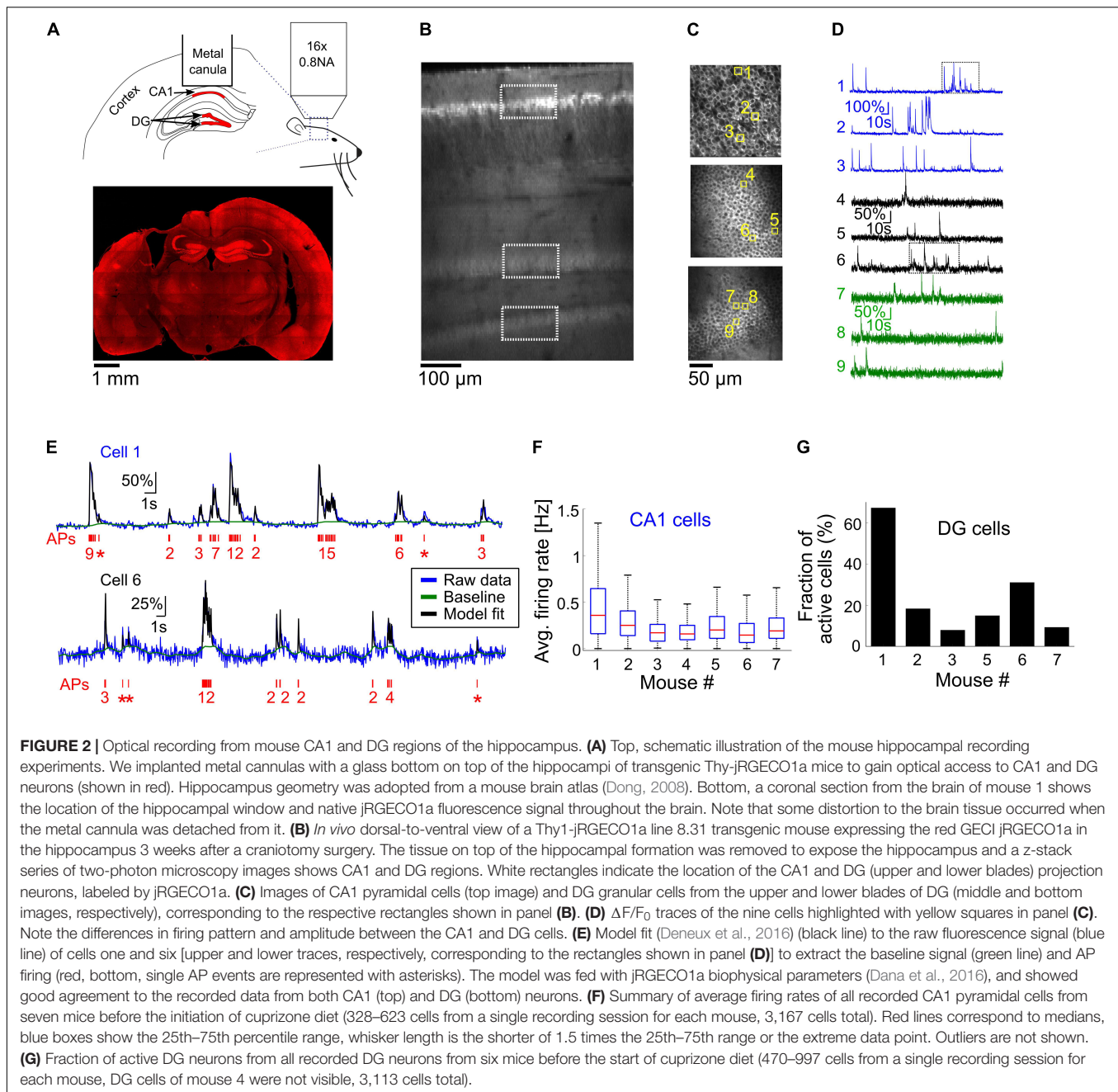
## RESULTS

### Demyelination Interrupts Synaptic Transmission in Hippocampal CA1 Neurons

Previous studies have identified that the hippocampus is severely demyelinated following 6–12 weeks of cuprizone diet, and that additional injections of rapamycin have eliminated the spontaneous remyelination that occurs when mice are fed with cuprizone (Sachs et al., 2014; Bai et al., 2016). These mice performed poorly in a hippocampus-dependent spatial-memory task (Dutta et al., 2013). Therefore, to investigate changes in neuronal activity in the hippocampus, we conducted a set of *in vitro* experiments in acute hippocampal slices. Forty-six mice were divided into seven cohorts and controls. The groups included 1, 3, 4, 5, or 6 weeks of cuprizone-diet-induced demyelination and daily rapamycin injections, and one group with 6 weeks of cuprizone diet with rapamycin injections, followed by an additional 6 weeks of remyelination with regular diet and no rapamycin injections (**Figure 1**). The control group received regular diet and daily rapamycin injections for 6 weeks, and recordings were performed at 0, 4, or 6 weeks to compare synaptic properties between demyelination and rapamycin-only conditions (**Supplementary Figure 1**). EPSPs together with clear AVs were evoked to monitor axon function in Schaeffer collateral commissural fibers. A successful synaptic transmission is a result of presynaptic input and a subsequent synaptic response. Sample traces shown in **Figure 1** denote that in every control slice following the stimulus artifact (blue line, due to square pulse delivered with the stimulation electrode), a prominent AV and EPSP were evoked (**Figure 1A**, 0 W C, red \*: AVs, black arrow for EPSPs). EPSPs presented







with a peak amplitude of  $\sim 2$  mV and an average area of  $5 \text{ mV} \times \text{s}$  (Figure 1B, white columns,  $n = 16$ ). As demyelination continued, EPSP peak amplitude and area gradually started to decline, becoming prominently low by 3–4 weeks (Figures 1A,B, blue and green columns,  $n = 17$  and 15, respectively) and almost completely diminishing by 6 weeks (Figures 1A,B, black columns,  $n = 6$ ). These changes were specific to cuprizone treatment because recordings in 4- and 6-week control groups were similar to 0-week control values (Supplementary Figure 1). Remyelination partially restored EPSPs, albeit with smaller amplitude compared to the control groups (Figures 1A–C, 6 W DM + RM,  $n = 7$ ). Therefore, demyelination effectively

interrupted synaptic transmission, characterized by loss of EPSPs, despite sustained presynaptic input, while remyelination partially restored synaptic transmission.

### Chronic Optical Recording of Neuronal Activity From CA1 and DG Cells of Thy1-jRGECO1a Mice

In order to further investigate the prevalence and time course of CA1 neuronal activity modulations, we conducted additional experiments for longitudinal optical recording of GECI signal from the hippocampus of lightly anesthetized mice ( $n = 7$  mice,

10–17 weeks old when implanted with an optical window; mice 1, 4, and 7 were males; mice 2, 3, 5, and 6 were females). Optical recording from CA1 cells usually requires removal of the cortical tissue on top of the recorded area (Dombeck et al., 2010; Ziv et al., 2013; Lee et al., 2019). Recordings from the DG area have also required removal of the CA1 region, causing severe damage to the hippocampal circuit (Danielson et al., 2016, 2017). Recent developments in the field of three-photon functional microscopy offer deeper tissue penetration to depths greater than 1 mm, enabling the recording of CA1 cells under an intact cortex (Ouzounov et al., 2017); however, this method is not yet able to probe deeper structures such as the DG. To allow deep-hippocampal recording while minimizing disruption to its integrity, we followed previous studies that used red GECIs to facilitate deeper TPLSM imaging, which allows recording from the DG without removing the CA1 layer (Dana et al., 2016; Pilz et al., 2016). We used a recently developed transgenic line, Thy1-jRGECO1a line GP8.31, which expresses the state-of-the-art red GECI jRGECO1a under the Thy1 promoter. jRGECO1a is expressed mostly in projection neurons across various brain regions, including the CA1 pyramidal and DG granular layers of the hippocampus (Dana et al., 2018). The enhanced imaging depth and high sensitivity achieved with jRGECO1a compared to green GECIs like GCaMP that we previously used for cortical imaging (Dana et al., 2016) enabled us to record, in six out of the seven mice used in this study, from the upper and lower blades of the DG down to 650  $\mu\text{m}$  under the hippocampal surface using up to 120 mW of 1100 nm excitation light (**Figures 2A–D**).

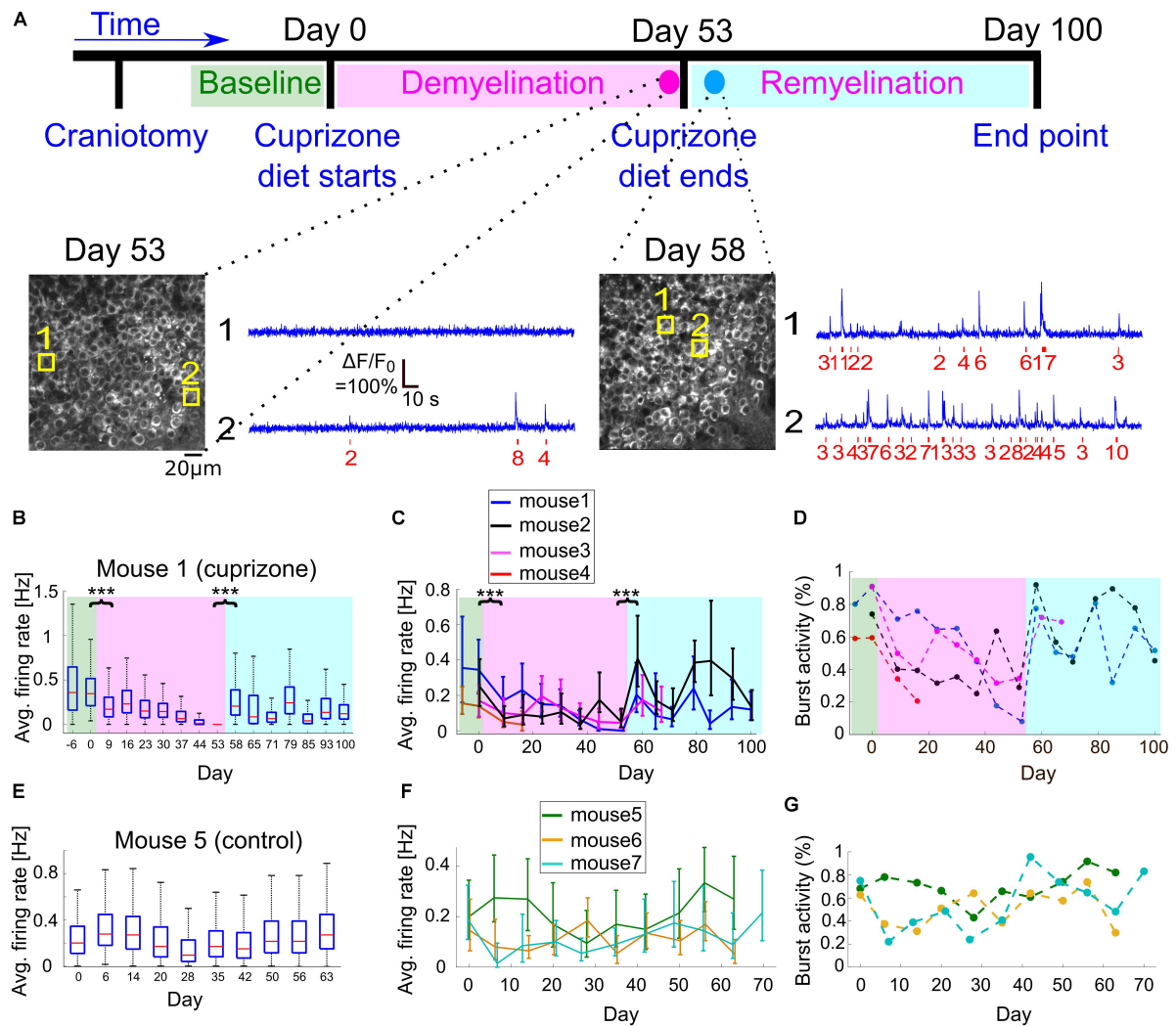
Recording of spontaneous activity from CA1 and DG neurons of lightly anesthetized mice revealed different firing patterns across the two populations (**Figure 2D** and **Supplementary Movies 1, 2**). To quantify activity patterns from the recorded fluorescence traces, we used a physiological model for extracting AP firing from calcium signals (**Figure 2E**) (Deneux et al., 2016). The majority of CA1 cells fired bursts of APs with a median average firing rate of 0.21 Hz and a maximal instantaneous firing rate of 8.15 Hz (3,114/3,167 CA1 cells were detected with at least firing of one AP; 2,099/3,167 cells fired bursts of APs, instantaneous firing rate was measured for 1-s time bins. Data from  $n = 7$  mice, one recording session for each mouse, **Figure 2F**). Most DG cells were not active during our recordings, and firing rates were substantially lower than those of CA1 cells (1,048/3,113 DG cells were detected with at least firing of one AP; only 184 cells from which were detected with average firing rate higher than 0.05 Hz;  $n = 6$  mice, one recording session for each mouse, **Figure 2G**).

Chronic activity recording from DG neurons proved to be more challenging than CA1 recording, since the deeper location of the DG resulted in a lower signal-to-noise ratio, caused by attenuation of the incoming laser beam and outgoing fluorescence signal. Moreover, we found that in some of the mice, the recorded image quality gradually degraded 6–12 weeks after cranial window implantation (**Supplementary Figure 2**, the DG of mouse 4 could not be recorded, the contrast of mouse 3's DG neurons deteriorated 1 month after the craniotomy surgery, and was excluded from the rest of the study), resulting in reduced sensitivity to AP detection, or even an inability to identify DG

cells. We quantified this degeneration by measuring the contrast between the cytosolic jRGECO1a signal and the nuclear signal, which should be much weaker in jRGECO1a-expressing neurons (Dana et al., 2016). The contrast of CA1 neurons was 2–5 times higher than DG neurons in the same animal. Data from DG neurons, recorded on dates with very low contrast, were excluded from our analysis (**Supplementary Figure 2B**).

## Cuprizone Diet Reduced CA1 Projection Neuron Firing Rates

To explore the reversible change in CA1 excitability (**Figure 1**) and to quantify how cuprizone-induced effects, such as demyelination and remyelination, affect the activity of single neurons in the hippocampus, we fed  $n = 4$  mice with 0.3% cuprizone diet ( $n = 3$  mice for 53 days, mouse 4 optical window quality deteriorated after 16 days of cuprizone diet so it was subsequently excluded from the rest of the study, **Figure 3A**). A control group of  $n = 3$  mice was implanted with a hippocampal window and received normal diet. These mice were not injected with Rapamycin in order to allow for faster remyelination after the end of the cuprizone diet period (Sachs et al., 2014). Weekly monitoring of CA1 and DG activity was conducted before, during, and after the cuprizone diet period, in order to identify changes to activity patterns in the same animal. Shortly after the initiation of the cuprizone diet, the average firing rate of CA1 cells was significantly decreased by 57% (comparing the mean of median firing rate values per mouse of  $n = 4$  mice, with 1,695 and 1,823 identified neurons on days 0 and 9 for cuprizone diet, respectively,  $P < 10^{-13}$  for the decrease in each mouse firing rate, Wilcoxon Rank Sum Test;  $P = 0.02$ , paired  $t$ -test between median firing rates of mice 1–4 on days 0 and 9; **Figures 3B,C**). During the 53 days of cuprizone diet, CA1 median firing rate significantly decreased for individual mice ( $P = 0.002, 0.064, 0.035$ , Mann-Kendall Trend Test for mice 1, 2, and 3, respectively, see examples in **Supplementary Figure 3**), but the group effect was not significant, presumably because of the small sample size ( $P = 0.07$ , paired  $t$ -test for change for median firing rates of mice 1–3). We also detected short-term increases in firing rates (**Figures 3B,C**, days 20–30) that might be associated with partial spontaneous remyelination, as was previously identified in cuprizone-treated mice (Sachs et al., 2014). On the last day of cuprizone diet, the average firing rate was significantly reduced to 16.5% of pre-diet levels (comparing the mean of median firing rate values per mouse of  $n = 3$  mice, with 1,135 and 1,356 identified neurons on days 0 and 53 for cuprizone diet, respectively,  $P < 10^{-36}$ , Wilcoxon Rank Sum Test, **Supplementary Movies 1, 3**). A similar decrease was identified in the fraction of cells that fired bursts on APs (**Figure 3D**, Methods). Monitoring CA1 activity of  $n = 3$  control mice showed no similar decrease. Changes in firing rates and burst activity were smaller than in the cuprizone group, had no identified monotonous trend, and presumably were the result of differences in anesthesia levels and brain state (**Figures 3E–G** and **Supplementary Movies 4, 5**;  $P = 0.99, 0.86, 0.14$ , Mann-Kendall Trend Test for mice 5, 6, and 7, respectively;  $P = 0.53$  and 0.49, paired  $t$ -test for changes of median firing rates of mice



**FIGURE 3 |** Changes to CA1 activity patterns during demyelination and remyelination. **(A)** Time line of the demyelination/remyelination experiment for mice 1–4. Craniotomy surgery was performed between day -14 and -7, and baseline activity recording from CA1 and DG neurons started between day -6 and day 0 [indicated by green background in panels (B–D)]. On day 0, after an activity recording session, we switched the diet to include 0.3% cuprizone. This diet was administered until day 53 [demyelination period, indicated by magenta background in panels (B–D)], while we maintained weekly activity recordings. On day 53, after an activity recording session was completed, we switched the mice back to normal diet and monitored activity until day 100 [remyelination period, indicated by cyan background in panels (B–D)]. Bottom, two example fields of view acquired from mouse 1 (cuprizone group) showing the CA1 layer and activity of two CA1 example cells on days 53 and 58. The estimated timing and number of APs is shown (red) beneath each raw data trace (blue).  $\Delta F/F_0 = 100\%$ , 10 s, 20  $\mu\text{m}$ . **(B)** Summary of the average firing rates from all recorded CA1 neurons from mouse 1 during 107 days of recording. Firing rates decreased significantly from 0.345 to 0.17 Hz between day 0 and 9 ( $P = 1.8 \times 10^{-37}$ , Wilcoxon Rank Sum Test), after cuprizone diet had been introduced. Activity levels continued to significantly decrease down to zero on day 53 ( $P = 0.002$ , Mann-Kendall Trend Test), and were significantly increased to 0.205 Hz on day 58, 5 days after normal diet was resumed ( $P = 4 \times 10^{-133}$ , Wilcoxon Rank Sum Test). Activity levels on the following days continued to increase compared to the demyelination period ( $P = 0.064$ , Mann-Kendall Trend Test), but remained lower than the pre-cuprizone period. Magenta and cyan backgrounds highlight the demyelination and remyelination periods, respectively; red lines correspond to medians, blue boxes show the 25th–75th percentile range, whisker length is the shorter of 1.5 times the 25th–75th range or the extreme data point. Outliers are not shown. \*\*\* $P < 0.001$ . **(C)** Summary of the average firing rates from all recorded CA1 neurons from all cuprizone-treated mice. Solid lines connect the distribution medians, and the error bars indicate the 25th–75th percentile range for each recording session. For all recorded mice, there was a significant decrease in the average firing rate upon the start of cuprizone diet, between day 0 and 9 ( $n = 4$  mice,  $P < 10^{-13}$ , Wilcoxon Rank Sum Test), and a significant increase upon the termination of cuprizone diet, between day 53 and 58 ( $n = 3$  mice,  $P < 10^{-32}$ , Wilcoxon Rank Sum Test). Note that the rapid increase in firing rate on day 58 was followed by a second decrease in activity rate. \*\*\* $P < 0.001$ . **(D)** Summary of the fraction of cells that fired bursts of APs from all recorded cells for all cuprizone-treated mice. This fraction decreased for all mice during the demyelination period and rapidly recovered upon the start of the remyelination period. Colors are the same as in panel (C).  $P$ -values for the decrease were 0.035, 0.108, and 0.064 for mice 1, 2, 3, respectively (Mann-Kendall Trend Test). **(E)** Summary of the average firing rates from all recorded CA1 neurons from control mouse 5, which received normal diet throughout the recording period, showing no similar decreases or increases in firing rate as those recorded from cuprizone-treated mice. **(F)** Summary of the average firing rates from all recorded CA1 neurons from all control mice. Solid lines connect the distribution medians, and the error bars indicate the 25th–75th percentile range for each recording session. None of the traces showed a significant monotonous trend ( $P = 0.99, 0.86, 0.14$ , for mice 5, 6, 7, respectively, Mann-Kendall Trend Test). **(G)** Summary of the fraction of cells that fired bursts of APs from all CA1-recorded neurons from all control mice. Colors are the same as in panel (F).



5–7 between days 0 and 7, and days 0 and 49, respectively; see examples in **Supplementary Figure 4**). A repeated ANOVA test between the cuprizone and control groups yielded no statistically significant differences in the group and the interaction between the time and group, respectively ( $P = 0.03$  for the time effect,  $P = 0.77$  for the group effect, and  $P = 0.18$  for the group-time interaction).

## Spontaneous Remyelination Restored the Activity of CA1 Excitatory Neurons

It has been shown multiple times that once cuprizone diet is stopped and mice are returned to their normal diet, spontaneous remyelination begins (Skripuletz et al., 2008; Kipp et al., 2009; Dutta et al., 2013; Sachs et al., 2014). Therefore, once we stopped the cuprizone diet and returned the mice to normal diet, we kept monitoring the same mice during the remyelination period. We identified a substantial and significant increase in the average firing rate of individual mice within 5 days after the end of the cuprizone diet (1,356 and 1,207 neurons from  $n = 3$  mice recorded on days 53 and 58, respectively.  $P < 10^{-32}$  for the change in individual mice firing rate, Wilcoxon Rank Sum Test), but the group effect was not significant ( $P = 0.08$ , paired  $t$ -test for change in median firing rates; **Supplementary Movies 3, 6**, see examples in **Supplementary Figure 3**). The amount of recovery was different across mice, but returned overall activity back to similar levels as the pre-cuprizone period ( $-40.5\%$ ,  $+4.8\%$ , and  $+104\%$  of the pre-cuprizone median firing rate,  $n = 3$  mice, 1,135 and 1,207 neurons from days 0 to 58, respectively). Interestingly, this recovery was not monotonous (non-significant results in Mann-Kendall Trend Test for days 53–100), and included a second cycle of decreasing and increasing of CA1 cell activity (**Figures 3B,C**, days 65–70). We monitored cellular activity for 47 additional days following the termination of cuprizone diet, and identified partial recovery of cellular firing rates, to lower levels than those before the start of cuprizone diet (35 and 52% of the activity level on day 0, data from 807 and 1,201 neurons from  $n = 2$  mice, measured on day 0 and 100, respectively; data shown in **Figures 3C,D**, **Supplementary Movie 7**, see examples in **Supplementary Figure 3**).

## Cuprizone Diet Reduced Activity Levels of DG Excitatory Neurons

For all tested mice, DG neuronal activity levels were lower than those of CA1 cells, and in the majority of DG neurons, firing of APs was not detected under our experimental conditions, similar to previously reported data (Pilz et al., 2016). In neurons that AP firing was detected, most fired a low number of APs. Therefore, we also quantified DG activity levels by assessing the fraction of cells that fired any number of APs, and the fraction of cells that fired at least one burst of more than five APs within a 660-ms time bin. Cuprizone diet caused a rapid decrease in the fraction of active cells by 49%, and an 89% decrease in bursting activity, but insufficient group size resulted in non-significant  $P$ -values (1,977 and 2,326 neurons recorded on days 0 and 9, respectively,  $n = 3$  mice;  $P = 0.19$  and  $0.26$ ,  $t$ -test for change in fraction of active and bursting cells, respectively). Median firing rate was significantly

decreased for two out of three mice ( $P < 10^{-15}$  for mice 1 and 2,  $P = 0.338$  for mouse 3, Wilcoxon Rank Sum Test). This decrease in activity levels continued during the cuprizone diet period, similar to the trend detected in CA1 cells (**Figures 4A,B**, see examples in **Supplementary Figure 5**). On the last day of the cuprizone diet, the fraction of active cells was decreased to 15% of its value on day 0 (1,419 and 1,334 neurons from  $n = 2$  mice, recorded on day 0 and 53, respectively,  $P < 10^{-10}$  for change in median firing rate, Wilcoxon Rank Sum Test, **Supplementary Movies 2, 8**). Activity recording in control mice did not show such a decrease ( $P = 0.59$  and  $0.30$ , paired  $t$ -test for change in fraction of active and bursting cells between first and second recording dates, respectively; **Figures 4C,D** and **Supplementary Movies 9, 10**, see examples in **Supplementary Figure 6**).

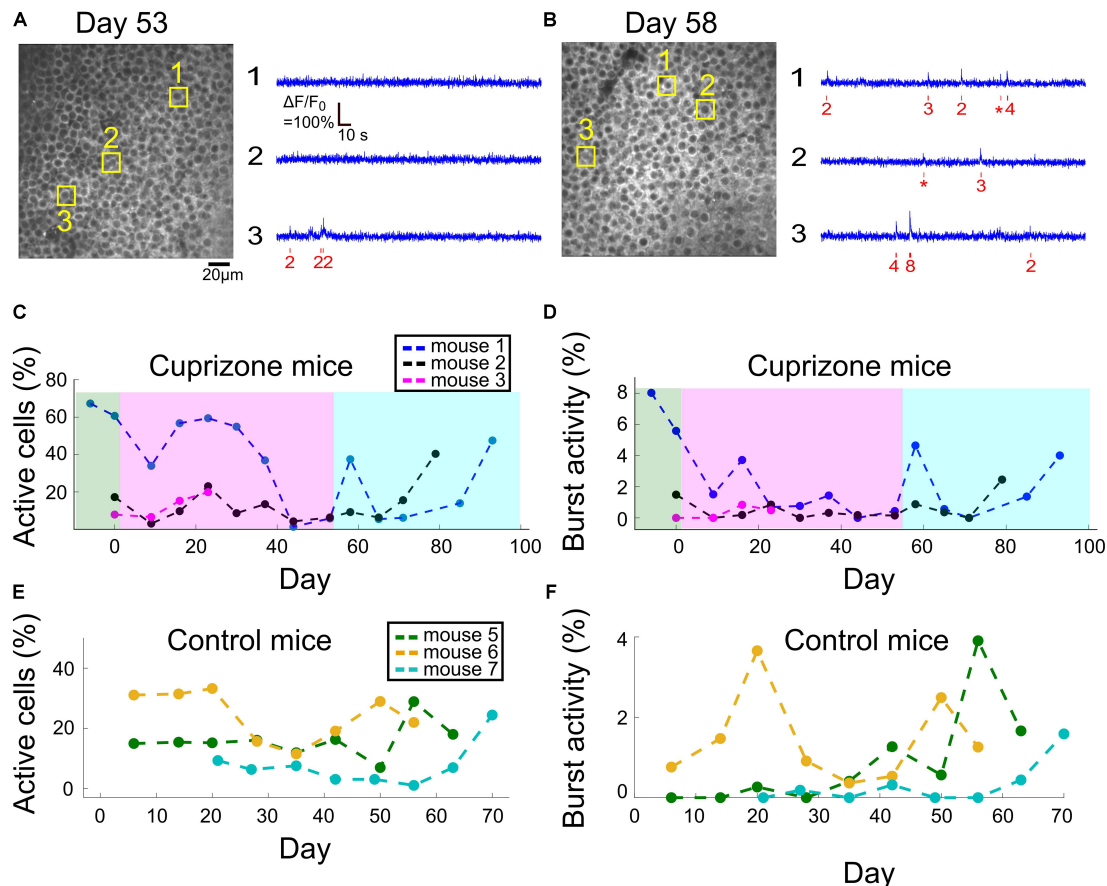
## Spontaneous Remyelination Restored the Activity of DG Projection Neurons

Dentate gyrus neurons presented a similar recovery pattern as CA1 neurons. DG cell activity increased rapidly upon termination of cuprizone diet, from 15 to 59% of the fraction of active cells on day 0 (1,419, 1,334, and 1,059 cells from  $n = 2$  mice on days 0, 53, and 58, respectively, **Supplementary Movie 11**, see examples in **Supplementary Figure 5**). This was followed by a second decrease and a second increase in activity levels, to reach comparable levels to day 0 (78.3 and 220.2% of fraction of active cells on day 0 for mice 1 and 3, respectively, data from 1,419 and 1,657 cells on day 0 and on the last day of recording, respectively; **Figures 4A,B**, **Supplementary Movie 12**, see examples in **Supplementary Figure 6**).

## DISCUSSION

Repeating cycles of demyelination and remyelination are associated with the progression of MS in the majority of patients, who first experience the relapsing-remitting form of the disease (Chang et al., 2012). This highlights the necessity to understand the impact of these cycles on brain activity. In this study, we measured the effects of cuprizone diet, such as demyelination and remyelination, on hippocampal activity, which recapitulates the loss and partial recovery of myelin, consistently in the same brain regions and with a reliable and reproducible time course (Dutta et al., 2013; Sachs et al., 2014; Bai et al., 2016). We combined electrophysiology and functional microscopy for acute and long-term monitoring of the activity of projection neurons in CA1 and DG regions with cellular resolution over more than 100 days, during both the demyelination and remyelination phases. We identified cuprizone-induced deterioration of synaptic transmission of CA1 cells, and quantified the longitudinal effect of this deterioration on hippocampal activity *in vivo*. We report large changes in neuronal firing rates, with both fast and long-term components that followed the initiation and cessation of cuprizone diet. These changes were associated with the demyelination and remyelination processes, as were previously reported, and are in agreement with behavioral deficits and recovery that were also reported in cuprizone mice (Sachs et al., 2014; Bai et al., 2016),





**FIGURE 4 |** Changes to DG activity patterns during demyelination and remyelination. **(A)** An example field of view of DG neurons from mouse 1, after 53 days of cuprizone diet, with activity traces of three example cells. The estimated timing and number of APs is shown (red) beneath each raw data trace (blue). **(B)** An example field of view of DG neurons from mouse 1, 5 days after the end of the cuprizone diet, with activity traces of three example cells. The estimated timing and number of APs is shown (red) beneath each raw data trace (blue). **(C)** Summary of the fraction of active DG cells from all recorded DG cells for all cuprizone-treated mice. The low-level recorded activity of DG cells is in line with previous findings (Pilz et al., 2016). However, the cuprizone diet reduced the activity even further, and the termination of cuprizone diet was followed by a noticeable recovery. DG cells of mouse 3 could be recorded only during the first four recording sessions. **(D)** Summary of the fraction of DG cells that fired bursts of APs from all recorded DG cells in cuprizone-treated mice shows a similar trend to the change in CA1 activity patterns. Colors are the same as in panel **(C)**. **(E)** Summary of the fraction of active DG cells from all recorded DG cells for all control mice. **(F)** Summary of the fraction of DG cells that fired bursts of APs from all recorded DG cells in control mice. Colors are the same as in panel **(E)**.

as well as changes to the excitability levels of single neurons (Praet et al., 2014; Hamada et al., 2017) and disrupted large-scale activity patterns (Hoffmann et al., 2008).

The time-scales of cuprizone-mediated brain activity degeneration, and recovery once cuprizone diet was stopped, are in agreement with previous studies (Sachs et al., 2014; Bai et al., 2016). However, our recordings have identified rapid changes and non-monotonous trends for both conditions that have not yet been reported. A large fraction of the activity change occurred within 5–9 days (one recording session) from the initiation and cessation of cuprizone diet, faster than the reported time scale of 3–6 weeks for demyelination and remyelination (Sachs et al., 2014; Bai et al., 2016). Interestingly, this relatively rapid change was followed by a “rebound” change in activity levels, i.e., the activity increased during cuprizone diet, and decreased during remyelination. Increased activity during demyelination, approximately 3–6 weeks

after the start of cuprizone diet, may be explained by partial remyelination due to maturation of the oligodendrocyte progenitor cells into mature myelinating oligodendrocytes (Sachs et al., 2014), but other characteristics of the effects of cuprizone on neuronal and non-neuronal cells, and how it translates to the reported rapid changes in activity, will require additional studies. It is possible that cuprizone has, in addition to the reported effect on oligodendrocytes, a direct effect on neuronal health, or alternatively an indirect effect mediated by glial cells, that resulted in the rapid changes we identified. In addition, this study included both male and female mice, and the reduction in activity levels seemed to be stronger in males (mice 1 and 4). Though the number of mice used in this study does not allow for a definitive assessment of sex-specific differences, such differences may be expected based upon the existing findings (Kipp et al., 2009; Ohgomori and Jinno, 2019).

In agreement with fluorescent imaging results, electrophysiological recording of CA1 synaptic transmission showed significant depression starting at 3 weeks of demyelination, which is earlier than previously reported (Sachs et al., 2014). Depression of EPSPs progressed on a weekly basis, reaching a nadir level by 6 weeks of demyelination. Interestingly, AVs were well preserved, even in 6-week demyelinated slices, suggesting that the primary site of failure for synaptic transmission is post-synaptic. Indeed, cuprizone-induced demyelination reduces AMPA receptors in the CA1 region of hippocampus (Dutta et al., 2013). Additionally, deficits in excitatory synaptic transmission during experimental autoimmune encephalomyelitis (EAE) correlated with disruption of PSD-95 integrity involving both AMPA and NMDA receptor-mediated currents (Ziehn et al., 2012a,b) while preserving presynaptic function in CA1 neurons. In contrast, recordings in layer V pyramidal neurons in somatosensory cortex of mice that were kept on cuprizone diet for 5 weeks revealed that AP propagation switched from rapid saltatory conduction toward a slow continuous wave broadening the presynaptic AP, with reduced velocity presumably due to redistribution of fast-acting K channels (Hamada et al., 2017). Furthermore, AP changes were accompanied by demyelination of internodes, variable reorganization of nodal domains, and frequent sprouting of axons. Characterizing the structural changes in our animal model will require additional work. However, taken together, it seems that loss of myelin in gray matter causes a wide range of site-specific structural and functional changes.

Optical activity monitoring allows probing how connected brain regions are affected by external input, and how they affect each other. We recorded activity both from CA1 and DG neurons in the same mice, and identified substantial differences in their activity patterns (Figures 2–4), in agreement with previous studies (Ziv et al., 2013; Pilz et al., 2016). The deep-tissue location and low level of activity of DG neurons under anesthesia make them more challenging to monitor compared to CA1 neurons (Supplementary Figure 2). Therefore, more studies are required to obtain a better understanding of cuprizone-induced changes in DG cells, preferably in awake mice, where activity levels are expected to be higher (Pilz et al., 2016). Nevertheless, longitudinal DG recording is feasible using laser power that is not expected to produce substantial heating or thermal damage to the tissue (Podgorski and Ranganathan, 2016). Our electrophysiological studies have highlighted that cellular excitability of CA1 neurons was interrupted during cuprizone-induced demyelination, suggesting impaired synaptic transmission, which was restored during remyelination. Future studies may characterize how DG pre- and post-synaptic activity is modulated, and how it affects the CA1 pre-synaptic signal via feed-forward hippocampal circuitry. Such studies may reveal whether cuprizone-mediated diet attenuates activity in other brain regions, and hence also the input to the hippocampus, reduces the excitability of DG neurons via changes in excitation-inhibition balance, or similarly affects cellular excitability in both CA1 and DG neurons.

A limitation of the *in vivo* approach we used in this study is the relatively low number of mice in each group, which is

related to the amount of time required to record and analyze the activity data from each mouse. The small group size limited the significance of the statistical analyses that we performed. We received significant *P*-values for changes in activity characteristics from the same animal, which relied on the large number of cells that we sampled. However, our statistical analyses were less conclusive for *t*-tests across median values from mice in the same group, and were non-significant for a repeated ANOVA across the cuprizone and control groups. A preferred approach for overcoming this limitation is to increase the group sizes, which might require adopting an automatic analysis pipeline for improving the throughput of such experiments (Pachitariu et al., 2017).

Finally, applying optical methods for monitoring the brain offers an attractive approach for acquiring essential *in vivo* information to link structure, function, and behavior. We demonstrated that TPLSM recording of GECI signal enables direct evaluation of functional properties of neurons in a mouse model of MS-like symptoms. Moreover, we show that deterioration of synaptic transmission in CA1 cells is reflected in the activity levels of these neurons, and can be measured *in vivo* in a longitudinal manner. Future studies may combine this approach with emerging methods for *in vivo* measurements of the myelin sheath using label-free third harmonic generation (Farrar et al., 2011; Redlich and Lim, 2019) to allow for all-optical detection of demyelination and activity levels in the same cells. Complementary behavioral data can be acquired with standard behavioral and cognitive tests for assessing the mouse condition, such as the Morris water maze (Dutta et al., 2013). Such experimental platforms will provide a more holistic assessment of the mouse condition. Such an experimental platform may also be used as an evaluation testbed for comparing the efficacy of new pharmaceutical intervention treatments for protecting synaptic transmission and neuronal activity patterns, reducing demyelination levels, and/or relieving behavioral deficits.

## DATA AVAILABILITY STATEMENT

The datasets generated for this study are available on request to the corresponding author.

## ETHICS STATEMENT

The animal study was reviewed and approved by the Lerner Research Institute, Institutional Animal Care and Use Committee and Institutional Biosafety Committee.

## AUTHOR CONTRIBUTIONS

HD, BT, and SB initiated the project. SB, CB, and LT conducted the electrophysiological recording experiments and their analysis. AD conducted the optical recording experiments. AD, JS, TD, and HD performed the optical data analysis. HD and SB wrote the manuscript with comments from the other authors.

## FUNDING

This research was partially funded by an MS Society Pilot Grant (PP-1901-33093) to HD and NIH grants (R35NS09730) to BT and (AG033720) to SB.

## ACKNOWLEDGMENTS

We thank the HHMI Janelia GENIE project for developing and sharing the Thy1-jRGECO1a transgenic mice. We thank Dr. Vanzetta and his colleagues for developing and sharing the AP extraction model used in this study. We would like to thank Drs. Albert Lee and Jae Sung Lee for sharing their hippocampal

window implantation technique, Drs. Ranjan Dutta, Chris Nelson, and Dimitrios Davalos for reviewing the manuscript and for their insightful comments, and Sarah Stanko and Anthony Chomyk for assisting with mouse husbandry. Materials and data were provided by the Cleveland Clinic Foundation (CCF). All rights, title, and interest in the materials and data are owned by CCF.

## SUPPLEMENTARY MATERIAL

The Supplementary Material for this article can be found online at: <https://www.frontiersin.org/articles/10.3389/fncel.2019.00588/full#supplementary-material>

## REFERENCES

- Bai, C. B., Sun, S., Roholt, A., Benson, E., Edberg, D., and Medicetty, S. (2016). A mouse model for testing remyelinating therapies. *Exp. Neurol.* 283, 330–340. doi: 10.1016/j.expneurol.2016.06.033
- Chang, A., Staugaitis, S. M., Dutta, R., Batt, C. E., Easley, K. E., and Chomyk, A. M. (2012). Cortical remyelination: a new target for repair therapies in multiple sclerosis. *Ann. Neurol.* 72, 918–926. doi: 10.1002/ana.23693
- Chari, D. M. (2007). Remyelination in multiple sclerosis. *Int. Rev. Neurobiol.* 79, 589–620. doi: 10.1016/s0074-7742(07)79026-8
- Chen, T. W., Wardill, T. J., Sun, Y., Pulver, S. R., Renninger, S. L., and Baohan, A. (2013). Ultrasensitive fluorescent proteins for imaging neuronal activity. *Nature* 499, 295–300. doi: 10.1038/nature12354
- Chiaravalloti, N. D., and DeLuca, J. (2008). Cognitive impairment in multiple sclerosis. *Lancet Neurol.* 7, 1139–1151.
- Dana, H., Chen, T.-W., Hu, A., Shields, B. C., Guo, C., and Looger, L. (2014). Thy1-GCaMP6 transgenic mice for neuronal population imaging in vivo. *PLoS One* 9:e108697. doi: 10.1371/journal.pone.0108697
- Dana, H., Mohar, B., Sun, Y., Narayan, S., Gordus, A., and Hasseman, J. P. (2016). Sensitive red protein calcium indicators for imaging neural activity. *eLife* 5:e12727. doi: 10.7554/eLife.12727
- Dana, H., Novak, O., Guardado-Montesino, M., Fransen, J. W., Hu, A., and Borghuis, B. G. (2018). Thy1 transgenic mice expressing the red fluorescent calcium indicator jRGECO1a for neuronal population imaging in vivo. *PLoS One* 13:e0205444. doi: 10.1371/journal.pone.0205444
- Dana, H., Sun, Y., Mohar, B., Hulse, B. K., Kerlin, A. M., and Hasseman, J. P. (2019). High-performance calcium sensors for imaging activity in neuronal populations and microcompartments. *Nat. Methods* 16, 649–657. doi: 10.1038/s41592-019-0435-6
- Danielson, N. B., Kaifosh, P., Zaremba, J. D., Lovett-Barron, M., Tsai, J., and Denny, C. A. (2016). Distinct contribution of adult-born hippocampal granule cells to context encoding. *Neuron* 90, 101–112. doi: 10.1016/j.neuron.2016.02.019
- Danielson, N. B., Turi, G. F., Ladow, M., Chavlis, S., Petrantonakis, P. C., Poirazi, P., et al. (2017). In vivo imaging of dentate gyrus mossy cells in behaving mice. *Neuron* 93, 552.e4–559.e4. doi: 10.1016/j.neuron.2016.12.019
- Deneux, T., Kaszas, A., Szalay, G., Katona, G., Lakner, T., and Grinvald, A. (2016). Accurate spike estimation from noisy calcium signals for ultrafast three-dimensional imaging of large neuronal populations in vivo. *Nat. Commun.* 7:12190. doi: 10.1038/ncomms12190
- Dombeck, D. A., Harvey, C. D., Tian, L., Looger, L. L., and Tank, D. W. (2010). Functional imaging of hippocampal place cells at cellular resolution during virtual navigation. *Nat. Neurosci.* 13, 1433–1440. doi: 10.1038/nn.2648
- Dong, H. W. (2008). *The Allen Reference Atlas: A Digital Color Brain Atlas of the C57BL/6J Male Mouse*. Hoboken, NJ: John Wiley & Sons Inc.
- Dutta, R., Chomyk, A. M., Chang, A., Ribardo, M. V., Deckard, S. A., and Doud, M. K. (2013). Hippocampal demyelination and memory dysfunction are associated with increased levels of the neuronal microRNA miR-124 and reduced AMPA receptors. *Ann. Neurol.* 73, 637–645. doi: 10.1002/ana.23860
- Farrar, M. J., Wise, F. W., Fetcho, J. R., and Schaffer, C. B. (2011). In vivo imaging of myelin in the vertebrate central nervous system using third harmonic generation microscopy. *Biophys. J.* 100, 1362–1371. doi: 10.1016/j.bpj.2011.01.031
- Geurts, J. J., and Barkhof, F. (2008). Grey matter pathology in multiple sclerosis. *Lancet Neurol.* 7, 841–851.
- Goldenberg, M. M. (2012). Multiple sclerosis review. *Pharm. Therap.* 37, 175–184.
- Hamada, M. S., Popovic, M. A., and Kole, M. H. P. (2017). Loss of saltation and presynaptic action potential failure in demyelinated axons. *Front. Cell. Neurosci.* 11:45. doi: 10.3389/fncel.2017.00045
- Hoffmann, K., Lindner, M., Grötcke, I., Stangel, M., and Löscher, W. (2008). Epileptic seizures and hippocampal damage after cuprizone-induced demyelination in C57BL/6 mice. *Exp. Neurol.* 210, 308–321. doi: 10.1016/j.expneurol.2007.11.005
- Huebner, N. S., Mechling, A. E., Lee, H.-L., Reisert, M., Bienert, T., and Hennig, J. (2017). The connectomics of brain demyelination: functional and structural patterns in the cuprizone mouse model. *Neuroimage* 146, 1–18. doi: 10.1016/j.neuroimage.2016.11.008
- Kipp, M., Clarner, T., Dang, J., Copray, S., and Beyer, C. (2009). The cuprizone animal model: new insights into an old story. *Acta Neuropathol.* 118, 723–736. doi: 10.1007/s00401-009-0591-3
- Koutsoudaki, P. N., Skripuletz, T., Gudi, V., Moharregg-Khiabani, D., Hildebrandt, H., Trebst, C., et al. (2009). Demyelination of the hippocampus is prominent in the cuprizone model. *Neurosci. Lett.* 451, 83–88. doi: 10.1016/j.neulet.2008.11.058
- Lee, J. S., Briguglio, J., Romani, S., and Lee, A. K. (2019). The statistical structure of the hippocampal code for space as a function of time, context, and value. *bioRxiv[Preprint]*
- Madisen, L., Garner, A. R., Shimaoka, D., Chuong, A. S., Klapoetke, N. C., and Li, L. (2015). Transgenic mice for intersectional targeting of neural sensors and effectors with high specificity and performance. *Neuron* 85, 942–958. doi: 10.1016/j.neuron.2015.02.022
- Mahad, D. H., Trapp, B. D., and Lassmann, H. (2015). Pathological mechanisms in progressive multiple sclerosis. *Lancet Neurol.* 14, 183–193. doi: 10.1016/s1474-4422(14)70256-x
- Oghomori, T., and Jinno, S. (2019). Cuprizone-induced demyelination in the mouse hippocampus is alleviated by phytoestrogen genistein. *Toxicol. Appl. Pharmacol.* 363, 98–110. doi: 10.1016/j.taap.2018.11.009
- Ouzounov, D. G., Wang, T., Wang, M., Feng, D. D., Horton, N. G., and Cruz-Hernández, J. C. (2017). In vivo three-photon imaging of activity of GCaMP6-labeled neurons deep in intact mouse brain. *Nat. Methods* 14, 388–390. doi: 10.1038/nmeth.4183
- Pachitariu, M., Stringer, C., Dipoppa, M., Schröder, S., Rossi, L. F., and Dalgleish, H. (2017). Suite2p: beyond 10,000 neurons with standard two-photon microscopy. *bioRxiv[Preprints]*
- Pilz, G.-A., Carta, S., Stäubli, A., Ayaz, A., Jessberger, S., and Helmchen, F. (2016). Functional imaging of dentate granule cells in the adult mouse hippocampus. *J. Neurosci.* 36, 7407–7414. doi: 10.1523/JNEUROSCI.3065-15.2016

- Podgorski, K., and Ranganathan, G. (2016). Brain heating induced by near-infrared lasers during multiphoton microscopy. *J. Neurophysiol.* 116, 1012–1023. doi: 10.1152/jn.00275.2016
- Praet, J., Guglielmetti, C., Berneman, Z., Van der Linden, A., and Ponsaerts, P. (2014). Cellular and molecular neuropathology of the cuprizone mouse model: clinical relevance for multiple sclerosis. *Neurosci. Biobehav. Rev.* 47, 485–505. doi: 10.1016/j.neubiorev.2014.10.004
- Provencio, J. J., Swank, V., Lu, H., Brunet, S., Baltan, S., and Khapre, R. V. (2016). Neutrophil depletion after subarachnoid hemorrhage improves memory via NMDA receptors. *Brain Behav. Immun.* 54, 233–242. doi: 10.1016/j.bbi.2016.02.007
- Redlich, M. J., and Lim, H. (2019). A method to measure myeloarchitecture of the murine cerebral cortex in vivo and ex vivo by intrinsic third-harmonic generation. *Front. Neuroanat.* 13:65. doi: 10.3389/fnana.2019.00065
- Sachs, H. H., Bercury, K. K., Popescu, D. C., Narayanan, S. P., and Macklin, W. B. (2014). A new model of cuprizone-mediated demyelination/remyelination. *ASN Neuro* 6:1759091414551955. doi: 10.1177/1759091414551955
- Skipuletz, T., Lindner, M., Kotsiari, A., Garde, N., Fokuhl, J., and Linsmeier, F. (2008). Cortical demyelination is prominent in the murine cuprizone model and is strain-dependent. *Am. J. Pathol.* 172, 1053–1061. doi: 10.2353/ajpath.2008.070850
- Staffen, W., Mair, A., Zauner, H., Unterrainer, J., Niederhofer, H., and Kutzelnigg, A. (2002). Cognitive function and fMRI in patients with multiple sclerosis: evidence for compensatory cortical activation during an attention task. *Brain* 125, 1275–1282. doi: 10.1093/brain/awf125
- Svoboda, K., and Yasuda, R. (2006). Principles of two-photon excitation microscopy and its applications to neuroscience. *Neuron* 50, 823–839. doi: 10.1016/j.neuron.2006.05.019
- Tekkok, S., and Krnjevic, K. (1995). Long-term potentiation in hippocampal slices induced by temporary suppression of glycolysis. *J. Neurophysiol.* 74, 2763–2766. doi: 10.1152/jn.1995.74.6.2763
- Thevenaz, P., Ruttimann, U. E., and Unser, M. (1998). A pyramid approach to subpixel registration based on intensity. *IEEE Trans Image Process* 7, 27–41. doi: 10.1109/83.650848
- Vega-Riquer, J. M., Mendez-Victoriano, G., Morales-Luckie, R. A., and Gonzalez-Perez, O. (2019). Five decades of cuprizone, an updated model to replicate demyelinating diseases. *Curr. Neuropharmacol.* 17, 129–141. doi: 10.2174/1570159X15666170717120343
- Wallin, M. T., Culpepper, W. J., Campbell, J. D., Nelson, L. M., Langer-Gould, A., and Marrie, R. A. (2019). The prevalence of MS in the United States. A population-based estimate using health claims data. *Neurology* 92, e1029–e1040. doi: 10.1212/wnl.00000000000007035
- Wekselblatt, J. B., Flister, E. D., Piscopo, D. M., and Niell, C. M. (2016). Large-scale imaging of cortical dynamics during sensory perception and behavior. *J. Neurophysiol.* 115, 2852–2866. doi: 10.1152/jn.01056.2015
- Xu, H., Yang, H.-J., Zhang, Y., Clough, R., Browning, R., and Li, X.-M. (2009). Behavioral and neurobiological changes in C57BL/6 mice exposed to cuprizone. *Behav. Neurosci.* 123, 418–429. doi: 10.1037/a0014477
- Ziehn, M. O., Avedisian, A. A., Dervin, S. M., O'dell, T. J., and Voskuhl, R. R. (2012a). Estriol preserves synaptic transmission in the hippocampus during autoimmune demyelinating disease. *Lab. Invest.* 92, 1234–1245. doi: 10.1038/labinvest.2012.76
- Ziehn, M. O., Avedisian, A. A., Dervin, S. M., Umeda, E. A., O'Dell, T. J., and Voskuhl, R. R. (2012b). Therapeutic testosterone administration preserves excitatory synaptic transmission in the hippocampus during autoimmune demyelinating disease. *J. Neurosci.* 32, 12312–12324. doi: 10.1523/JNEUROSCI.2796-12.2012
- Ziv, Y., Burns, L. D., Cocker, E. D., Hamel, E. O., Ghosh, K. K., and Kitch, L. J. (2013). Long-term dynamics of CA1 hippocampal place codes. *Nat. Neurosci.* 16, 264–266. doi: 10.1038/nn.3329

**Conflict of Interest:** The authors declare that the research was conducted in the absence of any commercial or financial relationships that could be construed as a potential conflict of interest.

Copyright © 2020 Das, Bastian, Trestan, Suh, Dey, Trapp, Baltan and Dana. This is an open-access article distributed under the terms of the Creative Commons Attribution License (CC BY). The use, distribution or reproduction in other forums is permitted, provided the original author(s) and the copyright owner(s) are credited and that the original publication in this journal is cited, in accordance with accepted academic practice. No use, distribution or reproduction is permitted which does not comply with these terms.





# A Bright and Colorful Future for G-Protein Coupled Receptor Sensors

Luca Ravotto<sup>1</sup>, Loïc Duffet<sup>1</sup>, Xuehan Zhou<sup>1</sup>, Bruno Weber<sup>1,2</sup> and Tommaso Patriarchi<sup>1,2\*</sup>

<sup>1</sup> Institute of Pharmacology and Toxicology, University of Zurich, Zurich, Switzerland, <sup>2</sup> Neuroscience Center Zurich, Zurich, Switzerland

Neurochemicals have a large impact on brain states and animal behavior but are notoriously hard to detect accurately in the living brain. Recently developed genetically encoded sensors obtained from engineering a circularly permuted green fluorescent protein into G-protein coupled receptors (GPCR) provided a vital boost to neuroscience, by innovating the way we monitor neural communication. These new probes are becoming widely successful due to their flexible combination with state of the art optogenetic tools and *in vivo* imaging techniques, mainly fiber photometry and 2-photon microscopy, to dissect dynamic changes in brain chemicals with unprecedented spatial and temporal resolution. Here, we highlight current approaches and challenges as well as novel insights in the process of GPCR sensor development, and discuss possible future directions of the field.

## OPEN ACCESS

### Edited by:

Elizabeth C. Carroll,  
Delft University of Technology,  
Netherlands

### Reviewed by:

Terence Hébert,  
McGill University, Canada  
Josh Levitz,  
Weill Cornell Medicine, Cornell  
University, United States

### \*Correspondence:

Tommaso Patriarchi  
patriarchi@pharma.uzh.ch

### Specialty section:

This article was submitted to  
Cellular Neurophysiology,  
a section of the journal  
Frontiers in Cellular Neuroscience

**Received:** 03 January 2020

**Accepted:** 05 March 2020

**Published:** 20 March 2020

### Citation:

Ravotto L, Duffet L, Zhou X,  
Weber B and Patriarchi T (2020) A  
Bright and Colorful Future  
for G-Protein Coupled Receptor  
Sensors. *Front. Cell. Neurosci.* 14:67.  
doi: 10.3389/fncel.2020.00067

**Keywords:** neurotransmitters, neuromodulators, GPCRs, fluorescent proteins, genetically encoded sensors, *in vivo* imaging

## INTRODUCTION

A variety of neurochemicals, including transmitters, modulators, peptides and hormones, are constantly released within the brain during neuronal and glial communication, and play a fundamental role in coordinating physiological brain functions. Tools for monitoring the dynamic changes of individual neurochemicals are therefore highly desirable. For decades fast-scan cyclic voltammetry and microdialysis have been the gold-standard techniques used for measuring the extracellular concentrations of neurochemicals during animal behavior (Kehr and Yoshitake, 2013). However, intrinsic challenges of these analytical chemistry techniques, such the limited molecular specificity and number of detectable neurochemicals for voltammetry (Carter and Shieh, 2010), and poor temporal resolution for microdialysis (Chefer et al., 2009), as well as the low spatial resolution in both systems generated a great need for new technologies capable of bridging these gaps. Specific advantages and limitations of these techniques for monitoring individual neurotransmitters in brain tissue are reviewed in Zeng et al. (2019).

Optical microscopy techniques in combination with genetically encoded sensors are emerging as a powerful solution that can elegantly answer this need. In particular the recently introduced genetically encoded sensors based on a single circularly permuted green fluorescent protein (cpGFP) engineered into G-protein coupled receptors (GPCR), which for simplicity here we refer to as “GPCR sensors,” can enable the detection of neuromodulatory molecules at high resolution in awake behaving animals (Patriarchi et al., 2018; Sun et al., 2018). One of the greatest benefits of these new genetically encoded sensors is their unique ability to detect spatially resolved neuromodulatory signals at high-resolution, which was demonstrated using two-photon imaging in the fly brain (Sun et al., 2018; Handler et al., 2019) and in the mouse cortex (Patriarchi et al., 2018). Exciting new

questions in the field can now be addressed thanks to the level of spatial and temporal resolution allowed by these tools, such as whether neuromodulatory signals can be transmitted in a cell-type specific manner or heterogeneously from neuronal projections.

These tools purposely combine the high ligand-binding affinity and molecular specificity which were fine-tuned in the receptor by natural evolution, with the large sensitivity typical of intensity-based probes engineered from cpGFP (Marvin et al., 2011; Chen et al., 2013b; Marvin et al., 2013; Kostyuk et al., 2019). Because GPCRs are a very large family of receptors (class-A alone comprises approximately 350 members without including odorant receptors (Pándy-Szekeres et al., 2018), for an overview see **Figures 1A,B**), in principle they represent a largely unexplored pool from which novel fluorescent sensors could be developed to probe a vast amount of endogenous neurochemicals. Although FRET or BRET-based biosensors of GPCR activation have been available for a long time (Vilardaga et al., 2003; Sleno et al., 2016), to date only a few GPCR sensors have been introduced for *in vivo* sensing of dopamine (Patriarchi et al., 2018; Sun et al., 2018), acetylcholine (Jing et al., 2018, 2019a), and norepinephrine (Feng et al., 2019). The ability to reveal the intimate spatial and temporal details of neurotransmitter release in living animals is only possible with this new type of sensors and not with previously available FRET or BRET-based probes, due to their limited dynamic range (Jing et al., 2019b). Thus, the innovative field of GPCR sensor development represents a true technological breakthrough and, while still in its early days, is likely to continue expanding to cover many more neurochemical ligands as well as toward bright and colorful new directions.

## CURRENT STRATEGIES AND BOTTLENECKS IN GPCR-SENSOR DEVELOPMENT

The first examples of GPCR sensors were only recently introduced when two similar but independent engineering approaches were published almost simultaneously (Patriarchi et al., 2018; Sun et al., 2018). These studies produced the two alternative genetically encoded dopamine sensor families named dLight1 and GRAB-DA1. The general concept behind both approaches is similar: inserting cpGFP at specific locations between the transmembrane helix 5 (TM5) and 6 (TM6) of a human dopamine receptor is used as a mean to generate sensitive fluorescent reporters of receptor conformational change. Due to their genetically encoded nature these sensors can be easily expressed in living animals, and because conformational motion at the interface of TM5 and TM6 is a classical feature of GPCR activation and reflects ligand binding (Venkatakrisnan et al., 2013), their fluorescent signals can be used as a proxy of endogenous dopamine dynamics.

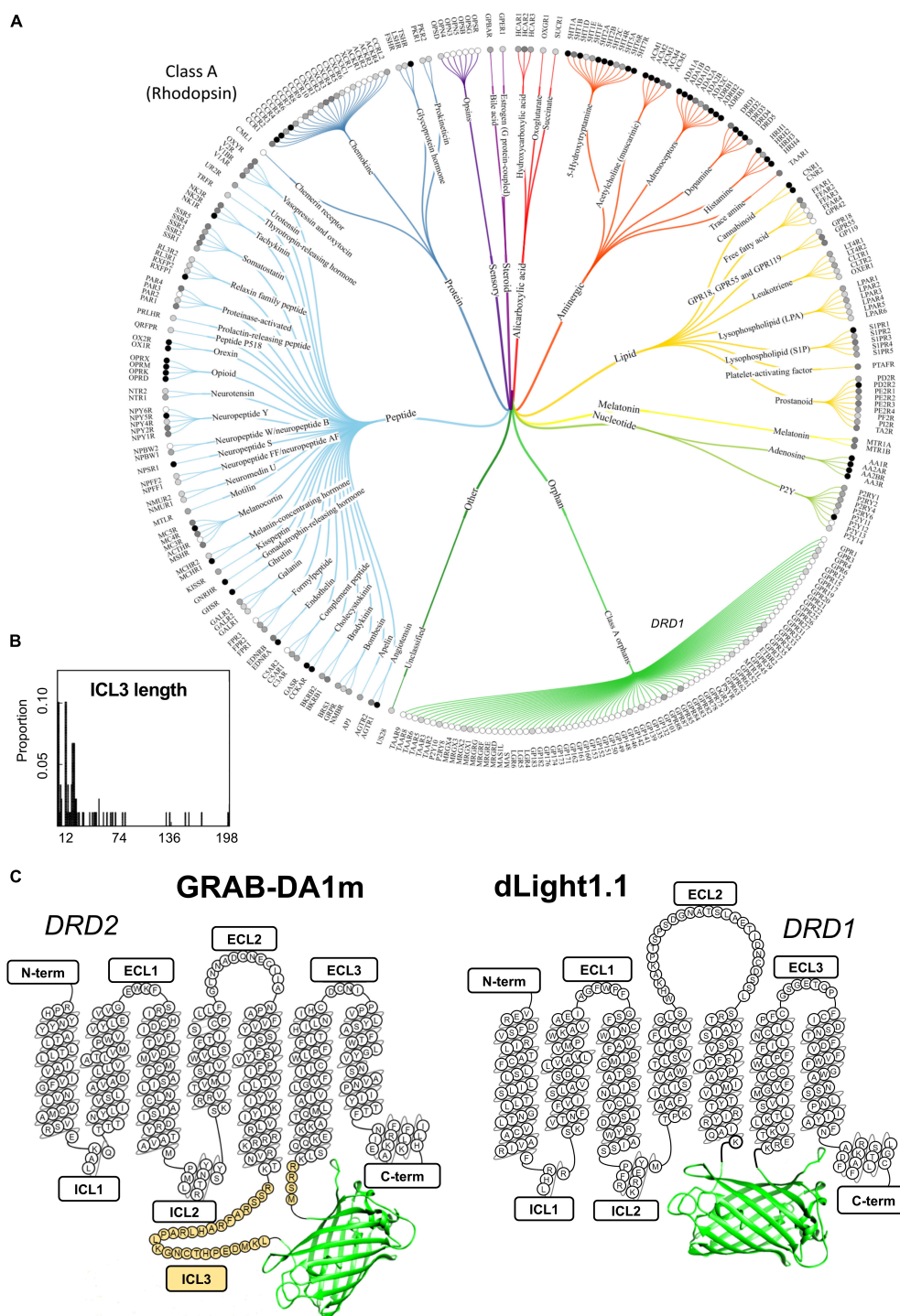
When compared side by side the approaches taken to develop the two classes of sensors have important differences. In dLight1 cpGFP completely replaces the third intracellular loop (ICL3) as well as small portions of TM5 and TM6 of the D1 dopamine

receptor (DRD1) (Patriarchi et al., 2018), while in GRAB-DA1 it is inserted within the ICL3 of the D2 dopamine receptor (DRD2), and a large stretch of 30 aminoacids is carried over from the original ICL3 (**Figure 1C**; Sun et al., 2018). Similar to GRAB-DA1 sensors, the approaches taken for developing both the acetylcholine and norepinephrine sensors also relied on the presence of a variable amount of ICL3 residues surrounding cpGFP (Jing et al., 2018; Feng et al., 2019).

In all cases, the final goal is to maximize the coupling between receptor conformational change and the fluorescence response of cpGFP. This process, builds on previous knowledge established for genetically encoded sensors of similar design (Chen et al., 2013b; Marvin et al., 2013) and mostly involves the generation of libraries where the linker regions connecting GPCR to cpGFP are subject to sequence randomization and the resulting sensor variants are individually screened for their fluorescence response.

Strikingly, the sensor design used in the development of dLight1, which is completely devoid of ICL3 residues, was demonstrated to be quite versatile. In fact, the simple grafting of a “fluorescent protein module” (i.e., cpGFP flanked by short linkers derived from the dopamine sensor) into other GPCR subtypes made it possible to rapidly generate preliminary sensors for norepinephrine, serotonin, melatonin, and opioid neuropeptides (Patriarchi et al., 2018). Although these prototype probes may not be sensitive enough for *in vivo* application, they may represent an ideal starting point for further optimization through targeted mutagenesis at a reduced number of sites, and thus could provide a useful shortcut in a process that is otherwise very costly and time-consuming. Considering that the ICL3 is an extremely variable region among different class-A GPCRs (**Figure 1B**) both in terms of size and composition (Otaki and Firestein, 2001; Unal and Karnik, 2012), and that this region is predicted to be intrinsically disordered, based on sequence composition (Jaakola et al., 2005), the presence of a considerable portion of the ICL3 in GRAB-DA1 is likely to prevent the versatile grafting of the fluorescent protein module for rapid engineering of novel GPCR sensors.

The concept of versatile engineering is somewhat reflected in the field of GPCR crystallography, where long and disordered ICL3 sequences are counterproductive and are thus commonly replaced with small fusion proteins (e.g., T4 lysozyme; Thorsen et al., 2014), or stabilized with the aid of nanobodies (Manglik et al., 2017). We believe that, in order to be most effective, future engineering efforts should follow a “semi-rational” approach where the starting point for cpGFP insertion into the TM5-TM6 interface of a GPCR is set by the receptor sequence (e.g., the positively charged residues identified during the development of dLight1; Patriarchi et al., 2018) and site-directed mutagenesis screening follows. In this regard, a deeper understanding of the relationship between the receptor, linker, and fluorescent protein components of the sensor, which could be obtained by structural studies. For instance a sensor structure obtained by cryogenic electron microscopy would provide important information on the specific orientation of charged, polar and hydrophobic residue sidechains at the GPCR/cpGFP interface, which could guide future sensor optimization efforts. The current lack of structural information for both dLight1 and GRAB-DA1



**FIGURE 1** | A snapshot of the current GPCR sensor engineering landscape. **(A)** Class-A GPCR family tree. Receptors are grouped and branches are color-coded based on ligand type. Gray-scale circles in front of the receptor name represent the number of currently available ligands (white: 0, light gray: >100, gray: >500 and black: >1000). Reproduced from Pándy-Szekeres et al. (2018). **(B)** Length distribution of ICL3 (region where cpGFP is inserted during the sensor engineering process) for several class-A GPCRs highlights the high degree of variability in this region among different receptors. The number of ICL3 aminoacid residues is shown on the x axis, while the relative probability of each length from a total of 89 analyzed GPCRs is shown on the y axis. Reproduced with permission from Otaki and Firestein (2001). **(C)** Schematic depiction of representative members of the two classes of genetically encoded dopamine sensor classes developed to date: dLight1.1 and GRAB-DA1m. Aminoacid residues of sensor sequence belonging to the original dopamine receptors (DRD1 and DRD2) are shown in the snake-plot. The insertion position of circularly permuted green fluorescent protein (cpGFP) is indicated for both sensor types. N-term, N-terminus; ICL, intracellular loop; ECL, extracellular loop; C-term, C-terminus. Third intracellular loop, ICL3, is highlighted in yellow.

sensors, makes it very difficult to achieve a clear understanding of how the receptor conformational change is capable of triggering the fluorescence of cpGFP, and to elucidate the role that linker regions and the residual ICL3 residues play in this process.

Overall, every screening approach in GPCR sensor development faces the same obstacle: a large number of variants to be screened and the low throughput of current mammalian cell-based screening assays. To overcome this hurdle possible strategies could make use of a recently established screening assay, combining Fluorescence-Activated Cell Sorting (FACS) with robotic cell-picking, which was successfully used to evolve voltage sensors derived from integral membrane proteins (Piatkevich et al., 2018). However, implementation of a robotic arm for cell-picking may not be easily applicable in many labs due to the inherent technical complexity of the system. As an alternative, we envision that in the future it may become advantageous to devise novel FACS-based screening methods, perhaps in combination with microfluidic channels that can cyclically integrate two independent cell-sorting steps. Such innovative assay concepts could in theory enable selection of sensor variants based on fluorescence in both an active and inactive state from a library pool of  $10^6$ – $10^9$  cells, which would ideally suit GPCR sensor development and dramatically increase the scale of the process.

Although all attention of current GPCR sensor screening approaches focuses on obtaining sensors with the largest maximal fluorescence changes, this property is not by itself sufficient to guarantee success when testing the probe in the living brain. The apparent affinity of the probe is another important factor to be considered when imaging neuromodulators. Owing to its design each probe can only reliably work within a narrow concentration range. Because the levels of release for endogenous neuromodulators are variable among different brain regions, mostly depending on the abundance of neuromodulatory projections in the area, multiple probes with complementary affinity ranges need to be developed in order to most sensitively detect the same neuromodulator in different regions. Up to now, sensors with different affinity ranges have been obtained mostly by using different receptor subtypes as a starting point (in the case of dopamine sensors, DRD1, DRD2, DRD4) (Patriarchi et al., 2018; Sun et al., 2018), and in few cases have been tuned by mutagenesis of one specific site in the GPCR moiety (Patriarchi et al., 2018; Feng et al., 2019). Future sensor development could tremendously benefit from computational modeling-based approaches aimed at fine tuning the sensor apparent affinity or even ligand-selectivity (Feng et al., 2017).

## THE OPPORTUNITY OF A LIFETIME

A deeper understanding of the basic photophysical properties of GPCR sensors may lead to novel applications based on different fluorescence properties (e.g., fluorescence lifetime) and open new research directions. In fact, while intensity-based fluorescence readouts can provide valuable information about the dynamics of biological systems using simple instrumentation, they suffer from limitations (e.g., wavelength-dependent

absorption and scattering, different detector sensitivities or expression dependence for single-wavelength sensors) that make them unsuitable for quantitative measurements of analyte concentrations (Waters, 2009; Yellen and Mongeon, 2015). These drawbacks are particularly critical for deep brain imaging or when comparing different samples or measurements done with different instrumentation. In the case of GPCR sensors, the kinetics of a biological response to stimulation can be reliably accessed (Patriarchi et al., 2018; Sun et al., 2018), but important parameters such as the absolute extent of the response or the baseline levels of the analyte are much more difficult to retrieve. On the contrary, fluorescence lifetime is an intensive rather than extensive physical quantity, which reflects the kinetics of excited to ground state relaxation and is independent on the absolute intensity of the signal (Lakowicz, 2006). This latter factor is critical as it eliminates the effects of laser fluctuations, tissue absorption and detector sensitivity. Also, in a microscopy or fiber photometry setup, the lifetime is much less affected by tissue scattering than intensity (Dowling et al., 1997; Vishwanath et al., 2002).

All these advantages have sparked a growing interest in techniques like fluorescence lifetime imaging (FLIM) (Berezin and Achilefu, 2010; Borst and Visser, 2010; Chen et al., 2013a) or fluorescence lifetime fiber photometry (FLiP) (Brown et al., 1994; Saxl et al., 2011; Lagarto et al., 2019; Lee et al., 2019a,b), which have been successfully applied to obtain more quantitative information on analyte concentrations (Díaz-García et al., 2017; Melo et al., 2017) or protein interactions (Yasuda et al., 2006; Sun et al., 2011; Walther et al., 2011). Recent studies investigated the optimization and application of fluorescent protein (FP) pairs to produce FLIM sensors based on fluorescence resonance energy transfer (FLIM-FRET) (Visser et al., 2010; George Abraham et al., 2015; Martin et al., 2018). The process of FRET introduces an additional path for the excited state decay of a “donor” fluorophore, due to the transfer of excitation energy to an “acceptor.” Due to the relationship between quantum yield and lifetime of a fluorophore (Lakowicz, 2006; Noomnarm and Clegg, 2009), the effect of FRET on lifetime is particularly straightforward (the higher the FRET efficiency, the shorter the donor lifetime) and the design of FLIM-FRET sensors is, at least in first approximation, conceptually simple.

On the other hand, the field of FLIM sensors based on circularly permuted fluorescent proteins (cpFPs) is still largely underdeveloped. While some groups have reported the use of cpFP sensors with FLIM readout (Tantama et al., 2011; Mongeon et al., 2016; Melo et al., 2017; Díaz-García et al., 2019), the sensor characterization has been mostly limited to empirical calibrations, and no clear guidelines for the choice of FPs that would give optimal lifetime changes currently exist. In our opinion, this is largely due to the complexity of the problem. While in FRET sensors a single photophysical process is responsible for the observed changes, in cpFPs a complex combination of effects needs to be taken into account (Barnett et al., 2017; Molina et al., 2019). In a cpFP sensor, the acid and basic forms of the chromophore exist in equilibrium. Each form has its own absorption spectrum and fluorescence quantum yield (usually, only the basic form has a high quantum



yield and is defined as “emissive” form), and the equilibrium concentrations can change upon opening and closing of the protein barrel (**Figure 2A**). Interconversion between the two forms can happen also in the excited state (Meech, 2009; Barnett et al., 2017), so that the excitation of the acid form can result in the emission of the basic one. In the case of multiphoton absorption, also the absorption cross-sections can depend on the barrel conformation (Molina et al., 2019). As a consequence of this complexity, the relation between intensity and lifetime is very difficult to predict.

Ignoring for simplicity excited-state dynamics and multiphoton effects, the photophysical basis of sensor function can be described by two limit cases (**Figure 2B**). In the first one, the changes in the fluorescence intensity of the sensor are due exclusively to changes in the relative abundance of the acid-base equilibrium forms of the chromophore upon analyte binding, while the quantum yield of the basic form (the emissive one) remains unaffected (**Figure 2A**). In this scenario, while fluorescence intensity changes can be large (and wavelength dependent), no change in lifetime is expected. In the second limit case, there are no changes in the acid-base equilibrium upon analyte binding, but the fluorescence quantum yield of the basic form changes. While this is not always the case, very often variations in fluorescence quantum yield are accompanied by variations in lifetime (Lakowicz, 2006). Real world scenarios lie in between these two extremes, and thus FLIM sensors with smaller or larger (and more or less wavelength-dependent) lifetime changes can in principle be developed based on these considerations.

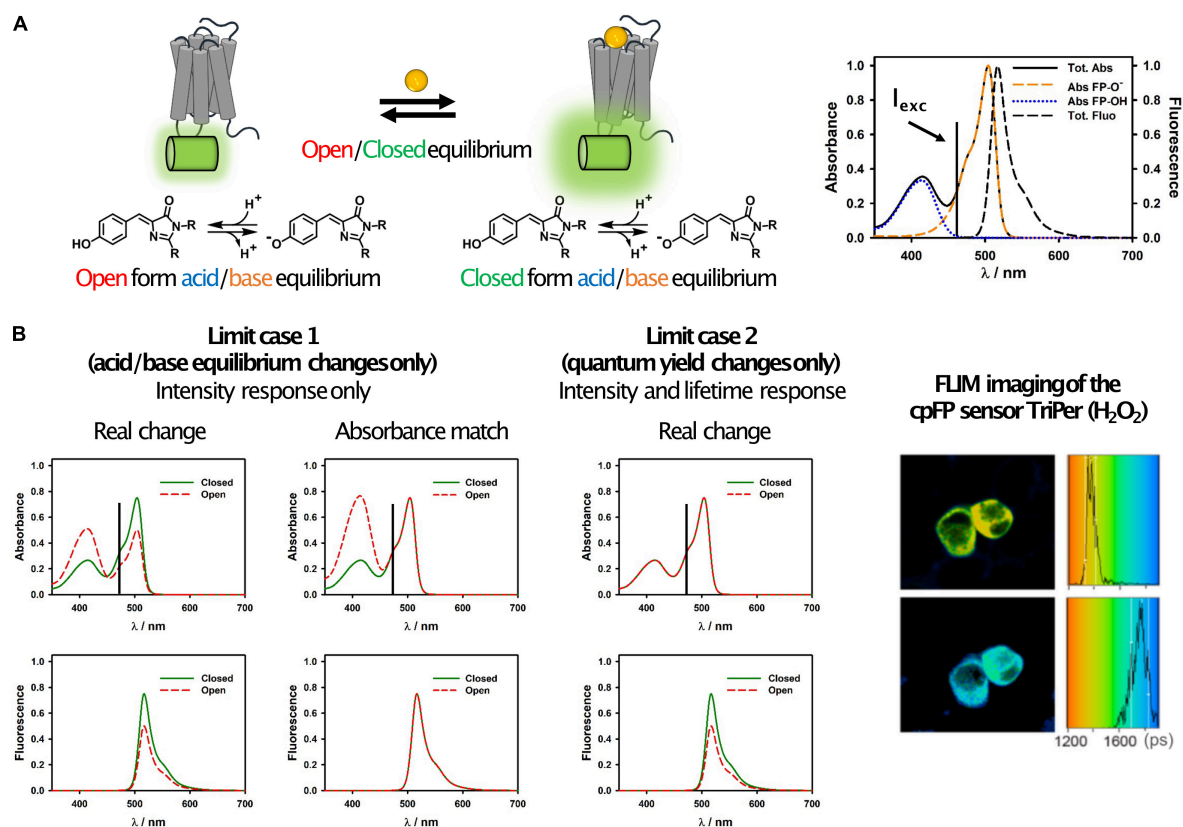
Careful photophysical studies (Barnett et al., 2017; Molina et al., 2019) have shown that even for seemingly similar cpFP sensors the mechanisms that determine the fluorescence response can change considerably, and that good candidates for FLIM definitely exist. We expect that in the future more studies will be devoted to this specific aspect and cpFPs optimized for FLIM readouts will start to emerge. This will in turn boost the field of GPCR-based sensors, paving the way toward a more quantitative understanding of the role of neurochemicals in brain functions. Particularly for physiological dynamics that do not manifest themselves in fast and quasi-binary transients (as is often the case for calcium signals), quantification of molar concentrations of the target molecule is essential. This will allow for reliable comparisons among different brain areas, different animals or data acquired by different labs, and for analyzing data obtained in chronic long-term imaging over days and months.

## THE PUSH TOWARD RED-SHIFTED WAVELENGTHS

It is reasonable to imagine that in the near future the development of GPCR sensors will also expand toward both red and near-infrared (NIR) wavelengths, by taking advantage of a large variety of fluorescent proteins available at these wavelengths (Rodriguez et al., 2017). This has for instance been the case for genetically

encoded calcium sensors, which have recently been developed at near-infrared wavelengths based on mIFP (Qian et al., 2019) or GAF-FP (Subach et al., 2019). Such GPCR sensors would benefit from inherent advantages of using red-shifted light for excitation, such as increased penetration depth and lower phototoxicity. They would also increase the quality and quantity of potential applications. For instance, the availability of red-shifted GPCR sensors would enable “mix and match” approaches where green and red sensors for two different neurotransmitters could be combined in dual-color fluorescence imaging, similar to what has been previously achieved for red calcium sensors (Dana et al., 2016). This approach could be used for instance to resolve long-standing challenges, such as the unequivocal proof of co-release between two neurotransmitters. A prominent example of this is the case of dopamine and norepinephrine: previous studies imply that the two catecholamines can be synthesized and simultaneously released by the locus coeruleus (Kempadoo et al., 2016; Takeuchi et al., 2016), however, direct evidence for this is lacking as well as the important information of whether this phenomenon is constitutive or regulated.

The landscape of raw materials for building GPCR sensors is constantly evolving, as new fluorescent and chromoproteins are added to the plate (Lambert et al., 2019). Development of GPCR sensors based on near-infrared fluorescent proteins could in principle expand the solution space for multiplex imaging, and allow us to image up to three different aspects of neural communication and activity simultaneously. In addition, the NIR window (650–900 nm) offers improved optical transmission properties in living animals because of the relatively lower absorption component of endogenous molecules such as hemoglobin or melanin (Ntzachristos et al., 2003). We predict that the development of GPCR sensors absorbing in this wavelength range, that could for instance be engineered based on bacterial phytochromes (e.g., BphP1; Yao et al., 2016), will enable successful application of the probes with optoacoustic imaging, a scalable imaging modality capable of resolving whole-brain activity three-dimensionally at millisecond time scale and 100  $\mu\text{m}$  resolution non-invasively (i.e., without the need for optical fiber or gradient index lense implantation) (Gottschalk et al., 2019). Another advantage of red/NIR FPs is that their photophysical properties are optimal for three-photon absorption (3PA) in the 1700 nm optical window (Horton et al., 2013; Deng et al., 2019), which is recently emerging as a superior technique for deep *in vivo* imaging (Horton et al., 2013; Miller et al., 2017). Due to the much reduced scattering and absorption, 3PA at these wavelengths is limited only by signal-to-noise ratio (which depends on protein brightness) up to more than 3 mm depth (Horton et al., 2013), and structural imaging of neurons has already been demonstrated at a depth of 1.4 mm (Horton et al., 2013), reaching the subcortical region of the mouse brain. Especially if combined with FLIM detection (Ni et al., 2019), that eliminates artifacts due to absorption and scattering, 3PA at 1700 nm would constitute a promising strategy for non-invasive imaging of neurochemicals in deep brain regions, while at the same time improving the cell resolution ability in densely labeled samples with respect to two-photon absorption (Ouzounov et al., 2017).



**FIGURE 2 |** Simplified photophysical description of cpFP sensors with emphasis on FLIM. **(A)** Schematic representation of the equilibrium occurring in GPCR sensors (left) and of their spectroscopic properties (right). It can be observed how the absorption spectrum is actually the sum of two bands, one due to the protonated (acid) form of the chromophore and one to the deprotonated (basic) one. The latter is also the only emissive form in most cpFPs used in sensors. This is certainly true if the sensor is excited at longer wavelengths, as shown in these examples, where only the basic form absorbs. **(B)** Representative spectral changes for the two limit cases described in the text (left), and FLIM images and histograms of RINm5f cells expressing the cpFP sensor TriPer before (right, top) and after (right, bottom) exposure to 0.2 mM H<sub>2</sub>O<sub>2</sub> (reproduced without modifications from Melo et al., 2017; under Creative Commons license: <http://creativecommons.org/licenses/by/4.0/>). Possible candidates for FLIM can be identified by looking at the changes of the absorption and fluorescence spectra of the sensors upon analyte binding. If only the acid/base equilibrium changes, but not the quantum yield of the basic form, then no lifetime change is expected (limit case 1). An easy way to conceptualize this phenomenon is that if the absorbance of the open and closed forms at the excitation wavelength would be the same (i.e., if the two would absorb the same number of photons), then their fluorescence intensity would also be the same (column “absorbance match”). On the other hand, if there are changes in the fluorescence intensity but not in the acid/base equilibrium (limit case 2), then changes in the quantum yield are occurring and will likely (but not necessarily) result in a lifetime change. We note that this is a simplified scheme which takes into account only a subset of the photophysical processes occurring in cpFP sensors, thus: (a) unexpected results may occur by strictly following this simplified scheme as a general rule for all sensors, (b) lifetime changes can occur also as result of other mechanisms.

## DISCUSSION

Considering the important and multifaceted roles that neurochemicals play in the nervous system, the thirst for novel sensor types capable of probing these molecules in their natural environment is likely to continue increasing. Although GPCR sensors are an elegant technological solution, some caveats need to be considered. One example is the potential interference with endogenous neuromodulatory signaling of target cells, which has not yet been extensively characterized in living animals. Our hope is that, with time, a careful evaluation of the side-effects of GPCR sensor expression will elucidate best experimental practices that can allow us to make the most out of these tools without significantly altering the system under investigation. For a more in-depth discussion of the limitations

of these tools please refer to our previously published protocols (Patriarchi et al., 2019). All things considered, we envision a bright future for GPCR sensor development, with important achievements to be expected along at least three directions. First, the continuous improvement of existing GPCR sensors (in terms of increased dynamic range, basal brightness, kinetics, photostability, etc.) will follow an analogous path to that of the GCaMP family of calcium sensors (Dana et al., 2019), and will build upon the continuous discovery and directed evolution of novel and improved variants of fluorescent proteins and chromoproteins. Second, in striking difference with calcium sensors, the optical measurement of the actual concentrations of neurochemicals *in vivo*, rather than merely their dynamic behavior, is a much needed task. The demonstration that GPCR sensors can be utilized in quantitative techniques such as FLIM

and the design of specifically optimized sensors is still lacking and will likely be a central topic in the field in the near future. Third, the need for multiplexed imaging will not only spur the design of novel GPCR sensors to probe an increasing number of neurochemicals, but also the diversification of existing sensors in terms of emission wavelengths. The latter will dramatically expand the possibilities to simultaneously image multiple neurochemicals, or observe how their dynamics correlate with other important phenomena such as calcium or metabolite transients. While the path ahead for this new class of sensors certainly presents its challenges, some of which were highlighted in this work, their unique features and wide applicability will keep us and others motivated to develop new and improved variations which will clearly contribute to shape a bright and colorful future for neurochemical imaging.

## REFERENCES

- Barnett, L. M., Hughes, T. E., and Drobizhev, M. (2017). Deciphering the molecular mechanism responsible for GCaMP6m's  $\text{Ca}^{2+}$ -dependent change in fluorescence. *PLoS One* 12:e0170934. doi: 10.1371/journal.pone.0170934
- Berezin, M. Y., and Achilefu, S. (2010). Fluorescence lifetime measurements and biological imaging. *Chem. Rev.* 110, 2641–2684. doi: 10.1021/cr900343z
- Borst, J. W., and Visser, A. J. W. G. (2010). Fluorescence lifetime imaging microscopy in life sciences. *Meas. Sci. Technol.* 21:102002. doi: 10.1088/0957-0233/21/10/102002
- Brown, R. S., Brennan, J. D., and Krull, U. J. (1994). An optical fiber-based spectrometer for measurement of fluorescence lifetimes. *Microchem. J.* 50, 337–350. doi: 10.1006/mchj.1994.1098
- Carter, M., and Shieh, J. C. (2010). "Chapter 3 - stereotaxic surgeries and *In Vivo* techniques," in *Guide to Research Techniques in Neuroscience*, eds M. Carter, and J. C. Shieh, (New York, NY: Academic Press), 73–90. doi: 10.1016/b978-0-12-374849-2.00003-3
- Chefer, V. I., Thompson, A. C., Zapata, A., and Shippenberg, T. S. (2009). Overview of brain microdialysis. *Curr. Protoc. Neurosci.* 47, 7.7.1–7.1.28. doi: 10.1002/0471142301.ns0701s47
- Chen, L.-C., Lloyd, W. R., Chang, C.-W., Sud, D., and Mycek, M.-A. (2013a). Fluorescence lifetime imaging microscopy for quantitative biological imaging. *Methods Cell Biol.* 114, 457–488. doi: 10.1016/B978-0-12-407761-4.00020-8
- Chen, T.-W., Wardill, T. J., Sun, Y., Pulver, S. R., Renninger, S. L., Baohan, A., et al. (2013b). Ultrasensitive fluorescent proteins for imaging neuronal activity. *Nature* 499, 295–300. doi: 10.1038/nature12354
- Dana, H., Mohar, B., Sun, Y., Narayan, S., Gordus, A., Hasseman, J. P., et al. (2016). Sensitive red protein calcium indicators for imaging neural activity. *eLife* 5:e12727. doi: 10.7554/eLife.12727
- Dana, H., Sun, Y., Mohar, B., Hulse, B. K., Kerlin, A. M., Hasseman, J. P., et al. (2019). High-performance calcium sensors for imaging activity in neuronal populations and microcompartments. *Nat. Methods* 16, 649–657. doi: 10.1038/s41592-019-0435-6
- Deng, X., Zhuang, Z., Liu, H., Qiu, P., and Wang, K. (2019). Measurement of 3-photon excitation and emission spectra and verification of Kasha's rule for selected fluorescent proteins excited at the 1700-nm window. *Opt. Express* 27, 12723–12731. doi: 10.1364/OE.27.012723
- Díaz-García, C. M., Lahmann, C., Martínez-François, J. R., Li, B., Koveal, D., Nathwani, N., et al. (2019). Quantitative *in vivo* imaging of neuronal glucose concentrations with a genetically encoded fluorescence lifetime sensor. *J. Neurosci. Res.* 97, 946–960. doi: 10.1002/jnr.24433
- Díaz-García, C. M., Mongeon, R., Lahmann, C., Koveal, D., Zucker, H., and Yellen, G. (2017). Neuronal stimulation triggers neuronal glycolysis and not lactate uptake. *Cell Metab.* 26, 361.e4–374.e4. doi: 10.1016/j.cmet.2017.06.021
- Dowling, K., Hyde, S. C. W., Dainty, J. C., French, P. M. W., and Hares, J. D. (1997). 2-D fluorescence lifetime imaging using a time-gated image intensifier. *Opt. Commun.* 135, 27–31. doi: 10.1016/S0030-4018(96)00618-9

## AUTHOR CONTRIBUTIONS

TP and LR wrote the manuscript with contributions from XZ, LD, and BW.

## FUNDING

TP was supported by the Hartmann Müller-Stiftung and the Olga Mayenfisch Stiftung.

## ACKNOWLEDGMENTS

We thank the University of Zurich for financial support.

- Feng, J., Zhang, C., Lischinsky, J. E., Jing, M., Zhou, J., Wang, H., et al. (2019). A genetically encoded fluorescent sensor for rapid and specific *In Vivo* detection of norepinephrine. *Neuron* 102, 745.e8–761.e8. doi: 10.1016/j.neuron.2019.02.037
- Feng, X., Ambia, J., Chen, K.-Y. M., Young, M., and Barth, P. (2017). Computational design of ligand-binding membrane receptors with high selectivity. *Nat. Chem. Biol.* 13, 715–723. doi: 10.1038/nchembio.2371
- George Abraham, B., Sarkisyan, K. S., Mishin, A. S., Santala, V., Tkachenko, N. V., and Karp, M. (2015). Fluorescent protein based FRET pairs with improved dynamic range for fluorescence lifetime measurements. *PLoS One* 10:e0134436. doi: 10.1371/journal.pone.0134436
- Gottschalk, S., Degtyaruk, O., Mc Larney, B., Rebling, J., Hutter, M. A., Deán-Ben, X. L., et al. (2019). Rapid volumetric optoacoustic imaging of neural dynamics across the mouse brain. *Nat. Biomed. Eng.* 3, 392–401. doi: 10.1038/s41551-019-0372-9
- Handler, A., Graham, T. G. W., Cohn, R., Morante, I., Siliciano, A. F., Zeng, J., et al. (2019). Distinct dopamine receptor pathways underlie the temporal sensitivity of associative learning. *Cell* 178, 60.e19–75.e19. doi: 10.1016/j.cell.2019.05.040
- Horton, N. G., Wang, K., Kobat, D., Clark, C. G., Wise, F. W., Schaffer, C. B., et al. (2013). *In vivo* three-photon microscopy of subcortical structures within an intact mouse brain. *Nat. Photonics* 7, 205–209. doi: 10.1038/nphoton.2012.336
- Jaakola, V.-P., Prilusky, J., Sussman, J. L., and Goldman, A. (2005). G protein-coupled receptors show unusual patterns of intrinsic unfolding. *Protein Eng. Des. Sel.* 18, 103–110. doi: 10.1093/protein/gzi004
- Jing, M., Li, Y., Zeng, J., Huang, P., Skirzewski, M., Peng, W., et al. (2019a). An optimized acetylcholine sensor for monitoring *in vivo* cholinergic activity. *bioRxiv* [preprint],
- Jing, M., Zhang, Y., Wang, H., and Li, Y. (2019b). G-protein-coupled receptor-based sensors for imaging neurochemicals with high sensitivity and specificity. *J. Neurochem.* 151, 279–288. doi: 10.1111/jnc.14855
- Jing, M., Zhang, P., Wang, G., Feng, J., Mesik, L., Zeng, J., et al. (2018). A genetically encoded fluorescent acetylcholine indicator for *in vitro* and *in vivo* studies. *Nat. Biotechnol.* 36, 726–737. doi: 10.1038/nbt.4184
- Kehr, J., and Yoshitake, T. (2013). Monitoring molecules in neuroscience: historical overview and current advancements. *Front. Biosci.* 5, 947–954. doi: 10.2741/e674
- Kempadoo, K. A., Mosharov, E. V., Choi, S. J., Sulzer, D., and Kandel, E. R. (2016). Dopamine release from the locus coeruleus to the dorsal hippocampus promotes spatial learning and memory. *Proc. Natl. Acad. Sci. U.S.A.* 113, 14835–14840. doi: 10.1073/pnas.1616511114
- Kostyuk, A. I., Demidovich, A. D., Kotova, D. A., Belousov, V. V., and Bilan, D. S. (2019). Circularly permuted fluorescent protein-based indicators: history, principles, and classification. *Int. J. Mol. Sci.* 20:4200. doi: 10.3390/ijms20174200

- Lagarto, J. L., Credi, C., Villa, F., Tisa, S., Zappa, F., Shcheslavskiy, V., et al. (2019). Multispectral depth-resolved fluorescence lifetime spectroscopy using SPAD array detectors and fiber probes. *Sensors* 19:2678. doi: 10.3390/s19122678
- Lakowicz, J. R. (2006). *Principles of Fluorescence Spectroscopy*, 3rd Edn. New York, NY: Springer.
- Lambert, G. G., Depernet, H., Gotthard, G., Schultz, D. T., Navizet, I., Lambert, T., et al. (2019). *Aequorea victoria's* secrets. *bioRxiv* [preprint], doi: 10.1101/677344
- Lee, S. J., Chen, Y., Lodder, B., and Sabatini, B. L. (2019a). Monitoring behaviorally induced biochemical changes using fluorescence lifetime photometry. *Front. Neurosci.* 13:766. doi: 10.3389/fnins.2019.00766
- Lee, S. J., Lodder, B., Chen, Y., Patriarchi, T., Tian, L., and Sabatini, B. L. (2019b). Cell-type specific asynchronous modulation of PKA by dopamine during reward based learning. *bioRxiv* [preprint], doi: 10.1101/839035
- Manglik, A., Kobilka, B. K., and Steyaert, J. (2017). Nanobodies to study G protein-coupled receptor structure and function. *Annu. Rev. Pharmacol. Toxicol.* 57, 19–37. doi: 10.1146/annurev-pharmtox-010716-104710
- Martin, K. J., McGhee, E. J., Schwarz, J. P., Drysdale, M., Brachmann, S. M., Stucke, V., et al. (2018). Accepting from the best donor; analysis of long-lifetime donor fluorescent protein pairings to optimise dynamic FLIM-based FRET experiments. *PLoS One* 13:e0183585. doi: 10.1371/journal.pone.0183585
- Marvin, J. S., Borghuis, B. G., Tian, L., Cichon, J., Harnett, M. T., Akerboom, J., et al. (2013). An optimized fluorescent probe for visualizing glutamate neurotransmission. *Nat. Methods* 10, 162–170. doi: 10.1038/nmeth.2333
- Marvin, J. S., Schreiter, E. R., Echevarria, I. M., and Looger, L. L. (2011). A genetically encoded, high-signal-to-noise maltose sensor. *Proteins* 79, 3025–3036. doi: 10.1002/prot.23118
- Meech, S. R. (2009). Excited state reactions in fluorescent proteins. *Chem. Soc. Rev.* 38, 2922–2934. doi: 10.1039/b820168b
- Melo, E. P., Lopes, C., Gollwitzer, P., Lortz, S., Lenzen, S., Mehmeti, I., et al. (2017). TriPer, an optical probe tuned to the endoplasmic reticulum tracks changes in luminal H<sub>2</sub>O<sub>2</sub>. *BMC Biol.* 15:24. doi: 10.1186/s12915-017-0367-5
- Miller, D. R., Jarrett, J. W., Hassan, A. M., and Dunn, A. K. (2017). Deep tissue imaging with multiphoton fluorescence microscopy. *Curr. Opin. Biomed. Eng.* 4, 32–39. doi: 10.1016/j.cobme.2017.09.004
- Molina, R. S., Qian, Y., Wu, J., Shen, Y., Campbell, R. E., Drobizhev, M., et al. (2019). Understanding the fluorescence change in red genetically encoded calcium ion indicators. *Biophys. J.* 116, 1873–1886. doi: 10.1016/j.bpj.2019.04.007
- Mongeon, R., Venkatachalam, V., and Yellen, G. (2016). Cytosolic NADH-NAD(+) redox visualized in brain slices by two-photon fluorescence lifetime biosensor imaging. *Antioxid. Redox Signal.* 25, 553–563. doi: 10.1089/ars.2015.6593
- Ni, H., Xu, Z., Li, D., Chen, M., Tang, B. Z., and Qian, J. (2019). Aggregation-induced emission luminogen for in vivo three-photon fluorescence lifetime microscopic imaging. *J. Innov. Opt. Health Sci.* 12:1940005. doi: 10.1142/S1793545819400054
- Noomarm, U., and Clegg, R. M. (2009). Fluorescence lifetimes: fundamentals and interpretations. *Photosyn. Res.* 101, 181–194. doi: 10.1007/s11120-009-9457-8
- Ntziachristos, V., Bremer, C., and Weissleder, R. (2003). Fluorescence imaging with near-infrared light: new technological advances that enable *in vivo* molecular imaging. *Eur. Radiol.* 13, 195–208. doi: 10.1007/s00330-002-1524-x
- Otaki, J. M., and Firestein, S. (2001). Length analyses of mammalian G-protein-coupled receptors. *J. Theor. Biol.* 211, 77–100. doi: 10.1006/jtbi.2001.2272
- Ouzounov, D. G., Wang, T., Wang, M., Feng, D. D., Horton, N. G., Cruz-Hernández, J. C., et al. (2017). *In vivo* three-photon imaging of activity of GCaMP6-labeled neurons deep in intact mouse brain. *Nat. Methods* 14, 388–390. doi: 10.1038/nmeth.4183
- Pándy-Szekeres, G., Munk, C., Tsonkov, T. M., Mordalski, S., Harpsøe, K., Hauser, A. S., et al. (2018). GPCRdb in 2018: adding GPCR structure models and ligands. *Nucleic Acids Res.* 46, D440–D446. doi: 10.1093/nar/gkx1109
- Patriarchi, T., Cho, J. R., Merten, K., Howe, M. W., Marley, A., Xiong, W.-H., et al. (2018). Ultrafast neuronal imaging of dopamine dynamics with designed genetically encoded sensors. *Science* 360:eaat4422. doi: 10.1126/science.aat4422
- Patriarchi, T., Cho, J. R., Merten, K., Marley, A., Broussard, G. J., Liang, R., et al. (2019). Imaging neuromodulators with high spatiotemporal resolution using genetically encoded indicators. *Nat. Protoc.* 14, 3471–3505. doi: 10.1038/s41596-019-0239-2
- Piatkevich, K. D., Jung, E. E., Straub, C., Linghu, C., Park, D., Suk, H.-J., et al. (2018). A robotic multidimensional directed evolution approach applied to fluorescent voltage reporters. *Nat. Chem. Biol.* 14, 352–360. doi: 10.1038/s41589-018-0004-9
- Qian, Y., Piatkevich, K. D., Mc Larney, B., Abdelfattah, A. S., Mehta, S., Murdock, M. H., et al. (2019). A genetically encoded near-infrared fluorescent calcium ion indicator. *Nat. Methods* 16, 171–174. doi: 10.1038/s41592-018-0294-6
- Rodriguez, E. A., Campbell, R. E., Lin, J. Y., Lin, M. Z., Miyawaki, A., Palmer, A. E., et al. (2017). The growing and glowing toolbox of fluorescent and photoactive proteins. *Trends Biochem. Sci.* 42, 111–129. doi: 10.1016/j.tibs.2016.09.010
- Saxl, T., Khan, F., Ferla, M., Birch, D., and Pickup, J. (2011). A fluorescence lifetime-based fibre-optic glucose sensor using glucose/galactose-binding protein. *Analyst* 136, 968–972. doi: 10.1039/c0an00430h
- Sleno, R., Pétrin, D., Devost, D., Goupil, E., Zhang, A., and Hébert, T. E. (2016). Designing BRET-based conformational biosensors for G protein-coupled receptors. *Methods* 92, 11–18. doi: 10.1016/j.jmeth.2015.05.003
- Subach, O. M., Barykina, N. V., Anokhin, K. V., Piatkevich, K. D., and Subach, F. V. (2019). Near-infrared genetically encoded positive calcium indicator based on GAF-FP bacterial phytochrome. *Int. J. Mol. Sci.* 20:3488. doi: 10.3390/ijms20143488
- Sun, F., Zeng, J., Jing, M., Zhou, J., Feng, J., Owen, S. F., et al. (2018). A genetically encoded fluorescent sensor enables rapid and specific detection of dopamine in flies, fish, and mice. *Cell* 174, 481.e19–496.e19. doi: 10.1016/j.cell.2018.06.042
- Sun, Y., Day, R. N., and Periasamy, A. (2011). Investigating protein-protein interactions in living cells using fluorescence lifetime imaging microscopy. *Nat. Protoc.* 6, 1324–1340. doi: 10.1038/nprot.2011.364
- Takeuchi, T., Duszkiwicz, A. J., Sonneborn, A., Spooner, P. A., Yamasaki, M., Watanabe, M., et al. (2016). Locus coeruleus and dopaminergic consolidation of everyday memory. *Nature* 537, 357–362. doi: 10.1038/nature19325
- Tantama, M., Hung, Y. P., and Yellen, G. (2011). Imaging intracellular pH in live cells with a genetically encoded red fluorescent protein sensor. *J. Am. Chem. Soc.* 133, 10034–10037. doi: 10.1021/ja202902d
- Thorsen, T. S., Matt, R., Weis, W. I., and Kobilka, B. K. (2014). Modified T4 lysozyme fusion proteins facilitate G protein-coupled receptor crystallogenesis. *Structure* 22, 1657–1664. doi: 10.1016/j.str.2014.08.022
- Unal, H., and Karnik, S. S. (2012). Domain coupling in GPCRs: the engine for induced conformational changes. *Trends Pharmacol. Sci.* 33, 79–88. doi: 10.1016/j.tips.2011.09.007
- Venkatakrishnan, A. J., Deupi, X., Lebon, G., Tate, C. G., Schertler, G. F., and Babu, M. M. (2013). Molecular signatures of G-protein-coupled receptors. *Nature* 494, 185–194. doi: 10.1038/nature11896
- Villardaga, J.-P., Bünnemann, M., Krasel, C., Castro, M., and Lohse, M. J. (2003). Measurement of the millisecond activation switch of G protein-coupled receptors in living cells. *Nat. Biotechnol.* 21, 807–812. doi: 10.1038/nbt838
- Vishwanath, K., Pogue, B., and Mycek, M.-A. (2002). Quantitative fluorescence lifetime spectroscopy in turbid media: comparison of theoretical, experimental and computational methods. *Phys. Med. Biol.* 47, 3387–3405. doi: 10.1088/0031-9155/47/18/308
- Visser, A. J. W. G., Laptinok, S. P., Visser, N. V., van Hoek, A., Birch, D. J. S., Brochon, J.-C., et al. (2010). Time-resolved FRET fluorescence spectroscopy of visible fluorescent protein pairs. *Eur. Biophys. J.* 39, 241–253. doi: 10.1007/s00249-009-0528-8
- Walther, K. A., Papke, B., Sinn, M. B., Michel, K., and Kinkhabwala, A. (2011). Precise measurement of protein interacting fractions with fluorescence lifetime imaging microscopy. *Mol. Biosyst.* 7, 322–336. doi: 10.1039/c0mb00132e
- Waters, J. C. (2009). Accuracy and precision in quantitative fluorescence microscopy. *J. Cell Biol.* 185, 1135–1148. doi: 10.1083/jcb.200903097



- Yao, J., Kaberniuk, A. A., Li, L., Shcherbakova, D. M., Zhang, R., Wang, L., et al. (2016). Multiscale photoacoustic tomography using reversibly switchable bacterial phytochrome as a near-infrared photochromic probe. *Nat. Methods* 13, 67–73. doi: 10.1038/nmeth.3656
- Yasuda, R., Harvey, C. D., Zhong, H., Sobczyk, A., van Aelst, L., and Svoboda, K. (2006). Supersensitive Ras activation in dendrites and spines revealed by two-photon fluorescence lifetime imaging. *Nat. Neurosci.* 9, 283–291. doi: 10.1038/nn1635
- Yellen, G., and Monge, R. (2015). Quantitative two-photon imaging of fluorescent biosensors. *Curr. Opin. Chem. Biol.* 27, 24–30. doi: 10.1016/j.cbpa.2015.05.024
- Zeng, J., Sun, F., Wan, J., Feng, J., and Li, Y. (2019). New optical methods for detecting monoamine neuromodulators. *Curr. Opin. Biomed. Eng.* 12, 68–74. doi: 10.1016/j.cobme.2019.09.010

**Conflict of Interest:** TP was co-inventor on a patent application (WO/2018/098262A1) for the technology described in this paper.

The remaining authors declare that the research was conducted in the absence of any commercial or financial relationships that could be construed as a potential conflict of interest.

Copyright © 2020 Ravotto, Duffet, Zhou, Weber and Patriarchi. This is an open-access article distributed under the terms of the Creative Commons Attribution License (CC BY). The use, distribution or reproduction in other forums is permitted, provided the original author(s) and the copyright owner(s) are credited and that the original publication in this journal is cited, in accordance with accepted academic practice. No use, distribution or reproduction is permitted which does not comply with these terms.



# Red Photoactivatable Genetic Optical-Indicators

Wessal Hussein and Shai Berlin\*

Department of Neuroscience, The Ruth and Bruce Rappaport Faculty of Medicine, Technion – Israel Institute of Technology, Haifa, Israel

## OPEN ACCESS

### Edited by:

Annalisa Scimemi,  
University at Albany, United States

### Reviewed by:

Adam E. Cohen,  
Harvard University, United States  
Yongxin Zhao,  
Carnegie Mellon University,  
United States

### \*Correspondence:

Shai Berlin  
shai.berlin@technion.ac.il

### Specialty section:

This article was submitted to  
Cellular Neurophysiology,  
a section of the journal  
Frontiers in Cellular Neuroscience

**Received:** 29 January 2020

**Accepted:** 08 April 2020

**Published:** 28 May 2020

### Citation:

Hussein W and Berlin S (2020)  
Red Photoactivatable Genetic  
Optical-Indicators.  
Front. Cell. Neurosci. 14:113.  
doi: 10.3389/fncel.2020.00113

Emerging genetically-encoded  $\text{Ca}^{2+}$ -indicators (GECIs) are intensimetric reporters that increase in fluorescence when bound to  $\text{Ca}^{2+}$ ; highly suited for studying calcium-signaling in many cell types, notably neurons. Today, major efforts are devoted toward optimizing red-emitting [red fluorescent protein (RFP)-based] GECIs (R-GECI), as these provide several advantages over GFP-based reporters, for instance, increased imaging depth, reduced photodamage by longer imaging wavelengths and, in principle, are better suited for use with prevalent blue-absorbing optogenetic tools (e.g., channelrhodopsin). However, excessive fluorescence from intersecting neighboring cells in very dense tissues, notably the brain, hinders the ability to collect signals from single cells and their processes. This challenge can be addressed by photoactivatable (PA) fluorescent proteins that can be rendered fluorescent *on demand* by user-defined targeted light. This allows activation and, thereby, collection of fluorescent signals exclusively from desired cells and their processes, while leaving all neighboring cells in the dark (i.e., non-fluorescent). Nevertheless, there are no PA R-GECIs. Here, we sought to develop PA-R-GECIs. To do so, we initially explored a recently discovered phenomenon of  $\text{Ca}^{2+}$ -independent increases in fluorescence (i.e., artifacts) in an emerging R-GECI, which has led us to rationally engineer several functional PA-R-GECIs. We also take advantage of our findings to quickly engineer a novel PA-RFP, namely, PA-mRuby3.

**Keywords:** photoactivatable, GECI genetically encoded  $\text{Ca}^{2+}$  indicator, calcium, red fluorescent protein, optical tools

## INTRODUCTION

There is a growing interest in red-shifted genetically-encoded  $\text{Ca}^{2+}$ -indicators (R-GECI) as these are activated by longer and less cytotoxic wavelengths, provide deeper imaging depths and, importantly, ease on concomitant use with common optogenetic or synthetic optogenetic tools (Yizhar et al., 2011; Berlin and Isacoff, 2017; Piatkevich et al., 2019). R-GECIs are therefore ideal for *all optical* neural interrogation *in vivo* (Emiliani et al., 2015). However, when studying cellular and subcellular  $\text{Ca}^{2+}$ -dynamics *in vivo*, it is often difficult to monitor  $\text{Ca}^{2+}$ -signals from single neuronal somata owing to background fluorescence,

namely, fluorescence emanating from adjacent cells and processes located next to, above, or below the desired cell. Background fluorescence also makes it very challenging for tracing and assigning processes to defined somata. These limitations have previously motivated us to design green photoactivatable (PA)-GECIs (PA-GCaMP; Berlin et al., 2015). Akin to PA-GFP (e.g., Patterson and Lippincott-Schwartz, 2002), the capability to control the basal fluorescence of GCaMP in single cells by light enables users to optically label (“highlight”) selected cells with very high spatiotemporal resolution (Patterson and Lippincott-Schwartz, 2002; Piatkevich et al., 2013). This robustly improves the signal-to-noise ratio and permits subsequent collection of signals (i.e.,  $\text{Ca}^{2+}$ -dependent changes in fluorescence) exclusively from highlighted cells and their processes with higher certainty and ease. Whereas other methods can address some of these challenges by sparsely labeling single neurons (Lee et al., 2019), optical highlighting of cells provides one major advantage over these, namely, granting users access to all cells in the preparation (for instance, in a transgenic model), rather than restricting the user to a small and stochastic population of cells. Moreover, photoactivation can be performed sequentially thereby allowing to monitor many cells in the same preparation, including adjacent ones.

Of the handful photoconvertible (Hoi et al., 2012; Fosque et al., 2015; Zolnik et al., 2017) and PA-sensors (Matsuda et al., 2013; Berlin et al., 2015; Lee et al., 2019), *none* are of single red-emission (see Walia et al., 2018). We therefore sought to develop a single-emission red-PA-GECI. Sequence analysis of extant PA-red fluorescent proteins (RFPs) reveals that the most optimized R-GECI variants are based on RFPs to which there are no PA versions. Moreover, unlike green PA-FPs, there are no shared set of mutations that can be easily transferred among different members of the RFP superfamily to endow them with PA features. This likely stems from the fact that the structural basis for photoactivation in PA-RFPs is less understood (and likely less conserved) than in members of the GFP superfamily (Lukyanov et al., 2005; Piatkevich and Verkhusha, 2010). Consequently, PA-RFPs are almost exclusively engineered via random mutagenesis schemes. To rationally design PA-R-GECI, we began by focusing on R-GECO1 (red-genetically encoded  $\text{Ca}^{2+}$ -indicator for optical imaging; Zhao et al., 2011). R-GECO1 is a potent red-GECI with very large responses ( $\Delta F/F$ ), wide dynamic-range and is suitable for two-photon imaging, to name a few (Zhao et al., 2011; Dana et al., 2016). Importantly, R-GECO1 is based on mApple; a unique FP that exhibits intrinsic and transient photoconvertible behavior (Shaner et al., 2008). The functional outcome of this behavior is the appearance of transient light-dependent—and  $\text{Ca}^{2+}$ -independent—increases in fluorescence (here denoted artifacts) when illuminated with near-UV-to-green light (Wu et al., 2013 and see **Figure 1**). These artifacts display similar features (size and kinetics) as *bona fide*  $\text{Ca}^{2+}$ -dependent responses, making it very hard to distinguish between them. This limitation thereby complicates the use of R-GECO1 with near-UV-to-green light activated optogenetic tools (Shaner et al., 2008; Akerboom et al., 2013; Wu et al., 2013; Berlin et al., 2016; Piatkevich et al., 2019). Nevertheless, here we benefited

from this behavior for the development of PA Red-GECIs and a new PA-RFP.

## RESULTS

### Red $\text{Ca}^{2+}$ -Indicators Display Blue Emission and $\text{Ca}^{2+}$ -Independent Increases in Fluorescence

We, and others, have recently noted that R-GECO1 undergoes reversible photoactivation by blue-shifted wavelengths (e.g., Wu et al., 2013). Unfortunately, the mechanism of this phenomenon remains poorly understood (speculated to range from light-induced deprotonation, formation of new chromophore-type to chromophore isomerization) (Akerboom et al., 2013; Wu et al., 2013; Berlin et al., 2016). To try and harness this behavior for generating a PA R-GECI, we first turned to characterize this behavior in our system and cells. Cells expressing R-GECO1 and illuminated by 561 nm exhibit bright red fluorescence (**Figure 1A**, top micrograph and red plot, 561 nm excitation—yellow bar). When short and intermittent bouts of 405 nm illumination are applied, robust and transient increases in red fluorescence are obtained (i.e., artifacts); highly reminiscent of *bona fide*  $\text{Ca}^{2+}$ -dependent increases in fluorescence (**Figures 1B,C**). These observations suggest that R-GECO1 directly absorbs 405 nm. Indeed, 405 nm excitation elicits two emission peaks of blue and red fluorescence,  $\lambda_{\text{peak}} = 460$  and 600 nm, respectively (**Figure 1A**, bottom micrograph—note the apparent blue and red cells; and blue plot, 405 nm excitation—magenta bar). While R-GECO1 has been shown to absorb near-UV light (Akerboom et al., 2013; Wu et al., 2013), to the best of our knowledge, the description of its emission(s) in response to shorter wavelengths has not been reported. R-GECO1's emissions of blue and red spectra suggested to us the presence of two populations of R-GECO in cells; each with a different maturation state of its chromophore. In fact, most (if not all) RFPs begin as blue-emitters before their methionine-tyrosine-glycine (MYG) chromophore develops into its final red-emitting form (see full sequence, **Supplementary Figure 1**, red box) (Subach et al., 2008; Shcherbakova et al., 2012). Thus, the near-UV induced artifacts may result from several mechanisms, such as the direct excitation of the red-chromophore, light-induced isomerization, or, less likely, instantaneous maturation of the blue-chromophore into red (Wu et al., 2013 and see below).

### Generation of Photoactivatable Red $\text{Ca}^{2+}$ -Indicators

To benefit from the artifactual behavior of R-GECO, we first set out to locate residues within R-GECO1 (i.e., mApple) that would be amenable to rational mutagenesis so as to convert the transient photoconversion into stable photoactivation. We first examined the sequences of various PA-FPs, explicitly PA-GFP, PA-mCherry, and PA-TagRFP (Patterson and Lippincott-Schwartz, 2002; Lukyanov et al., 2005), in addition to sequences of RFPs that serve as templates for R-GECIs, namely, mPlum (backbone of R-GECO1.2; Wu et al., 2013) and mRuby

(backbone of RCaMP1h and jRCaMP; Akerboom et al., 2013; Dana et al., 2016; **Supplementary Figure 1**). Interestingly, PA-GFP and PA-RFPs show no obvious shared pattern of mutations, except for the involvement of the well-recognized polar residue essential for the PA behavior of PA-GFP (**Figure 2A**; black arrowhead and **Supplementary Figure 1**, black arrowhead; Patterson and Lippincott-Schwartz, 2002). Notably, whereas the 203rd residue is essential for the photoactivation of both red and green FPs, a histidine in that position does not seem to be essential for RFPs. For instance, PA-mCherry1, 2, and -3 (Subach et al., 2009), and PA-TagRFP (Subach et al., 2010) are PA but with an arginine substitution instead.

We therefore deemed it worthy to focus on this residue in R-GECO1 (mApple; residue I78) (see section “Materials and Methods” and primer list). Importantly, whereas PA-GFP required two additional mutations for photoactivation, specifically phenylalanine preceding the chromophore and a serine within it (F64 and S65; GFP numbering; Patterson and Lippincott-Schwartz, 2002), most PA and non-PA RFPs examined (including mApple of R-GECO1) retain the original chromophore (MYG) and the preceding hydrophobic phenylalanine (**Supplementary Figure 1**, red box). The only exception in our screen was mPlum (template for R-GECO1.2; Wu et al., 2013; and see below). mPlum does not bear the F64 residue, rather I64 (**Supplementary Figure 1**, blue circle). However, these two amino acids are similarly hydrophobic and therefore we did not deem it necessary to substitute it or any additional residues.

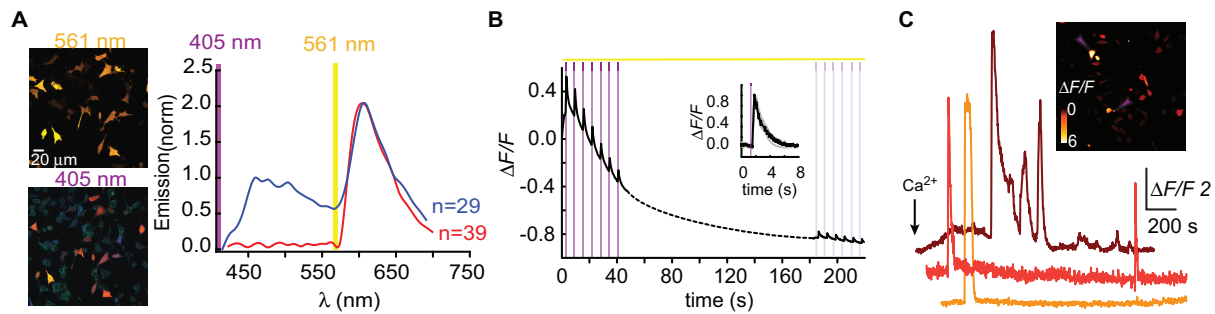
Based on the above-mentioned, we naturally turned to firstly engineer R-GECO1-I78H; R-GECO1<sub>H</sub> (**Figure 2**). When expressed in HEK293T cells, very low basal fluorescence (prior Ca<sup>2+</sup> addition or photoactivation) could be detected when imaged at 561 nm (**Figure 2B**, 0–20 s, top micrograph; before). After prolonged (seconds) near-UV (405 nm) illumination over a large field of view (objective 20x, NA = 1, digital zoom 0.7) using maximal laser power (see section “Materials and Methods” for details on laser power), we observed stable increases in fluorescence over a very broad range (mean photoactivation;  $\Delta F/F = 6.88 \pm 0.25$ ), likely due to very different expression levels in different HEK293 cells, rather than resting Ca<sup>2+</sup>-levels (**Figure 2B**, 80–120 s and bottom micrograph; after). This clone also showed that, whereas the 561 nm-induced emission spectrum of R-GECO1<sub>H</sub> prior photoactivation was indistinguishable from that of the parent R-GECO1<sub>wt</sub> (**Figure 2C**, red plot), the spectrum obtained by 405 nm illumination was strikingly different, namely, retained blue emission but with a complete loss of the second peak of red fluorescence (**Figure 2C**, blue plot and arrowhead). We then expressed the clone in HeLa cells with the intention to monitor activity as these cells are more Ca<sup>2+</sup>-active. Transfected HeLa cells exhibited lower basal fluorescence than levels in HEK293T cells, albeit detectable (**Figure 2D**, top micrograph). Of note, low, but extant, fluorescence allowed us to calculate  $\Delta F/F$  values without introducing near-zero division artifacts (see section “Materials and Methods” for more details). Importantly, we deem visible basal fluorescence as a highly useful feature for detecting cells that express the clone prior photoactivation.

This eliminates the need to introduce additional non-PA optical markers. In fact, basal fluorescence is so low in PA-GFP, and also in PA-GCaMP, therefore requiring imaging with low intensity 405 nm (that does not cause substantial photoactivation) for spotting positive cells; to then target for photoactivation (e.g., see protocol in Berlin et al., 2015). Owing to low levels of fluorescence, we performed gradual photoactivation to minimize photobleaching, consisting of shorter and repeated bouts of 405 nm until reaching maximal photoactivation (seen as steady state fluorescence). In HeLa cells, this protocol demonstrated that R-GECO1<sub>H</sub> underwent weak photoactivation (**Figure 2D** and **Table 1**). It has also revealed, unexpectedly, that this clone no longer exhibited the light-induced artifacts as seen with R-GECO1<sub>wt</sub> (compare **Figure 1** to **Figure 2D**, arrowheads). These observations rule-out the hypothesis that the light-induced artifacts directly stem from instantaneous maturation of the blue-emitting population. Importantly, this clone exhibited very robust Ca<sup>2+</sup>-performance in response to varying challenges commonly employed; histamine or excessive extracellular Ca<sup>2+</sup> (**Figure 2E**, left and right panels, respectively). Thus, the low extent of photoactivation was complemented by very large Ca<sup>2+</sup>-responses. We then expressed the clone in rat hippocampal neurons where R-GECO1<sub>H</sub> exhibited similar characteristics to those obtained from HeLa cells, namely, very low basal fluorescence and weak photoactivation (**Figure 2F**). As our primary goal is to express these probes in neurons, the quantitative similarities in basal fluorescence (likely due to similar expression levels) and the degree of photoactivation in HeLa and primary neurons indicated to us that HeLa cells are better suited for predicting expression/performances of our clones in neurons instead of HEK293 cells.

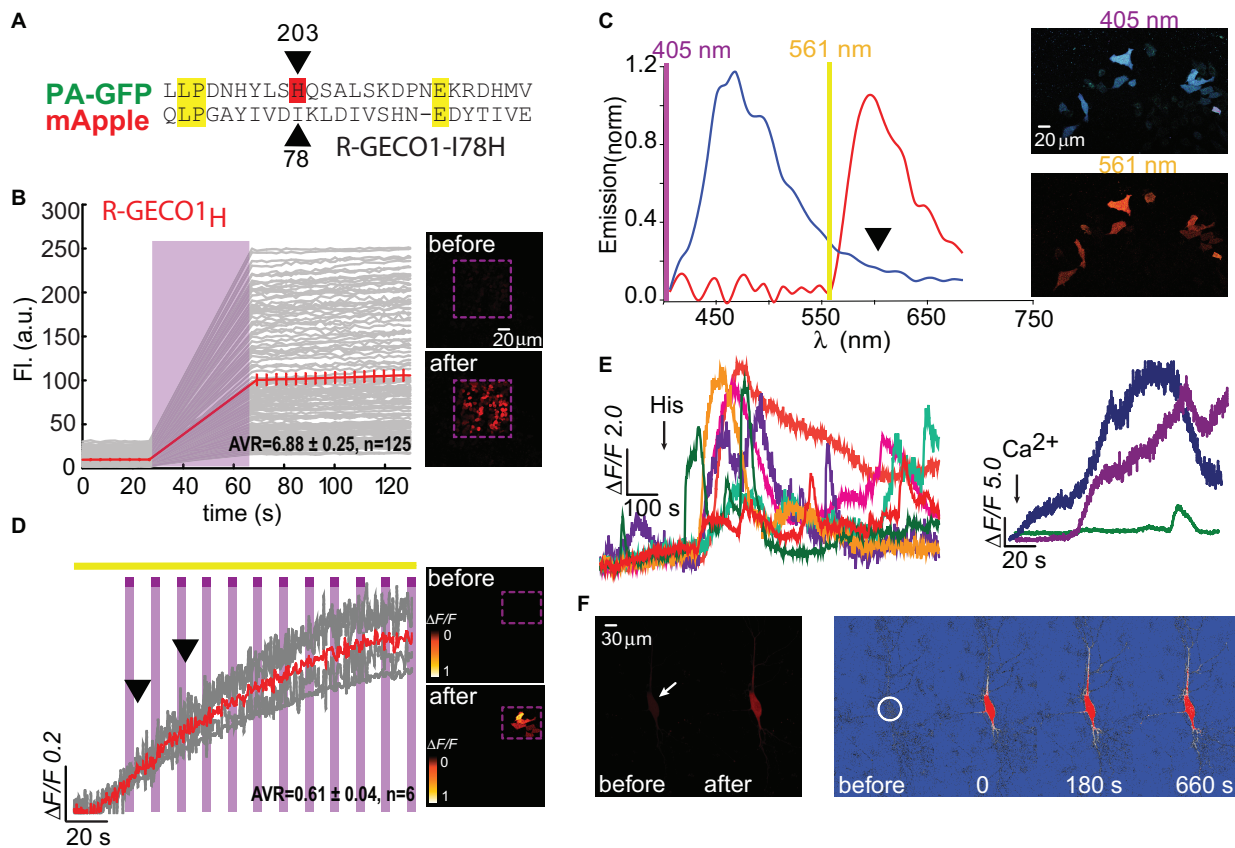
Dissatisfied with the PA performance of R-GECO1<sub>H</sub>, in all cell types, we were motivated to pursue our screen for better R-GECO mutants specifically in HeLa cells. We proceeded to make 17 more substitutions (see primers list), as we could not determine *a priori* which mutation would endow the best performances in photoactivation and in Ca<sup>2+</sup>-responsivity. Though most of the variants did not express at all (e.g., **Supplementary Figure 2a**, R-GECO1-I78R), it was surprising to find that multiple mutations could confer photoactivatability, for instance, I78Y, -S, and -E (**Supplementary Figure 2b** and **Table 1**). It was also surprising that the leucine-mutant (R-GECO1-I78L), despite the residue's high degree of homology to isoleucine as is originally found in R-GECO1<sub>wt</sub>, lost its direct 405 nm-induced red emission (**Supplementary Figure 3a**) and the large light-induced artifacts (**Supplementary Figure 3b**). Moreover, it did not display photoactivation. Unfortunately, this collection of variants (including R-GECO1-I78L) failed to respond to Ca<sup>2+</sup> (e.g., **Supplementary Figure 3c** for R-GECO1-I78L) and were not further characterized (see summary in **Table 1**).

We lastly engineered R-GECO1<sub>T</sub> (R-GECO1-I78T) and expressed it in HeLa cells. Notably, we did not expect this clone to display any photoactivation based on observations with PA-GFP in which T203H enables photoactivation, whereas H203T cancels it. Counterintuitively, R-GECO1<sub>T</sub> exhibited the largest extent of photoactivation of all clones tested, thus far, in HeLa cells ( $\Delta F/F = 2.65 \pm 0.64$ ,  $n = 6$ ) by short bouts of 405 nm





**FIGURE 1 |** R-GECO1 is blue and red-emitting fluorescent sensor. **(A)** Emission spectra collected after excitation with 405 nm (magenta bar, blue plot) and 561 nm (yellow bar, red plot). Insets—Micrographs of HeLa cells expressing R-GECO1 and illuminated by 561 nm (top) or 405 nm (bottom). Note the bright red fluorescence following 405 nm (e.g., white arrows). **(B)** R-GECO1 exhibiting transient photoconversion during intervals of near UV light irradiation (405 nm). **(C)** Representative traces of  $\text{Ca}^{2+}$ -activity induced by application of excessive  $\text{Ca}^{2+}$  (see section “Materials and Methods”).



**FIGURE 2 |** Photoactivatable R-GECO1H. **(A)** Partial sequence alignment between PA-GFP and mApple. Black arrow indicates T203H position and its parallel I78 in mApple. **(B)** R-GECO1H in HEK293T cells during prolonged photoactivation with 100% of 405 nm at ~1.7 mW (magenta bar). Insets—HEK cells imaged by 561 nm before (top) and after (bottom) photoactivation (magenta dashed square). **(C)** Emission spectra collected before photoactivation by use of 405 nm (blue plot) and 561 nm (red plot). Insets—Micrographs of HeLa cells expressing R-GECO1H and illuminated by 405 nm (top) or 561 nm (bottom). Note the lack of red fluorescence following 405 nm excitation. **(D)** Stable photoactivation of R-GECO1H in HeLa cells. Cells imaged by 561 nm (yellow bar) are intermittently excited by short (1 s) bouts of 405 nm (magenta bars) exhibit stable increase in  $\text{Ca}^{2+}$ -independent fluorescence, until reaching a plateau. Insets—HeLa cells imaged by 561 nm before (top) and after (bottom) photoactivation. **(E)** R-GECO1H is functional as a  $\text{Ca}^{2+}$ -probe. Representative traces showing  $\text{Ca}^{2+}$ -activity following the application of histamine (15  $\mu\text{M}$ , left) and  $\text{Ca}^{2+}$  (+50  $\mu\text{M}$ , right). **(F)** Hippocampal neuron before and after somatic photoactivation (left micrographs). Note the low, albeit noticeable, basal fluorescence (white arrow). Right images ( $\Delta F/F$ ) show spread of fluorescence throughout the dendritic arbor over 600 s, following somatic photoactivation of R-GECO1H (white circle).

illumination (**Figure 3A**). Akin to R-GECO1<sub>H</sub>, this mutation completely eliminated the light-dependent artifacts (**Figure 3A**), without abolishing the blue-emitting population (**Figure 3B**, blue plot). However, this mutation significantly reduced the appearance of the direct excitation of the red-fluorophore by 405 nm in comparison to R-GECO1<sub>wt</sub> (**Figure 3B**, arrowhead). We also noticed that single photoactivation bouts yielded very rapid and sharp increases in fluorescence, suggesting to us higher sensitivity to photoactivation. We tested different photoactivation protocols on single cells and found that efficient photoactivation could be obtained very rapidly by irradiating the cells with as brief as 500 ms bouts of 405 nm (**Figure 3C**). Lastly, R-GECO1<sub>T</sub> retained its responsiveness to Ca<sup>2+</sup> (**Figure 3D**), which increased after photoactivation (**Figure 3F** and **Supplementary Figure 4a**). These responses were on par with the responses obtained for R-GECO1<sub>H</sub> as well as for R-GECO1<sub>wt</sub> under similar conditions (compare **Figures 1, 2**, summarized in **Table 1**). In cultured hippocampal neurons, R-GECO1<sub>T</sub> exhibits detectable basal fluorescence (**Figure 3E**, top micrograph and **Figure 3F**, top magenta plot starts with noticeable fluorescence), undergoes photoactivation and readily reports on action potential (AP) firing (**Figures 3E,F**). Together, we find that R-GECO1<sub>T</sub> displayed the best combination of features, namely, moderate extent of photoactivation, large Ca<sup>2+</sup>-responsiveness, reduced artifacts, and reduced direct excitation of the mature red chromophore. We therefore denoted this clone PA-R-GECO1 (**Table 1**).

We were then curious as to whether the photoactivation of R-GECO1<sub>T</sub> showed dependence on Ca<sup>2+</sup> ions (as observed for another photoconvertible GECI denoted CaMPARI; Fosque et al., 2015). To address this, we expressed R-GECO1<sub>T</sub> in HEK293 cells for these are typically less Ca<sup>2+</sup>-active than HeLa cells (Morita et al., 2015), thereby with likely lower cytoplasmic Ca<sup>2+</sup> levels. We photoactivated cells in regular imaging medium (as used in experiments with HeLa cells), as well as in media with or without Ca<sup>2+</sup> (**Supplementary Figure 4b** and see section “Materials and Methods”). First, as seen with other clones, HEK293 cells showed much more robust (and variable) expression of R-GECO1<sub>T</sub> than when expressed in HeLa cells or in neurons (under similar conditions; “standard medium”). This translated into much higher degrees of photoactivation. More specifically, both standard- and Ca<sup>2+</sup>-free media enabled cells to undergo ~8 ( $\Delta F/F = 7.08 \pm 0.11$ ,  $n = 263$ ) and ~7 fold ( $\Delta F/F = 6.23 \pm 0.20$ ,  $n = 181$ ) increases in fluorescence (**Supplementary Figures 4b,c**, red and gray plots, respectively; raw data in **Supplementary Figures 4d,e**), whereas the presence of Ca<sup>2+</sup> significantly reduced the ability of the clone to undergo photoactivation ( $\Delta F/F = 0.71 \pm 0.01$ ,  $n = 294$ ), even to lower extents than seen in HeLa cells (**Supplementary Figure 4c**, blue plot and **Supplementary Figure 4f**; compare with **Figure 3**). These results show that the photoactivation of R-GECO1<sub>T</sub> does not depend on Ca<sup>2+</sup>, rather it diminishes it. We also find no changes in the fluorescence emission, before and after photoactivation, (regardless the media) when illuminated with 561 nm (**Supplementary Figure 4g**). However, the emissions resulting from 405 nm illumination did change after photoactivation—the direct red emission (at ~600 nm) was strongly increased by 405 nm irradiation no matter the medium

(**Supplementary Figure 4h**). These observations show that the chromophore undergoes irreversible chemistry by 405 nm (as is the case for PA-GFP and that this modification gives rise to enhanced direct absorption of 405 nm. Since this clone does not exhibit artifactual behavior as the original R-GECO1, it strengthens our hypothesis that the artifacts do not stem from direct red emission by 405 nm illumination, rather a transient change in the chromophore induced by 405 nm, most likely isomerization, and the I to T mutation disrupts or abolishes this ability while increasing 405 nm absorbance.

## Next-Generation PA-R-GECI

Having seen that a single point mutation could confer most of the traits desired in a PA Ca<sup>2+</sup>-probe, we were curious as to whether we could quickly engineer other PA-R-GECI with higher contrast using the same strategy. Naturally, we moved to an optimized version of R-GECO1 probe, namely, R-GECO1.2 (Wu et al., 2013). Of note, R-GECO1 and -1.2 are not based on the same RFP backbone, rather R-GECO1.2 is based on mPlum. However, mApple and mPlum both share the I78 residue (**Supplementary Figure 1**). We then generated 18 different R-GECO1.2 clones and found that most mutants failed to express, as seen with their R-GECO1 counterparts (**Table 1**), but with a few exceptions. For instance, whereas R-GECO1<sub>L</sub> almost lost its ability to sense Ca<sup>2+</sup>, R-GECO1.2<sub>L</sub> remained potent (compare **Supplementary Figures 3a,b**). The best performing clone was R-GECO1.2<sub>T</sub>, displaying moderate photoactivation ( $\Delta F/F = 1.25 \pm 0.19$ ) in HeLa cells (though to lower extent than R-GECO1<sub>T</sub>), but with significantly larger Ca<sup>2+</sup>-responses ( $\Delta F/F = 23.80 \pm 2.83$ ) (**Figures 4A,B** and **Table 1**). It also displayed strongly diminished red emission by direct 405 nm irradiation, not to mention loss of the near-UV light-induced artifacts (**Figures 4A,C** arrowhead). We also find that, analogous to R-GECO1<sub>T</sub>, this variant does not exhibit Ca<sup>2+</sup>-dependent photoactivation (**Supplementary Figures 5a,b**) and 561-nm induced emission remain similar before and after photoactivation, with or without Ca<sup>2+</sup> (**Supplementary Figure 5c**). Its emission in response to 405 nm, before and after photoactivation, showed the same trend as R-GECO1<sub>T</sub>, but to larger extents. More specifically, photoactivation enhanced the direct red emission by 405 nm (**Supplementary Figure 5d**). Moreover, photoactivation also strengthened the emission of another peak, ~512 nm (**Supplementary Figure 5d**, but also see **Supplementary Figure 4d**). This supports the notion that 405 nm irradiation causes a chemical change in the vicinity of the chromophore (likely by  $\beta$ -elimination; Miyawaki et al., 2012), and therefore creates a new stable chromophore with increased green emissions. We therefore denoted this clone PA-R-GECO1.2.

We then turned to test the newest R-GECO variant, jR-GECO1a; also based on mApple (Dana et al., 2016). Based on our experience with R-GECO1 and -1.2, we only produced three variants (I131T, H, and R), expecting these to provide the entire range of features, namely, T and H to perform well and R to serve as control for a poor expression variant. Indeed, jR-GECO1a-I131T behaved as PA-R-GECOs, explicitly retained blue population, lacked direct 405 nm-induced red emission and artifacts and exhibited brightest features (photoactivation,  $\Delta F/F = 2.12 \pm 0.13$ ; Ca<sup>2+</sup>-performance,  $\Delta F/F = 1.9 \pm 0.13$ ) (**Figures 5A–C**). Nevertheless, these were

**TABLE 1** | Summary of basal expression, extent of photoactivation, and Ca<sup>2+</sup>-performance.

HeLa cells	Mutation	Expression via 561 nm illumination (also basal fluorescence prior photoactivation)	Artifacts	Photoactivation	Ca <sup>2+</sup> response
R-GECO1 (mApple)	None (WT)	+++	+++	Transient	3.48 ± 0.76, <i>n</i> = 19
	I78T	+++	—	2.5 ± 0.24, <i>n</i> = 16 (HEK: 2.8 ± 0.23, <i>n</i> = 13) (neurons: 1.5 ± 0.18, <i>n</i> = 13)	1.31 ± 0.37, <i>n</i> = 10 (3.04 ± 0.18, <i>n</i> = 45) (neurons: 4.27 ± 0.77, <i>n</i> = 16)
	PA-R-GECO1				
	I78H	+++	—	0.61 ± 0.04, <i>n</i> = 6 (HEK: 6.88 ± 0.25, <i>n</i> = 125)	2.06 ± 1.15, <i>n</i> = 9
	I78A	++	—	0.96 ± 0.17, <i>n</i> = 2	1.79 ± 0.63, <i>n</i> = 5
	I78V	++	+++	0.82 ± 0.12, <i>n</i> = 4	1.44 ± 0.44, <i>n</i> = 6
	I78Y	+	++	1.94 ± 0.15, <i>n</i> = 6	—
	I78S	+	—	1.76 ± 0.114, <i>n</i> = 3	—
	I78E	++	—	1.33 ± 0.18, <i>n</i> = 11	—
	I78Q	+	—		—
	I78L	+++	++	Transient	0.84 ± 0.52, <i>n</i> = 2
	I78K	—			
	I78G	—			
	I78F	—			
	I78D	—			
	I78C	—			
	I78P	—			
	I78R	—			
	I78N	—			
	I78W	—			
R-GECO1.2 (mPlum)	Non (WT)	+++	+++	Transient	8.22 ± 1.03, <i>n</i> = 37
	I78L	+++	—	1.31 ± 0.09, <i>n</i> = 36	15.39 ± 1.65, <i>n</i> = 67
	I78T	+++	—	1.2 ± 0.13, <i>n</i> = 31 (in HEK: 4.64 ± 0.34, <i>n</i> = 22) (neurons: 2.3 ± 0.22, <i>n</i> = 5)	23.80 ± 2.83, <i>n</i> = 49 (in HEK: 3.18 ± 0.29, <i>n</i> = 11)
	PA-R-GECO1.2				
	I78N	++	—	0.4 ± 0.17, <i>n</i> = 6	—
	I78H	++	Inverse	0.9 ± 0.26, <i>n</i> = 6	—
	I78A	++	—		—
	I78Y	+	—		—
	I78Q	+	—	0.5 ± 0.03, <i>n</i> = 8	—
	I78PRO	+	—		—
	I78C	+	—		—
	I78K	+	—		—
	I78G	+	—		—
	I78F	—			—
	I78D	—			—
	I78E	—			—
	I78S	—			—
	I78R	—			—
	I78val	—			—
	I78W	—			—
jR-GECO1a (mApple)	I131T	+++	—	2.12 ± 0.129, <i>n</i> = 19 (in HEK: 14.28 ± 0.84, <i>n</i> = 53)	1.9 ± 0.18, <i>n</i> = 3
	I131H	—	—		
	I131R	—	—		

(Continued)

TABLE 1 | Continued

HeLa cells	Mutation	Expression via 561 nm illumination (also basal fluorescence prior photoactivation)	Artifacts	Photoactivation	Ca <sup>2+</sup> response
RCaMP1h (mRuby)	None (WT)	+++	+++	Transient	Not tested
	H115T	+++	+++	in HEK: $45.38 \pm 2.03$ , $n = 96$	$0.8 \pm 0.53$ , $n = 96$
jRCaMP1A (mRuby)	H134I	+++	—	$7.44 \pm 3.74$ , $n = 15$ (in HEK: $12.07 \pm 1.17$ , $n = 33$ )	$1.01 \pm 0.10$ , $n = 10$ (in HEK: $1.22$ , $n = 1$ )
	H134T	+++	—	$4.83 \pm 0.18$ , $n = 25$	$0.33 \pm 0.11$ , $n = 3$
jRCaMP1B (mRuby)	H134I	+++	—	$6.9 \pm 1.9$ , $n = 21$	$0.53 \pm 0.09$ , $n = 8$
	H134T	+++	—	$2.93 \pm 0.55$ , $n = 23$	$0.28 \pm 0.07$ , $n = 7$
	H134K	—	—		
	H134R	—	—		
mRuby3	H200I	+++	—	$13.63 \pm 1.37$ , $n = 29$	—
	H200T	+++	—	$4.9 \pm 0.29$ , $n = 23$	—

of lower amplitudes than those of PA-R-GECO1 and -1.2. In parallel, we explored a closely related R-GECI family denoted RCaMPs (RCaMP1h; Akerboom et al., 2013 and jRCaMP1a, -b; Dana et al., 2016; see Dana et al., 2016; Kerruth et al., 2019 for GECIs genealogy). RCaMPs are based on mRuby and therefore enclose a histidine in the 203rd position (H115, RCaMP1h numbering) (Supplementary Figure 1). We briefly examined the basic properties of the three RCaMPs using our protocols and found that, akin to R-GECOs, 405 nm excitation yielded blue emitting populations, but without direct excitation of the red chromophore (Supplementary Figure 6a). RCaMP1h also displayed similar light-induced artifacts as observed for R-GECO1 and -1.2 (Supplementary Figure 6b), whereas jRCaMPa did not (Supplementary Figure 6c).

We began engineering H115T mutants because, so far, substitution to a threonine yielded best performances. We also made a H115I substitution because we were curious to see the potential involvement of this in the transient photoactivation seen in all R-GECOs, including RCaMP1h. Surprisingly, all six clones exhibited robust and stable photoactivation; much larger than most of the responses obtained for the different R-GECO variants (Supplementary Figure 7). Notably, RCaMP1h<sub>T</sub> exhibited the largest extent of photoactivation with contrast as high as ~100 fold in HEK293 cells (mean photoactivation,  $\Delta F/F = 45.38 \pm 2.03$ ,  $n = 96$ ) (Figure 6A). However, all RCaMP-variants did not yield very strong Ca<sup>2+</sup>-responses (Figure 6B and Supplementary Figure 7). In general, we note a weak, albeit non-significant, inverse relationship between Ca<sup>2+</sup>-performance and extent of photoactivation among all R-GECO and RCaMP variants tested (Supplementary Figure 7g). We hypothesize this to stem from the fact that both capabilities compete for the same mechanism, namely, deprotonation of the chromophore and increase in fluorescence. In other words, the addition of Ca<sup>2+</sup> (akin to increase in basal fluorescence) reduces the effective range for photoactivation, while maintaining the same total fluorescence (see Supplementary Figures 4d–f). Lastly, RCaMP1h<sub>T</sub> retained

its light-induced artifacts by 405 nm irradiation (Figure 6C). Thus, owing to these limitations, we did not continue with the RCaMP family for further development of red PA Ca<sup>2+</sup>-probes, but we did find their FP backbone to be highly relevant for the generation of novel PA-RFPs (below).

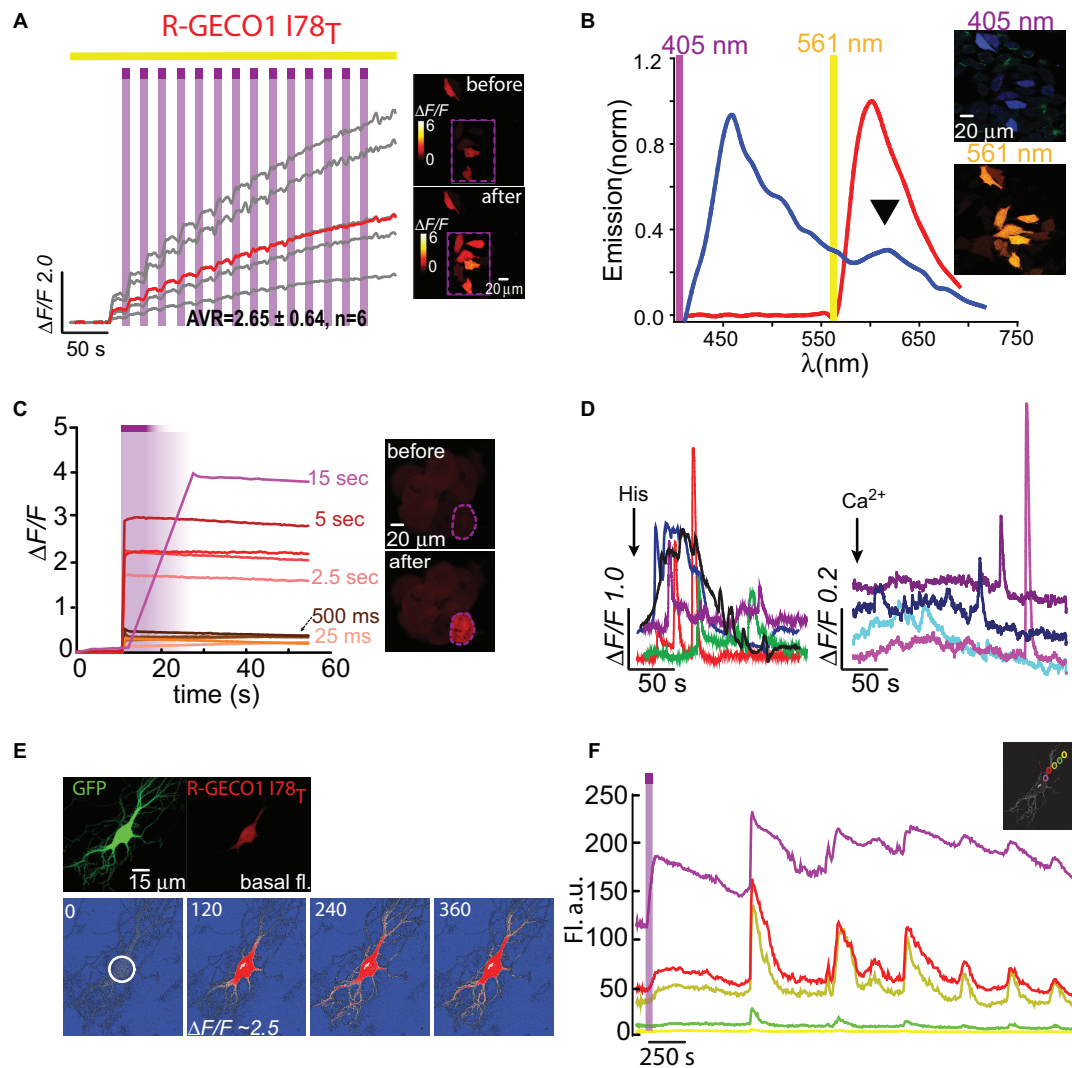
### Engineering a Novel PA-mRuby3

Owing to the fact that RCaMPs, in particular RCaMP1-H115I and H115T, showed very robust photoactivation among the clones tested, we wondered whether it would be possible to use this knowledge for rational engineering of a novel PA-RFP, namely, PA-mRuby. Notably, there is no PA-mRuby. We therefore turned to the newest and brightest mRuby denoted mRuby3 (Bajar et al., 2016). We mutated its corresponding 203rd residue (i.e., H200) to either isoleucine or threonine; producing mRuby3-H200I and -H200T. Analysis of emission spectra showed that both variants did not show any 405 nm-induced emissions by the chromophore as compared to their parent protein with its minimal, albeit noticeable, direct excitation (Figure 7A, arrowhead, Figures 7B,C). Importantly, both variants rendered mRuby3 photoactivatable, with mRuby3-H200I exhibiting more potent photoactivation ( $\Delta F/F = 13.63 \pm 1.37$ ,  $n = 29$ ) in HeLa cells (Figures 7D,E). Therefore, we denoted this clone PA-mRuby3<sub>I</sub>.

## DISCUSSION

Here, we describe a simple rational design strategy with which we have created a palette of unique PA red-GECIs, along a novel PA-RFP. These, unlike PA-GFP and PA-RFPs, only required a single point mutation (equivalent to T203H mutation as in PA-GFP; Baird et al., 1999; Patterson and Lippincott-Schwartz, 2002). Moreover, these variants did not need to be optimized for better folding and emission at physiological conditions (pH and temperature), as was the case with green PA-GECI (Berlin et al., 2015) and PA-GEVI (Lee et al., 2019). In a previous attempt to



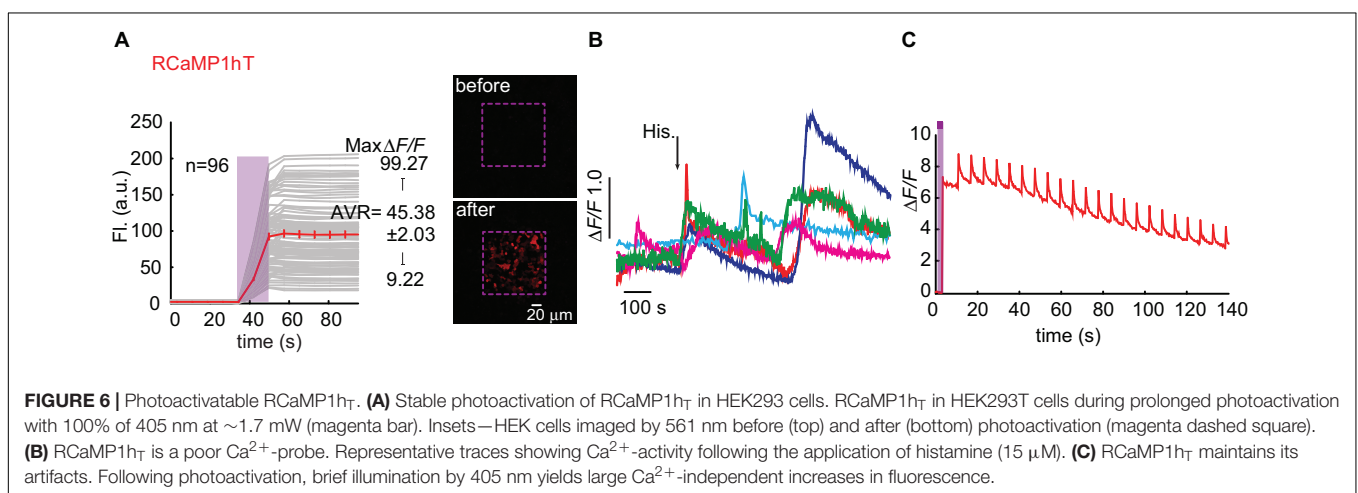
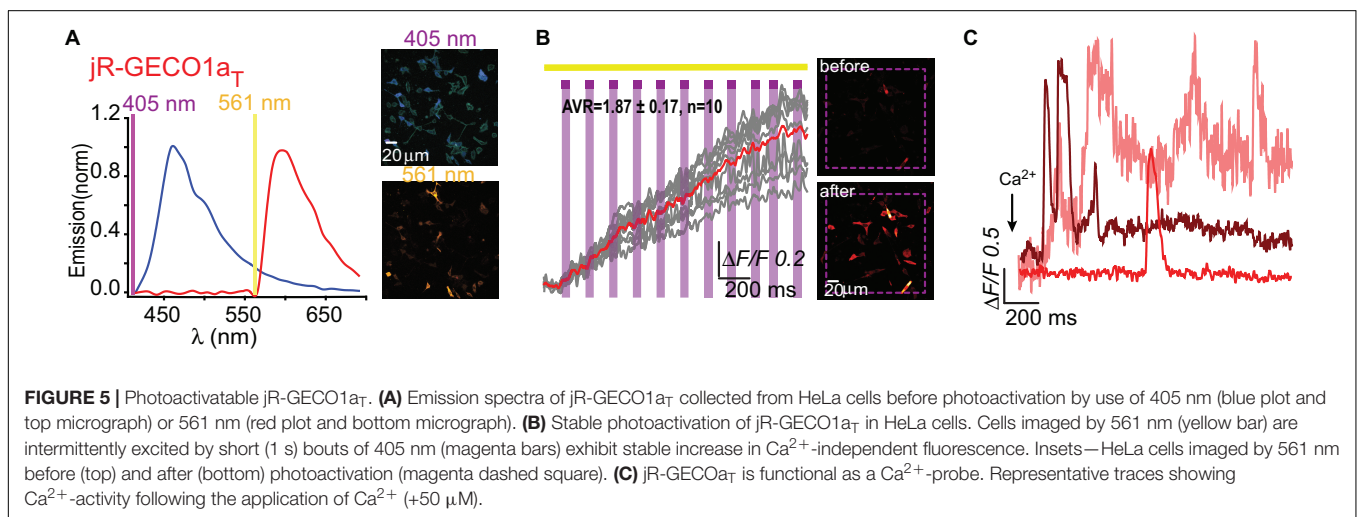
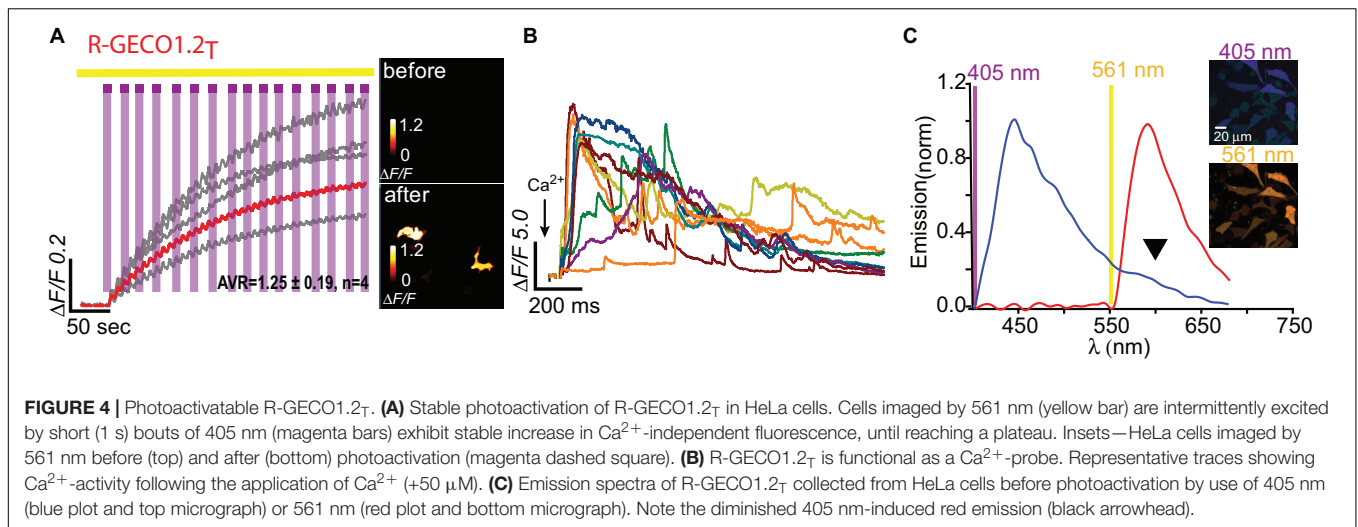


**FIGURE 3 |** Photoactivatable R-GECO1<sub>T</sub>. **(A)** Stable photoactivation of R-GECO1<sub>T</sub> in HeLa cells. Cells imaged by 561 nm (yellow bar) are intermittently excited by short (1 s) bouts of 405 nm (magenta bars) exhibit stable increase in Ca<sup>2+</sup>-independent fluorescence, until reaching a plateau. Insets—HeLa cells imaged by 561 nm before (top) and after (bottom) photoactivation (magenta dashed square). **(B)** Emission spectra of R-GECO1<sub>T</sub> collected from HeLa cells a before photoactivation by use of 405 nm (blue plot and top micrograph) or 561 nm (red plot and bottom micrograph). Note the diminished 405 nm-induced red emission (black arrowhead). **(C)** R-GECO1<sub>T</sub> exhibits rapid photoactivation. Very brief photoactivation bouts (25–500 ms) yield robust photoactivation. 5 s 405 nm illumination yields 85% of that obtained by longer exposures (15 s). Insets—single cell before (top) and after (bottom) photoactivation (magenta dashed region). **(D)** R-GECO1<sub>T</sub> is functional as a Ca<sup>2+</sup>-probe. Representative traces showing Ca<sup>2+</sup>-activity following the application of histamine (15 μM, left) or Ca<sup>2+</sup> (+50 μM, right). **(E)** Hippocampal neuron co-transfected with GFP and R-GECO1<sub>T</sub>, showing the noticeable basal fluorescence of this clone prior photoactivation (top right micrograph). Bottom images show spread of fluorescence, following somatic photoactivation of R-GECO1<sub>T</sub> (white circle). **(F)** Ca<sup>2+</sup>-activity is larger in highlighted regions. Traces show that soma and nearby dendrites exhibit larger ΔF/F than distant dendrites.

create a PA version of R-GECO1 (Hoi et al., 2012), the authors introduced multiple mutations as are found in PA-mCherry. However, since R-GECO1 is not based on mCherry, this scheme likely yielded low photocontrast and, more importantly, this clone displayed poor Ca<sup>2+</sup> responses.

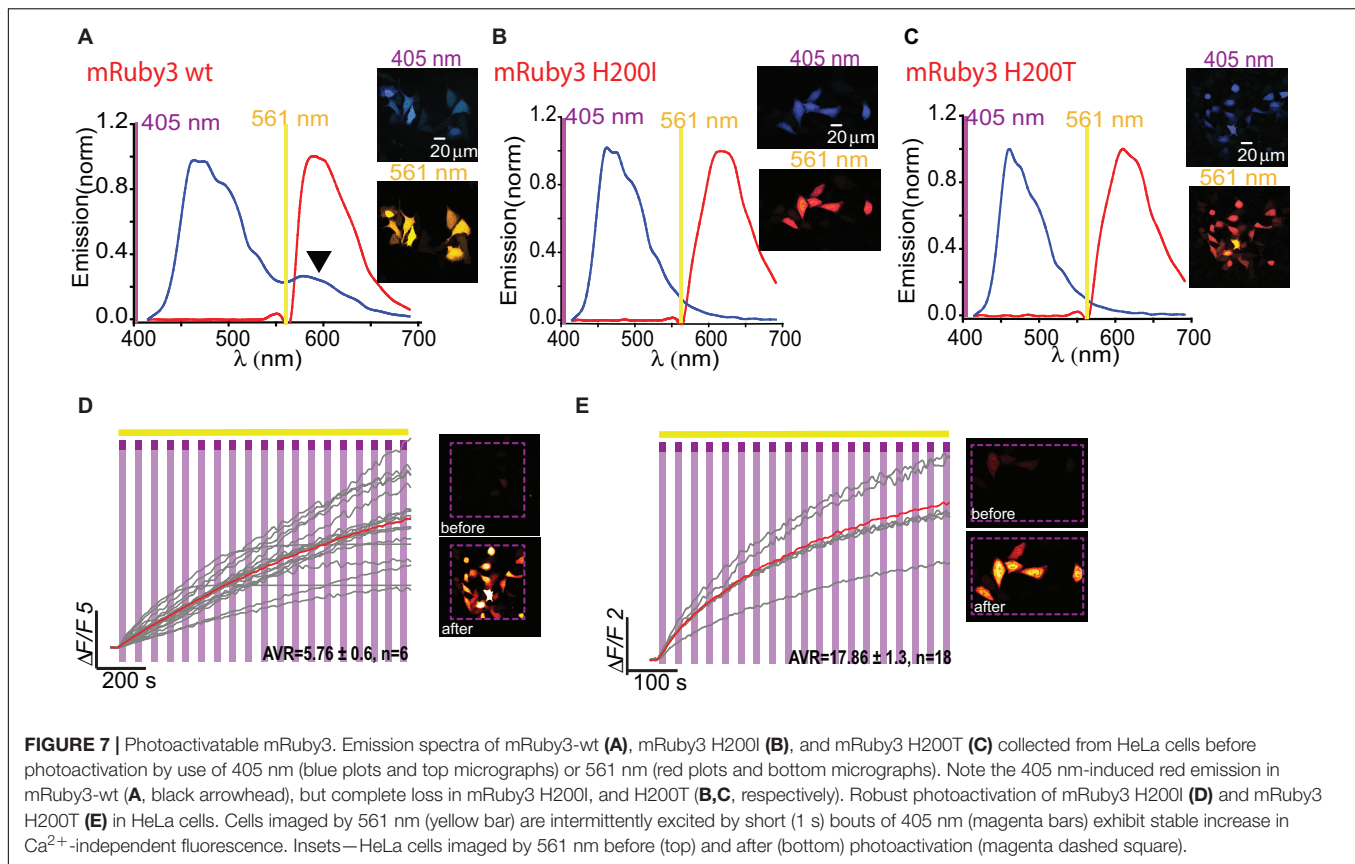
Substitution of isoleucine to threonine at position 78 (I78T) in mApple or mPlum-based probes, namely, R-GECO1 and -1.2, respectively, resulted in generating functional and PA probes. More specifically, PA-R-GECO1 and -1.2 express efficiently at 37°C in HEK293, HeLa

cells, as well as in cultured primary neurons, undergo robust 405 nm-induced photoactivation and readily report on Ca<sup>2+</sup>-activity (especially PA-R-GECO1.2 with Ca<sup>2+</sup>-dependent increases in fluorescence of up to 24 fold). In addition, these display low to moderate basal fluorescence (e.g., Figure 2B, pre-photoactivation), a trait we deem highly useful for initial detection of cells that express the clone prior photoactivation, without the need of additional fluorescent markers (such as GFP) or illumination with low-intensity near-UV (Berlin et al., 2015). Importantly, these probes also



show greatly diminished (or completely eliminated) artifactual behavior which should make them ideal for concomitant use with many blue light-absorbing optogenetic tools,

such as blue-absorbing opsins (Akerboom et al., 2013; Wu et al., 2013). We also report on the rapid engineering of a high-contrast PA-mRuby3<sub>I</sub>. Notably, PA-mRuby3<sub>I</sub> is based



on a highly optimized, bright, and stable monomeric RFP (Piatkevich and Verkhusha, 2010).

Although beyond the scope of this work, our systematic comparison between different mutations within multiple GECIs also sheds light on the transient photoconversion mechanism of R-GECOs. We observe that most variants can no longer emit red fluorescence when illuminated by near-UV light, despite retaining a blue-emitting population (Figures 3, 4). This observation rules-out the involvement of direct 405 nm-excitation of the red chromophore as the culprit for the transient increases in fluorescence. It also rules-out the instantaneous light-dependent maturation of the blue chromophore. The fact that many different mutations introduced around the chromophore abolished photoconversion and stabilized photoactivation support the notion that, unlike in GFP, light induces a chemical shift in the chromophore that is sufficiently long-lived (hundreds of ms to seconds) to enable increase in absorbance of 561 nm, so that when we revert back to 561 nm imaging of the probe, this is seen as a large increase in  $\text{Ca}^{2+}$ -independent fluorescence that disappears within half a second. Such long-lived isomerization of the red chromophore to an anionic fluorescent state (Wu et al., 2013), could then allow for, akin to GFP, further permanent chemical changes such as decarboxylation of the E222 residue (GFP numbering, Patterson and Lippincott-Schwartz, 2002; van Thor et al., 2002).

We note that probes that exhibit better photoactivation are also probes that tend to respond less well to  $\text{Ca}^{2+}$ .

For GCaMPs, binding of  $\text{Ca}^{2+}$ -ions changes their absorption spectrum, effectively increasing their ability to absorb 488 nm (i.e., the imaging wavelength) (Barnett et al., 2017). However, in the case of R-GECIs, binding of  $\text{Ca}^{2+}$ -ions can also increase their quantum yield (Molina et al., 2019). In fact, R-GECO and RCaMP exhibit very different mechanisms that engender increase in fluorescence when bound to  $\text{Ca}^{2+}$ . Specifically, whereas the fluorescence change in R-GECO is mostly due to a dramatic increase in the excitable protonation state (i.e., shift in absorption spectrum), akin to GCaMPs, RCaMPs (RCaMP1h and jRCaMPa or b) belong to a second class in which the increase in fluorescence depends on both  $\text{Ca}^{2+}$ -induced shift in fluorescence and in the quantum yield of the excitable state. Thus, in the case of R-GECI, it can be assumed that mutations around the chromophore that enhance photoactivation limit the subsequent increase in absorption following  $\text{Ca}^{2+}$ -binding. Conversely, studies of R-GECO's unique photoconversion behavior show that short wavelengths (405 and 488 nm) shift the absorbance of the calcium-bound population of R-GECO1 to the right therefore decreasing its fluorescence (by up to 40%) when illuminated with its optimal imaging wavelength (i.e., 561 nm) (Akerboom et al., 2013). Thus, it can be assumed that after loading the probe with calcium, its absorption of short wavelengths (employed for photoactivation) is also decreased and therefore would yield lower photoactivation. Inversely, when devoid of  $\text{Ca}^{2+}$ , illumination of R-GECO1 by short wavelengths results in an apparent decrease in the absorbance of protonated chromophore

**TABLE 2 |** Lack of correlation between amino acid properties and extent of photoactivation and  $\text{Ca}^{2+}$ -performance.

Amino acid	Polarity <sup>1</sup>	Hydrophobicity <sup>2</sup>	Volume <sup>3</sup>	Extent of photoactivation of R-GECO1	$\text{Ca}^{2+}$ -response
Ser	9.2	0.76	60.8	1.76	1.31
Arg	10.5	1.03	111.5		
Leu	4.9	-21.91	107.5		
Pro	8	-0.49	81		
Thr	8.6	0.59	77.1	2.5	
Ala	8.1	0.96	60.6	0.96	1.79
Val	5.9	-3.74	91.3	0.82	1.44
Gly	9	1.12	43.5		
Ile	5.2	-15.16	107.5		
Phe	5.2	-17.28	121.3		
Tyr	6.2	-15.09	123.6	1.94	
Cys	5.5	0.69	72.5		
His	10.4	1.03	99.3	0.61	2.06
Gln	10.5	1.21	93.9		
Asn	11.6	1.17	78		
Lys	11.3	0.92	108.5		
Asp	13	0.96	74.1		
Glu	12.3	0.86	90.4	1.33	
Met	5.7	-3.01	105.1		
Trp	5.4	-9.63	144.1		

<sup>1</sup>Grantham, R. Amino Acid Difference Formula to Help Explain Protein Evolution. *Science* 185, 862-864 (1974). <sup>2</sup>Bull, H.B. & Breese, K. Surface tension of amino acid solutions: a hydrophobicity scale of the amino acid residues. *Arch Biochem Biophys* 161, 665-670 (1974). <sup>3</sup>Kyte, J. & Doolittle, R.F. Simple method for calculating the average hydropathic character of a protein. *J. Mol. Biol.* 32, 325-332 (1972).

and a simultaneous increase in absorbance in deprotonated chromophore. In this case, it can therefore be assumed that stable photoactivation would mimic this scenario, namely, enabling R-GECO to absorb 561 better when it is devoid of  $\text{Ca}^{2+}$ , thereby performing less well when saturated by  $\text{Ca}^{2+}$  (Akerboom et al., 2013; Molina et al., 2019).

Lastly, we could not find any correlation between the property of the amino acids (hydrophobicity, polarity, or volume) and the extent of photoactivation or  $\text{Ca}^{2+}$ -performance (Table 2). This is not completely surprising as estimating how an amino acid substitution would affect the entire network around the chromophore, *a priori*, is extremely challenging without detailed spectroscopic analysis (Heim et al., 1994). Future spectroscopic work should shed light on the nature of these phenomena.

Together, we describe a fast and simple method for generating PA-GECIs from the R-GECO and RCaMP family. The best performing probes, namely, R-GECO1<sub>T</sub> and -1.2<sub>T</sub>, display basal fluorescence that can be imaged by very low 561 nm laser powers. This should therefore allow to detect the probes *in vivo* by use of two-photon imaging (Drobizhev et al., 2014). In addition, photoactivation by 405 light can be obtained via wide-field epifluorescence, as previously shown for similar probes at similar laser powers (e.g., CaMPARI; Ebner et al., 2019) or via light-guides (Sileo et al., 2015). However, as short wavelengths poorly penetrate tissues and scatter (Carmi et al., 2019), it would seem more attractive should these probes be compatible with two-photon illumination. Though we do not test for the latter in this work, previous work show the feasibility of photoconversion and imaging of RFPs (mApple and mPlum in

particular) using multiphoton lasers (Drobizhev et al., 2009, 2014; Molina et al., 2019).

## CONCLUSION

The ability to generate numerous PA-GECIs, by incorporation of a single point mutation at position 203 (GFP numbering), suggests that this mechanism is not restricted to a handful of RFP and should therefore be transferrable to other R-GECIs (and likely other RFPs). We anticipate that the PA-GECIs developed here will serve as a starting point for the development of additional or enhanced versions (of larger photoactivation contrast and larger  $\text{Ca}^{2+}$ -responses) by additional methods, such as directed evolution, and expect to see the emergence of new PA-R-GECIs in the very near future.

## MATERIALS AND METHODS

### cDNA Constructs and Site Directed Mutagenesis

R-GECO1, R-GECO1.2, RCaMP1h, and jRCaMP1a/b were purchased from Addgene (addgene clones: # 32444, 45494, #32444, #42874, respectively). Point mutations were introduced by PCR, saturating position I78 (equivalent to T203 in GFP) by all other amino acids: I78L, I78T, I78N, I78H, I78A, I78Y, I78Q, I78P, I78C, I78K, I78G, I78E, I78D, I78E, I78S, I78R, I78V, I78W (see list of primers at **Supplementary Table 1**). PCR reactions



were carried out with the use of Pfu polymerase (Promega, United States), at annealing temperatures of 60°C (1:30 min); extension at 68 °C (15 min). RCaMP1h was removed from its original bacterial expression vector using standard PCR reaction and inserted into a mammalian expression vector.

## Tissue Culture

Heterologous cell lines, HEK293 or HeLa cells, were grown to ~50% confluence on poly-D-lysine-coated 12 mm coverslips (Bar-Naor, Israel) and transfected with 0.5–1 µg plasmid DNA with the use of ViaFect (Promega, United States) for overnight incubation in Dulbecco's modified Eagle's medium (DMEM) with 5–10% fetal bovine serum (FBS) at 37°C and 5% CO<sub>2</sub>. Primary neuronal hippocampal neurons were collected as previously described (Berlin and Isacoff, 2018). Briefly, hippocampi were harvested from rat neonates (P0-1) and plated at a density of ~100K cells/well (24 well-plate) on PDL-coated 12 mm glass coverslips, grown at 37°C. At 7 days *in vitro* (DIV), neurons were transfected with 0.5–1 µg DNA of the different variants by the calcium-phosphate transfection method (Berlin and Isacoff, 2018) and imaged at 9–13 DIV. All animal procedures were approved by the Technion's Institutional Animal Care and Use Committee (permit no. IL-130-09-17).

## Imaging

Imaging was performed on a Zeiss Laser Scanning Confocal Microscope equipped with a spectrally resolved 32-pixel GaAsP detector array (LSM-880-meta detector; Zeiss, Germany). We monitored emission at 8 nm intervals. Excitation of R-GECIs was performed by 405 and 561 nm lasers. Brief pulses of 405 nm (typically rastering over defined regions of interest at 0.64 µs/pixel dwell time). The output power of the 405 nm laser line was ~3.4 mW when using an air objective (10x/0.45). It is measured at 100% power slider without laser blinking (i.e., bi-directional scanning). Our experiments were always performed by uni-directional scanning, hence the power is corrected by a factor of ~0.5, hence ~1.7 mW. Our experiments were conducted using a water immersion objective lens 20x [a water Plan-Apochromat objective lens; 20x/1.0 DIC D = 0.17 (UV) VIS-IR M27 75 mm] with a focal spot diameter of 0.5 µm (D = 1.2 \* λ/NA). This lens transmits identically to the one used for power measurements of the 405 nm laser line and it illuminates an area on the sample of 0.2 µm<sup>2</sup>. The power density (PD) under these conditions is ~10<sup>6</sup> W/cm<sup>2</sup>. The AOTF transmission is calibrated to be linear so that 1% laser power slider is equivalent to 10 KW/cm<sup>2</sup> @ 405 nm. Cells were imaged in a standard imaging solution containing (in mM): 138 NaCl, 1.5 KCl, 1.2 MgCl<sub>2</sub>, 2.5 CaCl<sub>2</sub>, 10 D-glucose, 10 HEPES, pH 7.4. Ca<sup>2+</sup>-imaging was performed for several minutes with low intensity 561 nm to avoid bleach. To test functionality, we applied histamine (15 µM; final concentration) or additional Ca<sup>2+</sup> (denoted Ca<sup>2+</sup>-challenge, +50 µM) when using HeLa or HEK293 cells, as previously described (Berlin et al., 2015). For imaging photoactivation in Ca<sup>2+</sup>-Free or Ca<sup>2+</sup>-saturated states, cells were either incubated for 10 min in nominally Ca<sup>2+</sup>-free imaging medium supplemented with the Ca<sup>2+</sup>-chelator EDTA (5 mM) and a Ca<sup>2+</sup>-ionophore;

ionomycin (10 µM). This treatment induces Ca<sup>2+</sup>-release and promotes Ca<sup>2+</sup>-depletion from cells. For saturating Ca<sup>2+</sup>, we incubated cells with extracellular Ca<sup>2+</sup> (2 mM) and ionomycin (10 µM) (McCombs and Palmer, 2008). Image acquisition and photoactivation (i.e., bleach mode; Zen software, Zeiss) are performed intermittently so that no image (i.e., fluorescence) is acquired during illumination with 405 nm. Time resolved fluorescence plots thereby present data from images acquired before and after the 405 nm photoactivation bouts. Construction of a continuous fluorescence plot is done by connecting the data from images acquired before photoactivation to the images following the bout (appearing as slopes, e.g., **Figure 3**; 15 s).

## Statistical Analysis

Change in fluorescence ( $\Delta F/F$ ) was calculated by  $(F_t - F_0)/F_0$ , where  $F_t$  is measured fluorescence (in arbitrary units, a.u.) at a given time  $t$  and  $F_0$  is initial baseline fluorescence, typically calculated from averaging the 10 first images.  $\Delta F/F = 1$  describes an increase by 100%, equivalent to twofold increase in fluorescence. Owing to easily observable basal fluorescence (see **Supplementary Figures 4e–g** for multiple examples), we did not need encounter near division-by-zero artifacts. For collecting emission spectra, we used small imaging intervals (8 nm, see above) which allowed us to plot the data as smooth (splined) curves rather than straight lines (SigmaPlot 11). We find no differences between the two plots (e.g., **Supplementary Figure 5e**). All results are displayed as mean ± SEM. Sample sizes are provided (summarized in **Table 1**). Significance was tested using one-way ANOVA (*post hoc* Tukey) where relevant and relationship between Ca<sup>2+</sup>-performance and extent of photoactivation was tested by Spearman correlation using SigmaPlot 11.

## DATA AVAILABILITY STATEMENT

All datasets generated for this study are included in the article/**Supplementary Material**.

## ETHICS STATEMENT

The animal study was reviewed and approved by the Technion's Institutional Animal Care and Use Committee (permit No. IL-130-09-17).

## AUTHOR CONTRIBUTIONS

WH and SB designed, performed, and analyzed the experiments and wrote the manuscript.

## FUNDING

Support was provided by the Israel Science Foundation (SB; 1096/17) and the Mallat Family Fund for Medical research (SB; 1015018). The research submitted is in partial fulfillment for a doctoral degree for WH.

## SUPPLEMENTARY MATERIAL

The Supplementary Material for this article can be found online at: <https://www.frontiersin.org/articles/10.3389/fncel.2020.00113/full#supplementary-material>

**FIGURE S1** | Sequence alignment of green and red fluorescent proteins. Homologous residues are color coded, whereas homology shared by all proteins is highlighted in yellow. Stars indicate the chromophore. Isoleucine residue in mPlum is indicated by blue circle. The T203 position (GFP numbering) is indicated by black arrowhead. Note that several PA-RFPs share positively charged amino acids (H or R) at the corresponding T203 position.

**FIGURE S2** | R-GECO1<sub>R</sub> and R-GECO1<sub>Y</sub>. **(a)** R-GECO1<sub>R</sub> does not express nor undergoes photoactivation in HeLa cells. Micrographs show HeLa cell before (left) and after (right) photoactivation (magenta dashed square). **(b)** R-GECO1<sub>Y</sub> undergoes photoactivation in HeLa cells. Micrographs show HeLa cell before (left) and after (right) photoactivation (magenta dashed square).

**FIGURE S3** | R-GECO1<sub>L</sub> retains light-induced artifacts. **(a)** Emission spectra of R-GECO1<sub>L</sub> collected from HeLa cells before photoactivation by use of 405 nm (blue plot and top micrograph) or 561 nm (red plot and bottom micrograph). Arrowhead indicates the weak direct excitation of the red chromophore by 405 nm. **(b)** R-GECO1<sub>L</sub> does not undergo photoactivation in HeLa cells. Cells imaged by 561 nm (yellow bar) are intermittently excited by short (1 s) bouts of 405 nm (magenta bars) does not exhibit stable increases in Ca<sup>2+</sup>-independent fluorescence but exhibits light-induced artifacts. **(c)** R-GECO1<sub>L</sub> does not responding to Ca<sup>2+</sup> (left), whereas R-GECO1.2<sub>L</sub> does (right).

**FIGURE S4** | Characterization of the effect of Ca<sup>2+</sup> on photoactivation and emission spectra of R-GECO1-I78T. **(a)** Ca<sup>2+</sup>-activity before and after photoactivation. Left: micrographs of R-GECO1-I78T expressed in HEK293 cells; initially (1), during photoactivation (2; before and after), and after photoactivation (3). Data are summarized in plot (right). Note the large increase in the amplitudes of the spontaneous Ca<sup>2+</sup>-oscillations after photoactivation (magenta bar). **(b,c)** Extent of photoactivation of R-GECO1-I78T under different conditions. **(b)** Micrographs of R-GECO1-I78T expressed in HEK293 cells in standard medium (top, red), Ca<sup>2+</sup>-free (middle, gray) and Ca<sup>2+</sup>-saturated (bottom, dark blue) conditions, before and after photoactivation. Data are summarized in **c**. Note that Ca<sup>2+</sup>-free and standard conditions are beneficial to photoactivation, whereas the presence of Ca<sup>2+</sup> is detrimental. **(d-f)** Representative experiment showing raw fluorescence traces before and after photoactivation of HEK293 cells in different media (as summarized in **c**). These show the detectable basal fluorescence (above zero) from which we could faithfully calculate  $\Delta F/F$  (see section “Materials and

Methods”). Traces also show that the baseline drastically changes, though maximal fluorescence is obtained under all conditions. Emission spectra induced by 561 nm illumination **(g)** or 405 nm **(h)**, under different conditions (color coded as in **e**).

**FIGURE S5** | Characterization of the effect of Ca<sup>2+</sup> on photoactivation and emission spectra of R-GECO1.2-I78T. **(a)** Micrographs of R-GECO1.2-I78T expressed in HEK293 cells in standard medium (top, red), Ca<sup>2+</sup>-free (middle, gray), and Ca<sup>2+</sup>-saturated (bottom, dark blue) conditions, before and after photoactivation. **(b)** Extent of photoactivation of R-GECO1.2-I78T under different conditions (color coded as in **a**). Note that Ca<sup>2+</sup>-free and standard conditions are beneficial to photoactivation, whereas the presence of Ca<sup>2+</sup> is detrimental. Emission spectra induced by 561 nm illumination **(c)** or 405 nm **(d)**, under different conditions (color coded as in **a**). Note the striking increase in the emission of 512 nm. **(e)** Comparison between straight and smoothed lines for plotting emission spectra. A representative emission spectrum induced by 561 nm. Data points are collected every 8 nm (open circles; see section “Materials and Methods”). Plot is constructed by straight lines (black) or smoothed (splined, red plot). Note the agreement between both plots.

**FIGURE S6** | Characterization of RCaMP1h and JRCaMP1b. **(a)** Emission spectra of RCaMP1h collected from HeLa cells before photoactivation by use of 405 nm (blue plot and top micrograph) or 561 nm (red plot and bottom micrograph). RCaMP1h **(b)** exhibits transient photoconversion during intervals of near UV light irradiation (405 nm), whereas JRCaMP1a **(c)** does not, rather undergoes slight photobleaching.

**FIGURE S7** | Photoactivatable JRCaMP1a and JRCaMP1b are poor Ca<sup>2+</sup>-probes. Emission spectra of JRCaMP1a<sub>1</sub> **(a)** and JRCaMP1a<sub>7</sub> **(b)** collected from HeLa cells before photoactivation by use of 405 nm (blue plots and top micrographs) or 561 nm (red plots and bottom micrographs). Stable photoactivation of JRCaMP1a<sub>1</sub> **(c)**, JRCaMP1a<sub>7</sub> **(d)**, JRCaMP1b<sub>1</sub> **(e)**, or JRCaMP1b<sub>7</sub> **(f)** in HeLa cells. Cells imaged by 561 nm (yellow bar) are intermittently excited by short (1 s) bouts of 405 nm (magenta bars) exhibit stable increase in Ca<sup>2+</sup>-independent fluorescence. Micrographs show HeLa cells imaged by 561 nm before (top) and after (bottom) photoactivation (magenta dashed square). (Right) Representative traces showing Ca<sup>2+</sup>-activity following the application of Ca<sup>2+</sup> (+50  $\mu$ M) of JRCaMP1a<sub>1</sub> **(c)**, JRCaMP1a<sub>7</sub> **(d)**, JRCaMP1b<sub>1</sub> **(e)**, and JRCaMP1b<sub>7</sub> **(f)**. **(g)** Correlation between extent of photoactivation and Ca<sup>2+</sup>-performance of various probes in HeLa cells and in HEK293 cells (inset). R-GECO1-I78T (red) and R-GECO1.2-I78T (blue) are highlighted. Note the inverse trend between the features (though non-significant, Spearman correlation, see section “Materials and Methods”).

**TABLE S1** | List of primers used to generate the various mutants tested. Mutated residues are highlighted (yellow).

## REFERENCES

- Akerboom, J., Carreras Calderón, N., Tian, L., Wabnig, S., Prigge, M., Toló, J., et al. (2013). Genetically encoded calcium indicators for multi-color neural activity imaging and combination with optogenetics. *Front. Mol. Neurosci.* 6:2. doi: 10.3389/fnmol.2013.00002
- Baird, G. S., Zacharias, D. A., and Tsien, R. Y. (1999). Circular permutation and receptor insertion within green fluorescent proteins. *Proc. Natl. Acad. Sci. U.S.A.* 96, 11241–11246. doi: 10.1073/pnas.96.20.11241
- Bajar, B. T., Wang, E. S., Lam, A. J., Kim, B. B., Jacobs, C. L., Howe, E. S., et al. (2016). Improving brightness and photostability of green and red fluorescent proteins for live cell imaging and FRET reporting. *Sci. Rep.* 6:20889. doi: 10.1038/srep20889
- Barnett, L. M., Hughes, T. E., and Drobizhev, M. (2017). Deciphering the molecular mechanism responsible for GCaMP6m's Ca<sup>2+</sup>-dependent change in fluorescence. *PLoS One* 12:e0170934. doi: 10.1371/journal.pone.0170934
- Berlin, S., Carroll, E. C., Newman, Z. L., Okada, H. O., Quinn, C. M., Kallman, B., et al. (2015). Photoactivatable genetically encoded calcium indicators for targeted neuronal imaging. *Nat. Methods* 12:852. doi: 10.1038/nmeth.3480
- Berlin, S., and Isacoff, E. Y. (2017). Synapses in the spotlight with synthetic optogenetics. *EMBO Rep.* 18, 677–692. doi: 10.15252/embr.201744010
- Berlin, S., and Isacoff, E. Y. (2018). “Optical control of glutamate receptors of the nmda-kind in mammalian neurons, with the use of photoswitchable ligands,” in *Biochemical Approaches for Glutamatergic Neurotransmission*. eds S. Parrot, and L. Denoroy, (Berlin: Springer), 293–325. doi: 10.1007/978-1-4939-7228-9\_10
- Berlin, S., Szobota, S., Reiner, A., Carroll, E. C., Kienzler, M. A., Guyon, A., et al. (2016). A family of photoswitchable NMDA receptors. *eLife* 5:e12040. doi: 10.7554/eLife.12040
- Carmi, I., De Battista, M., Maddalena, L., Carroll, E. C., Kienzler, M. A., and Berlin, S. (2019). Holographic two-photon activation for synthetic optogenetics. *Nat. Protoc.* 14, 864–900. doi: 10.1038/s41596-018-0118-2
- Dana, H., Mohar, B., Sun, Y., Narayan, S., Gordus, A., Hasseman, J. P., et al. (2016). Sensitive red protein calcium indicators for imaging neural activity. *eLife* 5:e12727. doi: 10.7554/eLife.12727
- Drobizhev, M., Stoltzfus, C., Topol, I., Collins, J., Wicks, G., Mikhaylov, A., et al. (2014). Multiphoton photochemistry of red fluorescent proteins in solution and live cells. *J. Phys. Chem. B* 118, 9167–9179. doi: 10.1021/jp502477c
- Drobizhev, M., Tillo, S., Makarov, N., Hughes, T., and Rebane, A. (2009). Absolute two-photon absorption spectra and two-photon brightness of orange and red fluorescent proteins. *J. Phys. Chem. B* 113, 855–859. doi: 10.1021/jp8087379
- Ebner, C., Ledderose, J., Zolnik, T. A., Dominiak, S. E., Turko, P., Papoutsi, A., et al. (2019). Optically induced calcium-dependent gene activation and labeling of

- active neurons using CaMPARI and Cal-Light. *Front. Synaptic Neurosci.* 11:16. doi: 10.3389/fnsyn.2019.00016
- Emiliani, V., Cohen, A. E., Deisseroth, K., and Häusser, M. (2015). All-optical interrogation of neural circuits. *J. Neurosci.* 35, 13917–13926. doi: 10.1523/jneurosci.2916-15.2015
- Fosque, B. F., Sun, Y., Dana, H., Yang, C.-T., Ohshima, T., Tadross, M. R., et al. (2015). Labeling of active neural circuits in vivo with designed calcium integrators. *Science* 347, 755–760. doi: 10.1126/science.1260922
- Heim, R., Prasher, D. C., and Tsien, R. Y. (1994). Wavelength mutations and posttranslational autooxidation of green fluorescent protein. *Proc. Natl. Acad. Sci. USA* 91, 12501–4. doi: 10.1073/pnas.91.26.12501
- Hoi, H., Matsuda, T., Nagai, T., and Campbell, R. E. (2012). Highlightable Ca<sup>2+</sup> indicators for live cell imaging. *J. Am. Chem. Soc.* 135, 46–49. doi: 10.1021/ja310184a
- Kerruth, S., Coates, C., Dürst, C. D., Oertner, T. G., and Török, K. (2019). The kinetic mechanisms of fast-decay red-fluorescent genetically encoded calcium indicators. *J. Biol. Chem.* 294, 3934–3946. doi: 10.1074/jbc.RA118.004543
- Lee, S., Song, Y.-K., and Baker, B. J. (2019). Engineering photoactivatability in genetically encoded voltage and pH indicators. *Front. Cell. Neurosci.* 13:482. doi: 10.3389/fncel.2019.00482
- Lukyanov, K. A., Chudakov, D. M., Lukyanov, S., and Verkhusha, V. V. (2005). Photoactivatable fluorescent proteins. *Nat. Rev. Mol. Cell Biol.* 6:885.
- Matsuda, T., Horikawa, K., Saito, K., and Nagai, T. (2013). Highlighted Ca<sup>2+</sup> imaging with a genetically encoded 'caged' indicator. *Sci. Rep.* 3:1398. doi: 10.1038/srep01398
- McCombs, J. E., and Palmer, A. E. (2008). Measuring calcium dynamics in living cells with genetically encodable calcium indicators. *Methods* 46, 152–159. doi: 10.1016/j.ymeth.2008.09.015
- Miyawaki, A., Shcherbakova, D. M., and Verkhusha, V. V. (2012). Red fluorescent proteins: chromophore formation and cellular applications. *Curr. Opin. Struct. Biol.* 22, 679–688. doi: 10.1016/j.sbi.2012.09.002
- Molina, R. S., Qian, Y., Wu, J., Shen, Y., Campbell, R. E., Drobizhev, M., et al. (2019). Understanding the fluorescence change in red genetically encoded calcium ion indicators. *Biophys. J.* 116, 1873–1886. doi: 10.1016/j.bpj.2019.04.007
- Morita, M., Nakane, A., Fujii, Y., Maekawa, S., and Kudo, Y. (2015). High cell density upregulates calcium oscillation by increasing calcium store content via basal mitogen-activated protein kinase activity. *PLoS One* 10:e0137610. doi: 10.1371/journal.pone.0137610
- Patterson, G. H., and Lippincott-Schwartz, J. (2002). A photoactivatable GFP for selective photolabeling of proteins and cells. *Science* 297, 1873–1877. doi: 10.1126/science.1074952
- Piatkevich, K. D., Murdock, M. H., and Subach, F. V. (2019). Advances in engineering and application of optogenetic indicators for neuroscience. *Appl. Sci.* 9:562. doi: 10.3390/app9030562
- Piatkevich, K. D., Subach, F. V., and Verkhusha, V. V. (2013). Far-red light photoactivatable near-infrared fluorescent proteins engineered from a bacterial phytochrome. *Nat. Commun.* 4:2153. doi: 10.1038/ncomms3153
- Piatkevich, K. D., and Verkhusha, V. V. (2010). Advances in engineering of fluorescent proteins and photoactivatable proteins with red emission. *Curr. Opin. Chem. Biol.* 14, 23–29. doi: 10.1016/j.cbpa.2009.10.011
- Shaner, N. C., Lin, M. Z., McKeown, M. R., Steinbach, P. A., Hazelwood, K. L., Davidson, M. W., et al. (2008). Improving the photostability of bright monomeric orange and red fluorescent proteins. *Nat. Methods* 5, 545–551. doi: 10.1038/nmeth.1209
- Shcherbakova, D. M., Subach, O. M., and Verkhusha, V. V. (2012). Red fluorescent proteins: advanced imaging applications and future design. *Angew. Chem. Int. Ed.* 51, 10724–10738. doi: 10.1002/anie.201200408
- Sileo, L., Pisanello, M., Patria, A., Della, Emhara, M. S., Pisanello, F., and De Vittorio, M. (2015). "Optical fiber technologies for in-vivo light delivery and optogenetics," in *Proceedings of 2015 17th International Conference on Transparent Optical Networks (ICTON)*, (Budapest: IEEE).
- Subach, F. V., Patterson, G. H., Manley, S., Gillette, J. M., Lippincott-Schwartz, J., and Verkhusha, V. V. (2009). Photoactivatable mCherry for high-resolution two-color fluorescence microscopy. *Nat. Methods* 6:153. doi: 10.1038/nmeth.1298
- Subach, F. V., Patterson, G. H., Renz, M., Lippincott-Schwartz, J., and Verkhusha, V. V. (2010). Bright monomeric photoactivatable red fluorescent protein for two-color super-resolution sptPALM of live cells. *J. Am. Chem. Soc.* 132, 6481–6491. doi: 10.1021/ja100906g
- Subach, O. M., Gundorov, S. I., Yoshimura, M., Subach, F. V., Zhang, J., Grünwald, D., et al. (2008). Conversion of red fluorescent protein into a bright blue probe. *Chem. Biol.* 15, 1116–1124. doi: 10.1016/j.chembiol.2008.08.006
- van Thor, J. J., Gensch, T., Hellingwerf, K. J., and Johnson, L. N. (2002). Phototransformation of green fluorescent protein with UV and visible light leads to decarboxylation of glutamate 222. *Nat. Struct. Mol. Biol.* 9:37.
- Walia, A., Waadt, R., and Jones, A. M. (2018). Genetically encoded biosensors in plants: pathways to discovery. *Annu. Rev. Plant Biol.* 69, 497–524. doi: 10.1146/annurev-arplant-042817-040104
- Wu, J., Liu, L., Matsuda, T., Zhao, Y., Rebane, A., Drobizhev, M., et al. (2013). Improved orange and red Ca<sup>2+</sup> indicators and photophysical considerations for optogenetic applications. *ACS Chem. Neurosci.* 4, 963–972.
- Yizhar, O., Fenno, L. E., Davidson, T. J., Mogri, M., and Deisseroth, K. (2011). Optogenetics in neural systems. *Neuron* 71, 9–34. doi: 10.1016/j.neuron.2011.06.004
- Zhao, Y., Araki, S., Wu, J., Teramoto, T., Chang, Y.-F., Nakano, M., et al. (2011). An expanded palette of genetically encoded Ca<sup>2+</sup> indicators. *Science* 333, 1888–1899. doi: 10.1126/science.1208592
- Zolnik, T. A., Sha, F., Johnenning, F. W., Schreiter, E. R., Looger, L. L., Larkum, M. E., et al. (2017). All-optical functional synaptic connectivity mapping in acute brain slices using the calcium integrator CaMPARI. *J. Physiol.* 595, 1465–1477. doi: 10.1113/JP273116

**Conflict of Interest:** The authors declare that the research was conducted in the absence of any commercial or financial relationships that could be construed as a potential conflict of interest.

Copyright © 2020 Hussein and Berlin. This is an open-access article distributed under the terms of the Creative Commons Attribution License (CC BY). The use, distribution or reproduction in other forums is permitted, provided the original author(s) and the copyright owner(s) are credited and that the original publication in this journal is cited, in accordance with accepted academic practice. No use, distribution or reproduction is permitted which does not comply with these terms.



# Nanobody-Based Probes for Subcellular Protein Identification and Visualization

Marit A. de Beer<sup>†</sup> and Ben N. G. Giepmans<sup>\*</sup>

Department of Biomedical Sciences of Cells and Systems, University of Groningen, University Medical Center Groningen, Groningen, Netherlands

## OPEN ACCESS

### Edited by:

Shai Berlin,  
Technion Israel Institute  
of Technology, Israel

### Reviewed by:

Serge Muyldermans,  
Vrije University Brussel, Belgium  
Mario Valentino,  
University of Malta, Malta

### \*Correspondence:

Ben N. G. Giepmans  
b.n.g.giepmans@umcg.nl

### <sup>†</sup>Present address:

Marit A. de Beer,  
Department of Biochemistry,  
Radboud University Medical Center,  
Nijmegen, Netherlands

### Specialty section:

This article was submitted to  
Non-Neuronal Cells,  
a section of the journal  
Frontiers in Cellular Neuroscience

**Received:** 16 June 2020

**Accepted:** 05 October 2020

**Published:** 02 November 2020

### Citation:

de Beer MA and Giepmans BNG  
(2020) Nanobody-Based Probes for  
Subcellular Protein Identification  
and Visualization.  
Front. Cell. Neurosci. 14:573278.  
doi: 10.3389/fncel.2020.573278

Understanding how building blocks of life contribute to physiology is greatly aided by protein identification and cellular localization. The two main labeling approaches developed over the past decades are labeling with antibodies such as immunoglobulin G (IgGs) or use of genetically encoded tags such as fluorescent proteins. However, IgGs are large proteins (150 kDa), which limits penetration depth and uncertainty of target position caused by up to ~25 nm distance of the label created by the chosen targeting approach. Additionally, IgGs cannot be easily recombinantly modulated and engineered as part of fusion proteins because they consist of multiple independent translated chains. In the last decade single domain antigen binding proteins are being explored in bioscience as a tool in revealing molecular identity and localization to overcome limitations by IgGs. These nanobodies have several potential benefits over routine applications. Because of their small size (15 kDa), nanobodies better penetrate during labeling procedures and improve resolution. Moreover, nanobodies cDNA can easily be fused with other cDNA. Multidomain proteins can thus be easily engineered consisting of domains for targeting (nanobodies) and visualization by fluorescence microscopy (fluorescent proteins) or electron microscopy (based on certain enzymes). Additional modules for e.g., purification are also easily added. These nanobody-based probes can be applied in cells for live-cell endogenous protein detection or may be purified prior to use on molecules, cells or tissues. Here, we present the current state of nanobody-based probes and their implementation in microscopy, including pitfalls and potential future opportunities.

**Keywords:** nanobody, chromobody, fluobody, probes, light microscopy, super-resolution microscopy, electron microscopy, tagging

## INTRODUCTION

Defining protein identity and visualizing protein localization is fundamental in biology. Uncovering dynamics of protein localization and function were boosted when green fluorescent protein (GFP) and other fluorescent proteins (FPs) were developed and used to tag proteins of interest (Tsien, 1998; Giepmans et al., 2006; Rodriguez et al., 2017). Advantages of these chimeric fusion proteins include the lack of distance between protein of interest and label, thereby improving the resolution, as well as the specificity of labeling derived from the genetic fusion. Disadvantages include modification of the target protein, with the consequence that



unmodified endogenous proteins cannot be studied (Giepmans et al., 2006). To detect endogenous proteins, immunolabeling using antibodies (immunoglobulins, mostly of the IgG isotype; IgGs) conjugated with small fluorophores are typically applied. However, for intracellular targeting IgGs require plasma membrane permeabilization leading to a damaged ultrastructure (Schnell et al., 2012). Furthermore, IgGs are large (~150 kDa; ~14 nm long; **Table 1**). This may result in a distance greater than 25 nm between target and label in indirect conventional immunolabeling, the so-called linkage error (Muyldermans, 2013; Mikhaylova et al., 2015). In addition, IgGs are multidomain proteins which require post-translational modifications (Muyldermans, 2013) and therefore preclude routine controlled genetic modification and modular expression in conjunction with e.g., GFP.

Nanobodies are single variable domains of heavy-chain only antibodies (hcAB) derived from *Camelidae* species (Hamers-Casterman et al., 1993; Muyldermans, 2013; Helma et al., 2015; Van Audenhove and Gettemans, 2016), but do not compromise in the binding-affinity compared to IgGs, due to its complementarity-determining region (CDR) organization (Muyldermans et al., 2001; Muyldermans, 2013; Beghein and Gettemans, 2017). Nanobodies have been explored since 2006 as labeling tools in light microscopy (LM) (Rothbauer et al., 2006), because of the several potential advantages of nanobodies over other labeling techniques. Nanobody-mediated targeting for protein identification is more precise than IgG targeting, as nanobodies are only ~15 kDa with a diameter of 2–3 nm (**Table 1**) and can be encoded by a relative short stretch single cDNA of 360 base pairs (Van Audenhove and Gettemans, 2016; Traenkle and Rothbauer, 2017; Carrington et al., 2019). This cDNA can genetically be fused to FPs cDNAs for intracellular (live-cell) imaging or tags can be added for purification and chemical modifications. Like IgGs, customized nanobodies can be created against a protein of interest and the cDNA can be

shared free of charge, as opposed to IgGs (Zuo et al., 2017; McMahon et al., 2018). Here, an overview is given about the past and potential future of nanobody application in microscopy.






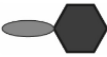






## NANOBODIES IN LIGHT MICROSCOPY

Nanobodies (see **Box 1** for terminology) can be expressed in cells conjugated to a detection module (like GFP) to target endogenous intracellular proteins, or they can be expressed, purified and then applied in immunolabeling resembling traditional immunofluorescence approach. Conventional immunolabeling is performed using IgGs, but for an improved penetration nanobodies can be used as an alternative (Fang et al., 2018). The improved penetration of nanobodies is illustrated in nuclear labeling of anti-GFP labeling targeting Histone2B (H2B)-GFP. Note that, in an equal labeling time, the nanobodies are colocalizing in the nucleus with the GFP, whereas the IgGs are mainly localized in the cytoplasm (**Figure 1A**). Though the anti-GFP is the best characterized and most used nanobody to date (**Table 2**), nanobodies are also used for visualizing endogenous proteins (**Figure 1B** and **Table 2**). Finally, nanobodies can be applied for live-cell imaging, both as purified proteins typically targeting extracellular antigens or being expressed from its introduced cDNA and targeted to intracellular antigens (Rothbauer et al., 2006; Ries et al., 2012).

### cDNA Delivery of Chromobodies for Intracellular Targeting

The first nanobody-based visualization of intracellular targets was achieved by the fusion to FPs (“chromobodies” Rothbauer et al., 2006; **Table 1**), being expressed in the target cells. Since then more nanobodies where developed targeting proteins inside cells (**Table 2**, delivered as cDNA). These intracellular chromobodies have been applied in small organisms like Danio

**TABLE 1 |** Overview of different probes used in microscopy.

	IgG	FP	Nanobody	Chromobody	Fluorescent nanobody	APEX2-Nanobody	FLIPPER-body
Reagent							
Synonyms	-	-	VhH, sdAB	Fluorescent intrabody	Fluobody	-	HRP-mCherry nanotrap
Size (kDa)	150	27	15	42	15	43	86
Cellular expression							
Endogenous detection							
Live-cell LM	*		*				
EM	*		*				
Color code	positive		moderate		Negative		
	 IgG	 nanobody	 FP	 Chemical dye	 Peroxidase		

\*Requires secondary labeling step.

**BOX 1 | Nanobody terminology Nanobody**

**Synonyms:** single domain antibody (sdAB), variable domain of heavy-chain only antibody (VhH), nAbs.

Small antigen binding protein, derived from heavy-chain only antibodies (hcAB). These are produced in cell culture or in bacteria.

**Intrabody**

The cDNA of this probe is expressed in the cells for intracellular antigen targeting.

**Chromobody**

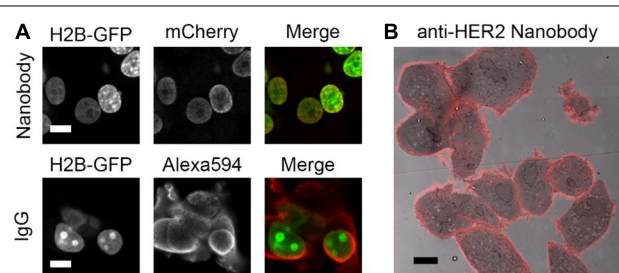
**Synonyms:** Fluobody, fluorescent nanobody.

Genetic fusion of intrabody and fluorescent protein. Direct visualization with microscopy is possible.

**Labeled nanobodies**

**Synonyms:** fluobody, fluorescent nanobody.

Nanobodies protein purified and tagged in vitro with e.g., a chemical dye.



**FIGURE 1 |** Nanobodies improve penetration and detect endogenous proteins. **(A)** Anti-GFP nanobody labeling (mCherry and peroxidase fused) and IgG labeling in H2B-GFP expressing cells. Cells permeabilized for 5 min with 0.1% Triton before labeling. Nanobodies and primary and secondary antibodies incubated for 1 h each. Note the colocalization between GFP and mCherry (nanobody), most prominently in the low-expressing cells, while Alexa Fluor 594 (IgG) mainly localizes in the cytoplasm. **(B)** High HER2 expressing cells, SkBr3, labeled with nanobodies targeting HER2. Overlay of nanobody fluorescence and EM image. Note the positive labeling at cell-cell contact sites. Bars: 10  $\mu$ m. Reproduced from De Beer et al. (2018), <http://creativecommons.org/licenses/by/4.0/>.

erio (Panza et al., 2015), *Drosophila melanogaster* (Harmansa et al., 2017), *Caenorhabditis elegans* (Pani and Goldstein, 2018) and *Toxoplasma gondii* (Tosetti et al., 2019) allowing live-cell and intravital microscopy. Intracellular expression of chromobodies in mice was successfully achieved by infecting the mice with adeno-associated viral particles containing the coding sequence of the chromobody (**Figure 2A**) (Wegner et al., 2017). Importantly, these chromobody approaches opens the opportunity for intravital imaging of endogenous proteins.

Next to defining protein localization, chromobodies can also relay functional changes in cells by fusing the nanobody to a fluorescent sensor for e.g.,  $\text{Ca}^{2+}$  or pH (Prole and Taylor, 2019). For instance, anti-GFP nanobodies are fused to a  $\text{Ca}^{2+}$  sensor targeting GFP labeled mitochondria (Zhao et al., 2011). The nanobody facilitates the  $\text{Ca}^{2+}$  sensor to be in close proximity of the mitochondria to allow for  $\text{Ca}^{2+}$  dependent fluorescence readout. This results in the imaging of the local  $\text{Ca}^{2+}$  concentrations upon different stimuli. In the same study, anti-GFP nanobodies were conjugated to a SNAP-tag, a 20 kDa protein, modified from the human DNA repair protein O<sup>6</sup>-alkylguanine-DNA alkyltransferase (Keppler et al., 2003). The SNAP-tag is used to recruit a chemical dye, which facilitates live-cell imaging for Chromophore-Assisted Light Inactivation (CALI) (Jacobson et al., 2008): laser-induced

subcellular destruction of a protein of interest. Thus nanobodies allow precise molecular targeting and enable analysis of the function of biomolecules, as well as precise protein manipulation with CALI allowing a direct cause/consequence study in living cells.

**Fluorescence Signal From Unbound Chromobodies**

Despite the success of chromobodies as intracellular probes, a disadvantage is their continued presence. Chromobodies fluoresce whether or not they bind to their target, as opposed to immunolabeling techniques that include multiple wash-out steps for unbound reagents or genetic fusions between target and FPs. To reduce the signal from non-bound chromobodies, conditionally stable chromobodies have been developed (Tang et al., 2016b). These modified anti-GFP chromobodies are instable and rapidly degraded by the proteasome. When stabilized, however, these chromobodies will bind their target and consequently will no longer be degraded. Indeed, engineering and application of conditionally stable anti-GFP chromobodies resulted in a reduced background fluorescence (Tang et al., 2016b). The mutations in the genetically modified nanobodies are highly conserved within nanobodies and therefore the switching from stable to instable nanobodies is generically applicable.

Non-targeted fluorescence can also be reduced by enhancer nanobodies (Roebroek et al., 2015). When the enhancer nanobodies bind with GFP, it increases the fluorescence and stability of the GFP. Enhancer nanobodies were also applied in a method to track single molecules in live-cell imaging (Ghosh et al., 2019). Here, an array of nanobodies is fused to the protein of interest, and expressed in cells with cytosolic monomeric GFP. Upon GFP binding to the array of nanobodies, the GFP molecules increase in fluorescent intensity, resulting in an increased signal-to-noise ratio. This binding can in the microscope be seen as a single dot, that represents a single protein of interest. In conclusion, the signal-to-noise ratio of chromobodies can be improved by degrading unbound chromobodies or by enhancing the fluorescence of bound FPs, which both will be beneficial in the detection of proteins.

**Delocalization of Targeted Proteins**

Modifying cellular systems, in any way, may of course result in altered biology (Schnell et al., 2012). Interactions between endogenous proteins and ectopically expressed chromobodies can potentially influence the localization and function of the protein of interest. Binding of nanobodies to their target during

**TABLE 2 |** Nanobody implemented in microscopy – An overview of targets that have been visualized using nanobodies and microscopy.

Target	Delivered as	Technique	References
Actin	cDNA or Protein	LM / SR	Rocchetti et al., 2014; Panza et al., 2015; Plessner et al., 2015; Moutel et al., 2016; Periz et al., 2017; Wegner et al., 2017; Abdellatif et al., 2019; Tosetti et al., 2019
Active $\beta$ 2-Ars	cDNA	LM	Irannejad et al., 2013
Alexandrium Minutum	cDNA	LM	Mazzega et al., 2019
ALFA-tag	cDNA or Protein	LM / SR	Gotzke et al., 2019
AMIGO-1	cDNA	LM	Dong et al., 2019
Amyloid $\beta$	Protein	LM	Li et al., 2016
Arabidopsis Thaliana	Protein	EM	De Meyer et al., 2014
ARTC2	Protein	LM	Bannas et al., 2015a,b
ATP7B	cDNA	LM	Huang et al., 2014
bacteriophage p2	Protein	EM	De Haard et al., 2005
BC2-tag	Protein	LM / SR	Braun et al., 2016; Virant et al., 2018
$\beta$ -catenin	cDNA or Protein	LM	Traenkle et al., 2015; Hebbrecht et al., 2020
BFP	Protein	SR	Sograte-Idrissi et al., 2019
CapG	cDNA	LM	De Clercq et al., 2013; Van Audenhove et al., 2013; Van Impe et al., 2008
CD11b	Protein	LM / CLEM	Rashidian et al., 2015; Duarte et al., 2016; Fang et al., 2018; Wöll et al., 2018; Cheloha et al., 2019
CEA	Protein	LM	Hafian et al., 2014; Ramos-Gomes et al., 2018
<i>C. Jejuni</i>	Protein	LM	Riazi et al., 2013
Clostridium Difficile toxin	Protein	LM	Pizzo et al., 2018
Cortactin	cDNA	LM	Van Audenhove et al., 2014, 2015; Bertier et al., 2018; Hebbrecht et al., 2020
Ebolavirus	Protein	LM	Darling et al., 2017; Sherwood and Hayhurst, 2019
EGFR	Protein	LM / CLEM	Iqbal et al., 2010a; Oliveira et al., 2012; Van De Water et al., 2012; Zarschler et al., 2014; Kooijmans et al., 2016; Krüwel et al., 2016; Van Driel et al., 2016; De Beer et al., 2018; Beltrán Hernández et al., 2019; Karges et al., 2019
Eps15	cDNA	LM	Traub, 2019
Extracellular vesicles	Protein	EM	Popovic et al., 2018
Fascin	cDNA	LM	Van Audenhove et al., 2015; Gross et al., 2016
FGFR1	cDNA	LM	Monegal et al., 2009
$\gamma$ -H2Ax	cDNA	LM	Rajan et al., 2015
GPCR	cDNA	SR	Sungkaworn et al., 2017
Gelsolin	cDNA	LM	Van Impe et al., 2008; Van Den Abbeele et al., 2010; De Clercq et al., 2013; Van Audenhove et al., 2013
Gephyrin	cDNA	LM	Dong et al., 2019
GFAP	Protein	LM / CLEM	Li et al., 2012; Fang et al., 2018
GFP / YFP	cDNA or Protein	LM / SR/ CLEM	Rothbauer et al., 2006, 2008; Bazl et al., 2007; Schornack et al., 2009; Kirchhofer et al., 2010; Caussin et al., 2011; Casas-Delucchi et al., 2012; Han et al., 2012; Li et al., 2012; Pellis et al., 2012; Ries et al., 2012; Hecce et al., 2013, 2017; Szymborska et al., 2013; Truan et al., 2013; Bleck et al., 2014; Wang et al., 2014; Ariotti et al., 2015, 2017, 2018; Finnigan et al., 2015; Harmansa et al., 2015, 2017; Kamiyama et al., 2015; Kaplan and Ewers, 2015; Katoh et al., 2015; Klamecka et al., 2015; Nieuwenhuizen et al., 2015; Platonova et al., 2015a,b; Roebroek et al., 2015; Shin et al., 2015; Wedeking et al., 2015; Berry et al., 2016; Chamma et al., 2016, 2017; Drees et al., 2016; Gross et al., 2016; Harper et al., 2016; Joensuu et al., 2016; Künzl et al., 2016; Moutel et al., 2016; Tang et al., 2016a,b; Teng et al., 2016; Wendel et al., 2016; Katrukha et al., 2017; Roder et al., 2017; Almuedo-Castillo et al., 2018; Buser et al., 2018; De Beer et al., 2018; Gadok et al., 2018; Klein et al., 2018; Pani and Goldstein, 2018; Temme et al., 2018; Buser and Spiess, 2019; Cramer et al., 2019; Ghosh et al., 2019; Mann et al., 2019; Osswald et al., 2019; Prole and Taylor, 2019; Seitz and Rizzoli, 2019; Sograte-Idrissi et al., 2019; Farrants et al., 2020; Joshi et al., 2020

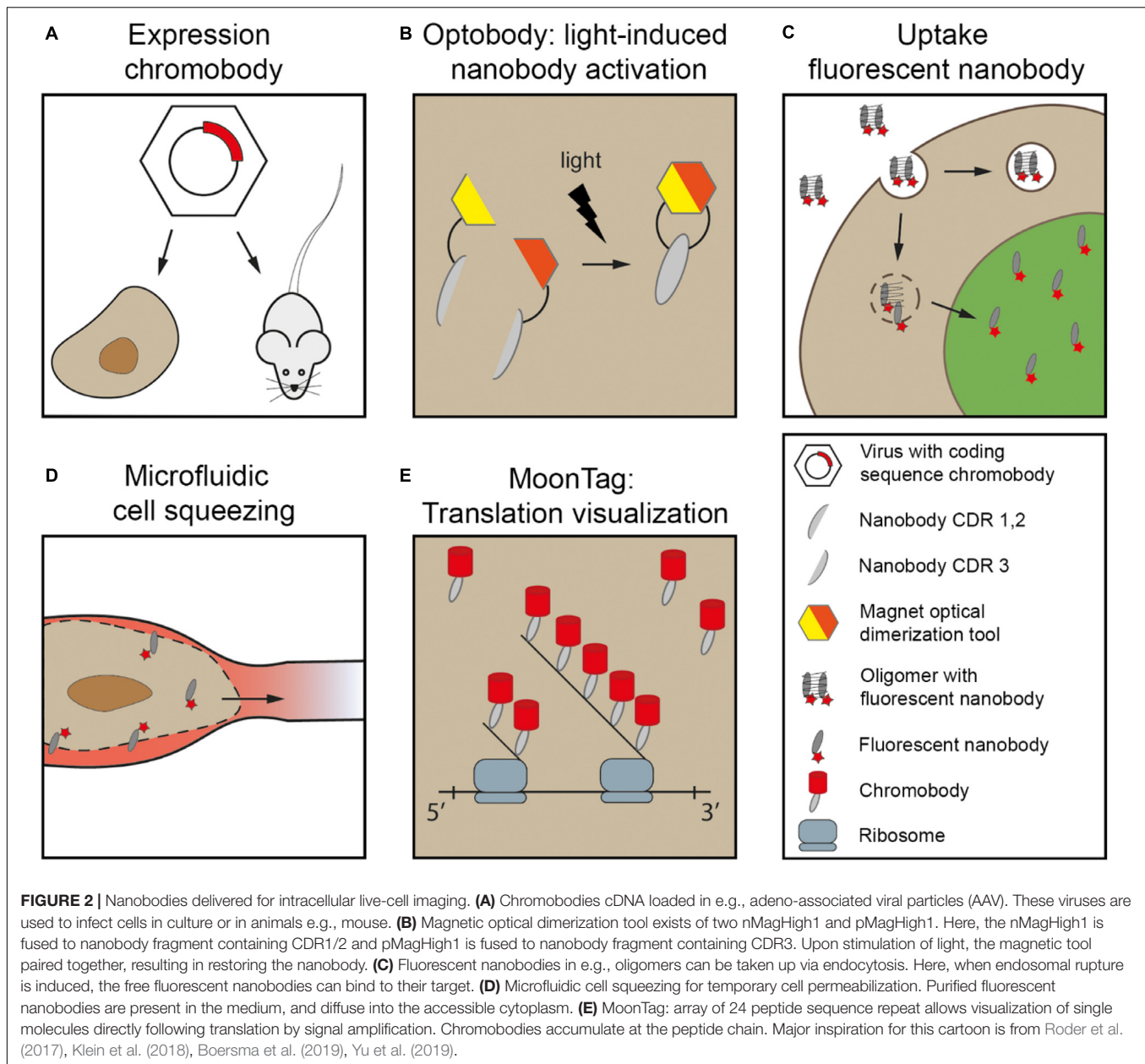
(Continued)

**TABLE 2 |** Continued

Target	Delivered as	Technique	References
Gp41 (HIV)	cDNA	LM	Lutje Hulsik et al., 2013; Boersma et al., 2019
H2A-H2B	cDNA	LM	Jullien et al., 2016
HER2	Protein	LM / CLEM	Kijanka et al., 2013; Rakovich et al., 2014; Zou et al., 2015; D'Hollander et al., 2017; Kijanka et al., 2017; De Beer et al., 2018; Ramos-Gomes et al., 2018; Martinez-Jothar et al., 2019; Debie et al., 2020
HIF-1 $\alpha$	Protein	LM	Groot et al., 2006
HIV-1	cDNA	LM / SR	Helma et al., 2012
Heterochromatin	cDNA or Protein	LM	Moutel et al., 2016
Protein 1 $\alpha$	Protein		
Homer1	cDNA or Protein	LM / SR	Dong et al., 2019
Human Neonatal Fc Receptor	Protein	LM	Andersen et al., 2013
Huntingtin	cDNA	LM	Southwell et al., 2008; Maiuri et al., 2017
IGFBP7	Protein	LM	Iqbal et al., 2010b; Tomanek et al., 2012
IRSp53	cDNA	LM	Dong et al., 2019
Lamin	cDNA or Protein	LM / SR	Rothbauer et al., 2006; Schmidthals et al., 2010; Roder et al., 2017; Klein et al., 2018
L-plastin	cDNA	LM	Delanote et al., 2010; De Clercq et al., 2013
LY-6C/6G	Protein	CLEM	Fang et al., 2018
Marburgvirus	Protein	LM	Darling et al., 2017; Sherwood and Hayhurst, 2019
MHC II	Protein	LM	Rashidian et al., 2015; Duarte et al., 2016; Cheloha et al., 2019
Mouse IgG	Protein	LM / SR	Pleiner et al., 2018
NFT2	cDNA	LM	Van Audenhove et al., 2013
NTA domain	cDNA	LM	Bertier et al., 2018
cortactin			
Nup35	Protein	SR	Ma et al., 2017
Nup37	Protein	SR	Ma et al., 2017
Nup85	Protein	LM / SR	Pleiner et al., 2015
Nup93	Protein	LM / SR	Pleiner et al., 2015; Göttfert et al., 2017
Nup98	Protein	LM / SR	Pleiner et al., 2015; Göttfert et al., 2017
Nup155	Protein	LM / SR	Pleiner et al., 2015
n-WASP	cDNA	LM	Hebbrecht et al., 2017
p53	cDNA or Protein	LM	Moutel et al., 2016
PARP1	cDNA	LM	Buchfellner et al., 2016
PCNA	cDNA	LM	Burgess et al., 2012; Panza et al., 2015; Schorpp et al., 2016
PepTag	cDNA	LM	Traenkle et al., 2020
PFR1	Protein	LM	Obishakin et al., 2014
POM121	Protein	SR	Ma et al., 2017
PSMA	Protein	LM	Fan et al., 2015
Rabbit IgG	Protein	LM / SR	Pleiner et al., 2018
RFP / mCherry	cDNA or Protein	LM / SR / CLEM	Ries et al., 2012; Bleck et al., 2014; Platonova et al., 2015a,b; Wedeking et al., 2015; Moutel et al., 2016; Teng et al., 2016; Ariotti et al., 2018; Buser et al., 2018; Buser and Spiess, 2019; Cramer et al., 2019; Prole and Taylor, 2019; Sograte-Idrissi et al., 2019
SAPAP2	cDNA	LM	Dong et al., 2019
NAP-25	Protein	LM / SR	Maidorn et al., 2019
Survivin	cDNA	LM	Beghein and Gettemans, 2017
Syntaxin 1A	Protein	LM / SR	Maidorn et al., 2019
Tau (phosphorylated)	Protein	LM	Li et al., 2016
Tubulin	cDNA or Protein	LM / SR	Olichon and Surrey, 2007; Mikhaylova et al., 2015; Moutel et al., 2016
VEGFR	cDNA	LM	Ahani et al., 2016
Vimentin	cDNA or Protein	LM / SR	Maier et al., 2015, 2016; Klein et al., 2018
VSG	Protein	LM	Stijlemans et al., 2004
Vsig4	Protein	LM	Zheng et al., 2019
V $\gamma$ 9V $\delta$ 2-T cell	Protein	LM	De Bruin et al., 2016

EM, electron microscopy; SR, super resolution fluorescence microscopy; CLEM, correlated LM/EM.





or post-translationally may disrupt proper protein folding, macromolecule organization and/or transport. Despite the often-highlighted benefits of nanobody-technology, like any other technique their use should be validated including the effect on protein localization. Artificial modifying localization of proteins can be used on purpose for targeted interference. Chromobodies targeting endogenous actin-binding proteins, like gelsolin and cortactin, led to a disturbed actin distribution (Van Audenhove et al., 2013; Hebbrecht et al., 2017; Wegner et al., 2017; Bertier et al., 2018) paralleled with a decrease in both the number of invadopodia as well as extracellular matrix degradation. These factors are important in cell migration (Wolf and Friedl, 2009). Thus, chromobodies-assisted protein modulation allows to study the contribution of specific proteins of biology, including cell

migration or some of its consequences, like the delay of metastasis (Bertier et al., 2018).

### Controlled Nanobody Activation

Spatiotemporal control of chromobody function is desirable in several assays. To initiate functionalized chromobodies in a controlled manner, chemogenetics or light stimuli can be applied to influence the binding capacity of the nanobody during and after synthesis. Such chemogenetic control employs ligand-modulated antibody fragments (LAMAs): a circularly permuted bacterial dihydrofolate reductase (cpDHFR) linked to the nanobody is in such a conformation that it recognizes and binds to the nanobody target. In the presence of cell permeable DHFR inhibitors, the conformation changes precluding the antigen

binding site of the nanobody binding the target, and thereby loss of association of nanobody and target. This process can be reversed to activate the nanobody binding (Farrants et al., 2020).

The light-dependent nanobody, termed photobody, uses a genetic photocaged tyrosine variant that results in the inactivation of the antigen-binding site (Arbely et al., 2012; Mootz et al., 2019). The photocaged tyrosine is photo-labile, and upon light induction (365 nm) the antigen-binding properties of the chromobodies are restored. Optobody, a second light-dependent tool, uses a split nanobody with a N-terminal fragment containing CDR1 and CDR2, and a C-terminal fragment containing CDR3 (**Figure 2B**; Yu et al., 2019). When both fragments are genetically fused to an optical-induced dimerization tool [MagHigh (Kawano et al., 2015)], the complete nanobody folds upon light stimulus and thereby forms the antigen-binding site. However, a generic position to split the nanobody is lacking, and thus for every different nanobody optimization and validation is needed. Overall, the activation of nanobodies using light or chemogenetic stimuli gives spatiotemporal control over the nanobodies, allowing precise subcellular modulation followed by direct readout of the biological consequences on targets studied.

## Purified Fluorescent Nanobodies Delivered for Live-Cell Imaging

Nanobodies can also be generated in cellular systems, subsequently purified and/or modified and then used in bioassays. Typically, these are secreted by mammalian cells or produced in high yields by bacteria (Harmsen and De Haard, 2007). After purification, the nanobody can for instance be coupled to chemical dyes (Beghein and Gettemans, 2017) to create fluorescent nanobodies (**Tables 1, 2**). Dyes suitable for super-resolution microscopy (SRM), i.e., LM beyond the diffraction limit resulting in typically 20 – 100 nm lateral resolution [reviewed in (Schermele et al., 2019)], will increase the resolution when using nanobodies compared to IgGs because of the smaller size of the reagents used, reducing the linkage error discussed above (Ries et al., 2012). Alternative to conjugation of purified nanobody with small fluorescent molecules, chromobodies can be expressed and purified. These chromobodies can then be directly used in fluorescent microscopy studies because they contain both the targeting module as well as the fluorescent module (**Figure 1**). The benefit of using cDNA encoding protein modules is the ease to switch target or color with molecular cloning tools. To employ these fluorescent nanobodies in live-cells different delivery mechanisms for extracellular or intracellular targets have been created.

### Extracellular Targets

The extracellular domain of peripheral membrane proteins in cultured cells is well accessible to ectopic added reagents and therefore straightforward to target in live-cell imaging. Nanobodies that target extracellular receptors may trigger receptor specific endocytosis, which can be important for e.g., drug delivery. Endocytosis can be triggered via binding with

the human epidermal growth factor receptor 2 (HER2). Anti-HER2 nanobodies (Kijanka et al., 2013) coupled to fluorescent, drug containing nanoparticles (Martinez-Jothar et al., 2019), were indeed able to trigger endocytosis. After the trigger, uptake and cell viability was visualized to examine the effect of the therapeutic nanoparticles. So, receptor mediated endocytosis can be activated using fluorescent nanobodies to study therapeutic agents coupled to the nanobodies.

Super resolution localization of GFP surface-exposed by cells has been achieved while studying dynamic changes at the plasma membrane: The glycosylphosphatidylinositol (GPI)-anchored GFP reporter was further probed with Alexa647-conjugated nanobodies to enable SRM based on the blinking of the Alexa-dye. This resulted in higher resolution imaging of dynamic changes and detection of protein enrichments in the plasma membrane (Ries et al., 2012; Virant et al., 2018). Indirect visualization enables newly displayed proteins at the plasma membrane. Here, all available antigens first are blocked by unconjugated nanobody. Upon exocytosis stimuli, at the plasma membrane, new extracellular exposed antigens can be detected with fluorescent nanobodies (Seitz and Rizzoli, 2019). This pulse-chase approach allows dynamic studies, e.g., protein turnover, of receptors and other cell surface proteins.

### Intracellular Targets

The plasma membrane is a physical barrier for the nanobodies to target intracellular proteins in live-cells. Therefore, custom delivery methods are needed to target endogenous proteins in (living) cells without permeabilizing the plasma membrane. If nanobody expression is not an option because it first needs chemical modification or the concentration should be well-controlled, a purified nanobody may be delivered to cells. Fluorescent nanobodies can enter cells via endocytosis, when they formed non-covalent complexes with oligomers (**Figure 2C**; Roder et al., 2017) or they undergo lipid-based protein transfection (Oba and Tanaka, 2012; Virant et al., 2018). After endocytosis, the nanobodies need to escape the endosomal system and the formed complexes need to be degraded. However, using this strategy one has to take into account that the efficiency of endosomal escape is low (Stewart et al., 2016) and the nanobodies in the endosomes are already fluorescent, resulting in localized labeling of the endosomal system.

To prevent cellular uptake via endocytosis, cell-permeable nanobodies were generated by the addition of a cyclic cell-penetrating peptide [cCPP; (Herce et al., 2017)]. cCPPs are arginine-rich peptides that facilitates direct penetration of the plasma membrane to enter directly into the cytoplasm, independent of endocytosis. The efficiency of the labeling is expected to be increased because endosomal escape after endocytic uptake is omitted. Another advantage of using the cell-penetrating peptide is the ability to co-transport recombinant proteins, e.g., GFP, inside the cells, when both are bound to the nanobody. Although the efficiency of this co-transport was low, this cell-permeable nanobody can be further explored to serve as a drug delivery vehicle. A major disadvantage of the cCPPs however, is the strong tendency to accumulate in the nucleolus.

Generating temporary permeable plasma membranes is another approach to artificially deliver cargo inside cells. Different methods to temporarily permeabilize the membrane have been developed: (i) Electroporation to deliver nanobodies linked to fluorescent quantum dots (QDs) into cells (Shi et al., 2018). The QDs were used for single particle visualization of intercellular transport by targeting kinesin motor proteins (Katrukha et al., 2017); (ii) Artificial plasma membrane channels that allow chromobody delivery into cells can be formed by bacterial Streptolysin O (Teng et al., 2016). Unbound nanobodies are removed during rinsing and the channels are closed upon switching to a recovery medium; (iii) Photoporation in which a laser-induced transfection enables the delivery of the nanobodies intracellular, and when these are fluorescently labeled, these can be directly detected (Hebbrecht et al., 2020). (iv) Another method to induce temporary damage to the plasma membrane is cell squeezing through the small capillaries of a microfluidic system resulting in fragility of the plasma membrane (Figure 2D; Klein et al., 2018). While the cells are squeezed, extracellular proteins can diffuse into the cells. When cells leave the small capillary the plasma membrane recovers to its normal state. Obviously, the effect of any temporary permeabilization approach used to enable nanobodies entrance into cells, is that endogenous molecules might diffuse out or targets may delocalize.

## General Applicable Peptide Tags

Genetic fusion with FPs cDNA is the widely used technique for protein visualization in living systems, but sometimes smaller peptide tags are preferred. Currently, there are no nanobodies available against common generic peptide tags (Muyldermans et al., 2001; Stijlemans et al., 2004; De Genst et al., 2006; Braun et al., 2016). Hence, three new small tags have been developed along with their respective targeting nanobodies. (i) The BC2-tag is a 12 amino acid peptide sequence originating from  $\beta$ -catenin (Braun et al., 2016; Virant et al., 2018), but the nanobody does not recognize endogenous  $\beta$ -catenin making it fairly specific for the tag only. (ii) The ALFA-tag (13 amino acids) forms an  $\alpha$ -helix and is naturally absent in eukaryotes (Gotzke et al., 2019), also making it a specific target for its nanobody, which also counts for the (iii) Pep-Tag (15 amino acids) (Traenkle et al., 2020).

An array of peptides fused to the protein of interest can amplify the fluorescent signal, and thus increase the signal-to-noise ratio. A peptide-repeat called MoonTag (Boersma et al., 2019) was created to visualize active translation (Figure 2E). Here, an array of a 15 amino acid peptide sequence was added N-terminal of the protein of interest. The newly formed peptide chain forms a docking site for chromobodies. The MoonTag can be combined with the SunTag; an intracellular expressed single-chain variable fragment (scFV; Tanenbaum et al., 2014). Combining the two tags will allow visualization of different reading frames within a single mRNA or can be used to amplify the signal from different targets. Given the mechanism of probing the target with a cDNA encoded peptide repeat, making use of the same antibodies, this is a highly versatile enhancer system.

## NANOBODIES IN ELECTRON MICROSCOPY

While resolution of targets in LM is improved by using nanobodies because of a reduced linkage error compared to IgG targeting, the ultrastructural remains unexplored. In electron microscopy (EM), the ultrastructure is revealed, but localizing the protein of interest within this structure also requires probes. EM-visualization of targets benefits from the nanobody-technology because the probe is small and thus penetrates better. Therefore, milder permeabilization is needed, better preserving the ultrastructure. Moreover, the small size improves the resolution compared to traditional immuno-EM because the target and identifiable tag are in close proximity. Also in EM proteins can be specifically identified using genetically encoded or affinity-based probes. Genetically encoded probes may be based on peroxidases that creates black precipitates in the presence of diaminobenzidine (DAB) and  $H_2O_2$ . Affinity-based probes include electron dense nanoparticles like nanogold and QDs (De Boer et al., 2015). Of course the genetically encoded probes form good candidates to use in conjunction with nanobodies as a multi-modular probe for EM studies.

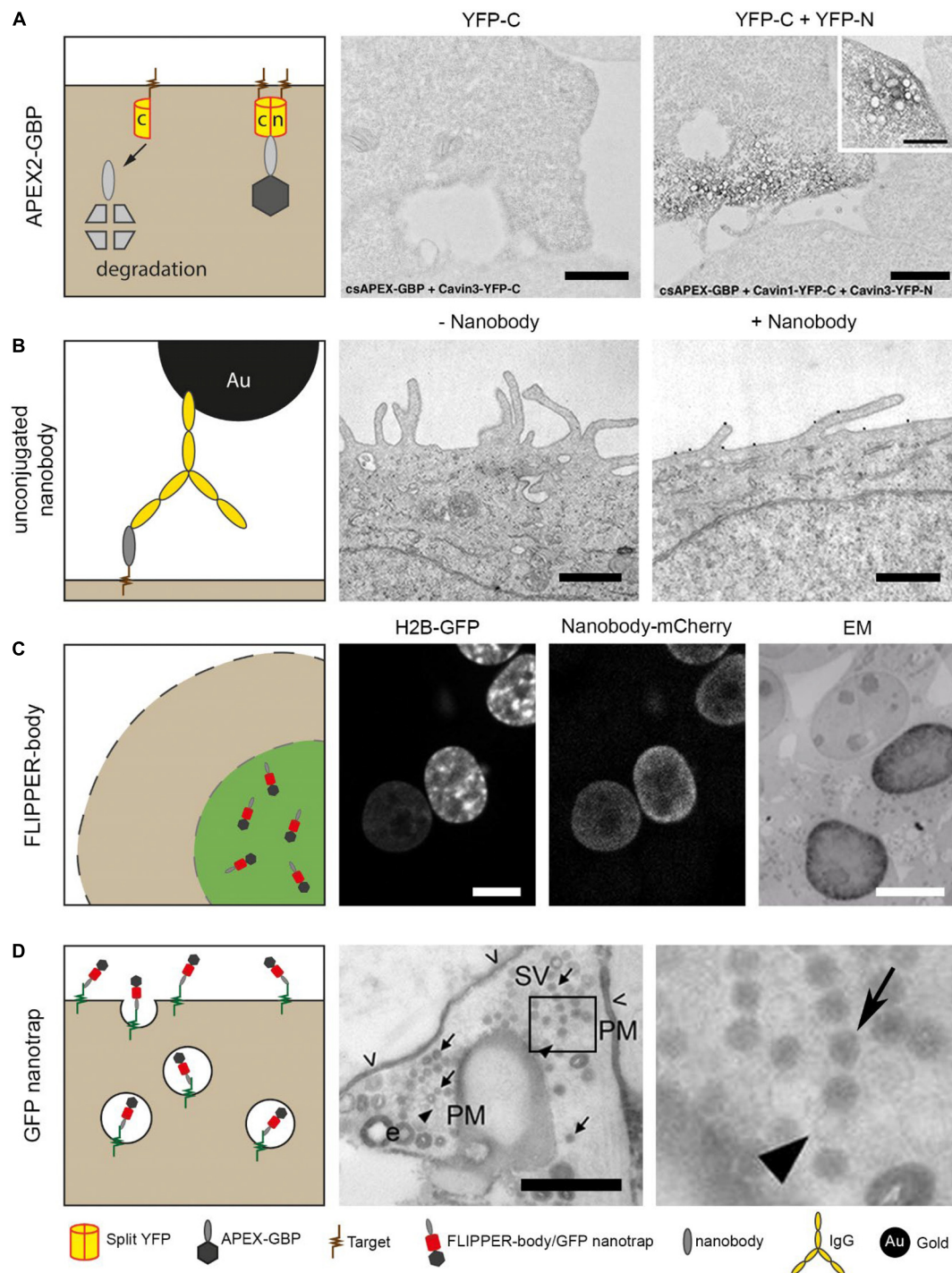
## Intracellular Nanobody Expression

Intracellular nanobodies fused with soybean ascorbate peroxidase (APEX2) (Lam et al., 2015) can target GFP or mCherry to add an electron dense mark to the protein of interest at EM level (Ariotti et al., 2015, 2017). This APEX2-nanobody can be applied as general CLEM (correlated LM/EM) probe because many cells and small organisms have already been engineered to express GFP or mCherry. Using conditionally stable nanobodies (section Nanobodies In Light Microscopy), unbound APEX2-nanobody is degraded and thereby improve EM detection of the target proteins (Ariotti et al., 2018). The conditionally stable APEX2-nanobody enables studying protein-protein interactions by making use of splitFPs as target (Figure 3A; Ghosh et al., 2000; Hu and Kerppola, 2003). Here, a protein of interest and its potential interacting protein are genetically fused with different segment of e.g., GFP. Anti-GFP APEX2-nanobody can only bind to the folded GFP, representing the interaction between the two proteins of interest. When GFP is absent, the conditionally stable APEX2-nanobodies are degraded. Another alternative to study protein-protein interactions would be by using nanobodies fused to splitHRP or splitAPEX2 (Martell et al., 2016; Han et al., 2019). Two distinct nanobodies recognizing proteins within close proximity will facilitate the refolding of the peroxidase, which will result in DAB precipitates at that location in the sample. The split peroxidase thus reduces the signal of unbound nanobodies, leading to a more conclusive picture. In conclusion, where chromobodies allow dynamic studies of endogenous proteins, APEX2-nanobodies enable high resolution analysis in the ultrastructural context.

## Nanobodies as Immunolabeling Reagent

Purified nanobodies can be applied for affinity-based immunolabeling, and thereby replace conventional IgGs. Immunolabeling with unconjugated nanobodies was used to





**FIGURE 3 |** Nanobody technology for EM. **(A)** Cells were expressing only C-terminus YFP or both C- and N-terminus YFP. The cells also expressed a conditionally stable anti-YFP, for proteasomal degradation of unbound probe. The nanobodies were genetically fused with peroxidase, APEX2, for EM detection. Note that only black precipitation is visible in cells expressing C-terminus YFP and N-terminus YFP. This confirmed the degradation of the nanobody with the peroxidase. Bars: 1  $\mu$ m. **(B)** Purified nanobodies were used as primary antigen binding protein to reduce the distance between label and antigen. Nanobodies can be detected using an anti-VhH IgG conjugated to gold for EM visualization. Bars: 0.5  $\mu$ m. **(C)** Cells express H2B-GFP from **Figure 1A**, and are permeabilized after fixation followed by labeling with anti-GFP FLIPPER-bodies. Note the colocalization in LM and the dark, positive nucleus in EM versus an unlabeled nucleus. Bars: 10  $\mu$ m. **(D)** Neuronal cells expressing pHluorin on the plasma membrane. Added anti-GFP nanobodies bind to the pHluorin, and after a pulse stimulation, synaptic vesicles are formed. In EM, a population of unlabeled and labeled synaptic vesicles is detected. Arrows indicate synaptic vesicles, arrow heads indicate unstained vesicles and open arrow heads indicate residual staining (PM, plasma membrane, SV, Synaptic vesicle). Bar: 0.5  $\mu$ m. The images in **(A–D)** have been reproduced from the following studies (Joensuu et al., 2016; Kijanka et al., 2017; Ariotti et al., 2018; De Beer et al., 2018), all of which have been published under a Creative Commons Attribution License.



label HER2 in breast cancer cells, followed by a secondary anti-nanobody IgG conjugated with nanogold (**Figure 3B**; Kijanka et al., 2017). Although this already improved the resolution, it could benefit more by replacing the IgG a direct labeling method using conjugated nanobodies.

## CLEM and Nanobodies

Reagents used in CLEM that are readily detectable both in the FLM and EM, like nanogold or QDs, are relatively large and/or bulky in comparison to 15–30 kDa range FPs or even smaller fluorescent dyes like FITC. These inorganic nanoparticles whether or not conjugated to nanobodies, will have limited penetration (Giepmans et al., 2005; Schnell et al., 2012). Therefore, we developed a completely protein-based probe, called “FLIPPER”-body (Kuipers et al., 2015; De Beer et al., 2018) with (i) a nanobody as targeting module; (ii) a FP for LM analysis; and (iii) a horseradish peroxidase (HRP) for EM analysis. The FLIPPER-bodies were produced by mammalian cells applied as immunoreagent to label e.g., intracellular GFP (**Figure 3C**). Other targets were generated by simple molecular cloning interchanging the modules of the probe. FLIPPER-bodies improve penetration due to its size and flexibility compared to IgGs-targeted nanoparticles and thus lead to a better target detection while maintaining reasonable ultrastructure.

In conventional EM glutaraldehyde is used to fix the samples for ultrastructural preservation (Schnell et al., 2012). However, cells fixed with paraformaldehyde become permeable for small molecules like e.g., small fluorescent nanobodies (Fang et al., 2018). This labeling without adding permeabilization reagents method was further developed to stain intracellular targets in fixed mouse tissue slices. When targeting an intracellular target with both nanobody and IgG, the nanobody penetrated up to 100  $\mu\text{m}$  into a brain tissue slice, while the IgGs only stained the surface of the slice. Subsequently, the same cells were imaged with EM and ultrastructural details were well preserved due to glutaraldehyde fixation after performing the nanobody labeling. So, detergent treatment is not required when using small nanobody probes and thus cellular structure is better preserved. The technique needs to mature further to establish the ratio of positives and false negatives to determine if the recognition of the targets is generically reliable. Moreover, the accessibility of targets within organelles, like mitochondria or nucleus, remains to be studied further.

## Nanobodies for Live-Cell Imaging and EM

Alternatively to expressing nanobody-based probes in the cellular system of interest, they also can first be purified and then applied to cells. An elegant example of this approach has been used to visualize the formation of synaptic vesicles in living cells (Joensuu et al., 2016). Ultrastructural localization of newly formed synaptic vesicles can be examined using peroxidase-fused nanobodies. Vesicle-associated membrane protein 2 (VAMP2) mediates the formation of synaptic vesicles and is expressed at the plasma membrane of neuronal cells. Anti-GFP nanobodies were applied to target pHluorin, a GFP derivative, fused with VAMP2 (**Figure 3D**). Upon  $\text{K}^+$  stimulation, pHluorin-VAMP2 with bound nanobody is endocytosed, and new synaptic vesicles

are formed. After EM preparation, the newly formed synaptic vesicles were stained black, as a result of the peroxidase attached to the nanobody, whereas older synaptic vesicles remained unstained. Thus, the endocytic route of specific proteins of interest can be visualized.

Purified nanobodies, fused to a FP and a peroxidase, were used to analyze the retrograde transport system in live-cells (Buser and Spiess, 2019) or within ultrastructural context (Buser et al., 2018) to study the transport from the cell surface to the Golgi complex. Cells with GFP-modified cycling reporter proteins at the plasma membrane captured the nanobodies extracellular and transported them in the cells. CLEM revealed the dynamic behavior of different cycling reporter proteins, and showed the ultrastructural localization of the reporter proteins. Overall, these nanobody-based CLEM probes can reveal the localization of plasma membrane proteins and visualize their dynamics, together with the ultrastructural context.

## Nanobodies in Cryo-EM

Structural analysis of proteins at atomic resolution is achieved by cryo-EM [reviewed in (Kühlbrandt, 2014; Egelman, 2016; Cheng, 2018)]. However different conformations of proteins may be present, hindering the structural determination of specific states. Here, nanobodies can help to stabilize the proteins into a certain conformational state [reviewed in (Uchański et al., 2020)], especially as the targeting module in rigid chimeras termed megabodies. These stabilizing nanobody-chimeras recently have been used to solve the type A  $\gamma$ -aminobutyric (GABA<sub>A</sub>) structure in membranes-like structures in presence and absence of natural ligands and antagonists (Lavery et al., 2019; Masiulis et al., 2019). Using the megabodies, no longer the target proteins themselves need to be engineered and thus structure on the endogenous proteins is being revealed. Likely, nanobody technology will further contribute to structural biology on many other target proteins by facilitating single conformational protein states and better understand the dynamic regulation of biomolecules by their ligands without directly altering the proteins at study.

## NANOBODIES FOR MICROSCOPY: TO DATE A GREAT POTENTIAL BUT SUCH A LIMITED USE

Nanobodies have clear benefits over conventional IgGs antibodies or genetically encoded probes. Nanobodies (i) have a small diameter resulting in better resolution and better penetration; (ii) can visualize endogenous proteins in live-cell imaging; (iii) are encoded by a one cDNA, which enables easy molecular cloning; (iv) allow researchers to create and produce custom multi-modal probes. Potential artifacts specific for nanobody technology in microscopy include signal from chromobodies independent of target binding and modified localization of the protein target, as detailed above.

Nanobodies are still limited used in research, mainly due to the limitation in the availability of nanobodies for general targets compared to IgGs and researchers are not aware of the possibilities of nanobody in microscopy.

Here, we aim to increase the visibility of opportunities and benefits highlighted in the main text, but also exemplified by the successful new insights and new nanobody-based reagents by many (Table 2). Other ways to improve the use of nanobodies in research are open access sharing of nanobodies cDNA to allow researchers to create and manipulate their own labeling reagent and to increase the nanobody database of general targets. Currently, most nanobodies are generated via *Camelidae* immunization, a route that may be a (seemingly) hurdle for scientists. However, these days the generation of nanobodies is both economically and time-wise competitive with generation of newly synthesized rabbit IgG against specific targets. The novice user obviously will benefit of expertise and accessibility to the needed infrastructure by more experienced users mentioned throughout this review. In addition, a fast method based on a yeast display platform to select nanobodies *in vitro* has been established (McMahon et al., 2018).

## From Current State to Future Outlook: Nanobodies Towards a Common Technique

Protein identification in microscopy has been greatly aided by immunolabeling using IgGs as well as the application of genetically encoded tags. Nanobody technology, being explored for approximately 25 years is a great additional tool. Like IgGs, endogenous proteins can be easily studied without direct modification. Moreover, the single domain properties and therefore the easy use as a module in other genetically encoded probes allow freedom of use of tags and targeting module. In line with SRM techniques, nanobodies have the added benefit over IgGs that they hardly provide distance between target and label

(linkage error). The major limitation in the use of nanobodies in general is the sparse availability of high affinity nanobodies for specific targets. Increasing the availability for different targets using immunization and/or micro-organism-based libraries will increase the variation in the decade to come. When more targets can be studied with nanobodies these will become a common tool in the lab and share the top-3 podium with genetically encoded tags as well as IgGs since they share benefits of both approaches to identify and visualize targets of interest in dynamic systems and with high precision.

## AUTHOR CONTRIBUTIONS

MB performed the experiment and made the figures. MB and BG wrote the manuscript. Both authors contributed to the article and approved the submitted version.

## FUNDING

All sources of funding received for the research have been submitted. Open access publication fee was partially waived by FiCN.

## ACKNOWLEDGMENTS

We thank our lab members for discussions; financial support by Netherlands Organization for scientific research (STW Microscopy Valley 12718, NWO 175-010-2009-023, and ZonMW 91111.006) and de Cock-Hadders Stichting.

## REFERENCES

- Abdellatif, M. E. A., Hipp, L., Plessner, M., Walther, P., and Knöll, B. (2019). Indirect visualization of endogenous nuclear actin by correlative light and electron microscopy (CLEM) using an actin-directed chromobody. *Histochem. Cell Biol.* 152, 133–143. doi: 10.1007/s00418-019-01795-3
- Ahani, R., Roohvand, F., Cohan, R. A., Etemadzadeh, M. H., Mohajel, N., Behdani, M., et al. (2016). Sindbis virus-pseudotyped lentiviral vectors carrying VEGFR2-specific nanobody for potential transductional targeting of tumor vasculature. *Mol. Biotechnol.* 58, 738–747. doi: 10.1007/s12033-016-9973-7
- Almuedo-Castillo, M., Bläpfe, A., Mörsdorf, D., Marcon, L., Soh, G. H., Rogers, K. W., et al. (2018). Scale-invariant patterning by size-dependent inhibition of Nodal signalling. *Nat. Cell Biol.* 20, 1032–1042. doi: 10.1038/s41556-018-0155-7
- Andersen, J. T., Gonzalez-Pajuelo, M., Foss, S., Landsverk, O. J. B., Pinto, D., Szyroki, A., et al. (2013). Selection of nanobodies that target human neonatal Fc receptor. *Sci. Rep.* 3:1118.
- Arbely, E., Torres-Kolbus, J., Deiters, A., and Chin, J. W. (2012). Photocontrol of tyrosine phosphorylation in mammalian cells via genetic encoding of photocaged tyrosine. *J. Am. Chem. Soc.* 134, 11912–11915. doi: 10.1021/ja3046958
- Ariotti, N., Hall, T. E., and Parton, R. G. (2017). Correlative light and electron microscopic detection of GFP-labeled proteins using modular APEX. *Methods Cell Biol.* 140, 105–121. doi: 10.1016/bs.mcb.2017.03.002
- Ariotti, N., Hall, T. E., Rae, J., Ferguson, C., McMahon, K. A., Martel, N., et al. (2015). Modular detection of GFP-labeled proteins for rapid screening by electron microscopy in cells and organisms. *Dev. Cell* 35, 513–525. doi: 10.1016/j.devcel.2015.10.016
- Ariotti, N., Rae, J., Giles, N., Martel, N., Sierceki, E., Gambin, Y., et al. (2018). Ultrastructural localisation of protein interactions using conditionally stable nanobodies. *PLoS Biol.* 16:e2005473. doi: 10.1371/journal.pbio.2005473
- Bannas, P., Lenz, A., Kunick, V., Fumey, W., Rissiek, B., Schmid, J., et al. (2015a). Validation of nanobody and antibody based in vivo tumor xenograft NIRF-imaging experiments in mice using ex vivo flow cytometry and microscopy. *J. Vis. Exp.* 98:e52462.
- Bannas, P., Lenz, A., Kunick, V., Well, L., Fumey, W., Rissiek, B., et al. (2015b). Molecular imaging of tumors with nanobodies and antibodies: timing and dosage are crucial factors for improved in vivo detection. *Contrast Media Mol. Imaging* 10, 367–378. doi: 10.1002/cmmi.1637
- Bazl, M. R., Rasaee, M. J., Foruzandeh, M., Rahimpour, A., Kiani, J., Rahbarizadeh, F., et al. (2007). Production of chimeric recombinant single domain antibody-green fluorescent fusion protein in Chinese hamster ovary cells. *Hybridoma* 26, 1–9. doi: 10.1089/hyb.2006.037
- Beghein, E., and Gettemans, J. (2017). Nanobody technology: a versatile toolkit for microscopic imaging, protein-protein interaction analysis, and protein function exploration. *Front. Immunol.* 8:771.
- Beltrán Hernández, I., Rompen, R., Rossin, R., Xenaki, K. T., Katrukha, E. A., Nicolay, K., et al. (2019). Imaging of tumor spheroids, dual-isotope SPECT, and autoradiographic analysis to assess the tumor uptake and distribution of different nanobodies. *Mol. Imaging Biol.* 21, 1079–1088. doi: 10.1007/s11307-019-01320-x
- Berry, L. K., Ölafsson, G., Ledesma-Fernández, E., and Thorpe, P. H. (2016). Synthetic protein interactions reveal a functional map of the cell. *eLife* 5:e13053.
- Bertier, L., Hebbrecht, T., Mettepenningen, E., De Wit, N., Zwaenepoel, O., Verhelle, A., et al. (2018). Nanobodies targeting cortactin proline rich, helical

- and actin binding regions downregulate invadopodium formation and matrix degradation in SCC-61 cancer cells. *Biomed. Pharmacother.* 102, 230–241. doi: 10.1016/j.biopha.2018.03.064
- Bleck, M., Itano, M. S., Johnson, D. S., Thomas, V. K., North, A. J., Bieniasz, P. D., et al. (2014). Temporal and spatial organization of ESCRT protein recruitment during HIV-1 budding. *Proc. Natl. Acad. Sci. U.S.A.* 111, 12211–12216. doi: 10.1073/pnas.1321655111
- Boersma, S., Khuperkar, D., Verhagen, B. M. P., Sonneveld, S., Grimm, J. B., Lavis, L. D., et al. (2019). Multi-color single-molecule imaging uncovers extensive heterogeneity in mRNA decoding. *Cell* 178, 458–472.e19.
- Braun, M. B., Traenkle, B., Koch, P. A., Emele, F., Weiss, F., Poetz, O., et al. (2016). Peptides in headlock—a novel high-affinity and versatile peptide-binding nanobody for proteomics and microscopy. *Sci. Rep.* 6:19211.
- Buchfellner, A., Yurlova, L., Nuske, S., Scholz, A. M., Bogner, J., Ruf, B., et al. (2016). A New nanobody-based biosensor to study endogenous PARP1 in vitro and in live human cells. *PLoS One* 11:e0151041. doi: 10.1371/journal.pone.0151041
- Burgess, A., Lorca, T., and Castro, A. (2012). Quantitative live imaging of endogenous DNA replication in mammalian cells. *PLoS One* 7:e45726. doi: 10.1371/journal.pone.0045726
- Buser, D. P., Schleicher, K. D., Prescianotto-Baschong, C., and Spiess, M. A. (2018). versatile nanobody-based toolkit to analyze retrograde transport from the cell surface. *Proc. Natl. Acad. Sci. U.S.A.* 115, E6227–E6236.
- Buser, D. P., and Spiess, M. (2019). Analysis of endocytic uptake and retrograde transport to the trans-golgi network using functionalized nanobodies in cultured cells. *J. Vis. Exp.* 144:e59111.
- Carrington, G., Tomlinson, D., and Peckham, M. (2019). Exploiting nanobodies and Affimers for superresolution imaging in light microscopy. *Mol. Biol. Cell* 30, 2737–2740. doi: 10.1091/mbc.e18-11-0694
- Casas-Delucchi, C., Becker, A., Bolijs, J. J., and Cardoso, M. C. (2012). Targeted manipulation of heterochromatin rescues MeCP2 Rett mutants and re-establishes higher order chromatin organization. *Nucleic Acids Res.* 40:e176. doi: 10.1093/nar/gks784
- Causinus, E., Kanca, O., and Affolter, M. (2011). Fluorescent fusion protein knockout mediated by anti-GFP nanobody. *Nat. Struct. Mol. Biol.* 19, 117–121. doi: 10.1038/nsmb.2180
- Chamma, I., Letellier, M., Butler, C., Tessier, B., Lim, K., Gauthereau, I., et al. (2016). Mapping the dynamics and nanoscale organization of synaptic adhesion proteins using monomeric streptavidin. *Nat. Commun.* 7:10773.
- Chamma, I., Rossier, O., Giannone, G., Thoumine, O., and Sainlos, M. (2017). Optimized labeling of membrane proteins for applications to super-resolution imaging in confined cellular environments using monomeric streptavidin. *Nat. Protoc.* 12, 748–763. doi: 10.1038/nprot.2017.010
- Cheloha, R. W., Li, Z., Bousbaine, D., Woodham, A. W., Perrin, P., Volarić, J., et al. (2019). Internalization of Influenza virus and cell surface proteins monitored by site-specific conjugation of protease-sensitive probes. *ACS Chem. Biol.* 14, 1836–1844. doi: 10.1021/acscchembio.9b00493
- Cheng, Y. (2018). Single-particle cryo-EM—How did it get here and where will it go. *Science* 361, 876–880. doi: 10.1126/science.aat4346
- Cramer, K., Bolender, A., Stockmar, I., Jungmann, R., Kasper, R., and Shin, J. Y. (2019). Visualization of bacterial protein complexes labeled with fluorescent proteins and nanobody binders for STED microscopy. *Int. J. Mol. Sci.* 20:3376. doi: 10.3390/ijms20143376
- Darling, T. L., Sherwood, L. J., and Hayhurst, A. (2017). Intracellular crosslinking of filoviral nucleoproteins with xintrabodies restricts viral packaging. *Front. Immunol.* 8:1197.
- De Beer, M. A., Kuipers, J., Van Bergen En Henegouwen, P. M. P., and Giepmans, B. N. G. (2018). A small protein probe for correlated microscopy of endogenous proteins. *Histochem. Cell Biol.* 149, 261–268. doi: 10.1007/s00418-018-1632-6
- De Boer, P., Hoogenboom, J. P., and Giepmans, B. N. (2015). Correlated light and electron microscopy: ultrastructure lights up! *Nat. Methods* 12, 503–513. doi: 10.1038/nmeth.3400
- De Bruin, R. C. G., Lougheed, S. M., Van Der Kruk, L., Stam, A. G., Hooijberg, E., Roovers, R. C., et al. (2016). Highly specific and potentially activating Vγ9Vδ2-T cell specific nanobodies for diagnostic and therapeutic applications. *Clin. Immunol.* 169, 128–138. doi: 10.1016/j.clim.2016.06.012
- De Clercq, S., Zwaenepoel, O., Martens, E., Vandekerckhove, J., Guillaubert, A., and Gettemans, J. (2013). Nanobody-induced perturbation of LFA-1/L-plastin phosphorylation impairs MTOC docking, immune synapse formation and T cell activation. *Cell Mol. Life Sci.* 70, 909–922. doi: 10.1007/s00018-012-1169-0
- De Genst, E., Silence, K., Decanniere, K., Conrath, K., Loris, R., Kinne, J., et al. (2006). Molecular basis for the preferential cleft recognition by dromedary heavy-chain antibodies. *Proc. Natl. Acad. Sci. U.S.A.* 103, 4586–4591. doi: 10.1073/pnas.0505379103
- De Haard, H. J. W., Bezemer, S., Ledebor, A. M., Müller, W. H., Boender, P. J., Moineau, S., et al. (2005). Llama antibodies against a lactococcal protein located at the tip of the phage tail prevent phage infection. *J. Bacteriol.* 187, 4531–4541. doi: 10.1128/jb.187.13.4531-4541.2005
- De Meyer, T., Eeckhout, D., De Rycke, R., De Buck, S., Muyldermans, S., and Depicker, A. (2014). Generation of VHH antibodies against the Arabidopsis thaliana seed storage proteins. *Plant Mol. Biol.* 84, 83–93. doi: 10.1007/s11103-013-0118-0
- Debie, P., Lafont, C., Defrise, M., Hansen, I., Van Willigen, D. M., Van Leeuwen, F. W. B., et al. (2020). Size and affinity kinetics of nanobodies influence targeting and penetration of solid tumours. *J. Control Release* 317, 34–42. doi: 10.1016/j.jconrel.2019.11.014
- Delanote, V., Vanloo, B., Catillon, M., Friederich, E., Vandekerckhove, J., and Gettemans, J. (2010). An alpaca single-domain antibody blocks filopodia formation by obstructing L-plastin-mediated F-actin bundling. *FASEB J.* 24, 105–118. doi: 10.1096/fj.09-134304
- D'Hollander, A., Jans, H., Velde, G. V., Verstraete, C., Massa, S., Devoogdt, N., et al. (2017). Limiting the protein corona: a successful strategy for in vivo active targeting of anti-HER2 nanobody-functionalized nanostars. *Biomaterials* 123, 15–23. doi: 10.1016/j.biomaterials.2017.01.007
- Dong, J. X., Lee, Y., Kirmiz, M., Palacio, S., Dumitras, C., Moreno, C. M., et al. (2019). A toolbox of nanobodies developed and validated for use as intrabodies and nanoscale immunolabels in mammalian brain neurons. *Elife* 8:48750. doi: 10.7554/eLife.48750
- Drees, C., Raj, A. N., Kurre, R., Busch, K. B., Haase, M., and Piehler, J. (2016). Engineered upconversion nanoparticles for resolving protein interactions inside living cells. *Angew. Chem. Int. Ed. Engl.* 55, 11668–11672. doi: 10.1002/anie.201603028
- Duarte, J. N., Cragolini, J. J., Sweet, L. K., Bilate, A. M., Bader, J., Ingram, J. R., et al. (2016). Generation of immunity against pathogens via single-domain antibody-antigen constructs. *J. Immunol.* 197, 4838–4847. doi: 10.1049/jimm.201600692
- Egelman, E. H. (2016). The current revolution in cryo-EM. *Biophys. J.* 110, 1008–1012. doi: 10.1016/j.bpj.2016.02.001
- Fan, X., Wang, L., Guo, Y., Tu, Z., Li, L., Tong, H., et al. (2015). Ultrasonic nanobubbles carrying Anti-PSMA nanobody: construction and application in prostate cancer-targeted imaging. *PLoS One* 10:e0127419. doi: 10.1371/journal.pone.0127419
- Fang, T., Lu, X., Berger, D., Gmeiner, C., Cho, J., Schalek, R., et al. (2018). Nanobody immunostaining for correlated light and electron microscopy with preservation of ultrastructure. *Nat. Methods* 15, 1029–1032. doi: 10.1038/s41592-018-0177-x
- Farrants, H., Tarnawski, M., Müller, T. G., Otsuka, S., Hiblot, J., Koch, B., et al. (2020). Chemogenetic control of nanobodies. *Nat. Methods* 17, 279–282. doi: 10.1038/s41592-020-0746-7
- Finnigan, G. C., Booth, E. A., Duvalyan, A., Liao, E. N., and Thorner, J. (2015). The carboxy-terminal tails of tins Cdc11 and Shs1 recruit myosin-II binding factor Bni5 to the bud neck in *Saccharomyces cerevisiae*. *Genetics* 200, 843–862. doi: 10.1534/genetics.115.176503
- Gadok, A. K., Zhao, C., Meriwether, A. I., Ferrati, S., Rowley, T. G., Zoldan, J., et al. (2018). The display of single-domain antibodies on the surfaces of connectosomes enables gap junction-mediated drug delivery to specific cell populations. *Biochemistry (N. Y.)* 57, 81–90. doi: 10.1021/acs.biochem.7b00688
- Ghosh, I., Hamilton, A. D., and Regan, L. (2000). Antiparallel leucine zipper-directed protein reassembly: application to the green fluorescent protein. *J. Am. Chem. Soc.* 122, 5658–5659. doi: 10.1021/ja994421w
- Ghosh, R. P., Franklin, J. M., Draper, W. E., Shi, Q., Beltran, B., Spakowitz, A. J., et al. (2019). A fluorogenic array for temporally unlimited single-molecule tracking. *Nat. Chem. Biol.* 15, 401–409. doi: 10.1038/s41589-019-0241-6
- Giepmans, B. N., Adams, S. R., Ellisman, M. H., and Tsien, R. Y. (2006). The fluorescent toolbox for assessing protein location and function. *Science* 312, 217–224. doi: 10.1126/science.1124618



- Giepmans, B. N., Deerinck, T. J., Smarr, B. L., Jones, Y. Z., and Ellisman, M. H. (2005). Correlated light and electron microscopic imaging of multiple endogenous proteins using Quantum dots. *Nat. Methods* 2, 743–749. doi: 10.1038/nmeth791
- Göttfert, F., Pleiner, T., Heine, J., Westphal, V., Görlich, D., Sahl, S. J., et al. (2017). Strong signal increase in STED fluorescence microscopy by imaging regions of subdiffraction extent. *Proc. Natl. Acad. Sci. U.S.A.* 114, 2125–2130. doi: 10.1073/pnas.1621495114
- Gotzke, H., Kilisch, M., Martinez-Carranza, M., Sograte-Idrissi, S., Rajavel, A., Schlichthaefer, T., et al. (2019). The ALFA-tag is a highly versatile tool for nanobody-based bioscience applications. *Nat. Commun.* 10:4403.
- Groot, A. J., Verheesen, P., Westerlaken, E. J., Gort, E. H., Van Der Groep, P., Bovenschen, N., et al. (2006). Identification by phage display of single-domain antibody fragments specific for the ODD domain in hypoxia-inducible factor 1 $\alpha$ . *Lab. Invest.* 86, 345–356. doi: 10.1038/labinvest.3700395
- Gross, C., Wiesmann, V., Millen, S., Kalmer, M., Wittenberg, T., Gettemans, J., et al. (2016). The tax-inducible actin-bundling protein fascin is crucial for release and cell-to-cell transmission of human T-cell leukemia virus type 1 (HTLV-1). *PLoS Pathog.* 12:e1005916. doi: 10.1371/journal.ppat.1005916
- Hafian, H., Sukhanova, A., Turini, M., Chames, P., Baty, D., Pluot, M., et al. (2014). Multiphoton imaging of tumor biomarkers with conjugates of single-domain antibodies and quantum dots. *Nanomedicine* 10, 1701–1709. doi: 10.1016/j.nano.2014.05.014
- Hamers-Casterman, C., Atarhouch, T., Muyldermans, S., Robinson, G., Hamers, C., Songa, E. B., et al. (1993). Naturally occurring antibodies devoid of light chains. *Nature* 363, 446–448. doi: 10.1038/363446a0
- Han, Y., Branon, T. C., Martell, J. D., Boassa, D., Shechner, D., Ellisman, M. H., et al. (2019). Directed evolution of split APEX2 peroxidase. *ACS Chem. Biol.* 14, 619–635. doi: 10.1021/acscchembio.8b00919
- Han, Z., Zhang, B., Wang, Y. E., Zuo, Y. Y., and Su, W. W. (2012). Self-assembled amyloid-like oligomeric-cohesin Scaffoldin for augmented protein display on the saccharomyces cerevisiae cell surface. *Appl. Environ. Microbiol.* 78, 3249–3255. doi: 10.1128/aem.07745-11
- Harmansa, S., Alborelli, I., Bieli, D., Caussinus, E., and Affolter, M. (2017). A nanobody-based toolset to investigate the role of protein localization and dispersal in *Drosophila*. *eLife* 6:e22549.
- Harmansa, S., Hamaratoglu, F., Affolter, M., and Caussinus, E. (2015). Dpp spreading is required for medial but not for lateral wing disc growth. *Nature* 527, 317–322. doi: 10.1038/nature15712
- Harmen, M. M., and De Haard, H. J. (2007). Properties, production, and applications of camelid single-domain antibody fragments. *Appl. Microbiol. Biotechnol.* 77, 13–22. doi: 10.1007/s00253-007-1142-2
- Harper, C. B., Papadopoulos, A., Martin, S., Matthews, D. R., Morgan, G. P., Nguyen, T. H., et al. (2016). Botulinum neurotoxin type-A enters a non-recycling pool of synaptic vesicles. *Sci. Rep.* 6:19654.
- Hebbrecht, T., Liu, J., Zwaenepoel, O., Boddin, G., Van Leene, C., Decoene, K., et al. (2020). Nanobody click chemistry for convenient site-specific fluorescent labelling, single step immunocytochemistry and delivery into living cells by photoporation and live cell imaging. *N. Biotechnol.* 59, 33–43. doi: 10.1016/j.nbt.2020.05.004
- Hebbrecht, T., Van Audenhove, I., Zwaenepoel, O., Verhelle, A., and Gettemans, J. V. C. A. (2017). nanobodies target N-WASP to reduce invadopodium formation and functioning. *PLoS One* 12:e0185076. doi: 10.1371/journal.pone.0185076
- Helma, J., Cardoso, M. C., Muyldermans, S., and Leonhardt, H. (2015). Nanobodies and recombinant binders in cell biology. *J. Cell Biol.* 209, 633–644. doi: 10.1083/jcb.201409074
- Helma, J., Schmidthals, K., Lux, V., Nuske, S., Scholz, A. M., Krausslich, H. G., et al. (2012). Direct and dynamic detection of HIV-1 in living cells. *PLoS One* 7:e50026. doi: 10.1371/journal.pone.0050026
- Herce, H. D., Deng, W., Helma, J., Leonhardt, H., and Cardoso, M. C. (2013). Visualization and targeted disruption of protein interactions in living cells. *Nat. Commun.* 4:2660.
- Herce, H. D., Schumacher, D., Schneider, A. F. L., Ludwig, A. K., Mann, F. A., Fillies, M., et al. (2017). Cell-permeable nanobodies for targeted immunolabelling and antigen manipulation in living cells. *Nat. Chem.* 9, 762–771. doi: 10.1038/nchem.2811
- Hu, C. D., and Kerppola, T. K. (2003). Simultaneous visualization of multiple protein interactions in living cells using multicolor fluorescence complementation analysis. *Nat. Biotechnol.* 21, 539–545. doi: 10.1038/nbt816
- Huang, Y., Nokhrin, S., Hassanzadeh-Ghassabeh, G., Yu, C. H., Yang, H., Barry, A. N., et al. (2014). Interactions between metal-binding domains modulate intracellular targeting of Cu(I)-ATPase ATP7B, as revealed by nanobody binding. *J. Biol. Chem.* 289, 32682–32693. doi: 10.1074/jbc.M114.580845
- Iqbal, U., Albaghdadi, H., Luo, Y., Arbabi, M., Desvaux, C., Veres, T., et al. (2010a). Molecular imaging of glioblastoma multiforme using anti-insulin-like growth factor-binding protein-7 single-domain antibodies. *Br. J. Cancer* 103, 1606–1616. doi: 10.1038/sj.bjc.6605937
- Iqbal, U., Trojahn, U., Albaghdadi, H., Zhang, J., O'Connor-McCourt, M., Stanimirovic, D., et al. (2010b). Kinetic analysis of novel mono- and multivalent VHH-fragments and their application for molecular imaging of brain tumours. *Br. J. Pharmacol.* 160, 1016–1028. doi: 10.1111/j.1476-5381.2010.00742.x
- Irannejad, R., Tomshine, J. C., Tomshine, J. R., Chevalier, M., Mahoney, J. P., Steyaert, J., et al. (2013). Conformational biosensors reveal GPCR signalling from endosomes. *Nature* 495, 534–538. doi: 10.1038/nature12000
- Jacobson, K., Rajfur, Z., Vitriol, E., and Hahn, K. (2008). Chromophore-assisted laser inactivation in cell biology. *Trends Cell Biol.* 18, 443–450. doi: 10.1016/j.tcb.2008.07.001
- Joensuu, M., Padmanabhan, P., Durisic, N., Bademosi, A. T., Cooper-Williams, E., Morrow, I. C., et al. (2016). Subdiffractional tracking of internalized molecules reveals heterogeneous motion states of synaptic vesicles. *J. Cell Biol.* 215, 277–292. doi: 10.1083/jcb.201604001
- Joshi, B. S., de Beer, M. A., Giepmans, B. N. G., and Zuhorn, I. S. (2020). Endocytosis of extracellular vesicles and release of their cargo from endosomes. *ACS Nano* 14, 4444–4455. doi: 10.1021/acsnano.9b10033
- Jullien, D., Vignard, J., Fedor, Y., B ry, N., Olichon, A., Crozatier, M., et al. (2016). Chromatibody, a novel non-invasive molecular tool to explore and manipulate chromatin in living cells. *J. Cell Sci.* 129, 2673–2683. doi: 10.1242/jcs.183103
- Kamiyama, D., McGorty, R., Kamiyama, R., Kim, M. D., Chiba, A., and Huang, B. (2015). Specification of dendritogenesis site in *Drosophila* aCC motoneuron by membrane enrichment of Pak1 through Dscam1. *Dev. Cell* 35, 93–106. doi: 10.1016/j.devcel.2015.09.007
- Kaplan, C., and Ewers, H. (2015). Optimized sample preparation for single-molecule localization-based superresolution microscopy in yeast. *Nat. Protoc.* 10, 1007–1021. doi: 10.1038/nprot.2015.060
- Karges, J., Jakubaszek, M., Mari, C., Zarschler, K., Goud, B., Stephan, H., et al. (2019). Synthesis and characterization of an epidermal growth factor receptor-selective Ru(II) Polypyridyl-nanobody conjugate as a photosensitizer for photodynamic therapy. *ChemBiochem* 4, 531–542. doi: 10.1002/cbic.201900419
- Katoh, Y., Nozaki, S., Hartanto, D., Miyano, R., and Nakayama, K. (2015). Architectures of multisubunit complexes revealed by a visible immunoprecipitation assay using fluorescent fusion proteins. *J. Cell Sci.* 128, 2351–2362. doi: 10.1242/jcs.168740
- Katrakha, E. A., Mikhaylova, M., Van Brakel, H. X., Van Bergen En Henegouwen, P. M., Akhmanova, A., Hoogenraad, C. C., et al. (2017). Probing cytoskeletal modulation of passive and active intracellular dynamics using nanobody-functionalized quantum dots. *Nat. Commun.* 8:14772.
- Kawano, F., Suzuki, H., Furuya, A., and Sato, M. (2015). Engineered pairs of distinct photoswitches for optogenetic control of cellular proteins. *Nat. Commun.* 6:6256.
- Keppeler, A., Gendreizig, S., Gronemeyer, T., Pick, H., Vogel, H., and Johnsson, K. A. (2003). general method for the covalent labeling of fusion proteins with small molecules in vivo. *Nat. Biotechnol.* 21, 86–89. doi: 10.1038/nbt765
- Kijanka, M., Van Donselaar, E. G., Muller, W. H., Dorrestijn, B., Popov-Celeketi, D., El Khattabi, M., et al. (2017). A novel immuno-gold labeling protocol for nanobody-based detection of HER2 in breast cancer cells using immuno-electron microscopy. *J. Struct. Biol.* 199, 1–11. doi: 10.1016/j.jsb.2017.05.008
- Kijanka, M., Warnders, F. J., El Khattabi, M., Lub-de Hooge, M., Van Dam, G. M., Ntziachristos, V., et al. (2013). Rapid optical imaging of human breast tumour xenografts using anti-HER2 VHHs site-directly conjugated to IRDye 800CW for image-guided surgery. *Eur. J. Nucl. Med. Mol. Imaging* 40, 1718–1729. doi: 10.1007/s00259-013-2471-2
- Kirchofer, A., Helma, J., Schmidthals, K., Frauer, C., Cui, S., Karcher, A., et al. (2010). Modulation of protein properties in living cells using nanobodies. *Nat. Struct. Mol. Biol.* 17, 133–138. doi: 10.1038/nsmb.1727



- Klamecka, K., Severin, P. M., Milles, L. F., Gaub, H. E., and Leonhardt, H. (2015). Energy profile of nanobody-GFP complex under force. *Phys. Biol.* 12:056009. doi: 10.1088/1478-3975/12/5/056009
- Klein, A., Hank, S., Raulf, A., Joest, E. F., Tissen, F., Heilemann, M., et al. (2018). Live-cell labeling of endogenous proteins with nanometer precision by transduced nanobodies. *Chem. Sci.* 9, 7835–7842. doi: 10.1039/c8sc02910e
- Kooijmans, S. A. A., Aleza, C. G., Roffler, S. R., Van Solinge, W. W., Vader, P., and Schiffelers, R. M. (2016). Display of GPI-anchored anti-EGFR nanobodies on extracellular vesicles promotes tumour cell targeting. *J. Extracell. Vesicles* 5:31053. doi: 10.3402/jev.v5.31053
- Krūwel, T., Nevoltris, D., Bode, J., Dullin, C., Baty, D., Chames, P., et al. (2016). In vivo detection of small tumour lesions by multi-pinhole SPECT applying a (99m)Tc-labelled nanobody targeting the Epidermal Growth Factor Receptor. *Sci. Rep.* 6:21834.
- Kühlbrandt, W. (2014). Biochemistry. The resolution revolution. *Science* 343, 1443–1444.
- Kuipers, J., Van Ham, T. J., Kalicharan, R. D., Veenstra-Algra, A., Sjollem, K. A., Dijk, F., et al. (2015). FLIPPER, a combinatorial probe for correlated live imaging and electron microscopy, allows identification and quantitative analysis of various cells and organelles. *Cell Tissue Res.* 360, 61–70. doi: 10.1007/s00441-015-2142-7
- Künzl, F., Fröhlich, S., Fäßler, F., Li, B., and Pimpl, P. (2016). Receptor-mediated sorting of soluble vacuolar proteins ends at the trans-Golgi network/early endosome. *Nat. Plants* 2:16017.
- Lam, S. S., Martell, J. D., Kamer, K. J., Deerinck, T. J., Ellisman, M. H., Mootha, V. K., et al. (2015). Directed evolution of APEX2 for electron microscopy and proximity labeling. *Nat. Methods* 12, 51–54. doi: 10.1038/nmeth.3179
- Laverty, D., Desai, R., Uchański, T., Masiulis, S., Stec, W. J., Malinauskas, T., et al. (2019). Cryo-EM structure of the human  $\alpha 1\beta 3\gamma 2$  GABA(A) receptor in a lipid bilayer. *Nature* 565, 516–520.
- Li, T., Bourgeois, J., Celli, S., Glacial, F., Le Sourd, A., Mecheri, S., et al. (2012). Cell-penetrating anti-GFAP VHH and corresponding fluorescent fusion protein VHH-GFP spontaneously cross the blood-brain barrier and specifically recognize astrocytes: application to brain imaging. *FASEB J.* 26, 3969–3979. doi: 10.1096/fj.11-201384
- Li, T., Vandesquille, M., Koukoulis, F., Duffeffant, C., Youssef, I., Lenormand, P., et al. (2016). Camelid single-domain antibodies: a versatile tool for in vivo imaging of extracellular and intracellular brain targets. *J. Control Release* 243, 1–10. doi: 10.1016/j.jconrel.2016.09.019
- Lutje Hulsik, D., Liu, Y., Strokappe, N. M., Battella, S., El Khattabi, M., McCoy, L. E., et al. (2013). A gp41 MPEP-specific llama VHH requires a hydrophobic CDR3 for neutralization but not for antigen recognition. *PLoS Pathog.* 9:e1003202. doi: 10.1371/journal.ppat.1003202
- Ma, J., Kelch, J. M., Junod, S. L., and Yang, W. (2017). Super-resolution mapping of scaffold nucleoporins in the nuclear pore complex. *J. Cell Sci.* 130, 1299–1306. doi: 10.1242/jcs.193912
- Maidon, M., Olichon, A., Rizzoli, S. O., and Opazo, F. (2019). Nanobodies reveal an extra-synaptic population of SNAP-25 and Syntaxin 1A in hippocampal neurons. *MABs* 11, 305–321. doi: 10.1080/19420862.2018.1551675
- Maier, J., Traenkle, B., and Rothbauer, U. (2015). Real-time analysis of epithelial-mesenchymal transition using fluorescent single-domain antibodies. *Sci. Rep.* 5:13402.
- Maier, J., Traenkle, B., and Rothbauer, U. (2016). Visualizing epithelial-mesenchymal transition using the chromobody technology. *Cancer Res.* 76, 5592–5596. doi: 10.1158/0008-5472.can-15-3419
- Maiuri, T., Mocle, A. J., Hung, C. L., Xia, J., Van Roon-Mom, W. M., and Truant, R. (2017). Huntingtin is a scaffolding protein in the ATM oxidative DNA damage response complex. *Hum. Mol. Genet.* 26, 395–406.
- Mann, F. A., Lv, Z., Großhans, J., Opazo, F., and Kruss, S. (2019). Nanobody-conjugated nanotubes for targeted near-infrared in vivo imaging and sensing. *Angew. Chem. Int. Ed. Engl.* 58, 11469–11473. doi: 10.1002/anie.201904167
- Martell, J. D., Yamagata, M., Deerinck, T. J., Phan, S., Kwa, C. G., Ellisman, M. H., et al. (2016). A split horseradish peroxidase for the detection of intercellular protein-protein interactions and sensitive visualization of synapses. *Nat. Biotechnol.* 34, 774–780. doi: 10.1038/nbt.3563
- Martinez-Jothar, L., Beztsinna, N., Van Nostrum, C. F., Hennink, W. E., and Oliveira, S. (2019). Selective cytotoxicity to HER2 positive breast cancer cells by saporin-loaded nanobody-targeted polymeric nanoparticles in combination with photochemical internalization. *Mol. Pharm.* 16, 1633–1647. doi: 10.1021/acs.molpharmaceut.8b01318
- Masiulis, S., Desai, R., Uchański, T., Serna Martin, I., Laverty, D., Karia, D., et al. (2019). GABA(A) receptor signalling mechanisms revealed by structural pharmacology. *Nature* 565, 454–459. doi: 10.1038/s41586-018-0832-5
- Mazzega, E., Beran, A., Cabrini, M., and De Marco, A. (2019). In vitro isolation of nanobodies for selective Alexandrium minutum recognition: a model for convenient development of dedicated immuno-reagents to study and diagnostic toxic unicellular algae. *Harmful Algae* 82, 44–51. doi: 10.1016/j.hal.2019.01.002
- McMahon, C., Baier, A. S., Pascolutti, R., Wegrecki, M., Zheng, S., Ong, J. X., et al. (2018). Yeast surface display platform for rapid discovery of conformationally selective nanobodies. *Nat. Struct. Mol. Biol.* 25, 289–296. doi: 10.1038/s41594-018-0028-6
- Mikhaylova, M., Cloin, B. M., Finan, K., Van Den Berg, R., Teeuw, J., Kijanka, M. M., et al. (2015). Resolving bundled microtubules using anti-tubulin nanobodies. *Nat. Commun.* 6:7933.
- Monegal, A., Ami, D., Martinelli, C., Huang, H., Aliprandi, M., Capasso, P., et al. (2009). Immunological applications of single-domain llama recombinant antibodies isolated from a naive library. *Protein. Eng. Des. Sel.* 22, 273–280. doi: 10.1093/protein/gzp002
- Mootz, H. D., Jedlitzke, B., Yilmaz, Z., and Dörner, W. (2019). Photobodies: light-activatable single-domain antibody fragments. *Angew. Chem. Int. Ed. Engl.* 59, 1506–1510. doi: 10.1002/anie.201912286
- Moutel, S., Bery, N., Bernard, V., Keller, L., Lemesre, E., De Marco, A., et al. (2016). NaLi-H1: A universal synthetic library of humanized nanobodies providing highly functional antibodies and intrabodies. *Elife* 5:e16228.
- Muyldermans, S. (2013). Nanobodies: natural single-domain antibodies. *Annu. Rev. Biochem.* 82, 775–797. doi: 10.1146/annurev-biochem-063011-092449
- Muyldermans, S., Cambillau, C., and Wyns, L. (2001). Recognition of antigens by single-domain antibody fragments: the superfluous luxury of paired domains. *Trends Biochem. Sci.* 26, 230–235. doi: 10.1016/s0968-0004(01)01790-x
- Nieuwenhuizen, R. P. J., Bates, M., Szymborska, A., Lidke, K. A., Rieger, B., and Stallinga, S. (2015). Quantitative localization microscopy: effects of photophysics and labeling stoichiometry. *PLoS One* 10:e0127989. doi: 10.1371/journal.pone.0127989
- Oba, M., and Tanaka, M. (2012). Intracellular internalization mechanism of protein transfection reagents. *Biol. Pharm. Bull.* 35, 1064–1068. doi: 10.1248/bpb.b12-00001
- Obishakin, E., Stijlemans, B., Santi-Rocca, J., Vandenberghe, I., Devreese, B., Muldermans, S., et al. (2014). Generation of a nanobody targeting the paraflagellar rod protein of trypanosomes. *PLoS One* 9:e115893. doi: 10.1371/journal.pone.0115893
- Olichon, A., and Surrey, T. (2007). Selection of genetically encoded fluorescent single domain antibodies engineered for efficient expression in *Escherichia coli*. *J. Biol. Chem.* 282, 36314–36320. doi: 10.1074/jbc.m704908200
- Oliveira, S., Van Dongen, G. A., Stigter-Van Walsum, M., Roovers, R. C., Stam, J. C., Mali, W., et al. (2012). Rapid visualization of human tumor xenografts through optical imaging with a near-infrared fluorescent anti-epidermal growth factor receptor nanobody. *Mol. Imaging* 11, 33–46.
- Osswald, M., Santos, A. F., and Morais-de-Sá, E. (2019). Light-induced protein clustering for optogenetic interference and protein interaction analysis in *Drosophila* S2 cells. *Biomolecules* 9:61. doi: 10.3390/biom9020061
- Pani, A. M., and Goldstein, B. (2018). Direct visualization of a native Wnt in vivo reveals that a long-range Wnt gradient forms by extracellular dispersal. *eLife* 7:e38325.
- Panza, P., Maier, J., Schmees, C., Rothbauer, U., and Sollner, C. (2015). Live imaging of endogenous protein dynamics in zebrafish using chromobodies. *Development* 142, 1879–1884. doi: 10.1242/dev.118943
- Pellis, M., Pardon, E., Zolghadr, K., Rothbauer, U., Vincke, C., Kinne, J., et al. (2012). A bacterial-two-hybrid selection system for one-step isolation of intracellularly functional Nanobodies. *Arch. Biochem. Biophys.* 526, 114–123. doi: 10.1016/j.abb.2012.04.023
- Periz, J., Whitelaw, J., Harding, C., Gras, S., Del Rosario Minina, M. I., Latorre-Barragan, F., et al. (2017). Toxoplasma gondii F-actin forms an extensive filamentous network required for material exchange and parasite maturation. *Elife* 6:e24119.

- Pizzo, M. E., Wolak, D. J., Kumar, N. N., Brunette, E., Brunnquell, C. L., Hannocks, M., et al. (2018). Intrathecal antibody distribution in the rat brain: surface diffusion, perivascular transport and osmotic enhancement of delivery. *J. Physiol. (Lond.)* 596, 445–475. doi: 10.1113/jp275105
- Platonova, E., Winterflood, C. M., and Ewers, H. (2015a). A simple method for GFP- and RFP-based dual color single-molecule localization microscopy. *ACS Chem. Biol.* 10, 1411–1416. doi: 10.1021/acscchembio.5b00046
- Platonova, E., Winterflood, C. M., Junemann, A., Albrecht, D., Faix, J., and Ewers, H. (2015b). Single-molecule microscopy of molecules tagged with GFP or RFP derivatives in mammalian cells using nanobody binders. *Methods* 88, 89–97. doi: 10.1016/j.ymeth.2015.06.018
- Pleiner, T., Bates, M., and Gorlich, D. (2018). A toolbox of anti-mouse and anti-rabbit IgG secondary nanobodies. *J. Cell Biol.* 217, 1143–1154. doi: 10.1083/jcb.201709115
- Pleiner, T., Bates, M., Trakhanov, S., Lee, C., Schliep, J. E., Chug, H., et al. (2015). Nanobodies: site-specific labeling for super-resolution imaging, rapid epitope-mapping and native protein complex isolation. *eLife* 4:e11349.
- Plessner, M., Melak, M., Chinchilla, P., Baarlink, C., and Grosse, R. (2015). Nuclear F-actin formation and reorganization upon cell spreading. *J. Biol. Chem.* 290, 11209–11216. doi: 10.1074/jbc.m114.627166
- Popovic, M., Mazzega, E., Toffoletto, B., and De Marco, A. (2018). Isolation of anti-extra-cellular vesicle single-domain antibodies by direct panning on vesicle-enriched fractions. *Microb. Cell Fact.* 17:6.
- Prole, D. L., and Taylor, C. W. (2019). A genetically encoded toolkit of functionalized nanobodies against fluorescent proteins for visualizing and manipulating intracellular signalling. *BMC Biol.* 17:41.
- Rajan, M., Mortusewicz, O., Rothbauer, U., Hastert, F. D., Schmidthals, K., Rapp, A., et al. (2015). Generation of an alpaca-derived nanobody recognizing  $\gamma$ -H2AX. *FEBS Open Bio.* 5, 779–788. doi: 10.1016/j.fob.2015.09.005
- Rakovich, T. Y., Mahfoud, O. K., Mohamed, B. M., Prina-Mello, A., Crosbie-Staunton, K., Van Den Broeck, T., et al. (2014). Highly sensitive single domain antibody-quantum dot conjugates for detection of HER2 biomarker in lung and breast cancer cells. *ACS Nano* 8, 5682–5695. doi: 10.1021/nn500212h
- Ramos-Gomes, F., Bode, J., Sukhanova, A., Bozrova, S. V., Saccomano, M., Mitkovski, M., et al. (2018). Single- and two-photon imaging of human micrometastases and disseminated tumour cells with conjugates of nanobodies and quantum dots. *Sci. Rep.* 8:4595.
- Rashidian, M., Keliher, E. J., Bilate, A. M., Duarte, J. N., Wojtkiewicz, G. R., Jacobsen, J. T., et al. (2015). Noninvasive imaging of immune responses. *Proc. Natl. Acad. Sci. U.S.A.* 112, 6146–6151.
- Riazi, A., Strong, P. C. R., Coleman, R., Chen, W., Hiram, T., Van Faassen, H., et al. (2013). Pentavalent single-domain antibodies reduce *Campylobacter jejuni* motility and colonization in chickens. *PLoS One* 8:e83928. doi: 10.1371/journal.pone.0083928
- Ries, J., Kaplan, C., Platonova, E., Eghlidi, H., and Ewers, H. A. (2012). simple, versatile method for GFP-based super-resolution microscopy via nanobodies. *Nat. Methods* 9, 582–584. doi: 10.1038/nmeth.1991
- Rocchetti, A., Hawes, C., and Kriechbaumer, V. (2014). Fluorescent labelling of the actin cytoskeleton in plants using a cameloid antibody. *Plant Methods* 10:12. doi: 10.1186/1746-4811-10-12
- Roder, R., Helma, J., Preiss, T., Radler, J. O., Leonhardt, H., and Wagner, E. (2017). Intracellular delivery of nanobodies for imaging of target proteins in live cells. *Pharm. Res.* 34, 161–174. doi: 10.1007/s11095-016-2052-8
- Rodriguez, E. A., Campbell, R. E., Lin, J. Y., Lin, M. Z., Miyawaki, A., Palmer, A. E., et al. (2017). The growing and glowing toolbox of fluorescent and photoactive proteins. *Trends Biochem. Sci.* 42, 111–129. doi: 10.1016/j.tibs.2016.09.010
- Roebroek, T., Duwé, S., Vandenberg, W., and Dedecker, P. (2015). Reduced fluorescent protein switching fatigue by binding-induced emissive state stabilization. *Int. J. Mol. Sci.* 2017:5869.
- Rothbauer, U., Zolghadr, K., Muyldermans, S., Schepers, A., Cardoso, M. C., and Leonhardt, H. (2008). A versatile nanotrap for biochemical and functional studies with fluorescent fusion proteins. *Mol. Cell. Proteomics* 7, 282–289. doi: 10.1074/mcp.m700342-mcp200
- Rothbauer, U., Zolghadr, K., Tillib, S., Nowak, D., Schermelleh, L., Gahl, A., et al. (2006). Targeting and tracing antigens in live cells with fluorescent nanobodies. *Nat. Methods* 3, 887–889. doi: 10.1038/nmeth953
- Schermelleh, L., Ferrand, A., Huser, T., Eggeling, C., Sauer, M., Biehlmaier, O., et al. (2019). Super-resolution microscopy demystified. *Nat. Cell Biol.* 21, 72–84. doi: 10.1038/s41556-018-0251-8
- Schmidthals, K., Helma, J., Zolghadr, K., Rothbauer, U., and Leonhardt, H. (2010). Novel antibody derivatives for proteome and high-content analysis. *Anal. Bioanal. Chem.* 397, 3203–3208. doi: 10.1007/s00216-010-3657-0
- Schnell, U., Dijk, F., Sjollem, K. A., and Giepmans, B. N. (2012). Immunolabeling artifacts and the need for live-cell imaging. *Nat. Methods* 9, 152–158. doi: 10.1038/nmeth.1855
- Schornack, S., Fuchs, R., Huitema, E., Rothbauer, U., Lipka, V., and Kamoun, S. (2009). Protein mislocalization in plant cells using a GFP-binding chromobody. *Plant J.* 60, 744–754. doi: 10.1111/j.1365-3113.2009.03982.x
- Schorpp, K., Rothenaigner, I., Maier, J., Traenkle, B., Rothbauer, U., and Hadian, K. (2016). A multiplexed high-content screening approach using the chromobody technology to identify cell cycle modulators in living cells. *J. Biomol. Screen* 21, 965–977. doi: 10.1177/1087057116641935
- Seitz, K. J., and Rizzoli, S. O. (2019). GFP nanobodies reveal recently-exocytosed pHluorin molecules. *Sci. Rep.* 9:7773.
- Sherwood, L. J., and Hayhurst, A. (2019). Periplasmic nanobody-APEX2 fusions enable facile visualization of ebola, marburg, and mǎnglǎ virus nucleoproteins, alluding to similar antigenic landscapes among marburgvirus and dianlovirus. *Viruses* 11:364. doi: 10.3390/v11040364
- Shi, J., Ma, Y., Zhu, J., Chen, Y., Sun, Y., Yao, Y., et al. (2018). A review on electroporation-based intracellular delivery. *Molecules* 23:3044. doi: 10.3390/molecules23113044
- Shin, Y. J., Park, S. K., Jung, Y. J., Kim, Y. N., Kim, K. S., Park, O. K., et al. (2015). Nanobody-targeted E3-ubiquitin ligase complex degrades nuclear proteins. *Sci. Rep.* 5:14269.
- Sograte-Idrissi, S., Oleksievets, N., Isbaner, S., Eggert-Martinez, M., Enderlein, J., Tsukanov, R., et al. (2019). Nanobody detection of standard fluorescent proteins enables multi-target DNA-PAINT with high resolution and minimal displacement errors. *Cells* 8:48. doi: 10.3390/cells8010048
- Southwell, A. L., Khoshnan, A., Dunn, D. E., Bugg, C. W., Lo, D. C., and Patterson, P. H. (2008). Intrabodies binding the proline-rich domains of mutant huntingtin increase its turnover and reduce neurotoxicity. *J. Neurosci.* 28, 9013–9020. doi: 10.1523/jneurosci.2747-08.2008
- Stewart, M. P., Lorenz, A., Dahlman, J., and Sahay, G. (2016). Challenges in carrier-mediated intracellular delivery: moving beyond endosomal barriers. *Wiley Interdiscip. Rev. Nanomed. Nanobiotechnol.* 8, 465–478. doi: 10.1002/wnan.1377
- Stijlemans, B., Conrath, K., Cortez-Retamozo, V., Van Xong, H., Wyns, L., Senter, P., et al. (2004). Efficient targeting of conserved cryptic epitopes of infectious agents by single domain antibodies. African trypanosomes as paradigm. *J. Biol. Chem.* 279, 1256–1261. doi: 10.1074/jbc.m307341200
- Sungskaworn, T., Jobin, M., Burnecki, K., Weron, A., Lohse, M. J., and Calebiro, D. (2017). Single-molecule imaging reveals receptor-G protein interactions at cell surface hot spots. *Nature* 550, 543–547. doi: 10.1038/nature24264
- Szymborska, A., De Marco, A., Daigle, N., Cordes, V. C., Briggs, J. A. G., and Ellenberg, J. (2013). Nuclear pore scaffold structure analyzed by super-resolution microscopy and particle averaging. *Science* 341, 655–658. doi: 10.1126/science.1240672
- Tanenbaum, M. E., Gilbert, L. A., Qi, L. S., Weissman, J. S., and Vale, R. D. A. (2014). protein-tagging system for signal amplification in gene expression and fluorescence imaging. *Cell* 159, 635–646. doi: 10.1016/j.cell.2014.09.039
- Tang, A., Chen, H., Li, T. P., Metzbowser, S. R., MacGillivray, H. D., and Blanpied, T. A. (2016a). A trans-synaptic nanocolumn aligns neurotransmitter release to receptors. *Nature* 536, 210–214. doi: 10.1038/nature19058
- Tang, J. C., Drokhlyanskyy, E., Etemad, B., Rudolph, S., Guo, B., Wang, S., et al. (2016b). Detection and manipulation of live antigen-expressing cells using conditionally stable nanobodies. *Elife* 5:e15312.
- Temme, S., Baran, P., Bouvain, P., Grapentin, C., Krämer, W., Knebel, B., et al. (2018). Synthetic cargo internalization receptor system for nanoparticle tracking of individual cell populations by fluorine magnetic resonance imaging. *ACS Nano* 12, 11178–11192. doi: 10.1021/acsnano.8b05698
- Teng, K. W., Ishitsuka, Y., Ren, P., Youn, Y., Deng, X., Ge, P., et al. (2016). Labeling proteins inside living cells using external fluorophores for microscopy. *Elife* 5:e20378.

- Tomanek, B., Iqbal, U., Blasiak, B., Abulrob, A., Albaghdadi, H., Matyas, J. R., et al. (2012). Evaluation of brain tumor vessels specific contrast agents for glioblastoma imaging. *Neuro Oncol.* 14, 53–63. doi: 10.1093/neuonc/nor183
- Tosetti, N., Dos Santos Pacheco, N., Soldati-Favre, D., and Jacot, D. (2019). Three F-actin assembly centers regulate organelle inheritance, cell-cell communication and motility in *Toxoplasma gondii*. *Elife* 8:e42669.
- Traenkle, B., Emele, F., Anton, R., Poetz, O., Haeussler, R. S., Maier, J., et al. (2015). Monitoring interactions and dynamics of endogenous beta-catenin with intracellular nanobodies in living cells. *Mol. Cell Proteomics* 14, 707–723. doi: 10.1074/mcp.m114.044016
- Traenkle, B., and Rothbauer, U. (2017). Under the microscope: single-domain antibodies for live-cell imaging and super-resolution microscopy. *Front. Immunol.* 8:1030.
- Traenkle, B., Segan, S., Fagbadebo, F. O., Kaiser, P. D., and Rothbauer, U. (2020). A novel epitope tagging system to visualize and monitor antigens in live cells with chromobodies. *Sci. Rep.* 10:14267.
- Traub, L. M. (2019). A nanobody-based molecular toolkit provides new mechanistic insight into clathrin-coat initiation. *Elife* 8:e41768.
- Truan, Z., Tarancón Díez, L., Bönsch, C., Malkusch, S., Endesfelder, U., Munteanu, M., et al. (2013). Quantitative morphological analysis of arrestin2 clustering upon G protein-coupled receptor stimulation by super-resolution microscopy. *J. Struct. Biol.* 184, 329–334. doi: 10.1016/j.jsb.2013.09.019
- Tsien, R. Y. (1998). The green fluorescent protein. *Annu. Rev. Biochem.* 67, 509–544.
- Uchański, T., Pardon, E., and Steyaert, J. (2020). Nanobodies to study protein conformational states. *Curr. Opin. Struct. Biol.* 60, 117–123. doi: 10.1016/j.sbi.2020.01.003
- Van Audenhove, I., Boucherie, C., Pieters, L., Zwaenepoel, O., Vanloo, B., Martens, E., et al. (2014). Stratifying fascin and cortactin function in invadopodium formation using inhibitory nanobodies and targeted subcellular delocalization. *FASEB J.* 28, 1805–1818. doi: 10.1096/fj.13-242537
- Van Audenhove, I., Debeuf, N., Boucherie, C., and Gettemans, J. (2015). Fascin actin bundling controls podosome turnover and disassembly while cortactin is involved in podosome assembly by its SH3 domain in THP-1 macrophages and dendritic cells. *Biochim. Biophys. Acta* 1853, 940–952. doi: 10.1016/j.bbamcr.2015.01.003
- Van Audenhove, I., and Gettemans, J. (2016). Nanobodies as versatile tools to understand, diagnose, visualize and treat cancer. *EBioMedicine* 6, 40–48. doi: 10.1016/j.ebiom.2016.04.028
- Van Audenhove, I., Van Impe, K., Ruano-Gallego, D., De Clercq, S., De Muynck, K., Vanloo, B., et al. (2013). Mapping cytoskeletal protein function in cells by means of nanobodies. *Cytoskeleton (Hoboken)*. 70, 604–622. doi: 10.1002/cm.21122
- Van De Water, J. A. J. M., Bagci-Onder, T., Agarwal, A. S., Wakimoto, H., Roovers, R. C., Zhu, Y., et al. (2012). Therapeutic stem cells expressing variants of EGFR-specific nanobodies have antitumor effects. *Proc. Natl. Acad. Sci. U.S.A.* 109, 16642–16647. doi: 10.1073/pnas.1202832109
- Van Den Abbeele, A., De Clercq, S., De Ganck, A., De Corte, V., Van Loo, B., Soror, S. H., et al. (2010). A llama-derived gelsolin single-domain antibody blocks gelsolin-G-actin interaction. *Cell Mol. Life Sci.* 67, 1519–1535. doi: 10.1007/s00018-010-0266-1
- Van Driel, P. B. A. A., Boonstra, M. C., Slooter, M. D., Heukers, R., Stammes, M. A., Snoeks, T. J. A., et al. (2016). EGFR targeted nanobody-photosensitizer conjugates for photodynamic therapy in a pre-clinical model of head and neck cancer. *J. Control Release* 229, 93–105. doi: 10.1016/j.jconrel.2016.03.014
- Van Impe, K., Hubert, T., De Corte, V., Vanloo, B., Boucherie, C., Vandekerckhove, J., et al. (2008). A new role for nuclear transport factor 2 and Ran: nuclear import of CapG. *Traffic* 9, 695–707. doi: 10.1111/j.1600-0854.2008.00720.x
- Virant, D., Traenkle, B., Maier, J., Kaiser, P. D., Bodenhofer, M., Schmees, C., et al. (2018). A peptide tag-specific nanobody enables high-quality labeling for dSTORM imaging. *Nat. Commun.* 9:930.
- Wang, Y., Cai, E., Rosenkranz, T., Ge, P., Teng, K. W., Lim, S. J., et al. (2014). Small quantum dots conjugated to nanobodies as immunofluorescence probes for nanometric microscopy. *Bioconj. Chem.* 25, 2205–2211. doi: 10.1021/bc5004179
- Wedeking, T., Löchte, S., Richter, C. P., Bhagawati, M., Piehler, J., and You, C. (2015). Single cell GFP-trap reveals stoichiometry and dynamics of cytosolic protein complexes. *Nano Lett.* 15, 3610–3615. doi: 10.1021/acs.nanolett.5b01153
- Wegner, W., Ilgen, P., Gregor, C., Van Dort, J., Mott, A. C., Steffens, H., et al. (2017). In vivo mouse and live cell STED microscopy of neuronal actin plasticity using far-red emitting fluorescent proteins. *Sci. Rep.* 7:11781.
- Wendel, S., Fischer, E. C., Martínez, V., Seppälä, S., and Norholm, M. H. H. (2016). A nanobody:GFP bacterial platform that enables functional enzyme display and easy quantification of display capacity. *Microb. Cell Fact.* 15:71.
- Wolf, K., and Friedl, P. (2009). Mapping proteolytic cancer cell-extracellular matrix interfaces. *Clin. Exp. Metastasis* 26, 289–298. doi: 10.1007/s10585-008-9190-2
- Wöll, S., Bachran, C., Schiller, S., Schröder, M., Conrad, L., Swee, L. K., et al. (2018). Sortagable liposomes: evaluation of reaction conditions for single-domain antibody conjugation by Sortase-A and targeting of CD11b(+) myeloid cells. *Eur. J. Pharm. Biopharm.* 133, 138–150. doi: 10.1016/j.ejpb.2018.09.017
- Yu, D., Lee, H., Hong, J., Jung, H., Jo, Y., Oh, B. H., et al. (2019). Optogenetic activation of intracellular antibodies for direct modulation of endogenous proteins. *Nat. Methods* 16, 1095–1100. doi: 10.1038/s41592-019-0592-7
- Zarschler, K., Prapainop, K., Mahon, E., Rocks, L., Bramini, M., Kelly, P. M., et al. (2014). Diagnostic nanoparticle targeting of the EGF-receptor in complex biological conditions using single-domain antibodies. *Nanoscale* 6, 6046–6056. doi: 10.1039/c4nr00595c
- Zhao, Y., Araki, S., Wu, J., Teramoto, T., Chang, Y., Nakano, M., et al. (2011). An expanded palette of genetically encoded Ca<sup>2+</sup> indicators. *Science* 333, 1888–1891. doi: 10.1126/science.1208592
- Zheng, F., Luo, S., Ouyang, Z., Zhou, J., Mo, H., Schoonoooghe, S., et al. (2019). NIRF-molecular imaging with synovial macrophages-targeting vsig4 nanobody for disease monitoring in a mouse model of arthritis. *Int. J. Mol. Sci.* 20:3347. doi: 10.3390/ijms20133347
- Zou, T., Dembele, F., Beugnet, A., Sengmanivong, L., Trepout, S., Marco, S., et al. (2015). Nanobody-functionalized PEG-b-PCL polymersomes and their targeting study. *J. Biotechnol.* 214, 147–155. doi: 10.1016/j.biotech.2015.09.034
- Zuo, J., Li, J., Zhang, R., Xu, L., Chen, H., Jia, X., et al. (2017). Institute collection and analysis of Nanobodies (iCAN): a comprehensive database and analysis platform for nanobodies. *BMC Genomics* 18:797.

**Conflict of Interest:** The authors declare that the research was conducted in the absence of any commercial or financial relationships that could be construed as a potential conflict of interest.

Copyright © 2020 de Beer and Giepmans. This is an open-access article distributed under the terms of the Creative Commons Attribution License (CC BY). The use, distribution or reproduction in other forums is permitted, provided the original author(s) and the copyright owner(s) are credited and that the original publication in this journal is cited, in accordance with accepted academic practice. No use, distribution or reproduction is permitted which does not comply with these terms.



# NEXT-GENERATION GENETICALLY-ENCODED FLUORESCENT SENSORS

EDITED BY: Elizabeth C. Carroll and Shai Berlin

PUBLISHED IN: Frontiers in Cellular Neuroscience



**frontiers** Research Topics





# frontiers

## Frontiers eBook Copyright Statement

The copyright in the text of individual articles in this eBook is the property of their respective authors or their respective institutions or funders. The copyright in graphics and images within each article may be subject to copyright of other parties. In both cases this is subject to a license granted to Frontiers.

The compilation of articles constituting this eBook is the property of Frontiers.

Each article within this eBook, and the eBook itself, are published under the most recent version of the Creative Commons CC-BY licence.

The version current at the date of publication of this eBook is CC-BY 4.0. If the CC-BY licence is updated, the licence granted by Frontiers is automatically updated to the new version.

When exercising any right under the CC-BY licence, Frontiers must be attributed as the original publisher of the article or eBook, as applicable.

Authors have the responsibility of ensuring that any graphics or other materials which are the property of others may be included in the CC-BY licence, but this should be checked before relying on the CC-BY licence to reproduce those materials. Any copyright notices relating to those materials must be complied with.

Copyright and source acknowledgement notices may not be removed and must be displayed in any copy, derivative work or partial copy which includes the elements in question.

All copyright, and all rights therein, are protected by national and international copyright laws. The above represents a summary only. For further information please read Frontiers' Conditions for Website Use and Copyright Statement, and the applicable CC-BY licence.

ISSN 1664-8714

ISBN 978-2-88966-401-6

DOI 10.3389/978-2-88966-401-6

## About Frontiers

Frontiers is more than just an open-access publisher of scholarly articles: it is a pioneering approach to the world of academia, radically improving the way scholarly research is managed. The grand vision of Frontiers is a world where all people have an equal opportunity to seek, share and generate knowledge. Frontiers provides immediate and permanent online open access to all its publications, but this alone is not enough to realize our grand goals.

## Frontiers Journal Series

The Frontiers Journal Series is a multi-tier and interdisciplinary set of open-access, online journals, promising a paradigm shift from the current review, selection and dissemination processes in academic publishing. All Frontiers journals are driven by researchers for researchers; therefore, they constitute a service to the scholarly community. At the same time, the Frontiers Journal Series operates on a revolutionary invention, the tiered publishing system, initially addressing specific communities of scholars, and gradually climbing up to broader public understanding, thus serving the interests of the lay society, too.

## Dedication to Quality

Each Frontiers article is a landmark of the highest quality, thanks to genuinely collaborative interactions between authors and review editors, who include some of the world's best academicians. Research must be certified by peers before entering a stream of knowledge that may eventually reach the public - and shape society; therefore, Frontiers only applies the most rigorous and unbiased reviews.

Frontiers revolutionizes research publishing by freely delivering the most outstanding research, evaluated with no bias from both the academic and social point of view. By applying the most advanced information technologies, Frontiers is catapulting scholarly publishing into a new generation.

## What are Frontiers Research Topics?

Frontiers Research Topics are very popular trademarks of the Frontiers Journals Series: they are collections of at least ten articles, all centered on a particular subject. With their unique mix of varied contributions from Original Research to Review Articles, Frontiers Research Topics unify the most influential researchers, the latest key findings and historical advances in a hot research area! Find out more on how to host your own Frontiers Research Topic or contribute to one as an author by contacting the Frontiers Editorial Office: [researchtopics@frontiersin.org](mailto:researchtopics@frontiersin.org)

# NEXT-GENERATION GENETICALLY-ENCODED FLUORESCENT SENSORS

Topic Editors:

**Elizabeth C. Carroll**, Delft University of Technology, Netherlands

**Shai Berlin**, Technion Israel Institute of Technology, Israel

**Citation:** Carroll, E. C., Berlin, S., eds. (2021). Next-Generation Genetically-Encoded Fluorescent Sensors. Lausanne: Frontiers Media SA.  
doi: 10.3389/978-2-88966-401-6

# Table of Contents

- 04 Editorial: Next-Generation Genetically-Encoded Fluorescent Sensors**  
Shai Berlin and Elizabeth C. Carroll
- 06 Development and Application of Sub-Mitochondrial Targeted  $\text{Ca}^{2+}$  Biosensors**  
Markus Waldeck-Weiermair, Benjamin Gottschalk, Corina T. Madreiter-Sokolowski, Jeta Ramadani-Muja, Gabriela Ziomek, Christiane Klec, Sandra Burgstaller, Helmut Bischof, Maria R. Depaoli, Emrah Eroglu, Roland Malli and Wolfgang F. Graier
- 18 Fluorescent Biosensors for Neurotransmission and Neuromodulation: Engineering and Applications**  
Anna V. Leopold, Daria M. Shcherbakova and Vladislav V. Verkhusa
- 36 Engineering Photoactivatability in Genetically Encoded Voltage and pH Indicators**  
Sungmoo Lee, Yoon-Kyu Song and Bradley J. Baker
- 46 Biosensors Show the Pharmacokinetics of S-Ketamine in the Endoplasmic Reticulum**  
Kallol Bera, Aron Kamajaya, Amol V. Shivange, Anand K. Muthusamy, Aaron L. Nichols, Philip M. Borden, Stephen Grant, Janice Jeon, Elaine Lin, Ishak Bishara, Theodore M. Chin, Bruce N. Cohen, Charlene H. Kim, Elizabeth K. Unger, Lin Tian, Jonathan S. Marvin, Loren L. Looger and Henry A. Lester
- 58 Live-Cell Assays for Cell Stress Responses Reveal New Patterns of Cell Signaling Caused by Mutations in Rhodopsin,  $\alpha$ -Synuclein and TDP-43**  
Kevin M. Harlen, Elizabeth C. Roush, Joseph E. Clayton, Scott Martinka and Thomas E. Hughes
- 72 Reversible Loss of Hippocampal Function in a Mouse Model of Demyelination/Remyelination**  
Aniruddha Das, Chinthasagar Bastian, Lexie Trestan, Jason Suh, Tanujit Dey, Bruce D. Trapp, Selva Baltan and Hod Dana
- 84 A Bright and Colorful Future for G-Protein Coupled Receptor Sensors**  
Luca Ravotto, Loïc Duffet, Xuehan Zhou, Bruno Weber and Tommaso Patriarchi
- 93 Red Photoactivatable Genetic Optical-Indicators**  
Wessal Hussein and Shai Berlin
- 107 Nanobody-Based Probes for Subcellular Protein Identification and Visualization**  
Marit A. de Beer and Ben N. G. Giepmans

# Advantages of publishing in Frontiers



## OPEN ACCESS

Articles are free to read  
for greatest visibility  
and readership



## FAST PUBLICATION

Around 90 days  
from submission  
to decision



## HIGH QUALITY PEER-REVIEW

Rigorous, collaborative,  
and constructive  
peer-review



## TRANSPARENT PEER-REVIEW

Editors and reviewers  
acknowledged by name  
on published articles

## Frontiers

Avenue du Tribunal-Fédéral 34  
1005 Lausanne | Switzerland

Visit us: [www.frontiersin.org](http://www.frontiersin.org)

Contact us: [info@frontiersin.org](mailto:info@frontiersin.org) | +41 21 510 17 00



## REPRODUCIBILITY OF RESEARCH

Support open data  
and methods to enhance  
research reproducibility



## DIGITAL PUBLISHING

Articles designed  
for optimal readership  
across devices



## FOLLOW US

@frontiersin



## IMPACT METRICS

Advanced article metrics  
track visibility across  
digital media



## EXTENSIVE PROMOTION

Marketing  
and promotion  
of impactful research



## LOOP RESEARCH NETWORK

Our network  
increases your  
article's readership